Photonic Integrated Circuits for the Generation of Coherent Optical Signals

Padraic Morrissey
BSc
105428963

NATIONAL UNIVERSITY OF IRELAND, CORK

Faculty of Science

Department of Physics

Thesis submitted for the degree of Doctor of Philosophy

July 2014

Supervisor: Dr. Frank Peters

Head of Department/School: Prof. John McInerney

Contents

List of Figures v
List of Tables xiv
Acknowledgements xvii
Abstract xviii
List of Publications xix
Glossary xx

1 Introduction **1**
1.1 Optical Communications 1
1.2 Photonics and Photonics Systems 4
1.2.1 Advanced Modulation Formats 6
1.2.2 Modulation of optical signals 8
1.2.2.1 Electro-optic modulators 9
1.2.2.2 Electro-absorption modulators 12
1.2.2.3 Compact high speed QPSK EAM based modulator . 12
1.3 Photonic Integration 15
1.3.1 Hybrid Integration 17
1.3.2 Monolithic Integration 17
1.4 Optical Injection Locking 18
1.5 Thesis Motivation and Outline 19
1.5.1 Thesis Motivation 19
1.5.2 Thesis Outline 23

2 Optical Waveguides and Couplers **25**
2.1 Planar Waveguides 25
2.1.1 Graphical Solution Method of Slab Waveguide 29
2.1.2 Root Solving Method of Slab Waveguide 31
2.2 Rectangular Waveguides 33
2.2.1 Effective Index Method 35
2.3 Multimode Interference Couplers 37
2.3.1 MMI Design using Modal Propagation Analysis 39
2.3.2 Internal Reflections in MMIs 43
2.3.3 Fabrication Tolerances of MMIs 43
2.4 Conclusion 44

3 MMI Modelling and Optimisation **46**
3.1 Introduction 46
3.2 MMI Design using Modal Propagation Analysis 47
3.2.1 Effective Index Method Modal Propagation Analysis 47
3.2.1.1 1 x M MMI Couplers 53
3.2.1.2 M × N MMI Couplers 55
3.2.2 Scalar Finite Element Modal Propagation Analysis 57
3.2.3 Comparison between SFEM MPA and EIM MPA 59
3.3 MMIs as Single Mode Filters 61
3.4 MMI Design Optimisation 63
3.4.1 MMI Optimisation using EIM-MPA 63
3.4.2 MMI Parameter Optimisation 64
3.4.2.1 Predicted results from Theory and Simulation 67

3.4.2.2 Compact MMI Couplers . . . 68
3.5 MMIs with Fabrication Errors . . . 69
3.5.1 Lithography . . . 70
3.5.1.1 Fabrication Errors in MMI Length . . . 70
3.5.1.2 Fabrication Errors in MMI Width . . . 72
3.5.1.3 Fabrication Errors in MMI Width & Length . . . 74
3.5.2 Over & Under Etching . . . 75
3.6 Design and Testing of MMIs . . . 79
3.7 Conclusion . . . 82

4 Testing of Passive Waveguide Devices 83
4.1 Introduction . . . 83
4.2 Facet Scan Imaging . . . 85
4.3 Experimental Setup . . . 87
4.4 Optimising Waveguide Coupling . . . 88
4.4.1 Facet Edge and Lensed Fibre Focus . . . 89
4.4.2 Reflection Scan . . . 90
4.4.3 Scanning Transmitted Power . . . 92
4.4.4 Quick and Efficient Coupling . . . 96
4.5 Conclusion . . . 97

5 Photonic Integrated Circuit Design 98
5.1 Introduction . . . 98
5.2 Tunable Lasers for Photonic Integration . . . 99
5.3 Photonic Integrated Circuit Development . . . 100
5.3.1 Material Structure . . . 101
5.3.2 Waveguide Structure . . . 102
5.3.3 Multimode Interference Coupler Design . . . 103
5.3.4 Waveguide Taper Design . . . 105
5.3.5 Lasers for device integration . . . 106
5.3.5.1 Fabry Pérot Lasers . . . 106
5.3.5.2 Slotted Fabry Pérot Lasers . . . 107
5.3.6 Device Fabrication Steps . . . 109
5.4 Design/Layout of Photonic Integrated Devices . . . 110
5.4.1 PICDraw . . . 110
5.4.2 Layout of MMIs and SOAs . . . 111
5.4.3 Layout of Slotted Fabry Pérot Lasers . . . 113
5.4.4 Layout of Integrated Devices . . . 113
5.4.4.1 Integrated SFP Laser Power Splitter . . . 113
5.4.4.2 Integrated System of Mutually Coupled SFP Lasers . . . 115
5.4.5 Full Lithographical Mask Layout . . . 116
5.5 Conclusions . . . 119

6 Photonic Integrated Circuit Characterisation and Testing 121
6.1 Introduction . . . 121
6.2 Fabricated Devices . . . 121
6.3 Photonic Integrated Circuit Testing . . . 124
6.4 Fabry Pérot Laser Characterization . . . 125
6.4.1 FP Laser Testing . . . 125
6.4.2 FP Laser Optical Spectra and LIV Curves . . . 127

6.4.3 Group Index Calculation . . . 128
6.4.4 Slotted Fabry Pérot Laser Characterisation . . . 129
6.4.5 Tuning Maps of SFP Lasers . . . 133
6.4.6 Relaxation Oscillations . . . 137
6.5 SFP laser integrated with SOA and MMI . . . 138
6.6 Conclusion . . . 142

7 Injection Locking of Slotted Fabry Pérot Lasers 143
7.1 Introduction . . . 143
7.2 Injection Locking of Slotted Fabry Pérot Lasers to an external Tunable Laser Source . . . 144
7.3 Optical Phase Locking of Integrated Single Facet Slotted Fabry Pérot Lasers . . . 148
7.3.1 Phase Locking of Single Facet Slotted Fabry Pérot Lasers - Off Chip Locking . . . 150
7.3.2 Phase Locking of Single Facet Slotted Fabry Pérot Lasers - On Chip Locking . . . 152
7.3.3 Phase Locking of Single Facet Slotted Fabry Pérot Lasers - Variable Gain . . . 155
7.4 Simultaneous Injection Locking and Coherent Signals . . . 158
7.4.1 Free-Running Slotted Fabry Pérot Lasers . . . 159
7.4.2 Optically Phase Locked Slotted Fabry Pérot Lasers . . . 161
7.4.3 Coherence of Phase Locked Slotted Fabry Pérot Lasers . . . 163
7.5 Conclusion . . . 166

8 Conclusions and Future Work 168
8.1 Outlook and Future Work . . . 170
8.2 Summary . . . 172

A Matlab MMI Optimisation Code 191
A.1 MMI Code . . . 191
A.1.1 Main MMI Code . . . 192
A.1.2 MMI Subroutine . . . 193
A.1.3 Mode Solver Subroutine . . . 196
A.1.4 Overlap Subroutine . . . 197
A.1.5 Propagation Subroutine . . . 199

B Star Coupler Design 200
B.1 Star Couplers . . . 200
B.2 Gaussian Mode Analysis . . . 201
B.3 Star Coupler Design using Gaussian Mode Analysis . . . 204

C Comparison of Optimising MMIs using SFEM-MPA & EIM-MPA 209
C.1 InP based waveguides . . . 209
C.2 Si based waveguides . . . 211

D Ridge Waveguide Processing 214
D.1 Processing of a Ridge Waveguide . . . 214

E Compound Semiconductor Device Fabrication Ridge Laser Process 216
E.1 Ridge Laser Structure . . . 216

E.1.1 Ridge Lithography 217
E.1.2 Oxide Opening Lithography 218
E.1.3 P-Metal Lift-Off Lithography 218
E.1.4 Substrate Thinning and Chip Preparation 219

List of Figures

1.1 Growth of internet users per year [1, 2]. 1
1.2 Total number of internet users by geographical region [1, 2]. 2
1.3 Percentage of population with internet access based on geographical regions [1, 2]. 2
1.4 The international measured and predicted data rates per year [3]. . . . 3
1.5 Schematic outline of a WDM system. 4
1.6 Optical spectra from a trial using 96×12.3 Gb/s channels. (a) Shows the input signal while (b) shows the output spectrum after being transmitted 9000 km. 5
1.7 Basic modulation formats. 7
1.8 Advanced modulation formats. 8
1.9 A typical Mach-Zehnder modulator. By controlling the optical phase in each arm, constructive or destructive interference can be formed at the output. 10
1.10 Nested Mach-Zehnder modulators can be used to generate QPSK modulation schemes. 10
1.11 (a) A fabricated MZM from the Technische Universiteit Eindhoven [4]. (b) A fabricated traveling-wave based IQ Modulator formed from dual nested Mach-Zehnder modulators (NTT). 11
1.12 Schematic of an EAM based modulator. 12
1.13 EAM based IQ Modulator [5]. C. R. Doerr, et al. 13
1.14 Symbol configurations achievable for a QPSK modulation scheme by controlling the operational states of integrated EAMs. 14
1.15 EAM Based IQ Modulator [5]. C. R. Doerr, et al. 14
1.16 Large, power hungry photonic system setups. Tyndall National Institute. 15
1.17 (a) Photonic integrated circuits. Infinera. (b) InP monolithic tunable optical router (MOTOR) [6]. 16
1.18 Different techniques for monolithic photonic integration [7]. 18
1.19 Schematic of a typical injection locking experimental setup used to investigate a master-slave system. 19
1.20 An EAM based QPSK modulator with integrated SFP lasers. 20
1.21 SFP laser integrated with an MMI coupler and SOA. The building block of more advanced PICs. 21
1.22 Schematic of the most complicated PIC considered in this thesis. Multiple SFP lasers integrated together using an MMI coupler and SOA based optical interconnect. 22

2.1 Planar optical waveguide structure showing the refractive index variation across the layers. 26
2.2 Decay of the electric field distribution of waveguide mode into cladding and substrate layers. 28
2.3 Graphical solution method for finding propagation constants of different waveguide modes. 30
2.4 Results from the graphical solution method. 31
2.5 Plot of *F(v,m,b)*. The roots can be used to determine the effective index of each guided mode in a waveguide structure. 32
2.6 E_y and H_y components of TE and TM mode solutions. 33

2.7 Variations of Rectangular Waveguides. 33
2.8 Structure of a typical rib waveguide which can be modelled using SFEM mode solver tools. 34
2.9 Mode profile of an InP based rib waveguide as calculated from the SFEM mode solver [8]. 34
2.10 Rectangular waveguide is split into three separate regions. The effective index of the guided modes in each region can then be calculated by treating it has a slab waveguide. 35
2.11 The calculated effective indices in each region are used to form a new slab waveguide. The propagation constants of this waveguide determines the propagation constants of the original rectangular waveguide. . . . 36
2.12 (a) E_y field component of the TE mode of a two-dimensional waveguide in the x and y-directions. (b) full two-dimensional E_y component mode profile, which is a product of the separable x and y E_y field components of the mode. 37
2.13 TE field distribution of an MMI. The input field is re-imaged at specific points along the length of the MMI. Light can be decoupled from the MMI by placing output waveguides at these points. Figure generated using the MMI design tools developed during this work. 38
2.14 Schematic outline of an MMI. 39
2.15 Field distribution in an MMI at various increments along its length. . 42

3.1 Ridge waveguide structure with dimensions labelled. 47
3.2 Labelled MMI schematic. 48
3.3 (a) E_y component of TE mode field distribution of the input waveguide mode. (b) E_y component of TE modes supported in MMI region. . . 49
3.4 (a) Effective index of supported modes in MMI region. (b) Overlap coefficient of support modes in MMI region with input waveguide mode. 49
3.5 (a) Fresnel reflection coefficient between input and MMI supported waveguide modes. (b) Fresnel reflection coefficient between input and MMI supported waveguide modes weighted to the MMI mode Fourier coefficient. 50
3.6 Coupling efficiency of a 1×1 MMI along the length of the structure. The optimum length of the MMI can be determined by finding the peak of the coupling. 52
3.7 Re-imaged mode at an MMI length of L_{MMI}, overlapped with mode of the input waveguide. 52
3.8 TE field distribution of the optical field in an MMI. The input field is re-imaged at the end of the device. At the midway point the field is clearly shown to form two images of the input mode. 53
3.9 Coupling to the output waveguides of a 1×2 MMI as the length is varied from 0 to L_{MMI}. 53
3.10 Field distribution at the end of a 1×2 MMI. Two self-images of the input field to MMI are formed. 54
3.11 Electric field distribution in an MMI with W_{MMI} of 8.5 µm. Figure (a) demonstrates that two self-images of the input mode can be found at a particular length along the device, thereby forming a 1×2 splitter. Figure (b) shows that at a shorter length, the same MMI can generate three self-images of the input mode and form a 1×3 splitter. 55
3.12 Schematic of a 2×2 MMI Coupler. 56

3.13 Field distribution a 2×2. The input field to one port is re-imaged at the end of the MMI on the opposite port. 56
3.14 Field distribution a 2×2. The input field is re-imaged over both output ports of the MMI at the end of the device. 57
3.15 TE modes as calculated from the SFEM code of [8] for waveguides of various etch depths. (a) Etch=0.5 µm (b) Etch=0.7 µm (c) Etch=1.0 µm (d) Etch=1.25 µm. 58
3.16 SFEM code can be used to calculate higher order modes of arbitrary waveguide structures. 58
3.17 Field distribution of a 1×2 MMI as calculated using the two dimensional SFEM-MPA MMI solver. 59
3.18 Comparison between SFEM-MPA and EIM-MPA MMI solvers when calculating optimum MMI lengths for MMIs with increasing width. Excellent agreement is seen between both solvers. 60
3.19 (a) Second order excited mode of input waveguide.(b) Third order excited mode of input waveguide. 62
3.20 Field distribution of an optimally designed 1×2 MMI after being excited by the second order mode of the input waveguide. Almost no power couples to both output waveguides causing the MMI to act as an efficient single mode filter. 62
3.21 Field distribution of an optimally designed 1×2 MMI after being excited by the third order mode of the input waveguide. The MMI offers partial filtering of the mode. 63
3.22 (a) Maximum MMI coupling efficiency and optimised MMI length versus MMI waveguide width. (b) Close up view of maximum MMI coupling efficiency versus MMI width. Peak in coupling efficiency for an MMI of width 9.0 µm. 65
3.23 (a) Optimised max coupling efficiency of MMIs versus MMI width, as the input waveguide width is varied. (b) Close up view of maximum MMI coupling efficiency versus MMI width as input waveguide width is varied. Peak in coupling efficiency for each input waveguide width is indicated. 66
3.24 Optimised MMI length, as calculated from EIM-MPA, versus MMI width. 67
3.25 Optimised output waveguide separation, as calculated from EIM-MPA, versus MMI width. 67
3.26 Comparison between the analytical and computationally determined values of the MMI length to act as an efficient MMI coupler. 68
3.27 (a) Schematic of an MMI with fabrication error in the length of the device only. (b) Schematic of an MMI with fabrication error in the width of the device only. 70
3.28 Coupling efficiency versus fabrication error in MMI length and MMI width. 71
3.29 Coupling efficiency versus fabrication error as the MMI input waveguide width was varied. 71
3.30 Coupling efficiency versus fabrication error and MMI width. 72
3.31 Variation of MMI coupling efficiency as the MMI input waveguide width is varied versus fabrication error. 73

3.32 Maximised fabrication tolerances of MMIs due induced errors, as the input waveguide width is varied with MMI width optimised at each variation. . . . 73
3.33 Coupling efficiency of MMIs with induced errors in MMI width, overlapped with coupling efficiency of the same MMI with induced errors in both the MMI width and length. . . . 74
3.34 Schematic of a ridge waveguide where over or under etching of the ridge from the optimum depth can be seen. . . . 75
3.35 Max coupling efficiency of an MMI versus increasing etch depth. For shallow etches, the MMI displays poor coupling efficiency. The MMI performance increases as the waveguide approaches a deep etched structure. . . . 76
3.36 Shallow etch (a) and deep etch (b) waveguide structures. . . . 76
3.37 Ridge waveguide with induced errors in the etch depth. . . . 77
3.38 Coupling efficiency of deep and shallow etched MMIs versus error in the ridge etch depth. . . . 78
3.39 Quantum well based waveguide structure for MMI designs. . . . 79
3.40 A single MMI with major dimensions labelled. . . . 80
3.41 Fabricated MMIs with variations in length from the optically designed values. Provides a means of experimentally validating the EIM-MPA model for designing MMIs. . . . 80
3.42 Comparison between simulated and experimentally tested MMI designs. 81

4.1 A lensed fibre optimally coupled to a ridge waveguide. . . . 83
4.2 Lensed fibres aligned to the facets of an optical waveguide under test. 84
4.3 Principle of the facet scan imaging technique. As a lensed fibre moves across a ridge waveguide the back reflected light from incident light on the facet is measured. . . . 85
4.4 Reflected power as a facet scan is performed on the waveguide shown in Figure 4.3. . . . 86
4.5 Experimental setup shoing the a device under test. Computer controlled stages are used to provide fibre alignment in the XYZ directions. . . . 87
4.6 Schematic outline of the experimental used to align fibres using the facet scan technique. . . . 88
4.7 Structure of ridge waveguide used in the development of this fibre to waveguide coupling technique. . . . 89
4.8 Focusing of lensed fibres on waveguide facets. . . . 90
4.9 Reflection scans of facets showing waveguide ridge features. . . . 91
4.10 Cross section of reflection scan in the vertical direction as the lensed fibre sweeps over waveguide facet. . . . 92
4.11 Cross section of reflection scan in the horizontal direction as the lensed fibre sweeps across waveguide ridge. . . . 92
4.12 Transmitted power scans of waveguide facets. . . . 93
4.13 Contour plot of transmitted power measured as lensed fibre is scanned on (a) input and (b) output side of the optical circuit. Data is overlapped with reflection scan data from corresponding ridge waveguide. Contours represent convolution of the ridge waveguide mode with fibre mode. . 94
4.14 Calculated TE mode of the ridge waveguide used in the development of this waveguide to fibre coupling technique. . . . 95

5.1 Schematic of a single slot. 99
5.2 Schematic of multiple slots etched into a ridge waveguide structure. . . 100
5.3 Waveguide structure of the integrated devices. 102
5.4 Supported modes in waveguide structure as calculated from the SFEM mode solver. 103
5.5 Optimised MMI designs. 104
5.6 Simulation of linear tapers as waveguide width was increased from 2.5 µm to 3.5 µm. 105
5.7 A single slot 106
5.8 A schematic of a single facet slotted Fabry Pérot laser. 107
5.9 SEMs of T-Bar slots. 108
5.10 Lithographical steps required to fabricate the integrated devices. . . . 109
5.11 Example of an echelle grating as defined by PICDraw software. 110
5.12 Example on an MMI coupler as generated from PICDraw software. . . 111
5.13 1×2 MMI structure as defined on the PIC mask. The Figure shows MMI region contact pad to drive MMI section to transparency along with the common contact for MMI output bends and short SOA waveguide interconnect between SFP laser and MMI region. 112
5.14 Layout of SF-SFP laser as defined on the PIC mask. Green dashed line indicates the cleaved facet. Reflections from cleaved faceted and slots in the mirror section are also indicated. 113
5.15 Layout of an integrated device which combines an SF-SFP laser with an SOA and a 1×2 or 1×3 MMI coupler. 114
5.16 Optical and electrical solation slots. 115
5.17 Layout of an integrated device which combines an SF-SFP laser with an SOA and a 1×2 or 1×3 MMI coupler with further SF-SFP lasers integrated at MMI outputs. 116
5.18 Block of "Test Structure Devices" which can be cleaved and tested together experimentally. Consists of FP lasers, SFP lasers and test MMI structures. 117
5.19 Close up view of cleave marks which indicate the position of cleave planes on devices. 117
5.20 Block of integrated SFP devices. Consists of single facet SFP lasers integrated with SOAs, MMIs and output SFP lasers. Output SFP lasers can be cleaved off to investigate integration of SFPs with 1×2 and 1×3 power splitters. 118
5.21 Block of integrated SFP devices. Consists of single facet SFP lasers integrated with SOAs, MMIs and output SFP lasers. Output SFP lasers can be cleaved off to investigate integration of SFPs with 1×2 and 1×3 power splitters. 118
5.22 Photonic Integrated Circuit. 119

6.1 Fabricated PIC on $\frac{1}{4}$ inch wafer prior to any cleaving of devices. . . . 122
6.2 Test structure devices prior to cleaving. 123
6.3 Close up of integrated devices where multiple slotted Fabry Pérot lasers are coupled together though an MMI and SOA section. 123

6.4 Experimental setup showing a photonic device under test. Multiple probes were used to apply electrical current to individual sections of the device and were controlled using XYZ probe manipulators. Lensed fibres were coupled to the input and output waveguides of the device, where the light could be examined. 124
6.5 Experimental setup showing external probe manipulators positioned around an integrated device under test. 125
6.6 SEM images of the ridge waveguide after cleaving. (a) Shows the cleaved facet with deposited gold on top of the waveguide ridge. (b) Shows a broad area image of the deposited metal which connects to contact pads for probing. 126
6.7 Fabricated FP laser under test. Figure shows external probe making contact with large contact pad. 126
6.8 IV curve of FP lasers for various ridge waveguide widths. 127
6.9 LI curve of FP lasers for various ridge waveguide widths. 127
6.10 Free-running FP optical spectrum with ridge waveguide width of 2.5 µm while biased to 90 mA. 128
6.11 Close up view of free-running optical spectra of FP laser biased at 90 mA. Resonator modes are clearly visible. 129
6.12 SEM images of T-Bar slots. (a) Shows a close up view of a T-Bar slot where T structure can clearly be seen. (b) Shows a plan view of the slot where the deposited metal and oxide window opening are visible. . . . 130
6.13 Fabricated single facet slotted Fabry Pérot laser under test. Probes are in contact with metal contact pads to apply a bias across the mirror and gain sections of the laser. The lensed fiber is also shown where it is positioned close to the waveguide facet to collect the output light. . . 130
6.14 IV curve of the SFP laser under different mirror section biases. 131
6.15 LI curve of the SFP laser under different mirror section biases. 132
6.16 Free-running optical spectrum of the SFP laser under test. 132
6.17 Variation of SFP optical spectra with mirror section bias held fixed while the gain section bias was swept between 0 mA to 100 mA 133
6.18 Close up view of SFP spectral output with the gain section bias swept between 40 mA and 90 mA. The output was found to be tunable over this range. 134
6.19 SMSR of laser output spectra as the SFP mirror and gain sections were both biased. 134
6.20 Peak wavelength of the SFP optical spectra as the mirror and gain sections were both biased. 135
6.21 Modal behaviour of the SFP spectral output as the SFP mirror and gain sections were both biased. Z-axis indicates the multimode nature of the waveguide at particular biases. 136
6.22 Multimodal output of the SFP laser for a gain and mirror section bias of 80 mA and 50 mA respectively. 137
6.23 Power spectrum of SFP laser output as the gain section bias was varied with mirror section bias held fixed. Relaxation oscillations are observed. 137
6.24 Experimental testing of a device with a tunable laser integrated with an optical power splitter and SOA/VOA section. The device offers the first demonstration of an on chip integrated source and power splitter using monolithic integration requiring only a single growth step. 138

6.25 Optical spectra as measured from the cleaved facet of the SFP and MMI output waveguides, as the SOA regions were forward biased. 141
6.26 Overlapped optical spectra from the cleaved facet of the SFP and MMI output waveguides, as the SOA regions were forward biased. 142

7.1 Image of the PIC under test. A single SFP laser was integrated at the input of a 1×3 MMI which had three further SFPs integrated on its output arms. The input and central output SFPs were both probed which allowed for current injection into the different sections of each laser. 144
7.2 Outline of a typical injection locking setup. 145
7.3 Spectral output of the SFP with injected signal from the TLS. The mode chosen to be injected to is at 1565 nm where the detuned TLS input can also be seen. 145
7.4 OSA traces from SFP laser as the TLS wavelength was swept across resonance with a chosen mode of the SFP. Two different TLS powers are considered where the effect of higher injected powers can be seen. For close to zero detuning in both cases, significant suppression of the side modes of the SFP was observed and the SFP lases strongly at the injected wavelength. 146
7.5 ESA traces from SFP laser as the TLS wavelength was swept across resonance with a chosen mode of the SFP. The beat note between the two signals is observed and a quiet region is observed at close to zero detuning. 147
7.6 Schematic of PIC. Single Facet SFP Lasers are integrated at the input and outputs of a 1x3 MMI. The input SFP is used as the master laser in this experiment and can be tuned by varying the currents $I_{Gain\ 1}$ and $I_{Mirror\ 1}$. The central output SFP is used as the slave laser and can be tuned by varying the currents $I_{Gain\ 2}$ and $I_{Mirror\ 2}$. The outer SFPs are unbiased. 149
7.7 Experimental setup showing the off-chip coupling scheme between two lasers on the same integrated device. The waveguide interconnect linking both lasers was reverse biased to - 2V which removed any coupling between them on chip. Instead, light from the master laser was coupled via a circulator to the slave laser. 150
7.8 OSA trace from the S-SFP as the injected signal from the M-SFP was swept across resonance of one of its lasing modes. For close to zero detuning, suppression of the optical side modes was observed and SFP 2 was shown to lase strongly at the injected wavelength. 151
7.9 ESA trace from the S-SFP as the injected signal from the M-SFP was swept across resonance of one of its lasing modes. Here the beat note between the two signals is examined versus wavelength detuning. . . . 152
7.10 Experimental setup showing the on-chip coupling scheme between two lasers on the same integrated device. The waveguide interconnect linking both lasers was biased to transparency, causing the lasers to be coupled on chip without the need for a circulator. 153
7.11 OSA trace from the S-SFP as the injected signal from the M-SFP was swept across resonance with one of its lasing modes. For close to zero detuning, suppression of the optical side modes was observed and the S-SFP was shown to lase strongly at the injected wavelength. 154

7.12 ESA trace from S-SFP as the injected signal from the M-SFP was swept across resonance of one of its lasing modes. Here the beat note between the two signals is examined versus wavelength detuning. Close to zero detuning, the beat note is shown to disappear and the SFP lasers enter a stable phase locked regime. 155
7.13 ESA traces showing the beat note between the S-SFP and M-SFP as the main lasing mode of the M-SFP was swept across resonance with one of the S-SFP lasing modes. 157
7.14 Device used to investigate the simultaneous optical phase locking of multiple lasers on the same chip to a single master laster. The master laser (M-SFP) was integrated at the input of a 1×2 MMI, with two further identical SFP lasers integrated on the outputs of the MMI. By forward biasing the central variable gain section consisting of MMI, SOA and MMI output bends; light from the M-SFP could be coupled into both output lasers simultaneously. 158
7.15 Experimental setup showing the device from Figure 7.14 under test. Eight probes were required to bias all three two-section SFP lasers along with the MMI and SOA section. Lensed fibres are coupled at the input and output of the device. 159
7.16 Optical Spectra of free-running SFP lasers 160
7.17 Optical spectra of SFP lasers in optically phase locked regime. 162
7.18 Optical spectra from each SFP laser with the system in the phase locked regime. The S-SFP lasers are now lasing at the injected M-SFP wavelength with an increase in their peak powers. 163
7.19 Experimental setup showing the system used to test for coherent S-SFP in the optically phase locked regime. The phase locked signal from slave laser 1 or 2 is modulated and coupled with the unmodulated master laser output. 164
7.20 ESA traces showing the 20 GHz beat note between both side bands of the modulated M-SFP or S-SFP. 164
7.21 ESA trace of the 10 GHz tone generated from modulated S-SFP 1 beating with itself, overlapped with the tone generated from the modulated S-SFP 1 beating with the unmodulated M-SFP in the optically phase locked regime. 165
7.22 ESA trace of the 10 GHz tone generated from modulated S-SFP 2 beating with itself, overlapped with the tone generated from the modulated S-SFP 2 beating with the unmodulated M-SFP in the optically phase locked regime. 166

8.1 (a) Image of SFP laser integrated with an MMI and SOA. (b) Image of device with a system of mutually coupled SFP lasers. 169
8.2 An array of facetless Slotted Fabry Pérot lasers. 170
8.3 An array of facetless Slotted Fabry Pérot lasers integrated with a star coupler which can combine their outputs into a single waveguide. . . . 171
8.4 Facetless SFP lasers integrated together to form a system of mutually coupled system of lasers similar to device based on single facet SFP lasers examined in this thesis. 171
8.5 Schematic of proposed QPSK modulator. 172

A.1 Overview of MMI Optimisation Code 191

B.1 Schematic of an optical star coupler. Light from the input waveguide array can be coupled to the output waveguide array. 200
B.2 Arrangement of star couplers as used in an AWG. 201
B.3 Propagation of a gaussian beam in free-space. 202
B.4 Coupling from two waveguides axially aligned with a fixed separation. 203
B.5 Propagated mode from input waveguide A incident on output waveguide B, overlapped with the fundamental mode of waveguide B. 203
B.6 Coupling efficiency between two optical waveguides that are axially aligned as the separation between them in increased from 0 µm to 20 µm. 204
B.7 Star coupler operating in forward direction where light couples from input waveguide A to the output waveguides A, B and C. 205
B.8 Star coupler operating in the reverse direction where light is examined as it couples from output waveguide A to input waveguide A. 206
B.9 The green curve indicates the power coupled from input waveguide A to output waveguide A (forward). The red curve indicates the power coupled from output waveguide A to input waveguide A (forward). The blue curve represents the power coupled between the central waveguides in the forwards and reverse directions. 207

C.1 Waveguide Variations. (a) Si Waveguide. (b) InP Waveguide. 209
C.2 Maximum coupling efficiency versus MMI width for (a) shallow etched MMI and (b) deep etched MMI. 210
C.3 Optimised MMI Length versus MMI width for (a) shallow etched MMI and (b) deep etched MMI. 211
C.4 Maximum coupling efficiency versus MMI width for (a) shallow etched MMI and (b) deep etched MMI. 212
C.5 Optimised MMI Length versus MMI width for (a) shallow etched MMI and (b) deep etched MMI. 212

D.1 Overview of the steps required to fabricate a ridge waveguide using a typical process. 215

E.1 217
E.2 218
E.3 219
E.4 220

List of Tables

3.1 Waveguide Variations 48
3.2 Computational Times for MMI Analysis using EIM-MPA and SFEM-MPA. 61
3.3 Optimised MMI Parameters 79

4.1 Scan Times (seconds) 96

5.1 Material Structure. 101
5.2 Design Parameters for MMI. 104
5.3 Single facet slotted Fabry Pérot laser design parameters. 108

A.1 Input and Output Parameters - Main MMI Code 192
A.2 Input and Output Parameters - MMI Subroutine 193
A.3 Input and Output Parameters - Mode Solver Subroutine 196
A.4 Input and Output Parameters - Overlap Subroutine 197
A.5 Input and Output Parameters - Propagation Subroutine 199

E.1 Ridge Laser Parameters 216

I, Padraic Morrissey, certify that this thesis is my own work and I have not obtained a degree in this university or elsewhere on the basis of the work submitted in this thesis.

Padraic Morrissey

To my parents, Catherine and Pat
and my girlfriend, Gwen.

Acknowledgements

Firstly, I would like to thank my supervisor Dr. Frank Peters for giving me the opportunity to pursue a PhD within the Integrated Photonics Group at Tyndall. He provided support and guidance over the last four years, and his door was always open to scientific and non-scientific discussions alike. I would also like to thank Jo Peters for treating the entire research group like part of the family by having us over for great group lunches, and even better pizza.

A special thanks must go to Eddie Cotter. Not only did he give me an appreciation for MotoGP, his help and guidance has been invaluable since the first day I walked into the lab. We both managed to complete our PhDs from the first PIC we designed together which is something we should be immensely proud of. I doubt we'll ever forget "October2011.cpp". I would like to thank the past and present members of the research group who made it such a fantastic place to work over the last few years: Rob Sheehan, Chris Daunt, Eddie Cotter, Niall Kelly, Philip Marraccini, Mark Crowley, Fabien Dubois, Joe Cashell and Justin Alexander. I would like to especially thank Dave Goulding for his support throughout the work of this thesis. His help both in the lab and with scientific writing was invaluable. A special thanks must go to Brian Corbett for his guidance and expertise throughout my PhD. Without his work and that of his group including James O'Callaghan, Yang Hua and Brendan Roycroft, the devices used in the core of this work would not have been fabricated. Thank you to Bryan Kelleher and Simon Osborne of the Photonic Device Dynamics and Theory groups who I had the pleasure of working with during my time as a PhD student. Thanks also to Michael Gleeson for his extensive and detailed proof reading of this thesis; and also for his excellent management of FC Last Minute.

To Mossy, Tadhg, Brick, Steve and Lee; be it half-marathon running, bad movies or nights in the Abbott's Ale house, you all helped get me through my PhD. I would like to thank my parents Catherine and Pat, my sister Triona, and of course Holly, for their support and encouragement in everything I do. To Gwen, my constant source of inspiration and strength throughout my PhD. Your patience and support has taken me through the dark days in the lab, and even darker nights of thesis writing at the kitchen table. Little did we know how much our lives would change over the last four years, thank you for everything.

Abstract

The demand for optical bandwidth continues to increase year on year and is being driven primarily by entertainment services and video streaming to the home. Current photonic systems are coping with this demand by increasing data rates through faster modulation techniques, spectrally efficient transmission systems and by increasing the number of modulated optical channels per fibre strand. Such photonic systems are large and power hungry due to the high number of discrete components required in their operation. Photonic integration offers excellent potential for combining otherwise discrete system components together on a single device to provide robust, power efficient and cost effective solutions. In particular, the design of optical modulators has been an area of immense interest in recent times. Not only has research been aimed at developing modulators with faster data rates, but there has also a push towards making modulators as compact as possible.

Mach-Zehnder modulators (MZM) have proven to be highly successful in many optical communication applications. However, due to the relatively weak electro-optic effect on which they are based, they remain large with typical device lengths of 4 to 7 mm while requiring a travelling wave structure for high-speed operation. Nested MZMs have been extensively used in the generation of advanced modulation formats, where multi-symbol transmission can be used to increase data rates at a given modulation frequency. Such nested structures have high losses and require both complex fabrication and packaging. In recent times, it has been shown that Electro-absorption modulators (EAMs) can be used in a specific arrangement to generate Quadrature Phase Shift Keying (QPSK) modulation. EAM based QPSK modulators have increased potential for integration and can be made significantly more compact than MZM based modulators. Such modulator designs suffer from losses in excess of 40 dB, which limits their use in practical applications. The work in this thesis has focused on how these losses can be reduced by using photonic integration. In particular, the integration of multiple lasers with the modulator structure was considered as an excellent means of reducing fibre coupling losses while maximising the optical power on chip.

A significant difficultly when using multiple integrated lasers in such an arrangement was to ensure coherence between the integrated lasers. The work investigated in this thesis demonstrates for the first time how optical injection locking between discrete lasers on a single photonic integrated circuit (PIC) can be used in the generation of coherent optical signals. This was done by first considering the monolithic integration of lasers and optical couplers to form an on chip optical power splitter, before then examining the behaviour of a mutually coupled system of integrated lasers. By operating the system in a highly asymmetric coupling regime, a stable phase locking region was found between the integrated lasers. It was then shown that in this stable phase locked region the optical outputs of each laser were coherent with each other and phase locked to a common *master* laser.

List of Publications

Journal Articles

1. P. E. Morrissey, W. Cotter, D. Goulding, B. Kelleher, S. Osborne, H. Yang, J. O'Callaghan, B. Roycroft, B. Corbett, and F. Peters, "On-chip optical phase locking of single growth monolithically integrated slotted fabry perot lasers", Opt. Express, 21, 17315-17323 (2013)
2. P. E. Morrissey, D. Goulding, R. Sheehan, B. Roycroft, F. H. Peters, "Experimental technique for quick and efficient lensed fibre to ridge waveguide coupling", IET Optoelectronics, 7, (2), 57-61 (2013)
3. Y. Hua, P. E. Morrissey, W. Cotter, C. L. M. Daunt, J. O'Callaghan, B. Roycroft, Y. Nan, N. Kelly, B.Corbett, F. H. Peters,"Monolithic Integration of Single Facet Slotted Laser, SOA, and MMI Coupler", Photonics Technology Letters, IEEE , 25, (3), 257-260 (2013)

Conference Proceedings

1. P. E. Morrissey, W. Cotter, J. O'Callaghan, H. Yang, B. Roycroft, D. Goulding, B. Corbett, F. H. Peters, "Multiple coherent outputs from single growth monolithically integrated injection locked tunable lasers", Indium Phosphide and Related Materials (IPRM), International Conference on, 281-284 (2012)
2. W. Cotter, P. E. Morrissey, D. Goulding, B. Roycroft, Y. Hua, J. O'Callaghan, B. Corbett, F. H. Peters, "Coherent comb generation using integrated slotted Fabry Perot semiconductor lasers", Photonics Conference (IPC), IEEE, 848-849 (2012)
3. Y. Hua, P. E. Morrissey, Y. Qiao, W. Cotter, C. Daunt, J. O'Callaghan, H. G. Wei, W. Han, J. F. Donegan, B. Corbett, F. H. Peters, "Single facet slotted Fabry-Perot laser and its application in photonic integrated circuits", Semiconductor Lasers and Applications V, (2012)
4. P. E. Morrissey, R. Sheehan, D. Goulding, F. H. Peters,"Optimum Design of Multimode Interference Couplers with Fabrication Tolerances", Semiconductor and Integrated Optoelectronics (SIOE), (2011)

Glossary

List of Acronyms

Acronym	Definition
AR	Anti-Reflection
ASK	Amplitude-Shift Keying
AWG	Arrayed-Waveguide Grating
BC	Boundary Conditions
BPM	Beam Propagation Method
BPSK	Binary Phase-Shift Keying
CWDM	Coarse-Wavelength Division Multiplexing
DBR	Distributed Bragg Reflector
DFB	Distributed Feedback Laser
DPSK	Differential Phase-Shift Keying
DQPSK	Differential Quadrature Phase-Shift Keying
DUT	Device Under Test
DWDM	Dense-Wavelength Division Multiplexing
EAM	Electro-absorption Modulator
EIM	Effective Index Method
EIM-MPA	EIM-Modal Propagation Analysis
ESA	Electrical Spectrum Analyser
FP	Fabry Pérot
FSR	Free Spectral Range
IC	Integrated Circuits
IPG	Integrated Photonics Group
MMI	Multimode Interference Coupler
MOTOR	Monolithic Tunable Optical Router
MPA	Modal Propagation Analysis
M-SFP	Master Slotted Fabry Pérot
MZM	Mach-Zehnder Modulator
OOK	On-Off Keying
OSA	Optical Spectrum Analyser
PIC	Photonic Integrated Circuit
QPSK	Quadrature Phase-Shift Keying
QW	Quantum Well
QWI	Quantum Well Intermixing
RIN	Relative Intensity Noise
RO	Relaxation Oscillations
SCH	Separate Confinement Heterostructure
SFEM	Scalar Finite Element Method
SFP	Slotted Fabry Pérot
SF-SFP	Single Facet Slotted Fabry Pérot
SMSR	Side-Mode Suppression Ratio

List of Acronyms

Acronym	Definition
SOA	Semiconductor Optical Amplifier
S-SFP	Slave Slotted Fabry Pérot
TE	Transverse Electric
TEC	Thermoelectric Cooler
TLS	Tunable Laser Source
TM	Transverse Magnetic
VOA	Variable Optical Attenuator
WDM	Wavelength Division Multiplexing

Chapter 1

Introduction

1.1 Optical Communications

The development of optical communication systems in the 1970s signalled a change in the way people not only communicated but also viewed the world as a whole. Previous to this, the limitations of electronic communication systems had restricted the use of long-haul communications. The advent of optical fibre finally opened the door to true long-haul systems, where its low loss per kilometer and potential for high bandwidth transmission could be fully utilised. This kick started the *Information Age* and allowed the internet to develop into what it has become today.

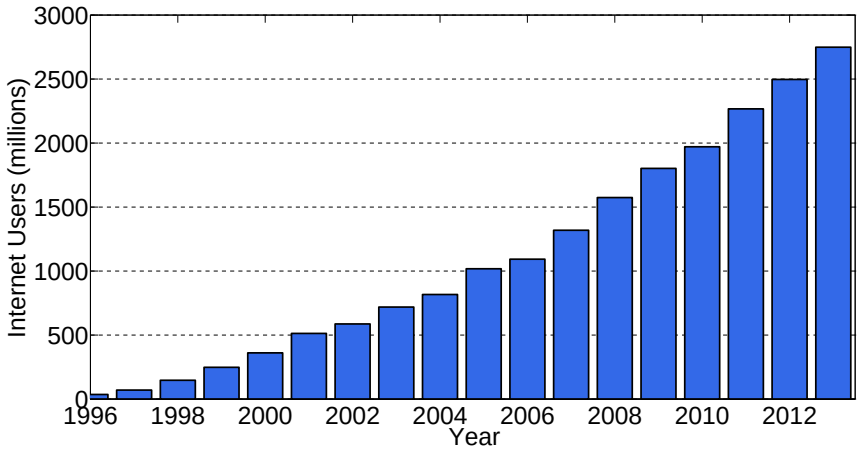

Figure 1.1: Growth of internet users per year [1, 2].

The emergence of personal computers in the late 1980's and early 1990's brought the internet, and in particular the *World Wide Web*, into the home for the first time. This sparked a remarkable growth in the number of internet users and started the *dot-com boom*, where numerous internet businesses and industries were born. In the mid-1990's approximately 40 million people were using the internet, with the majority of those

based in North-America. Figure 1.1 shows the incredible growth of the internet since then [2], where there is now (2013) in excess of 2.5 billion users worldwide. A breakdown of the users per geographic region is illustrated in Figure 1.2.

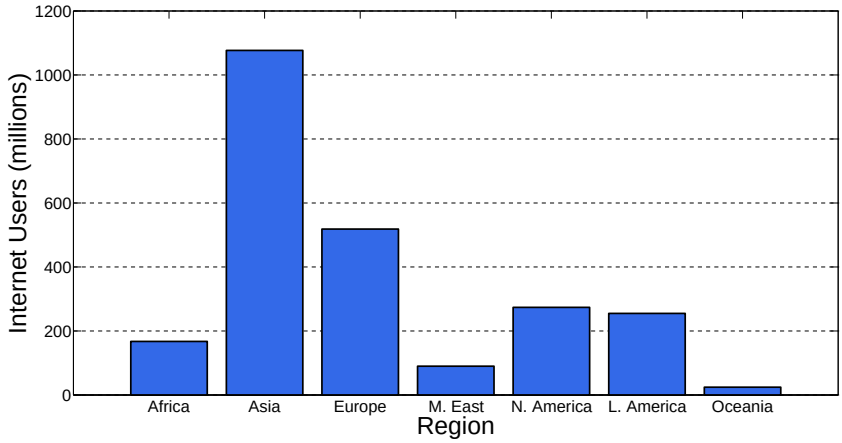

Figure 1.2: Total number of internet users by geographical region [1, 2].

These statistics indicate that over 1 billion internet users are from Asia, with Europe and North America lagging considerably behind with approximately 500 and 250 million users respectively. Figure 1.3 shows the internet penetration in each geographical region as a percentage of its total population.

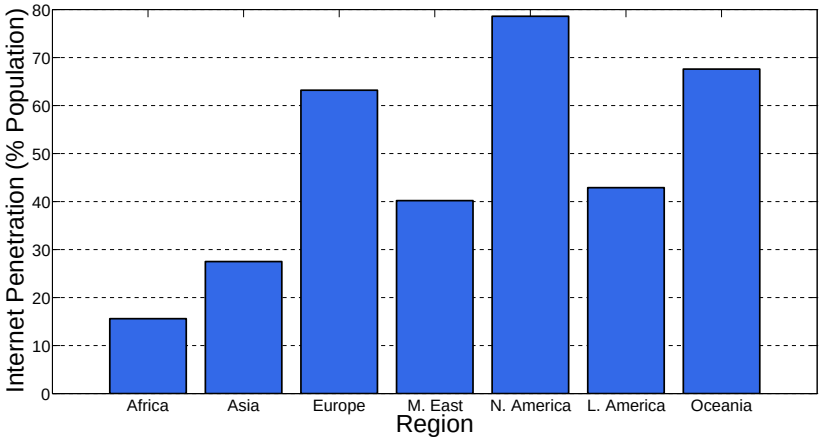

Figure 1.3: Percentage of population with internet access based on geographical regions [1, 2].

This clearly reflects the socioeconomic climate in each area, where wealthier regions such as Europe, North America and Oceania show high internet penetration values between 60 and 80 %, while typically poorer regions such as Africa show a mere 20 % internet penetration. Emerging markets in Africa, Brazil and India suggest that the number of internet users worldwide will continue to grow in a similar fashion to

that shown in Figure 1.1, at least until the year 2020. This will put significant strain on current optical communication systems. Along with this, the development of new technologies has leant itself to the creation of services which require ever increasing bandwidth capacity. These include fibre to the home technologies [9], cloud computing [10] and real-time entertainment services such as Netflix and YouTube [11]. These services combined have recently been shown to dominate internet bandwidth usage in North America with a share of over 50 % during peak usage times [12]. The global internet bandwidth usage has risen rapidly in recent times as can be seen in Figure 1.4. The required bandwidth is expected to continue to increase dramatically in the coming years, which raises questions as to how this demand will be met [13]. This will be driven primarily by the entertainment services as they extend their bandwidth share further in Europe and elsewhere, which will be compounded by the demand for higher image quality streaming such as *4K* [14] video.

Fibre optical transmission systems play a key role in satisfying the ever-increasing demand for data bandwidth. It forms the backbone for long-haul communication systems, where high bandwidth and low-loss transmission is required for transmission over tens and thousands of kilometers. Such systems continue to be improved by lowering the cost of optical to electrical (and vice-versa) conversions and by maximising data transfers. These improvements have been realised by significant advancements in the area of photonic systems, where highly sophisticated systems have been developed to improve speed, reliability and signal quality during optical transmission. Such improvements were essential in the realisation of current communication systems, and will play a key role in satisfying the ever increasing demand for bandwidth during the next two decades [15].

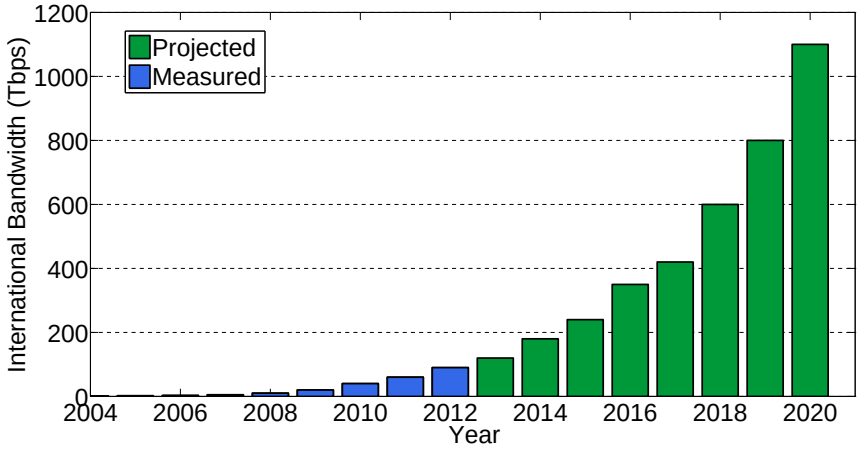

Figure 1.4: The international measured and predicted data rates per year [3].

1.2 Photonics and Photonics Systems

Similarly to how electronics is the study of the properties of electrons, photonics is the study of the properties of light and how it can be manipulated. Primarily driven by the development of the first laser in 1960 [16], photonics has grown to incorporate numerous different aspects and technologies. Photonics deals with the generation of light and also the development of optical amplifiers, photodetectors for detecting and measuring light and importantly, optical modulators. These photonic devices are now key components of current optical systems and are forming the backbone of next generation optical networks.

To satisfy the demand placed on current optical communication systems, improvements to infrastructure and novel transmission systems in the area of photonics are required and constantly under development. A key milestone in this progress was the investigation of multiplexed optical carrier signals on a single optical fibre, where each carrier signal was at a different wavelength [17]. This allowed for not only bi-directional data transfer through one fibre, but also dramatically increased the amount of data which could be transferred. This is similar to frequency division multiplexing [18, 19] in satellite and radio communications, where the total bandwidth provided is divided amongst carriers of different non-overlapping frequencies. In optical communication systems, this technology is referred to as Wavelength Division Multiplexing (WDM) [20, 21, 22, 23] and has been recognised as a key technology in the development of high bandwidth communications since the early 1980's. WDM can best be described by considering the simplified schematic shown in Figure 1.5.

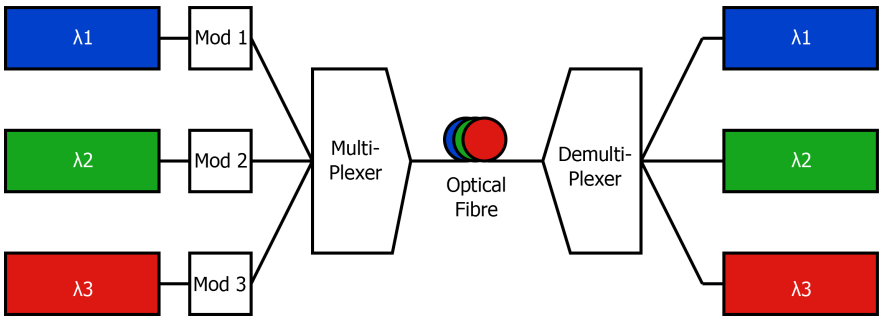

Figure 1.5: Schematic outline of a WDM system.

Three laser sources are shown in Figure 1.5, each operating with a single wavelength: λ_1, λ_2 and λ_3. These signals are individually modulated at 10 Gbps or greater, and then combined together into a single optical fibre using a wavelength multiplexer. This multiplexed optical signal is then transmitted across the network where it can be amplified as required. On the receiving end, the combined signal is demultiplexed, typically using an AWG [24, 25] or a tunable filter [26], after which the original modulated signals

are re-acquired.

Commercially, two forms of WDM are typically available, these are Coarse-WDM (CWDM) and Dense-WDM (DWDM) [27]. CWDM has applications in short-haul, metro lines where there are a relatively small number of channels with large channel spacing of > 100 GHz. This large channel spacing allows for more tolerance in the behaviour of the lasers used, resulting in cheaper overall operation. On the other hand DWDM requires very closely spaced channels, with current standards set [28] at a 12.5 GHz spacing for use within long-haul communication networks. Figure 1.6 shows an example of an optical spectra from a system field trial with ninety-six closely spaced channels [29]. Increasing the number of channels per wavelength band results in higher total bandwidths, since hundreds of simultaneous channels are possible. This offers a cost effective means of increasing network capacity without the need for replacing optical fibre, where data rates of Tb/s can now be seen in single fibres [30]. A consequence of this is the need for much higher wavelength (λ) tolerances of the input sources to prevent interference and cross-talk between these channels. Typically, laser sources are required to have excellent wavelength stability [31] of better than 10 pm, which must be maintained over a wide temperature and time range. This is a key issue with DWDM technologies, along with the need for amplification of the signal as it propagates through the network to compensate for power losses.

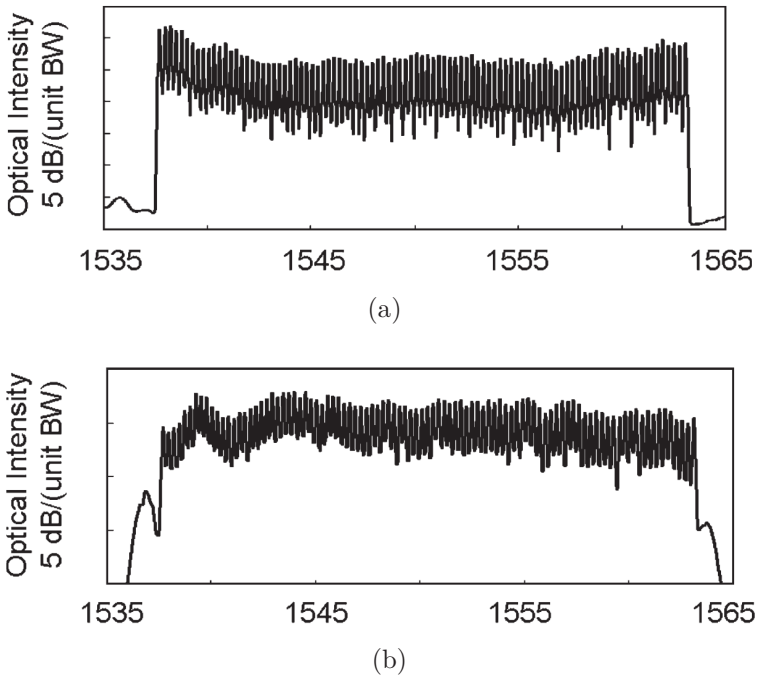

Figure 1.6: Optical spectra from a trial using 96×12.3 Gb/s channels. (a) Shows the input signal while (b) shows the output spectrum after being transmitted 9000 km.

Since the implementation of early DWDM systems in network applications in the mid-

1990's, the data rate per wavelength channel has continued to increase. The first systems showed data rates per channel of 2.5 Gb/s, with this increasing to 10.0 Gb/s in the early 2000's with 100G now becoming more common [32, 33]. This increase in performance was due to a number of factors, namely the development of coherent technologies [34, 35, 36], improvements in modulator design and a better understanding of the loss mechanisms in optical fibre for long-haul applications [37]. Of particular importance when pushing data rates to 10 Gb/s and beyond was the investigation of higher order modulation formats for use with WDM [38, 39]. In early commercial applications, a mechanism referred to as On/Off Keying (OOK) was typically used with a high degree of success. This is still the most widely used modulation format for long-haul 10 Gb/s communications due to its cost effective transmitter and receiver structures. However, as data rates were pushed higher than 10 Gb/s, this technique encountered significant issues with dispersion [40, 41] and was also limited by its spectral efficiency (the amount of information transferred over a given bandwidth) and tolerances when using narrow channel separations. Growing research into more robust technologies allowed for the possibility of using advanced modulation formats to push through the 10Gb/s barrier for long-haul transmission where 40 Gb/s and 100 Gb/s systems can be realised. Advanced modulation formats provide an excellent means of increasing the potential bandwidth available in existing communication networks with fewer limitations than OOK and are certainly key to satisfying the ever increasing demands placed on optical networks.

1.2.1 Advanced Modulation Formats

In communication systems, the spectral efficiency of a signal is typically measured in (bits/s)/Hz [42] or *bit/symbol*. Along with improvements to modulator design and further advancements with coherent technologies, increasing net spectral efficiency provides an interesting means of expanding the bandwidth capacity of current fibre networks. When transmitting a signal there are three main steps required. These are:

1. the transmitter generates a carrier wave,
2. information is encoded on the carrier wave via modulation,
3. the receiver detects the modulated carrier and decodes the modulation.

For optical communications, the carrier signal is light in an optical fibre where its intensity, wavelength, phase and polarization can be modulated to carry information. Typically, modulation states are represented by components of an electric field vector on an In-phase (I) and Quadrature (Q) constellation diagram. From this, information on the phase and amplitude of a modulated signal can be extracted. OOK, as mentioned previously is the most widely exploited non-coherent modulation format currently used in optical communications. In OOK, information is encoded on the amplitude of an

optical single as it is varied from the null (off-state) to a peak amplitude value (on-state). In such a scheme, the phase of the signal in the on and off-states is fixed, which results in both symbols lying on the same positive side of the I-axis, as can be seen in the IQ diagram given in Figure 1.7a. Each symbol represents a different modulation state, i.e on or off-state, with x defined as the amplitude of the E-field. The vectorial length of each symbol from the origin relates to the amplitude of the electric field, with the angular component representing the phase. For OOK or Amplitude Shift Keying (ASK) as it is also known, one symbol is found at the origin with an amplitude of zero, while a second symbol is found at a finite magnitude on the same phase line.

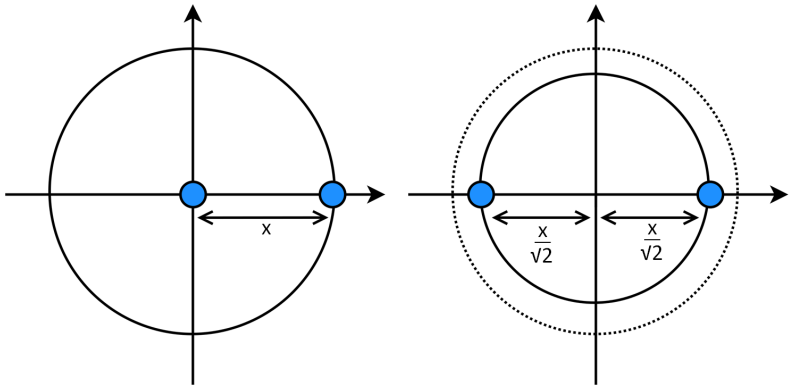

(a) Amplitude Shift Keying (b) Binary Phase Shift Keying

Figure 1.7: Basic modulation formats.

A more sophisticated binary (involves two different states) modulation format is known as Binary Phase Shift Keying (BPSK) which is based on coherent technologies. Unlike ASK, BPSK is performed by keeping a fixed carrier signal amplitude while the phase between symbols is varied. This is described by the constellation diagram shown in Figure 1.7b. Both symbols have identical vectorial lengths, indicating that no modulation of the signal amplitude occurs. Instead, there is a π phase shift between symbols. The advantage of BPSK over the simpler OOK mechanism becomes apparent when the distance between symbols is considered for both formats. The larger this distance, the less susceptible the modulation format is to transmission errors. In Figure 1.7, the average power for both modulation schemes is seen to be $\frac{1}{2}x^2$ in each case. However, the distance between the symbols using BPSK is $2 \times \frac{x}{\sqrt{2}}$, a factor of $\sqrt{2}$ greater than that of OOK. This larger symbol separation makes BPSK a more robust transmission system which is less susceptible to symbol errors. Another advantage is the lower overall peak power required in BPSK to attain the same symbol separation compared to OOK, this can minimise errors due to any non-linear effects present in an optical system [43]. A variation of BPSK is called Differential Phase Shift Keying (DPSK), which simplifies the receiver setup and does not require a synchronised, fixed phase carrier signal for absolute phase detection. This method works by encoding data based on the *differ-*

ence between preceding bits in a data sequence. More information on DPSK and these modulation formats can be found at [44, 45].

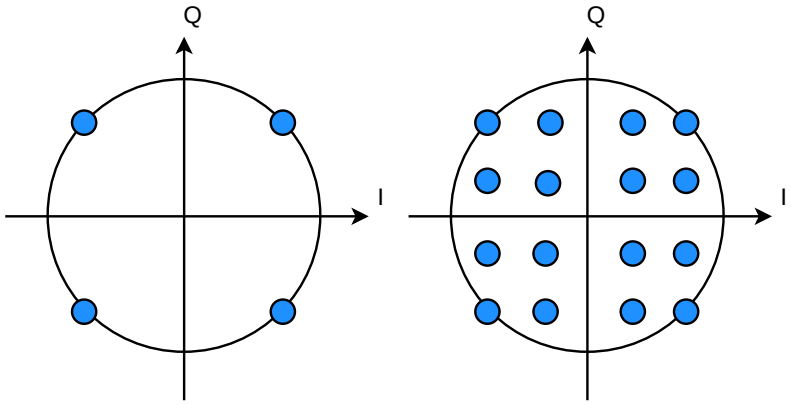

(a) QPSK (b) 16-QAM

Figure 1.8: Advanced modulation formats.

One method of increasing data rates using current optical fibre infrastructure involves using a modulation format with a higher symbol rate. For both OOK and (D)PSK, one bit is encoded per symbol. This can be increased by using more advanced higher order modulation formats, in particular Quadrature Phase Shift Keying (QPSK) [44, 46]. Similar to BPSK, QPSK does not involve amplitude modulation but instead varies the phase of the optical carrier signal to encode information. The constellation diagram for a typical QPSK modulation scheme is shown in Figure 1.8a. Here four symbols are present, with each symbol $\frac{\pi}{2}$ out of phase with each other and all having the same magnitude. The four symbols on the constellation diagram allow for two bits to be encoded per symbol. Each symbol differs by one bit to its adjacent symbol and bits $\{(10), (00), (01), (11)\}\}$ can be transmitted. QPSK offers twice the data rate of binary formats such as OOK and PSK; or equal data rates with half of the required bandwidth. QPSK has been found to be particularly interesting in the area of WDM, where it has been used to increase the data capacity of current networks through improvements in spectral efficiency. Higher order formats such as 16-QAM have also shown to be promising in WDM systems [47], where data rates can be increased by a factor of eight by using 4 bits per symbol. Similar to DPSK, Differential Quadrature Phase Shift Keying (DQPSK) techniques also exist for WDM systems, where high data rates have been achieved [48].

1.2.2 Modulation of optical signals

When considering the optical modulation of light and generation of advanced modulation formats, there are three main types of modulators used. These are:

1. Amplitude modulators
2. Phase modulators
3. Polarization modulators

Amplitude modulation has been the most wide spread modulation format used, due to its relatively simple transmitter and receiver structure. Varying the amplitude of light can occur by one of two different means. The simplest approach is referred to as *direct modulation* [49], where the amplitude of a signal can be controlled by varying the drive current of a laser. This approach can reach speeds of 40 Gb/s, however there remains the issue of unwanted chirp of the optical signal [50, 51] which becomes problematic at higher modulation speeds. By using external, or indirect modulation as it is also known, data rates can be improved and the effect of chirp and dispersion can be minimised compared to direct modulation methods. Two types of external modulators are typically used. These are *electro-optic modulators* and *electro-absorption modulators*. The following section will describe the operation of these modulators and consider their role in the generation of advanced modulation formats.

1.2.2.1 Electro-optic modulators

Electro-optic modulators are based on the principle that an applied external electric field can cause a change in refractive index of a material through either the Pockel's or Kerr effect [52]. Light of wavelength, λ, propagating through the material with refractive index, n, would then see a phase change over length, L, of

$$\phi = \frac{2\pi}{\lambda} nL \tag{1.1}$$

This allows for simple phase modulators where a time varying voltage field can cause a phase shift. A particularly useful application of the linear electro-optic effect is in the design of amplitude modulators, which as discussed previously, are still commonly used in communications systems. Using an interferometric approach, two optical signals may be combined together to form constructive or destructive interference, based on their relative phases which can be controlled. This is based on a Mach-Zehnder Modulator (MZM) type structure, as shown in Figure 1.9. Light is input from the left hand side of the device where it is divided in two and enters each arm of the modulator, where an applied voltage causes a phase change of the transmitted light. In its most simple configuration, one arm of the MZM is left unbiased, while a time varying voltage is applied to the second arm. This time varying voltage shifts the phase of the light until it is completely out of phase with the light in the unbiased arm. When the light from both arms is then re-combined at the output of the device, an amplitude minima (destructive) or maxima (constructive) is formed depending on the arm bias. This

results in a simple OOK modulator being formed, where the constellation diagram in Figure 1.7a can be generated. More sophisticated bias techniques such as *push-pull*, where both arms are biased with opposite voltages, can provide lower drive voltages which can also be used to generate BPSK. This is a key consideration when designing modulators for practical applications, particularly when trying to minimise the effects of chirp in a system [53, 54].

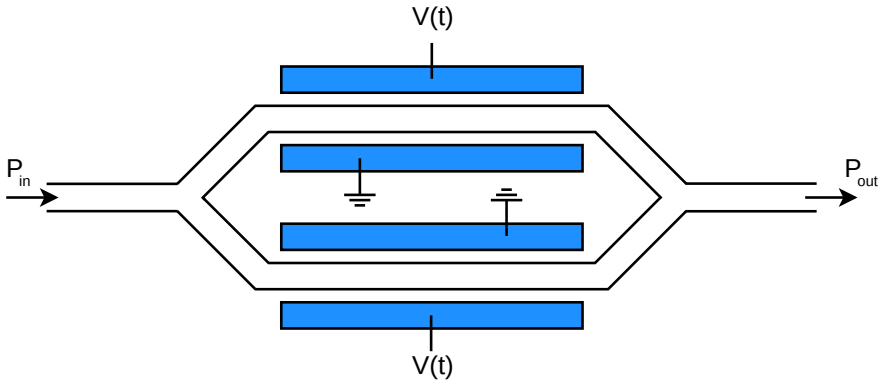

Figure 1.9: A typical Mach-Zehnder modulator. By controlling the optical phase in each arm, constructive or destructive interference can be formed at the output.

Further to this, MZMs can also be used to generate higher order modulation formats such QPSK [55] and 16-QAM [56], which have been described previously. A nested approach is used, where multiple single MZMs are combined together to form the required symbols for the modulation format. In the case of QPSK modulation, the MZM arrangement used is shown in Figure 1.10.

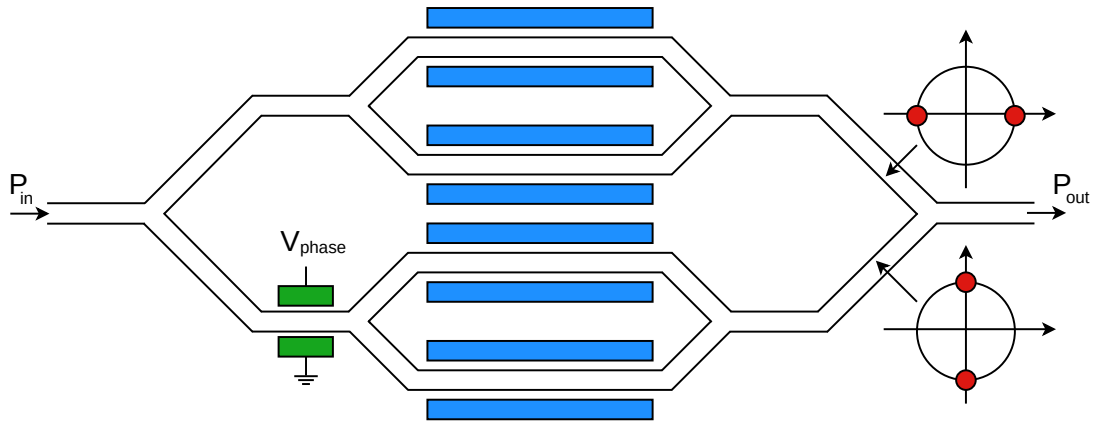

Figure 1.10: Nested Mach-Zehnder modulators can be used to generate QPSK modulation schemes.

The modulator is setup with two MZMs on the output ports of a 1×2 splitter. Each MZM can be driven to generate a BPSK symbol arrangement. A phase shifter before one MZM can be used to shift its optical phase by $\frac{\pi}{2}$ relative to the other MZM. In effect this offsets the constellation diagram by $\frac{\pi}{2}$, as can be seen in the constellation

diagrams in Figure 1.10. The outputs from both MZMs are then combined together, where any point on the constellation diagram can be generated through appropriate biasing of the individual MZMs.

Over 100 Gb/s data rates have been shown on a single transmitter [57] using such an arrangement. However, this approach is not without its limitations. A particular issue with such modulators is their size [58] when using materials such as $LiNbO_3$ or GaAs, due to the relatively weak electro-optic effect present. Examples of a typical MZM and nested-MZM modulators are shown in Figure 1.11.

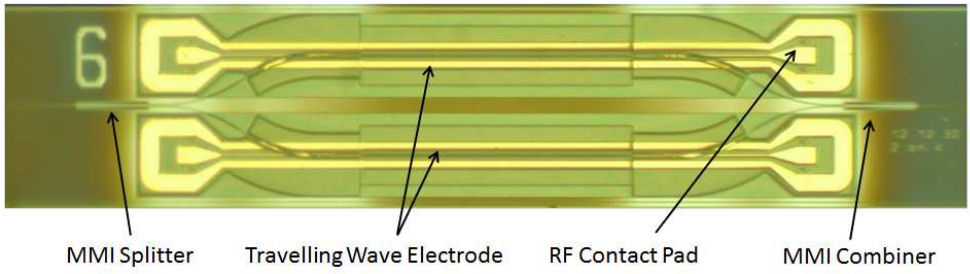

(a)

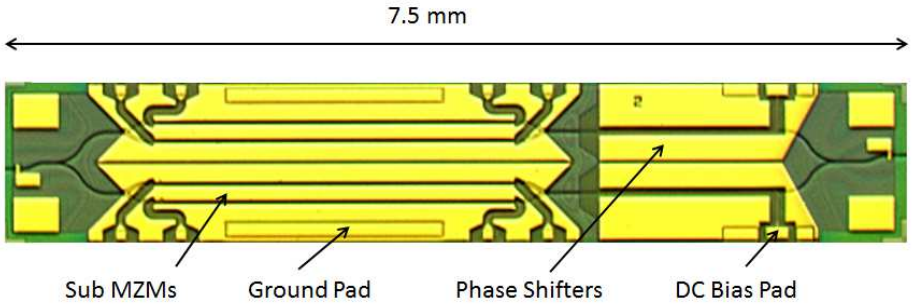

(b)

Figure 1.11: (a) A fabricated MZM from the Technische Universiteit Eindhoven [4]. (b) A fabricated traveling-wave based IQ Modulator formed from dual nested Mach-Zehnder modulators (NTT).

Figure 1.11a shows a single MZM modulator, where the RF contacts pads and waveguide splitters/combiners can be seen. Figure 1.11b shows an IQ modulator which can be used for the generation of QPSK modulation. Indicated in the Figure are the MZMs, phase-shifters and bias pads. The waveguide couplers (MMIs) can clearly be seen on the input and output sides of the device.

1.2.2.2 Electro-absorption modulators

Electro-absorption modulators (EAMs) are based on the principle that the bandgap of a semiconductor material can be decreased by applying an external bias across it. If light of energy $E = h\nu$ is considered as it travels through a medium, it will experience strong absorption if $E \geq E_g$, where E_g is the bandgap of the material. On the other hand, if $E < E_g$, the medium will experience no absorption and appear transparent to the transmitted light. Correct design of the bandgap of a material allows an external voltage to vary the bandgap sufficiently to act as a simple modulator [59]. An example of a typical EAM OOK modulator is shown in Figure 1.12, where the amplitude of the transmitted signal can be controlled by applying an external voltage to a ridge waveguide structure [60]. Such modulators have high modulation frequencies of 10 - 40 GHz [61], and can exhibit close to 20 dB attenuation. Although EAMs are somewhat limited in their operational wavelength, they offer excellent potential for integration with laser diodes [61, 62].

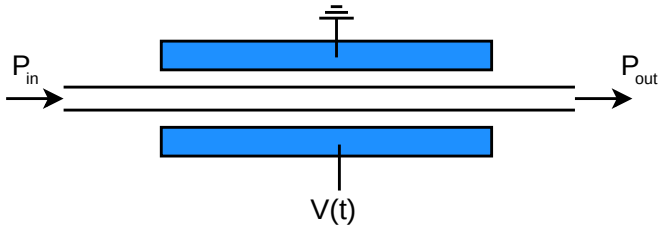

Figure 1.12: Schematic of an EAM based modulator.

BPSK can also be implemented using EAMs [60, 63, 64]. Such modulators offer a highly compact design which can be more suitable for integration with other devices. Design and fabrication can be made significantly easier by treating them as lumped element structures, rather than travelling wave devices [61, 65]. Further to this, the technique has been used in the development of more advanced modulators based on QPSK [5] and 16-QAM [66] modulation schemes. Compact modulators are highly important for state of the art systems and applications. They are of particular interest to the work presented in this thesis, where improvements to their designs are considered.

1.2.2.3 Compact high speed QPSK EAM based modulator

Advanced modulation formats can be used to increase the spectral efficiency of current optical communication networks. Traditional QPSK modulators make use of nested pairs of MZMs to generate the required symbols on a constellation diagram, as shown in Figure 1.10. The size of such a modulator is a significant limitation for their use in systems. This is mainly due to the relatively weak electo-optic effect of the materials employed, necessitating long phase change sections. This results in QPSK modulators

which are approximately 5 cm in length [67], making them unsuitable for compact integrated devices. As with BPSK modulators, QPSK modulators can also be developed on InP based materials which make use of the electo-absorption effect. This offers exciting possibilities for highly compact modulators due to the ability to form EAMs with very short lengths [5]. The outline of such a modulator is shown in Figure 1.13 and its operation will now be considered.

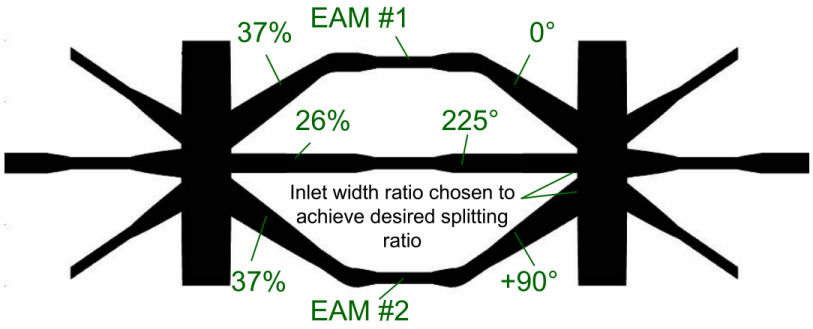

Figure 1.13: EAM based IQ Modulator [5]. C. R. Doerr, et al.

Figure 1.13 shows the modulator arrangement, where two EAMs are positioned on the outer branches of a three-arm interferometric structure. A relative phase difference of 90° exists between these two outer arms, which in turn are each out of phase with the central arm by 135°. The four points of a QPSK constellation diagram, as in Figure 1.8a, can be generated by varying the operation of each EAM from fully absorbing to fully transparent. The steps required to generate each symbol presented in Figure 1.13 are shown below.

- **Symbol 1:** The first symbol, as shown in Figure 1.14a, can be generated by having both EAMs fully absorbing. This means that the central arm is solely responsible for the symbol position on the constellation diagram.
- **Symbol 2:** By only setting the bottom EAM to transparency (with the top absorbing), the symbol can be shifted by −90° to the position illustrated in Figure 1.14b when combined with light from the central arm.
- **Symbol 3:** By only setting the top EAM to transparency (with the bottom absorbing), the symbol can be shifted by 90° to the position illustrated in Figure 1.14c when combined with light from the central arm.
- **Symbol 4:** With both EAMs set to transparency, the final symbol position is determined by all three arms interacting together. This causes the symbol to be shifted as in Figure 1.14d.

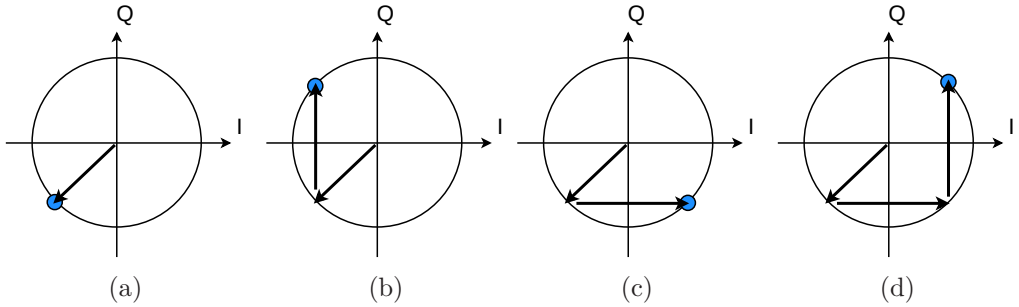

Figure 1.14: Symbol configurations achievable for a QPSK modulation scheme by controlling the operational states of integrated EAMs.

The experimental results for such a QPSK modulator [5] indicate that it can perform at speeds of up to 21 Gb/s. Figure 1.15 shows this fabricated modulator, where its overall length is measured at 1.7 mm. This length is significantly less than that of a standard MZM based QPSK modulator, which as can be seen from Figure 1.11b, can be over 7 mm in length. The main advantage of EAM based modulators is the significant decrease in the device length along with increased potential for integration with other devices. However, a considerable disadvantage of this modulator design is the high insertion loss present due to inherent modulator losses, coupler losses, absorption losses and waveguide loss. In total the combined losses are approximately 40 dB, which deters the use of this device in practical applications.

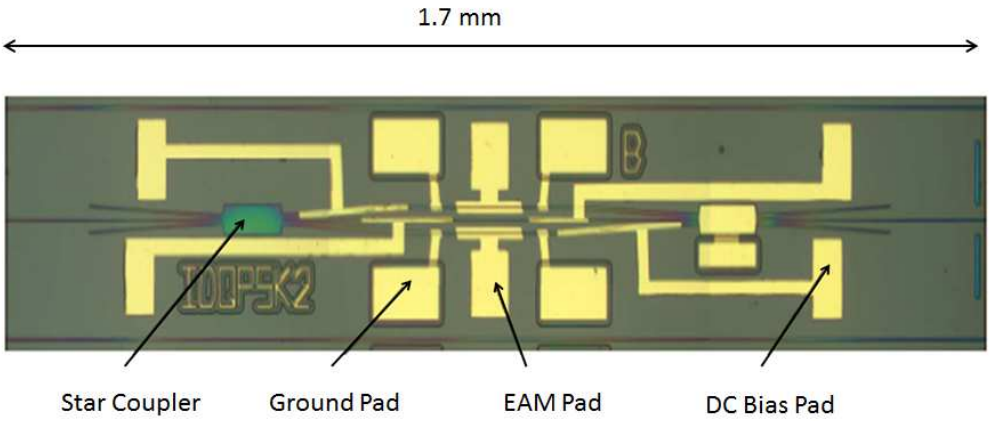

Figure 1.15: EAM Based IQ Modulator [5]. C. R. Doerr, et al.

The goal of this thesis involved the investigation of improvements to this modulator design which may make it viable for use in practical applications. A significant aspect of this was minimising the insertion losses present in the device. One interesting approach involves using integrated lasers with the modulator to improve its overall power performance. This would have the benefit of removing the need for an externally coupled laser source, while maximising the power output from each arm of the modulator. The details of these performance improvements will be discussed further in the following

section, where the benefits of photonic integration are explored. In particular, the role of integrated lasers in photonic devices will be examined. Attention will also be paid to the concept of *injection locked* lasers and the role they can play in complex photonic integrated circuits.

1.3 Photonic Integration

In the electronics industry, the push towards chip scale integrated circuits (ICs) allowed for a dramatic increase in the performance of everyday electrical devices. Since their invention by J. Kirby in 1954, the number of transistors on ICs has been doubling almost every 2 years in accordance with Moore's Law. Today, commercially available Intel Haswell 22 nm based CPUs rely on ICs with over 1.4 billion transistors, an astonishing rise in almost 60 years. In the photonics industry, the prospect of developing similar technologies with photonic integration offers incredible potential growth in the area. However, research and development of photonic integrated circuits (PICs) has progressed at a far slower rate than its electrical counterpart. This has been due to the larger number of sub-components in photonic devices. In any device there may be lasers, attenuators, modulators, couplers and detectors which each have to be considered when dealing with integration. As a consequence of this, each element of a device may also be based on a vastly different material structure (binary, quaternary alloys, III-V semiconductors etc.) which requires non-standard wafer processing techniques.

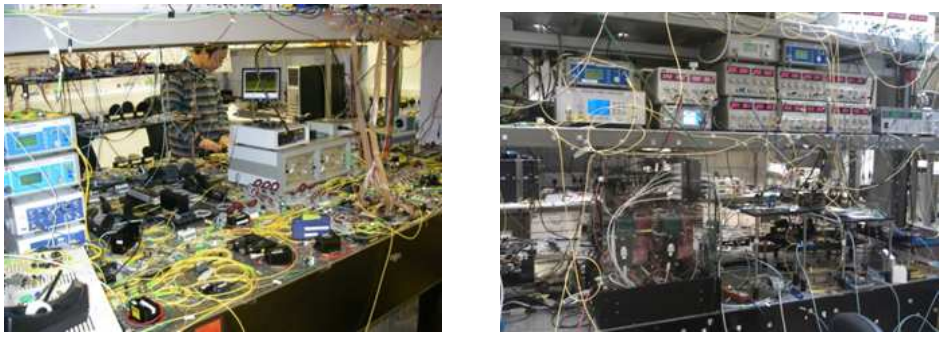

(a) (b)

Figure 1.16: Large, power hungry photonic system setups. Tyndall National Institute.

The first PIC was proposed by S.E. Miller in 1969 [68], and it is only in the last 10 years or so that these first true PICs have been realised for commercial applications. This has ushered in an era of excitement in the photonics community, as photonic integration is set to play a key role in helping satisfy the demands placed on current optical networks. The advantages of developing photonic integration and PICs are many-fold, but research is mainly driven by the potential benefits to:

1. Cost
2. System simplification
3. Reliability
4. Power consumption

Photonic integration can take large, power hungry system setups shown in Figure 1.16 and reduce them to compact and reliable PICs shown in Figures 1.17a and 1.17b.

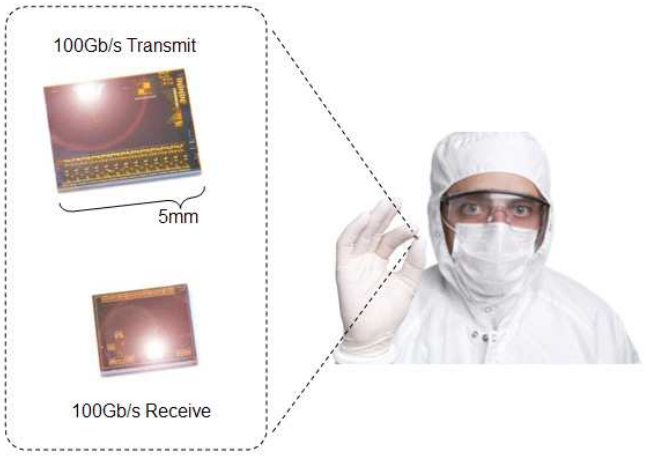

(a) Photonic integrated circuits (Infinera).

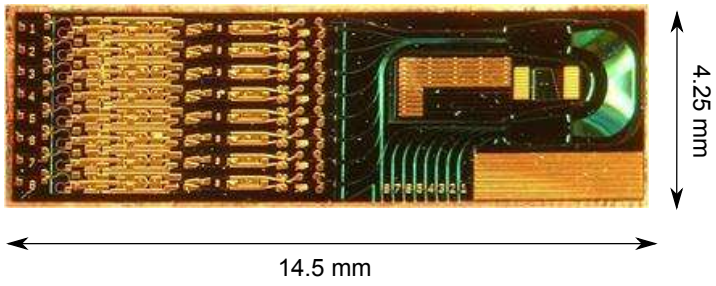

(b)

Figure 1.17: (a) Photonic integrated circuits. Infinera. (b) InP monolithic tunable optical router (MOTOR) [6].

From a systems point of view, the interconnection of discrete components together while forming subsystems can significantly add to the cost of an overall device. This results from extra photonic packaging, more fibre couplings, potential phase instabilities, polarization dependance and overall larger size. Large scale InP based PICs offer excellent potential in this area, and can greatly improve network flexibility and maximise functionality. One such PIC is shown in Figure 1.17b, where a highly compact Monolithic Tunable Optical Router (MOTOR) was produced with eight wavelength-tunable differential MZMs, semiconductor optical amplifier (SOA), wavelength converters with

pre-amplifiers and a passive 8×8 Arrayed-Waveguide Grating (AWG) router. PICs like these show the incredible potential integration technologies have to offer to optical systems. It is for this reason that photonic integration and PIC development is of particular interest to work carried out in this thesis.

PICs are typically comprised of a wide range of sub-devices such as tunable lasers, modulators, filters, multiplexers, optical splitters, optical combiners, etc. This leads to significant challenges when integrating such components together on one PIC. This can be overcome through expensive and time consuming fabrication, or by dealing with the challenges on the device packaging side. Since photonic integration is still in its relative infancy compared to its electronic counterpart, either of these solutions greatly adds to the expense of the photonic devices. The photonics industry has two primary solutions to tackle the issue of photonic integration, these are Hybrid and Monolithic Integration.

1.3.1 Hybrid Integration

Hybrid integration [69, 70], as with its electronic counter part, allows multiple discrete single function optical devices to be taken and integrated together on a common substrate. The discrete components are then linked together through optical couplings to form a single PIC, typically using flip-chip techniques [71]. This is a very complex and time consuming process, due to the high tolerances required when forming the interconnects between devices. Additionally, the varying mechanical properties of each device makes hybrid integration a highly challenging process.

With monolithic integration, each optical device is formed on a PIC with the same material substrate. This removes the need for optical interconnects to link each component since light is guided in the substrate medium. Monolithic integration often requires epitaxial regrowth to form areas on a substrate to act as either passive or active components, then complex fabrication can be used to form each device. The benefits of monolithic integration are well known and it is seen as an excellent means of merging different optical functions on one chip without the negative trade-offs in performance, higher costs and possible reduced functionality of some hybrid integration schemes. It is for this reason that monolithic integration plays a key role in the development of PICs in this thesis, where they are seen as an essential part of next generation networks. In what follows, different monolithic integration methods are examined.

1.3.2 Monolithic Integration

A multitude of different techniques exist for monolithic integration based on current technologies [72]. As can be seen in Figure 1.18, these methods make use of regrowth and etching to form photonic devices on a single substrate. The most common methods

used are vertical twin-guide [73, 74, 75], butt-joint regrowth [76, 77, 78], selective area regrowth [79, 80, 81], offset quantum wells [82], dual quantum wells and quantum well intermixing (QWI) [83, 84, 85].

For monolithic integration, additional regrowth steps can significantly add to the complexity and cost of fabrication processes. This is particularly true when integrating Distributed Feedback Laser (DFB) [86] lasers with other components for example, where two or more regrowth steps are required. QWI offers one potential solution [87] for such integration. However, more novel techniques for regrowth free integration exist. For DFB lasers this can be seen in Ref. [88] .

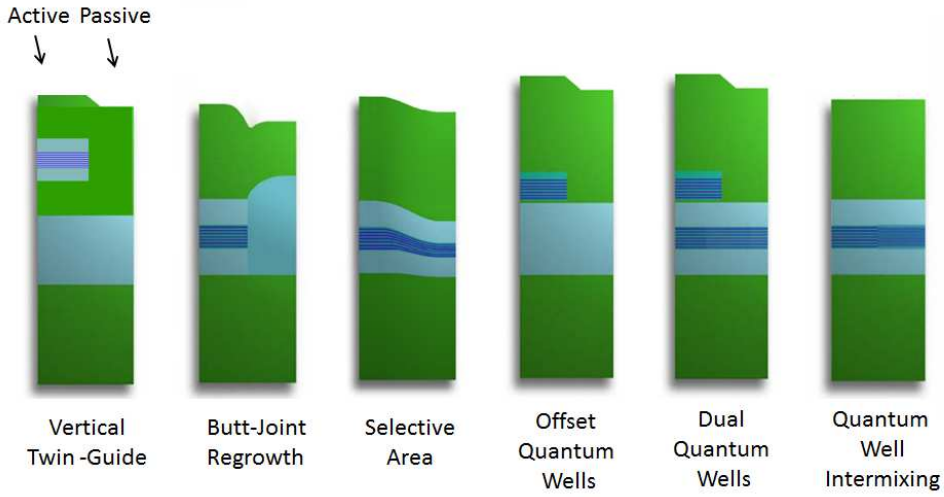

Figure 1.18: Different techniques for monolithic photonic integration [7].

The choice of a monolithic integration scheme was of critical importance to the work and devices considered in this thesis. Regrowth free integration was considered a key requirement, which simplified the fabrication steps during device processing, reduced cost and offered potentially larger device yields. Based on experience within the Tyndall National Institute and Integrated Photonics Group, a novel laser variation known as Slotted Fabry Pérot (SFP) lasers [89] were chosen, which offer excellent potential for regrowth free monolithic integration. This laser design allowed for single facet or completely facetless lasers to be realised through etching of mirror sections on ridge waveguides [89]. The operation of such lasers will be considered in more detail later in chapter 5.

1.4 Optical Injection Locking

Optical injection locking has shown a significant rise in interest where it has been used with directly modulated lasers to reduce the relative intensity noise (RIN) [90], increase laser modulation bandwidths [91] and have shown uses in single sideband

modulation [92] and opto-electronic oscillators [93]. These systems have typically been demonstrated using discrete optical components, however, there has been a push to use monolithic integration to improve performance and flexibility [94, 95, 96]. Such integrated devices have a significantly smaller device footprint along with lower power consumption and cost. Devices such as these are highly attractive for use in modern day telecommunication networks replacing the need for expensive free space optics and discrete components.

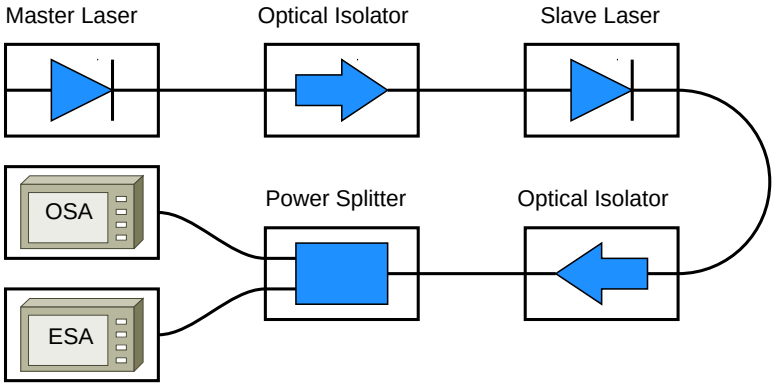

Figure 1.19: Schematic of a typical injection locking experimental setup used to investigate a master-slave system.

Optical injection describes the situation where light from one laser source is injected into the lasing cavity of a second laser. For sufficiently close frequency/wavelength detunings between the sources, one laser is found to lock its operating frequency to that of the other laser while maintaining a fixed relative phase offset. The laser which becomes locked is referred to as the "slave laser", whereas the injected source is referred to as the "master laser". In a typical situation, the discrete lasers of the master-slave system are coupled together using free-space optics or via optical fibre as in Figure 1.19. This allows the behaviour of the slave laser to be investigated on an electrical or optical spectral analyser under varying degrees of optical coupling. For many years, such systems have been a source of immense interest to the non-linear dynamics community, as injection locked semiconductor lasers can offer insights into excitability, multistability and chaotic behaviour which will be discussed further later in this thesis. The use of injection locked semi-conductor lasers plays a key role in the PICs investigated in this thesis, where they have excellent potential for use in coherent channel generation.

1.5 Thesis Motivation and Outline

1.5.1 Thesis Motivation

The motivation for this thesis was to investigate the development of a PIC for use in next generation modulation applications. As was discussed earlier in this chapter,

recent work has shown how QPSK modulation schemes can be implemented in a highly compact form using EAMs [5]. Such modulators offer a significant advantage over MZM based transmitters due to their more compact size. A major disadvantage of such a modulator is the high insertion loss present, which was shown to be ∼40 dB. This limits the use of the modulator in practical applications, or else necessitates the use of external optical amplifiers to amplify the signal after passing through the modulator. The recent push towards further photonic integration of different optical components lends itself well to potential improvements in this design. In particular, the insertion loss could be significantly reduced by incorporating integrated lasers with the modulator itself.

A limitation of this method is the difficulty when monolithically integrating different elements together on a single device, as discussed earlier in this chapter. In particular, the integration of active and passive components can be considerably challenging. For this reason, choosing a suitable laser for such integration was integral to the success of any new modulator design. Recent work on Slotted Fabry Pérot (SFP) lasers has shown them to be an excellent choice for monolithic integration with other devices due to their wide tunability and high SMSR. They have recently been successfully monolithically integrated with EAMs in a regrowth free process [97] and also shown to be easily integrated with semiconductor optical amplifiers (SOAs). This makes SFP lasers an excellent choice when considering a laser for integration with the modulator shown in Ref.[5].

The most simple variation of such a modulator would involve the integration of an SFP laser before the star coupler on the input side of the device shown in Figure 1.13. This would remove the initial coupling losses due to fibre coupling an external source to the modulator, providing at least a 3 dB power improvement. However, this SFP laser would have to be driven with a relatively high bias current to provide sufficient power throughput to each arm of the EAM based modulator. A considerable improvement to this would be the implementation shown in Figure 1.20, where not only is there a laser at the input of the device but also on each arm of the modulator before the EAM regions.

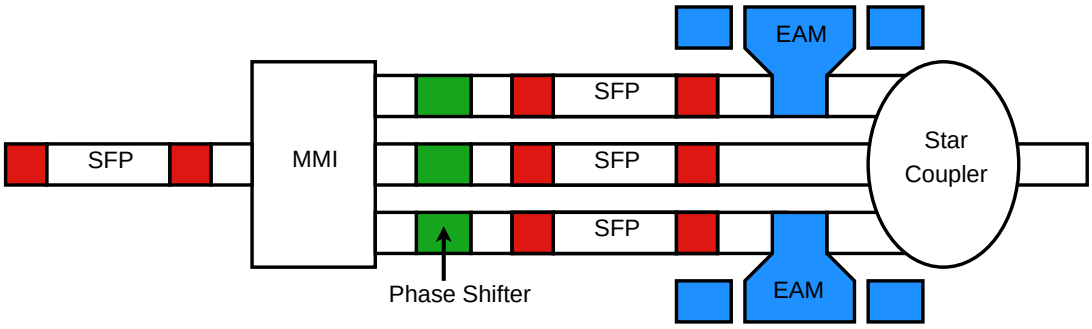

Figure 1.20: An EAM based QPSK modulator with integrated SFP lasers.

Such a layout lends itself well to the possibility of using injection locking to improve

the power performance of the modulator. The input SFP can be used as a master laser, with the SFPs on each arm treated as slave lasers. The slave SFP lasers in this arrangement can be biased to slightly above threshold where they are typically multimodal in operation (and so not suitable for operation in the modulator) but have a low power consumption. By operating the master SFP above threshold (where it can have a high SMSR and peak power) it has the potential to simultaneously lock the frequency and phase of each slave SFP to the master laser source, while making them coherent with respect to each other. In this arrangement the slave lasers would experience strong lasing action at the master laser frequency, with significant suppression of the other lasing modes. This can increase the power output of the slave lasers at the master lasers frequency by >10 dB while running at just above their threshold values, with the added benefit of ensuring coherence between the optical signals. Coherence between the light in each arm of the modulator is of critical importance when generating each symbol of the constellation diagram for this QPSK modulation scheme.

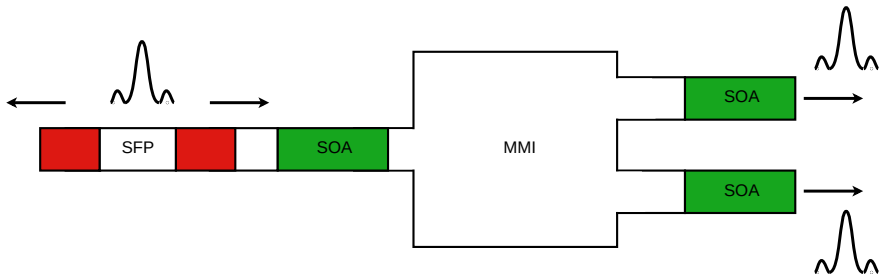

Figure 1.21: SFP laser integrated with an MMI coupler and SOA. The building block of more advanced PICs.

The development of a PIC that can integrate passive components, SFP lasers, EAMs and SOAs (for phase change) in the modulator shown in Figure 1.20 is a highly ambitious goal. Previous research has investigated the integration of SFP lasers with EAMs [97] and shown their excellent potential for PICs. However, there has been no previous investigation into the integration of multiple SFPs together or the integration of SFP lasers with passive waveguide splitters and combiners. Splitters and combiners play a key role in the operation of the proposed modulator in Figure 1.20, and are essential in almost all PICs considered in current research. Injection locking of SFP lasers plays a key role in the proposed method of coherent output generation and as such, needs to be investigated carefully. Performing injection locking with lasers on integrated circuits also poses difficulties due to the lack of functional optical isolators on chip. This means that a true master-slave system, with one way coupling is not currently possible to realise. Instead, any master-slave system on chip must be in a mutual coupling regime with bi-directional coupling [98], where the master can effect the slave, and vice-versa.

For these reasons, this thesis will focus on three primary areas of research which lend themselves not only to the device shown in Figure 1.20, but to any number of future

PICs. These are:

1. The design and application of optimum splitters and combiners for use in PICs
2. The integration of SFP lasers with optical amplifiers, splitters and combiners
3. The integration of multiple SFP lasers together with passive components (splitters/combiners) to investigate the use of injection locking on PICs

The optimum design of splitters and combiners plays a pivotal role in photonic integration. This is especially true when making compact devices, where couplers are required to be as small as possible while still maintaining excellent performance. The investigation of splitters and combiners was carried out with the goal of developing the device shown in Figure 1.21. This PIC allows the integration of an SFP laser with waveguide splitter/combiner and SOA sections to be examined. This device can be used as an optical power splitter on chip, and it is considered to be the fundamental building block of more advanced PICs. With such a building block in place, the integration of multiple SFP lasers was examined by considering the device shown in Figure 1.22.

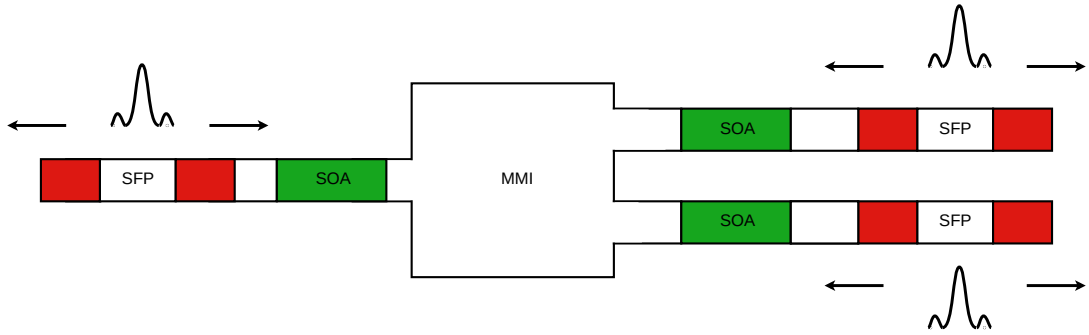

Figure 1.22: Schematic of the most complicated PIC considered in this thesis. Multiple SFP lasers integrated together using an MMI coupler and SOA based optical interconnect.

This device allowed for almost all components of the proposed QPSK modulator shown in Figure 1.20 to be investigated, apart from the EAMs which were shown in Ref. [97]. As a result, the main focus of this thesis will be developing these other aspects of the modulator while the EAMs remain outside of its scope. In particular, it allows the generation of coherent outputs on chip via injection locking of integrated lasers to be examined for the first time. The use of integrated lasers on chip in such a QPSK modulator design offers improvements to power consumption while minimising the insertion loss of the device. In particular, integrated lasers remove the need for an externally coupled laser source which improves the performance of the device by at least 3 dB. In addition to this, the use of multiple injection locked lasers can provide a power increase of $>$ 10 dB for slave lasers operating at just above threshold. This expected 13 dB reduction in device loss has the potential to make such modulators a viable alternative to MZM based QPSK modulators, particularly when their highly

compact size over traditional modulators is taken into account.

1.5.2 Thesis Outline

Chapter 1 has provided a general overview of photonics technologies and the motivation for this research. The primary focus of this work was to investigate the use of integrated lasers in PICs for coherent optical signal generation using single epitaxial growth, for monolithic integration. The realisation of such a device required the careful design of multiple different photonic components which were then brought together on a single chip. This included the design of optical waveguides, efficient optical couplers, amplifiers and of course, lasers. The development of these individual elements, their integration together and testing of the full integrated PIC, forms the basis of the work presented in this thesis.

Chapter 2 introduces optical waveguides and examines the underlying physics of how light is confined and guided on a PIC. Leading from this, optical couplers are described in detail with particular attention paid to the design of multimode interference (MMI) couplers. Chapter 3 examines the computational models used to design MMIs, which are then investigated in detail. This work was aimed at providing a rapid means of optimising the coupling efficiency of MMIs while ensuring they are sufficiently tolerant to fabrication errors. The completed models were used to design a series of MMIs based on a custom quantum well epitaxial structure. These were tested experimentally and the results compared to those predicted by the model.

The experimental testing of any PIC poses challenges due to the precision required when aligning optical fibre to the input and output waveguides to be coupled. Chapter 4 describes a new experimental technique which greatly simplifies how fibre coupling can be performed. The experimental setup and software required for such a coupling technique was developed during this work, where its functionality was extensively demonstrated. This method of efficient fibre coupling has widespread applicability to the testing of integrated optical devices in general. As such, the work contained in this chapter was published [99] by the Institution of Engineering Technology Optoelectronics.

Chapter 5 describes the design of PICs based on the schematics shown in Figures 1.21 and 1.22. The type of laser chosen for the integrated devices is examined in detail, with waveguide tapers and optical couplers designed based on the material and etch structure of the laser. The integration of waveguide couplers and lasers is then examined, with a particular focus on the operation and subsequent testing of each proposed device.

Chapter 6 explores the initial characterisation of the lasers used in the integrated devices designed in this work. With the lasers characterised, the first fully integrated device was considered which consisted of an SFP laser integrated with an SOA and optimised 1×2 MMI coupler. This integrated device was designed and tested experimentally as

part of the work undertaken in this thesis; and was the first demonstration of an SFP laser monolithically integrated with an MMI using a single epitaxial growth. Such a device forms the basis of the more complex PICs examined in later chapters and the results were published [100] in Photonics Technology Letters.

With the integration of SFP lasers and optical couplers demonstrated, chapter 7 investigates how these elements can be used to form a fully integrated system of mutually coupled SFP lasers linked through a passive waveguide interconnect and SOA section. This device was then used to examine the optical phase locking properties of integrated lasers in a highly asymmetric coupling regime, where the first example of on chip optical phase locking between a single master and slave laser was shown. The results of this experiment were published [101] in Optics Express. In addition to this, optical phase locking of multiple slave lasers to a single master laser was demonstrated via coupling through an optimally designed MMI. The results of which were presented [102] at the International Conference on Indium Phosphide and Related Materials (IPRM), where it was shown that this system could be used in the generation of multiple coherent optical signals on an integrated device.

Chapter 8 summarises the results and conclusions from this thesis, where the key developments and milestones are outlined. The thesis concludes by giving an outlook into future work which may arise from this study and discusses the impact it can have on future integrated modulator systems.

Chapter 2

Optical Waveguides and Couplers

There is a push towards using photonic integration in optical transmission systems to improve power consumption in devices while reducing both cost and size. The optimum design of photonic interconnects between optical devices on the same chip plays a key role. For larger systems, optical fibres are used in the transmission of light for distances of centimetres to many hundreds of kilometres [103, 104, 105, 106, 107]. In the area of photonic integration, optical fibres are replaced by optical waveguides which are used to channel and direct the light in compact optical circuits. In this chapter, the basic theory of optical waveguides is discussed, with particular attention paid to how light is confined in waveguide structures. A primary focus of this chapter is to investigate the design and application of passive waveguide couplers for use in PICs. Waveguide couplers are used extensively in PICs, where they can split light into multiple channels or combine different optical signals. These structures are analysed in detail, where a model is discussed that allows their optical performance to be examined. The work described in this chapter plays a key role in the development of the photonic integrated devices discussed in chapters 5 and 6.

2.1 Planar Waveguides

The first type of waveguide considered in this thesis is the *planar waveguide*, as shown in Figure 2.1. The structure of this waveguide consists of high refractive index material (the waveguide core) inserted between two lower refractive index materials (the waveguide substrate and cladding). Light in this arrangement is confined in the transverse x-direction across the waveguide. Due to total internal reflection, guided modes are supported between the cladding and substrate layers which are free to propagate in the z direction. Following from the analysis of Maxwell's Equations in Okamodo [108], two wave equations which describe the electro-magnetic field distribution in each of the core, cladding and substrate regions can be found. Two different solutions exist which

are related to the polarizations of the electric and magnetic fields. The Transverse Electric (TE) field polarization has an electric field in the y-direction, E_y, with no field component in the z or x-directions. The TE polarization is described by:

$$\frac{d^2E_y}{dx^2} + (k^2n^2 - \beta^2)E_y = 0, \tag{2.1}$$

with

$$H_x = \frac{-\beta}{\omega\mu_0}E_y \quad H_z = \frac{j}{\omega\mu_0}\frac{dE_y}{dx}. \tag{2.2}$$

where $j = \sqrt{-1}$ and n is the refractive index in core, cladding or substrate region. The permeability of free space is given by μ_0, where it is assumed that the permeability in the propagation medium, μ, is such that $\mu \approx \mu_0$. The wavenumber, k, is defined as $k = \frac{2\pi}{\lambda}$, which is related to angular frequency of the propagating light, ω, via $k = \frac{\omega}{c}$, where c is the speed of light in a vacuum. The Transverse Magnetic (TM) field polarization has a magnetic field directed in the y-direction, H_y, with no field component in the z-direction or x-direction. The TM polarization is described by:

$$\frac{d}{dx}(\frac{1}{n^2}\frac{dH_y}{dx} + (k^2 - \frac{\beta^2}{n^2})H_y = 0, \tag{2.3}$$

with

$$E_x = \frac{\beta}{\omega\mu_0 n^2}H_y \quad E_z = \frac{-j}{\omega\mu_0 n^2}\frac{dH_y}{dx} \tag{2.4}$$

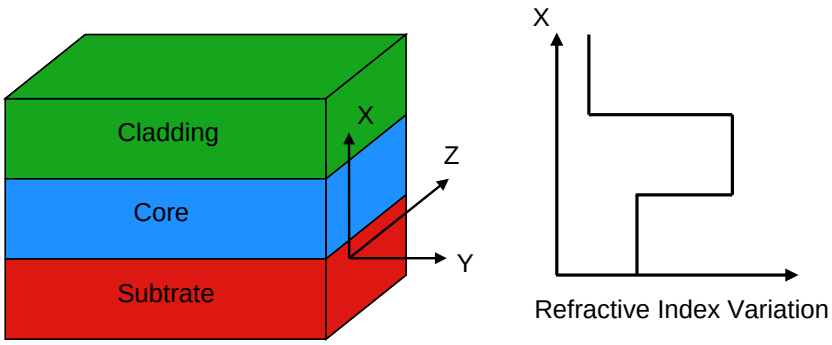

Figure 2.1: Planar optical waveguide structure showing the refractive index variation across the layers.

When calculating the electro-magnetic field distribution for either the TE or TM polarization, it is necessary to solve Equations (2.1) and (2.3) in the cladding, core and substrate regions. From this a complete picture of the field distribution in the waveguide can be determined. The refractive indices of the core, cladding and substrate

regions are referred to as n_{core}, n_{clad} and n_{sub}, respectively. The equations for the TE solution which follows from this is:

$$\frac{d^2E_y}{dx^2} + \kappa^2 E_y = 0, \text{ in the core region} \tag{2.5}$$

$$\frac{d^2E_y}{dx^2} - \sigma^2 E_y = 0 \text{ in the cladding region} \tag{2.6}$$

$$\frac{d^2E_y}{dx^2} - \xi^2 E_y = 0, \text{ in the substrate region} \tag{2.7}$$

with κ, σ and ξ representing the wave numbers in each region. They are defined as:

$$\kappa = \sqrt{k^2 n_{core}^2 - \beta^2}, \tag{2.8}$$

$$\sigma = \sqrt{\beta^2 - k^2 n_{clad}^2}, \tag{2.9}$$

$$\xi = \sqrt{\beta^2 - k^2 n_{sub}^2}. \tag{2.10}$$

where β is the modal propagation constant, defined as $\beta = kn_{eff}$, with n_{eff} represents the *effective index* of the supported mode in the waveguide. For a slab waveguide with core region of thickness 2a, as in Figure 2.2, the electric field must decay exponentially in the cladding and substrate regions, with sinusoidal confinement in the core region. The field then takes the form:

$$E_y = \begin{cases} A\cos(\kappa a - \phi)\exp(-\sigma(x-a)) & \text{if } x > a \quad (2.11a) \\ A\cos(\kappa x - \phi) & \text{if } -a < x < a \quad (2.11b) \\ A\cos(\kappa a + \phi)\exp(\xi(x+a)) & \text{if } x < -a \quad (2.11c) \end{cases}$$

This analysis assumes infinite cladding and substrate thicknesses, which are of course not present in physical waveguides. However, due to the large optical confinement present in typical waveguides, the exponential tail extends only slightly into these regions, making this a valid approximation.

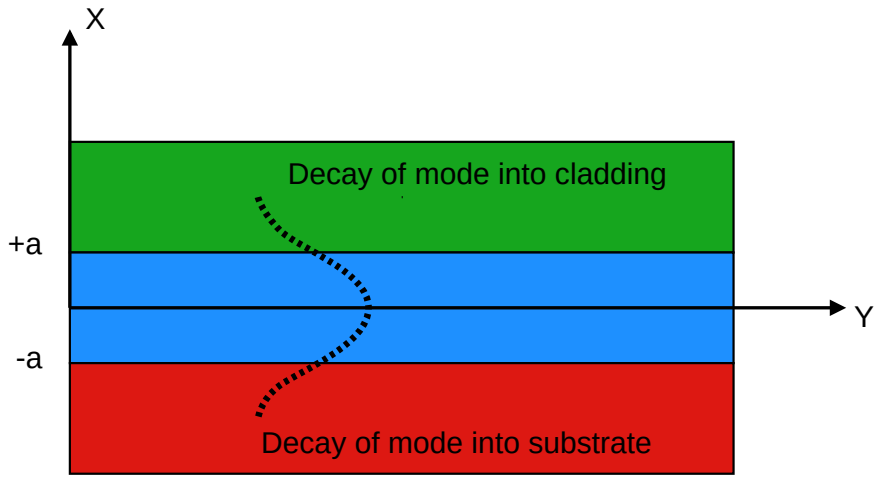

Figure 2.2: Decay of the electric field distribution of waveguide mode into cladding and substrate layers.

From the boundary conditions, E_y and H_z are continuous across the core, cladding and substrate interfaces for the TE mode solution. With H_z given by (2.2), dE_y/dx must also be continuous across each region and is given by:

$$\frac{dE_y}{dx} = \begin{cases} -\sigma A\cos(\kappa a - \phi)\exp(-\sigma(x-a)) & \text{if } x > a; \\ -\kappa A\cos(\kappa x - \phi) & \text{if } -a < x < a; \\ \xi A\cos(\kappa a + \phi)\exp(\xi(x+a)) & \text{if } x < -a. \end{cases}$$

Applying these equations across the boundary at $x = a$ gives:

$$\kappa A\sin(\kappa a - \phi) = \sigma A\cos(\kappa a - \phi) \tag{2.12}$$

Applying these equations across the boundary at $x = -a$ gives:

$$\kappa A\sin(\kappa a + \phi) = \xi A\cos(\kappa a + \phi) \tag{2.13}$$

Equations (2.12) and (2.13) can be rewritten as:

$$\tan(\kappa a - \phi) = \frac{\sigma}{\kappa} \tag{2.14}$$

and

$$\tan(\kappa a + \phi) = \frac{\xi}{\kappa} \tag{2.15}$$

By defining $u = \kappa a$, $w = \xi a$ and $w' = \sigma a$, Equations (2.14) and (2.15) can be written

as:

$$\tan(u - \phi) = \frac{w}{u} \tag{2.16}$$

$$\tan(u + \phi) = \frac{w'}{u} \tag{2.17}$$

Solving these equations for u and ϕ yields:

$$u = \frac{m\pi}{2} + \frac{1}{2}\arctan(\frac{w}{u}) + \frac{1}{2}\arctan(\frac{w'}{u}) \tag{2.18}$$

$$\phi = \frac{m\pi}{2} + \frac{1}{2}\arctan(\frac{w}{u}) - \frac{1}{2}\arctan(\frac{w'}{u}) \tag{2.19}$$

Solving Equations (2.18) and (2.19) allows the wave numbers of supported waveguide modes in the core, cladding and substrate regions to be determined. These can then be used to calculate the electric field distribution for the TE waveguide mode from Equations 2.11a – 2.11c

Similar expressions can be determined for the TM mode solution of the waveguide [108, 109, 110, 111]. Equations (2.18) and (2.19) can be solved graphically for a qualitative solutions, however, numerical methods can provide highly accurate solutions. In the sections that follow, these graphical and numerical methods are examined.

2.1.1 Graphical Solution Method of Slab Waveguide

The propagation constants for the TE mode of a slab waveguide can be found by solving the set of Equations (2.18) and (2.19). For simplicity, a symmetric slab waveguide is considered, where the cladding and substrate refractive indices are equal. The slab waveguide has a waveguide width, $2a = 5.0\mu m$; operating wavelength, $\lambda = 1.55\mu m$; $n_{core} = 3.38$ and $n_{sub} = n_{clad} = 3.17$. For a symmetric waveguide such as this, Equations (2.18) and (2.19) can be simplified to:

$$u = \frac{m\pi}{2} + \arctan(\frac{w}{u}) \tag{2.20}$$

$$\phi = \frac{m\pi}{2} \tag{2.21}$$

Equation (2.20) can also be written as:

$$w = u\tan(u - \frac{m\pi}{2}) \tag{2.22}$$

The wave numbers u and w are dependant on each other through Equations (2.8)-(2.9). This allows them to be rewritten as:

$$u^2 + w^2 = k^2a^2(n_{core}^2 - n_{clad}^2) \tag{2.23}$$

The propagation constants of the waveguide can then be found by solving Equations (2.22) and (2.23) graphically. The equations can be plotted on the same graph to determine κ and σ, where the points of intersection determine u and w for a particular mode. For the waveguide under consideration here, Figure 2.3 shows the two equations plotted together, substituting $x = \sigma a$, $y = \kappa a$ and $r^2 = k^2a^2(n_{core}^2 - n_{clad}^2)$.

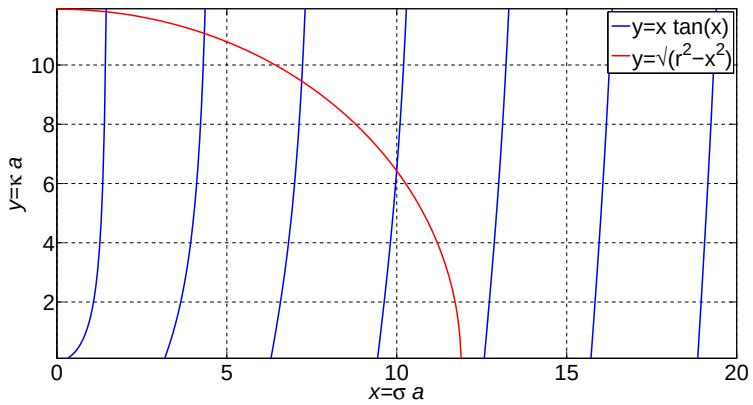

Figure 2.3: Graphical solution method for finding propagation constants of different waveguide modes.

A solution exists at every intersection point between the two curves. At this point, the value of κa or σa can be approximated and the equation solved. Solutions exist between each branch of $y = x\tan(x)$, which indicates that there is one solution within every $\frac{\pi}{2}$ interval. The V parameter of the waveguide determines the radius of the circle drawn in the graphical solution in Figure 2.3 and is given by,

$$V = ka\sqrt{n_{core}^2 - n_{clad}^2} = a(\sqrt{\sigma^2 + \kappa^2}). \tag{2.24}$$

By determining how many branches of the Tan function exist within this radius, the number of supported modes in the waveguide could be found. The number of supported modes in a waveguide is then seen to be given by $\frac{2V}{\pi}$. A waveguide can be designed to support only a single mode if $V \leq \frac{\pi}{2}$.

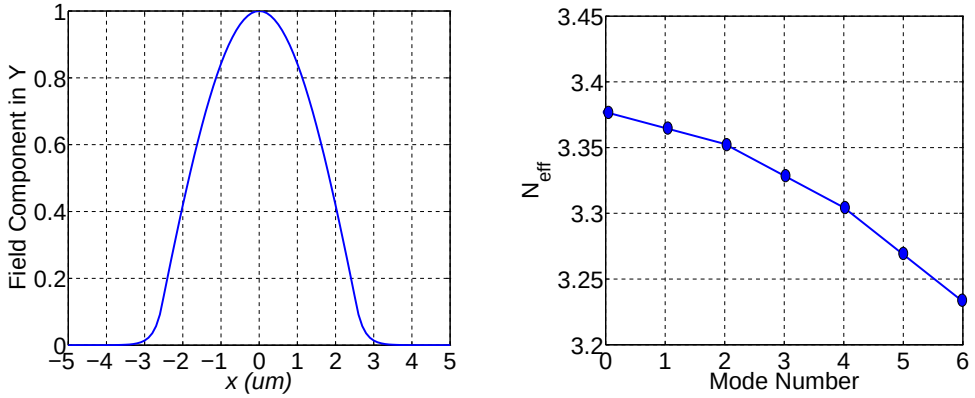

(a) E_y component of TE mode solution. (b) N_{eff} of TE mode versus mode number.

Figure 2.4: Results from the graphical solution method.

Solving Equations (2.22) and (2.23) using the graphical solution method allows the propagation constants of each guided mode in the waveguide to be determined. From this, the electrical field distribution can be calculated. The electric field for the TE excited waveguide mode is shown in Figure 2.4a. The effective index for each guided mode can also be found from this analysis. The effective indices plotted against mode number for the previous waveguide are shown in Figure 2.4b.

2.1.2 Root Solving Method of Slab Waveguide

The graphical method provides an approximate solution to Equations 2.18 and 2.19, however, numerical methods are required to provide more accurate solutions. These are developed extensively in Okamodo [108]. For such methods, a mode is said to be confined if the effective index of the mode, n_{eff}, is bounded as $n_{clad} \leq n_{eff} \leq n_{core}$. This defines a cut-off condition for guided modes, where they are restricted between:

$$0 \leq b \leq 1, \tag{2.25}$$

with the parameter b, referred to as a *normalised propagation constant*, defined as:

$$b = \frac{n_{eff}^2 - n_{clad}^2}{n_{core}^2 - n_{clad}^2}. \tag{2.26}$$

By writing the *normalized frequency*, v, as:

$$v = n_{core} k a \sqrt{\frac{n_{core}^2 - n_{clad}^2}{n_{core}^2}}, \tag{2.27}$$

the parameters u and w can be rewritten as:

$$u = \kappa a = v\sqrt{1-b} \tag{2.28}$$

$$w = \xi a = v\sqrt{b} \tag{2.29}$$

Following from [108], Equation (2.18) can then be written similarly to 2.20 for a symmetric waveguide as:

$$v\sqrt{1-b} = \frac{m\pi}{2} + \arctan\sqrt{\frac{b}{1-b}}, \tag{2.30}$$

or

$$F(v,m,b) = v\sqrt{1-b} - \frac{m\pi}{2} - \arctan\sqrt{\frac{b}{1-b}} = 0 \tag{2.31}$$

A *bisection method root solver* was constructed in Matlab to solve Equation (2.31) allowing for the n_{eff} of each guided mode of a waveguide to be calculated by determining b. This code can be seen in Appendix A. Equation (2.31) is plotted in Figure 2.5 for a series of different TE modes in a typical 2.0 μm wide InP based waveguide with core and cladding refractive indices of 3.38 and 3.17, respectively.

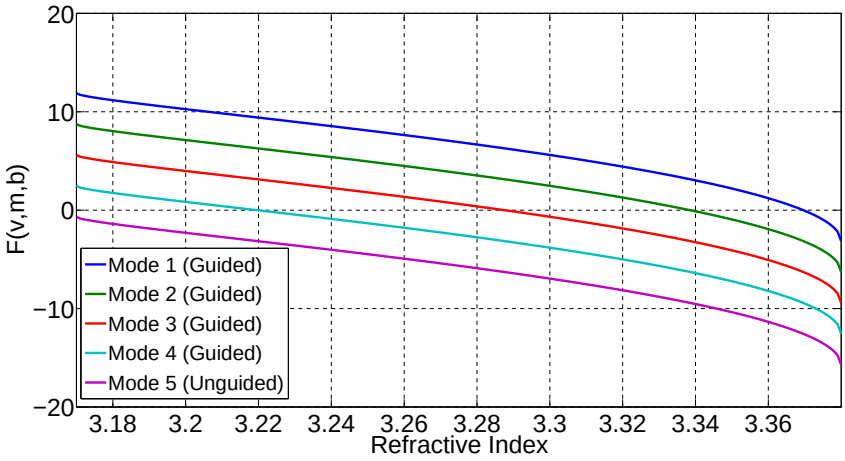

Figure 2.5: Plot of *F(v,m,b)*. The roots can be used to determine the effective index of each guided mode in a waveguide structure.

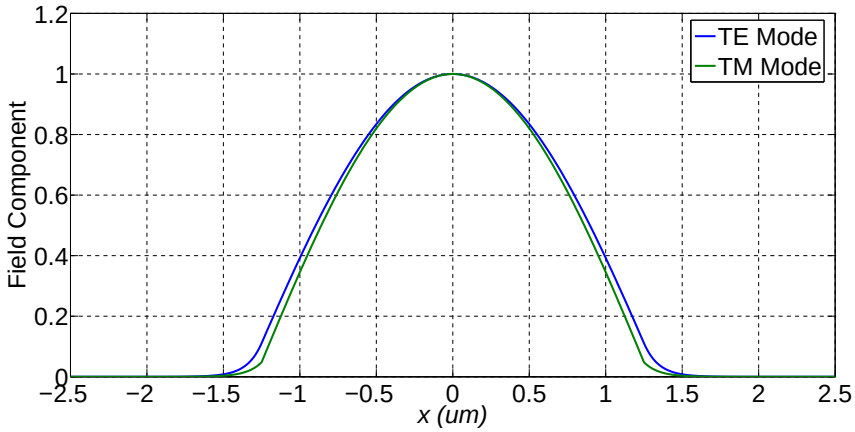

Figure 2.6: E_y and H_y components of TE and TM mode solutions.

Where the *F(v,m,b)* in Figure 2.5 cuts the x-axis can be used to determine the propagation constant (or effective refractive index) of a waveguide mode. With this method, the field distribution and propagation constants of any slab waveguide mode can be determined. Using this code, the field profiles generated for the fundamental TM and TE modes of a slab waveguide with thickness 1.0 µm and refractive indices of 1.45, 3.45 and 1.45 in the cladding, core and substrate respectively were calculated. The overlapped fields are shown in Figure 2.6.

2.2 Rectangular Waveguides

Unlike planar waveguides, rectangular waveguides confine light in both x and y-directions due to an index variation, *n(x, y)*. They represent the type of structures typically found and used in PICs. Some examples of rectangular waveguides are shown in Figure 2.7. The main variations considered are *ridge waveguides* and *rib waveguides*. In ridge waveguides the mode is typically highly confined due to the high index core being surrounded on all sides by the lower index cladding and core. The core of a rib waveguide is typically not surrounded on all sides by a lower index material and offers less mode confinement.

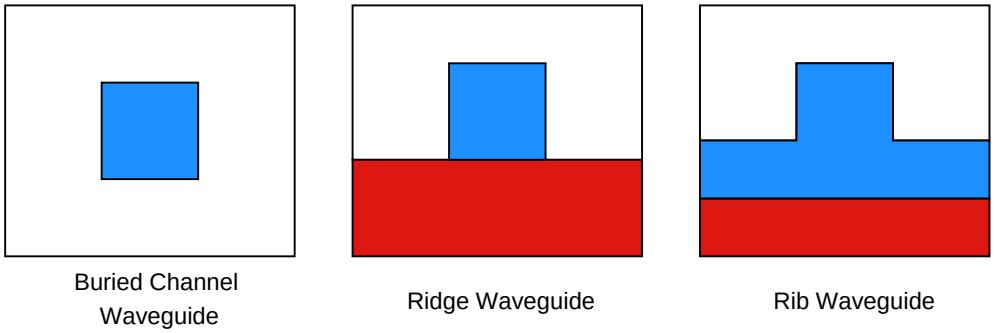

Figure 2.7: Variations of Rectangular Waveguides.

Similar to the slab planar waveguides discussed earlier, rectangular waveguides also support TE and TM guided modes. Waveguides support hybrid modes where the electro-magnetic field has component in all directions. Analytical solutions for these hybrid modes exist only in particular situations involving certain symmetries, for example in optical fibers themselves [112]. For waveguides where there are no analytical solutions, numerical methods such as the Beam Propagation Method (BPM) or the Scalar Finite Element Method (SFEM) are used to obtain accurate solutions. Research previously carried out within the Integrated Photonics Group (IPG) at Tyndall [8] has investigated the uses and application of such methods to the modelling of two-dimensional waveguide structures. These methods are beyond the scope of this thesis, but mode solver tools based on the SFEM code were made available for this work. Figure 2.8 shows a typical rib waveguide structure which can be modelled using the SFEM mode solver developed in Ref. [8]. To illustrate the application of this mode solver, an InP based ridge waveguide was considered with core index of 3.38 and substrate index of 3.17. The ridge width, thickness and height of the waveguide were 2.5 µm, 0.5 µm and 0.5 µm respectively. The fundamental TE mode of this waveguide was found using the SFEM simulation tool and is shown in Figure 2.9.

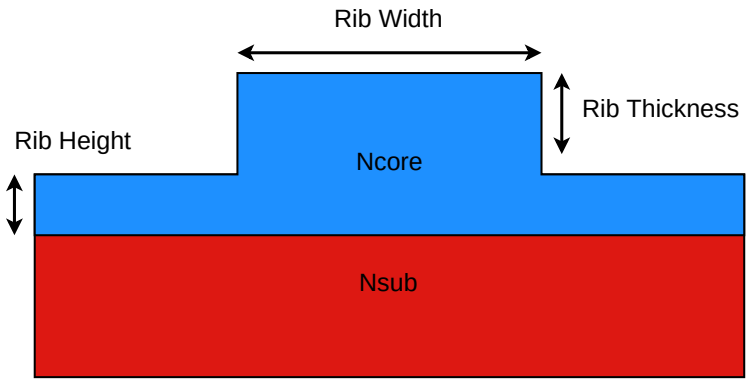

Figure 2.8: Structure of a typical rib waveguide which can be modelled using SFEM mode solver tools.

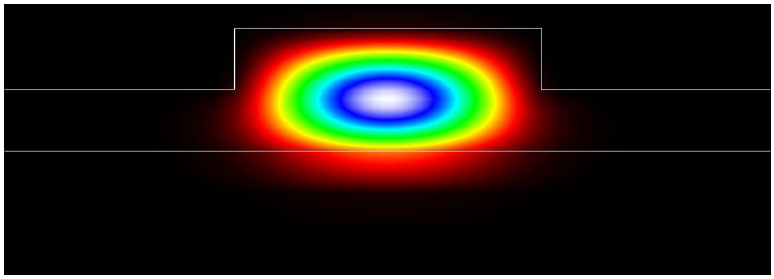

Figure 2.9: Mode profile of an InP based rib waveguide as calculated from the SFEM mode solver [8].

These tools were made available during the course of this work and proved to be useful for detailed analysis, as will be shown in later chapters. Considerable time

and computational power is required to provide accurate solutions using these tools, due to the complex numerical methods used. As a result, they are not practical for situations where rapid solutions are needed. Approximate solutions can be provided by other numerical methods, which are suitable for many applications. One of the most important approximate solutions to the wave equation of rectangular non-planar waveguides, is known as the Effective Index Method (EIM). This method can be applied to ridge and rib waveguides and compares favourably with other more accurate solutions depending on the waveguide structure and material type. In the next section the EIM is described in detail and its application to ridge waveguides is demonstrated.

2.2.1 Effective Index Method

Similar to Kumar's [113] and Marcatili's method [114], the EIM provides an estimate to the propagation constants of waveguide modes, which can in turn be used to determine the field distribution. Numerical methods such as BPM [115, 116, 117], FDM [118, 119, 120] and FEM [121, 122] are used where highly accurate solutions are required. Typically, these methods are numerically intensive and require long computational times. The EIM provides a sufficiently accurate solution for most practical applications and allows the mode characteristics of a waveguide to be examined.

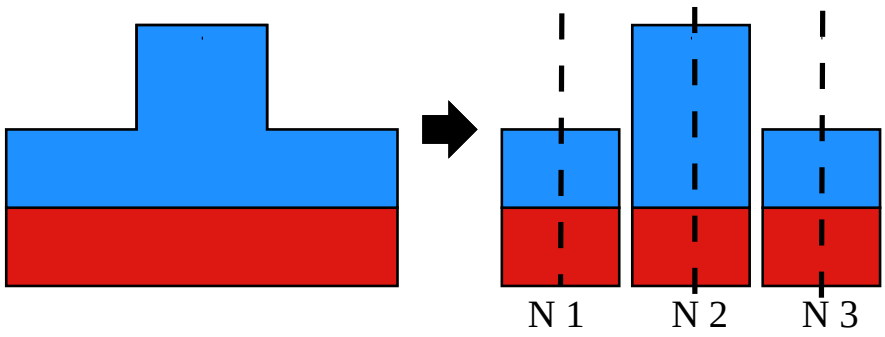

Figure 2.10: Rectangular waveguide is split into three separate regions. The effective index of the guided modes in each region can then be calculated by treating it has a slab waveguide.

The EIM can be used to determine the propagation constants of guided modes in rectangular waveguides by taking the waveguide structure and splitting it into three planar waveguides which can be examined individually, see Figure 2.10. If the mode confinement in the vertical direction across the thickness of the waveguide is stronger than that of the confinement in the horizontal direction across its width, then the mode defined by the structure is mainly due to the layer structure in the vertical direction. This mode is distorted by the etched structure in the lateral direction which results in waveguide modes where the electric and magnetic fields are not strictly TE or TM, as with a one-dimensional planar waveguide structure. However, modes of

rectangular waveguides which have their electric and magnetic fields directed mainly in the horizontal direction of the waveguide are referred to as TE or TM modes for convenience.

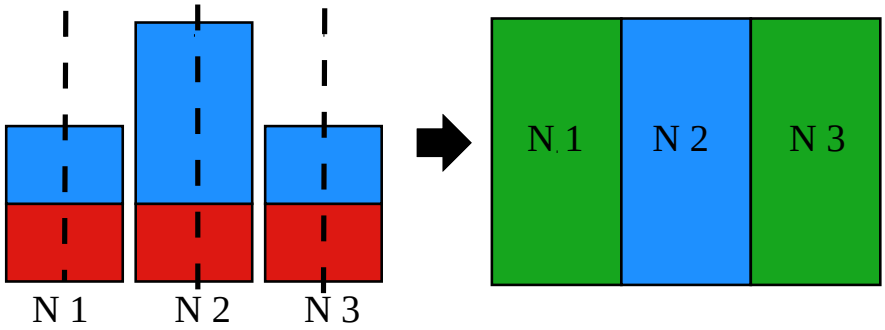

Figure 2.11: The calculated effective indices in each region are used to form a new slab waveguide. The propagation constants of this waveguide determines the propagation constants of the original rectangular waveguide.

Determining the propagation constants for a particular TE or TM polarised mode of a rectangular waveguide using the EIM involves taking a waveguide structure, Figure 2.8, and splitting it into three regions. Each region is treated as a planar waveguide structure, where the propagation constants of the guided modes in each section are calculated and the effective index determined, as in Figure 2.10. A new planar waveguide structure is formed using the calculated effective indices of the regions, N1, N2 and N3; with thickness equal to the width of the initial ridge waveguide structure, as seen in Figure 2.11. This new planar waveguide structure can then be solved for the slab TE and TM modes to determine the effective index of the overall rectangular mode. For an in depth analysis of this technique, see Ref. [123, 108].

An EIM mode solver was implemented in C++, see Appendix A, and was used to model the mode profiles and propagation constants of waveguide modes in waveguides. The EIM makes use of the one-dimensional mode solver, described previously, to solve for the modes in each step of the solution. This EIM code can be applied to the structure shown in Figure 2.8, which was previously modelled using SFEM. If the TE mode of this structure is considered, the application of the EIM involves first calculating the TE modes of the planar waveguide structures defined in the lateral and central regions of the rib waveguide. The effective indices of lateral and central regions were found to be 3.2458 and 3.3268, respectively. Due to the high optical confinement in the vertical direction over the waveguide, the mode profile in the central region relates strongly to the TE mode of the waveguide, but is distorted by the etched waveguide ridge. The profile of the mode in the central region is shown in Figure 2.12a, which represents the modal distribution of the y-direction. The effective indices of the modes in the lateral and central regions were then used to form the equivalent planar waveguide structure where the TM mode and effective index was considered. The mode profile of the TM

mode is also shown in Figure 2.12a and represents the modal distribution of the x-direction. It describes how the etched structure of the waveguide effects the waveguide mode. The product of these two modes defines the overall mode shape of the TE mode of the rib waveguide. The calculated effective index of the TE mode of this waveguide using the EIM was determined to be 3.3177. This compares favourably with the value calculated using the SFEM model, which was 3.3134. It should be noted that there is a vast difference in the computational times required between both the EIM and SFEM solutions. Using a PC with a 4th Generation Intel® Core™ i7 Processor and 8GB of RAM, for a moderate grid spacing of 0.75 µm, approximately one hundred seconds are required for the solution to be computed using the SFEM code. The EIM performs this calculation with the same hardware in a approximately one second, although generates only an approximate solution.

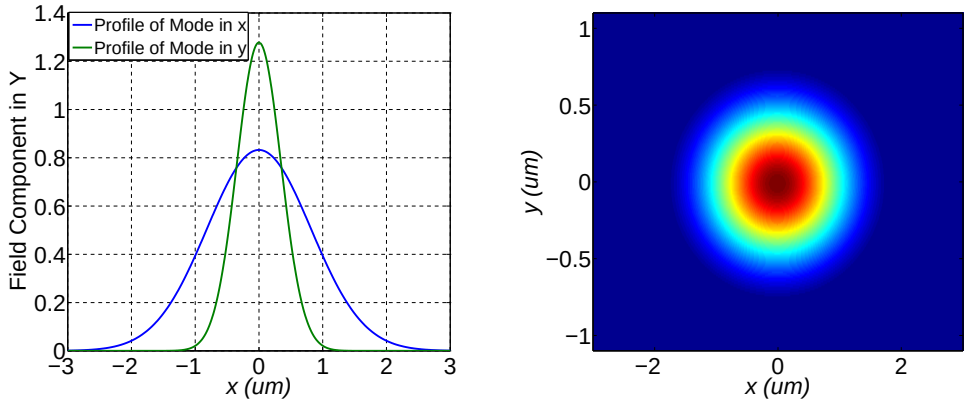

(a) (b)

Figure 2.12: (a) E_y field component of the TE mode of a two-dimensional waveguide in the x and y-directions. (b) full two-dimensional E_y component mode profile, which is a product of the separable x and y E_y field components of the mode.

2.3 Multimode Interference Couplers

The splitting or coupling of light on an integrated device can be realised in a number of different ways. These include using y-branch structures [124], directional couplers [125] and star couplers [126, 127]. The design of star couplers was considered in Appendix B. In addition to these, Multimode Interference Couplers (MMIs) have seen wide spread use in photonic devices [128, 129, 130], where they can be used in a range of configurations with single and multiple input and output ports. The analysis and design of MMIs has a key role in the work presented in this thesis, where they are used extensively in the integrated devices considered in chapter 5.

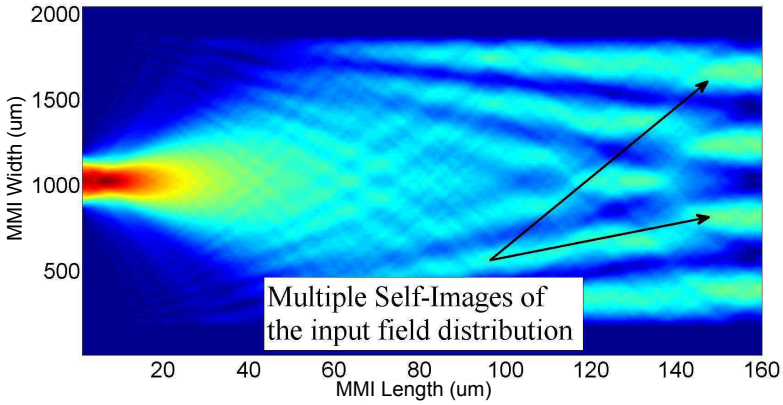

Figure 2.13: TE field distribution of an MMI. The input field is re-imaged at specific points along the length of the MMI. Light can be decoupled from the MMI by placing output waveguides at these points. Figure generated using the MMI design tools developed during this work.

MMIs [131] are based on the self-imaging principle [132], where an input field entering a multimode waveguide region becomes self-imaged periodically along the propagation direction of the structure. An example of this is shown in Figure 2.13, where the field distribution inside of an MMI is simulated.

Multiple equally spaced self-images are formed at specific intervals along the length of the device, which can be decoupled from the MMI by using strategically placed output waveguides. Determining the optimum position and spacing for these output waveguides is the basis for MMI optimisation. MMIs were originally developed in Ref. [131] and have been shown to be an essential element in PICs, because of their ability to split and couple optical signals compactly and efficiently compared to star couplers or y-branch couplers. The advantages of using MMIs include their ability to work over a wide wavelength band, insensitivity to different polarizations of light, ease of fabrication and compact size [133]. MMIs have found uses in more advanced PICs where novel functions and circuit layouts are required. The have shown particular prominence in Mach Zehnder Modulators (MZM) and Wavelength Division Multiplexers (WDM) where their low loss and integrability with other devices is a significant advantage [134, 135, 136, 137, 138].

Several methods exists for designing MMIs, these include using hybrid methods [139] and beam propagation techniques [140]. A full description of self-imaging in multimode waveguides can be explored by using Modal Propagation Analysis (MPA) techniques developed in Ref. [141]. With MPA, the input field in an optical waveguide can be decomposed into the guided modes of the waveguide itself. These individual supported modes can then be propagated along the structure where the field at any point can be determined by their superposition. Since MMIs are typically based on rectangular waveguides, as in Figure 2.7, two-dimensional mode solutions are required. The modes

of such waveguides can be calculated using FDM and FEM; or by using BPM where the field in an MMI can be formed by waves reflecting from the MMI walls.

The EIM model described earlier in this chapter can also be used to determine accurate mode solutions for rectangular waveguides. The advantage of the EIM is that it can reduce a two-dimensional rectangular waveguide structure down to an equivalent one dimensional planar structure which can simplify the modelling of MMIs. This allows for rapid computational analysis of MMI modes without the need for numerically intensive mode solvers. As a result, the MMI modelling tool developed during this thesis was based on an *Effective Index Modal Propagation Analysis* (EIM-MPA) technique. Further to this, a full two-dimensional MMI modelling program was also implemented during this thesis. This made use of the SFEM toolbox mode solver, as shown in Figure 2.9, which is referred to as the SFEM-MPA method. Both the EIM-MPA and SFEM-MPA MMI design tools will be described in greater detail in chapter 3, with MPA discussed further in what follows.

2.3.1 MMI Design using Modal Propagation Analysis

When light enters an MMI, it excites the modes in the multimode region. The number of modes excited depends on the properties and position of the input field. With MPA, the field at any point along the length of the MMI can be written as a summation of the guided modes to that point. In this way the full field distribution of an MMI can be determined. The main advantage of MPA is that it only requires accurate modal solutions to calculate the field at any given point. These solutions can be calculated just once and then reused to determine the electric field distribution at an arbitrary point along the MMI. The EIM mode solver, as mentioned previously, can be applied to the design of such structures and allows a means of optimising MMIs efficiently.

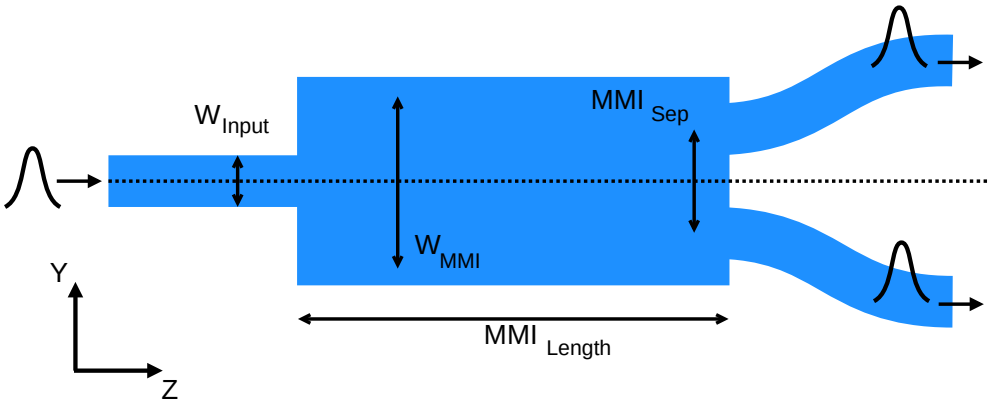

Figure 2.14: Schematic outline of an MMI.

To illustrate the design on an MMI using MPA consider the schematic of a standard MMI structure shown in Figure 2.14. A narrow waveguide, typically single moded,

is shown at the input side of a wider waveguide known as the MMI region. This input waveguide has a width W_{Input}, with the wider waveguide width referred to as W_{MMI}, which is typically wide enough to support a large number of higher order modes and W_{MMI}>W_{Input}. The wider region has a length of MMI_{Length}, with the output waveguides (in this case two such waveguides), positioned at a distance of MMI_{Sep} apart. Each supported mode in the MMI region has its own field distribution, $\psi_m(y)$ and effective index. As in Ref. [131], the incident light on the MMI region can be split up into the field distributions of the guided modes within the MMI region and be written as,

$$\psi(y,0) = \sum_{0}^{m} c_m \phi_m(y). \tag{2.32}$$

The amount by which each mode in the MMI region is excited by the input field is determined by the overlap integral between them, which is given by,

$$c_m = \frac{\int \psi(y,0)\phi_m(y)dy}{\int \phi_m(y)^2 dy}. \tag{2.33}$$

The field at any point along the direction of propagation, z, can then be determined from the superposition of the propagated guided modes which are weighted by the value of c_m from Equation (2.33). The field distribution can then be written as,

$$\psi(y,z) = \sum_{0}^{m} c_m \phi_m(y) exp(j(\beta_0 - \beta_m)z) \tag{2.34}$$

By definition, MMI waveguides are large and support a significant number of guided modes. For such waveguides, approximations can be found for the propagation constants of these modes. When solving Equations (2.22) and (2.23) graphically, it can be seen that for large waveguide widths, intersections occur at the asymptotes of the *tan* function. This allows u of each mode to be approximated as:

$$u_m \simeq \frac{(m+1)\pi}{2}. \tag{2.35}$$

From Equation 2.8 and noting that $u = \kappa a$, the propagation constant (β) of each guided mode in large waveguide can be written as:

$$\beta_m = \sqrt{k^2 n^2 - (2u_m/W)^2}. \tag{2.36}$$

where $W = 2a$. Using a binomial expansion, Equation (2.36) can be written as:

$$\beta_m \simeq kn - \frac{\lambda(m+1)^2\pi}{4nW^2}. \tag{2.37}$$

The beat length between the lowest order modes is defined as L_π, as is given by:

$$L_\pi = \frac{\pi}{\beta_0 - \beta_1}. \tag{2.38}$$

From Equation (2.37), L_π can be expressed as:

$$L_\pi = \frac{4W^2 n}{3\lambda}. \tag{2.39}$$

With this in place, $\beta_0 - \beta_m$ can then be rewritten as:

$$\beta_0 - \beta_m = \frac{(m+1)^2 \lambda\pi}{4nW^2} - \frac{\lambda\pi}{4nW^2} \tag{2.40}$$

Which can be simplified to:

$$\begin{aligned} \beta_0 - \beta_m &= \frac{(m^2+2m+1)\lambda\pi}{4nW^2} - \frac{\lambda\pi}{4nW^2} \\ &= \frac{(m^2+2m)\lambda\pi}{4nW^2} \end{aligned} \tag{2.41}$$

Using Equation (2.39), Equation (2.41) can then be expressed as:

$$\beta_0 - \beta_m = \frac{m(m+2)\pi}{3L_\pi} \tag{2.42}$$

Following from Equation (2.34), the electric field at any point along the length of the MMI is given by:

$$\psi(y,z) = \sum_0^m c_m \phi_m(y) exp\Big(j(\frac{m(m+2)\pi}{3L_\pi})z\Big). \tag{2.43}$$

The input field of the MMI, $\psi(y,z)$ will be reproduced in the MMI region at a distance L, where,

$$exp\Big(j(\frac{m(m+2)\pi}{3L_\pi})L\Big) = 1. \tag{2.44}$$

If symmetric interference is considered, as in a $1 \times N$ optically splitter, then the self-imaging length of the MMI coupler, L_{MMI}, can be written as [131]:

$$L_{MMI} = \frac{W_{MMI}^2 n}{\lambda}. \tag{2.45}$$

It has been shown that N-fold images of the input field can be found for MMI lengths, MMI_{Length}, given by:

$$MMI_{Length} = \frac{L_{MMI}}{N}. \tag{2.46}$$

The N output images formed are located equally spaced along the y-axis of the MMI schematic shown in Figure 2.14, with the separation between outputs given by W/N. When such images are formed, they can be de-coupled from the MMI via output waveguides placed at MMI_{Length}, thereby creating an optical splitter.

The EIM mode solver described earlier in this chapter, allows each mode of an MMI to be calculated accurately and efficiently. This allows for accurate field distributions of an MMI to be formed when using modal propagation analysis. By calculating the field of an MMI at specific points along its length, an overall picture of the optical distribution can be formed.

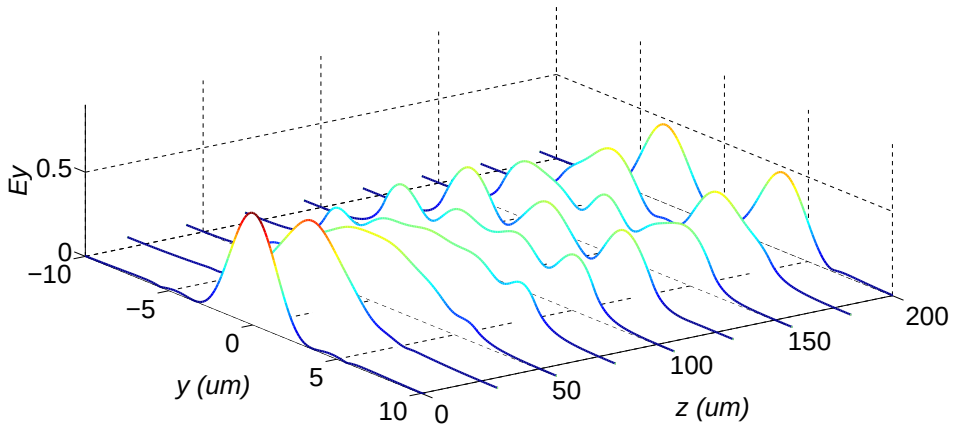

Figure 2.15: Field distribution in an MMI at various increments along its length.

Figure 2.15 shows the field distribution at specific points along the length of an MMI. The field from the single mode input waveguide is initially reproduced at the start of the MMI region. The mode diverges as it propagates, and a field distribution appears. At the end of the MMI, a double-fold image of the input field is clearly formed. This can then be used to determine the required length of an MMI to act as a 1×2 optical splitter. A more detailed analysis of this will be discussed in chapter 3, where the design and optimisation of MMIs is considered. Calculating the precise length of an MMI where the input field is re-imaged in an N-fold manner, is of critical importance when designing MMIs, since at non-optimum dimensions, the coupling efficiency of MMIs can be significantly impacted.

2.3.2 Internal Reflections in MMIs

The refractive index step formed as light couples between the MMI waveguide and the single mode waveguides at the beginning and end of the MMI, leads to reflections which can negatively impact on the MMI performance. These reflections have previously been examined with solutions to minimising MMI reflective losses suggested [142, 143, 144]. The effect of these reflections on the performance of MMIs can be estimated by considering the Fresnel reflection coefficient between the input and MMI supported waveguide modes. The Fresnel reflection coefficient is given by

$$r = \frac{n_1 - n_2}{n_1 + n_2}, \tag{2.47}$$

where n_1 and n_2 are the refractive indices of the modes under consideration. It will be shown in chapter 3 that losses due to reflective losses between the input and MMI waveguide modes of a coupler do not significantly impact device performance and can largely be ignored when designing MMIs using MPA.

2.3.3 Fabrication Tolerances of MMIs

In the previous section modal propagation analysis was described in the modelling of MMIs. This work will be further developed in chapter 3 where the optimisation of MMI designs is discussed in detail. When designing MMIs, device size and coupling efficiency are the two primary concerns. However, an important consideration when designing any device is to ensure that it maintains its functionality under variations which can occur during fabrication. Two main sources of such errors are

Etching where the ridge or rib waveguide formed on a PIC does not match the modelled structure due to being too deep if over etched, or shallow if under etched.

Lithography where the physical dimensions of the MMI structure do not match designed values to over or under exposure of the mask during processing.

When defining a ridge waveguide structure during the fabrication, over or under exposure of the lithographical mask can significantly impact on the dimensions of the structure. If an MMI is considered, variations to the ridge waveguide dimensions can affect the effective indices of the supported MMI modes, propagation constants and the mode profile itself. This causes the field distribution of the MMI to differ from the optimum field as determined from the model. The functionality of the device can now be adversely effected due to the output waveguides being at the incorrect location for optimal power coupling. This can result in excess reflections within the MMI structure which can further reduce the optical performance of the device[145]. Work such as Ref. [146] has shown how these unwanted reflections in MMIs can be minimised.

The effect of lithographical errors on MMI performance was investigated analytically by Besse [147]. This work discussed how to improve the tolerance of an MMI to deviations from the optically designed values in a qualitative means, without exploring how errors impacted specific MMIs quantitatively. The MPA model for designing MMIs discussed previously, lends itself ideally to further analysis of MMIs where fabrication errors are artificially introduced. As will be seen in chapter 3, the EIM-MPA MMI design tool can be used to investigate the performance of MMIs around these errors where tolerance to fabrication issues can be explored. One of the more difficult parts of the fabrication of waveguide devices or PICs, is ensuring the correct etch depth during processing. Errors can manifest themselves as over or under etches, which can significantly impact on the performance of a device. In Quantum Well (QW) based devices, etching to the correct depth is critical to ensure strong optical confinement in the well region. For all waveguide devices, under etching can be a significant issue when ensuring modes remain confined during propagation around waveguide bends etc. The effect of etch errors on the performance of MMIs has not previously been examined and will be discussed further in chapter 3 by using the SFEM-MPA MMI design tool.

2.4 Conclusion

In this chapter, attention was turned to the use of optical waveguides in photonic integrated circuits. Waveguides can channel light around an optical device by confining it to a high index medium through total internal reflection. The distribution of light in one-dimensional waveguides was first examined, with analytical and numerical methods provided to calculate the supported modes. This was then extended to waveguides with two-dimensional confinement as found on typical integrated devices. Due to the geometry of these waveguides, analytical solutions to their modal profile cannot typically be found. As a result, approximate solutions are required which make use of numerical methods. Different methods were discussed to solve such waveguides with particular attention paid to the use of the Effective Index Method (EIM). The EIM offers an approximate solution to the rectangular waveguide problem that is applicable to many waveguide variations. A two dimensional mode solver was then implemented in C++ using this method. Furthermore, the design of optical couplers was also investigated. For the photonic devices considered in this thesis, optical couplers are an essential component in the splitting and combining of light from integrated sources on a single chip. As a result of this, Multimode Interference Couplers (MMIs) were examined in detail as they offer excellent potential for integration in photonic devices. The design of MMIs was considered by introducing Modal Propagation Analysis (MPA). MPA provides a computationally efficient means of modelling MMIs, which can be used with any type of waveguide mode solver. An MMI design tool was implemented in C++ by using the EIM waveguide solver. The application and details of this mode solver are considered

in detail in chapter 3, where it is used extensively in the design and optimisation of MMIs for use in photonic integrated circuits.

Chapter 3

MMI Modelling and Optimisation

3.1 Introduction

As discussed in chapter 2, Modal Propagation Analysis (MPA) offers a computationally efficient means of modelling MMI structures. The precise length of a device to act as a splitter/combiner can be determined by calculating the field distribution along the device and matching the field with output waveguides to decouple the light from the MMI. Such analysis mainly requires insight into the properties of the guided modes in an MMI, which can be done through a number of different means. If a two-dimensional waveguide structure is considered, the modes can be calculated using the Effective Index Method (EIM) or the Scalar Finite Element Method (SFEM) Mode Solver, which was developed previously within the Integrated Photonics Group (IPG) at Tyndall. In this chapter, MPA was used to investigate the optimisation of MMIs to act as highly efficient splitters or combiners. The physical parameters of MMIs, such as their length and width, were varied across a large design space to determine the best means of optimising the structure. Optimisation routines were developed around this, which provided an excellent means of determining the best MMI dimensions for particular applications. The MPA analysis tools developed in this work also allowed for MMIs to be modelled where fabrication errors were included. The efficiency of MMIs which had small error deviations from their optimum length and widths were considered, and design rules were found to minimise the impact of these errors. Similar analysis was performed on MMI which were over or under etched when forming their ridge structure.

The MMI model presented in this work was finally used to design MMIs based on a quantum well based material. These designs were used to fabricate MMIs which were then tested experimentally to validate the MMI models.

3.2 MMI Design using Modal Propagation Analysis

MPA was introduced in chapter 2 as an effective method of modelling MMI structures. With MPA, the electrical field at any point in a waveguide region can be written as a summation of the propagated modes to that point. Designing MMIs using this method offers rapid solutions compared to more numerically intensive techniques discussed previously. The accuracy of MPA solutions depends fundamentally on how well the guided modes in a waveguide can be calculated. The more precise these modes are known the better the end result. Two different mode solvers were used in the MPA models developed for MMI design in this thesis. These were a Scalar Finite Element Method (SFEM) mode solver and an Effective Index Method (EIM) mode solver. As described in chapter 2, the SFEM mode solver was made available from previous research carried out in the IPG group at Tyndall [8], while an EIM mode solver was implemented in Matlab/C++ during this work. The application of both these methods to MMI design using MPA will now be examined.

3.2.1 Effective Index Method Modal Propagation Analysis

For typical ridge and rib waveguide structures, the effective index method (EIM) can be used to provide approximate solutions for the field distributions, propagation constants and effective indices of the supported modes in a waveguide. The two-dimensional structure of a waveguide can be reduced to a one-dimensional version and solved, as described in chapter 2. These modes and propagation constants can then be used in MPA to solve for the full field distribution in an MMI waveguide. The *Effective Index Method for Modal Propagation Analysis* (EIM-MPA) for modelling MMIs will now be applied to the waveguide structure shown in Figure C.1. The waveguide considered for this analysis is referred to as *Waveguide A*, with dimensions summarized in Table 3.1.

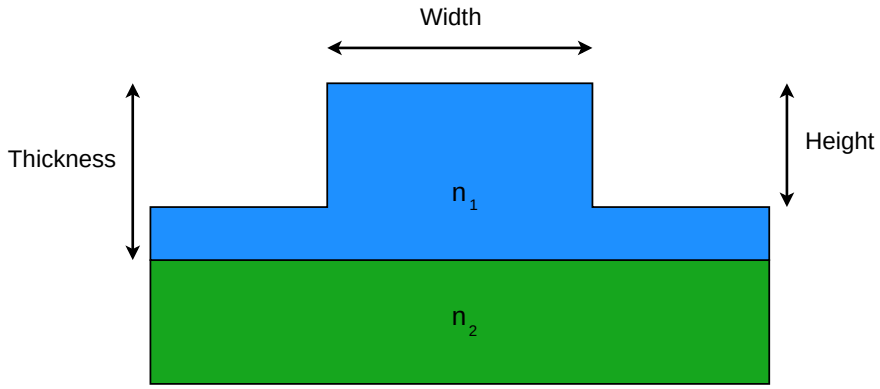

Figure 3.1: Ridge waveguide structure with dimensions labelled.

Table 3.1: Waveguide Variations

Name	Width (µm)	Height (µm)	Thickness (µm)	n_1	n_2
Waveguide A	2.5	2.5	2.5	3.38	3.17
Waveguide B	2.5	1.3	1.3	3.38	3.17

The design of a 1×2 MMI coupler was first considered on this structure. The operational polarization of the device was chosen to be TE, which determined the order in which the two-dimensional waveguide structure was reduced to a one-dimensional equivalent using the EIM. The TE modes in vertical cross sections of the waveguide were first calculated based on this. These were found to be 1.0, 3.368 and 1.0, for the cladding, core and substrate sections, respectively. These indices were used to form the one-dimensional equivalent waveguide, where the approximate mode solutions of the original structure were calculated by analysis of the TM mode solutions of the simplified waveguide. From this, an MMI based on the original waveguide structure can be described using a one-dimensional model. A schematic outline of a 1 × 2 MMI with its physical dimensions labelled, is shown in Figure 3.2.

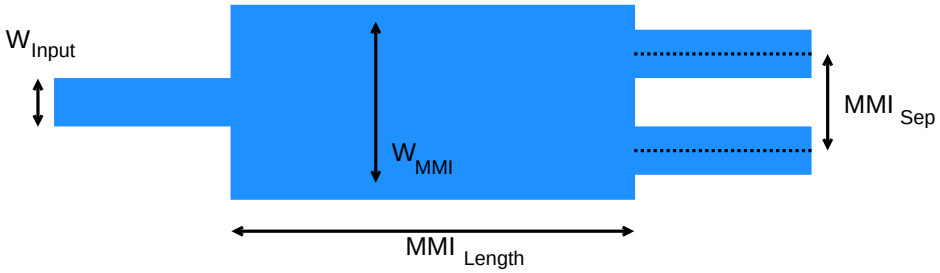

Figure 3.2: Labelled MMI schematic.

The EIM-MPA method was applied by calculating the TM modes in the vertical direction across the narrow input and wide MMI waveguide regions. The calculated effective index was then used to form an equivalent waveguide where the TE mode solutions represented the TE modes of the original two-dimensional waveguide structure. The modes in the input and MMI region were both determined in this way and then normalised such that supported modes in each region had equal peak powers. For the MMI under consideration, the input waveguide width, W_{Input}, was 2.5 µm. The fundamental mode of this waveguide is shown in Figure 3.3a. The width of the wide MMI waveguide, W_{MMI}, was set to 8.5 µm. The first 10 supported modes in this waveguide are shown in Figure 3.3b. Note that the peak power of each of the MMI waveguide modes have been normalised to a fixed value.

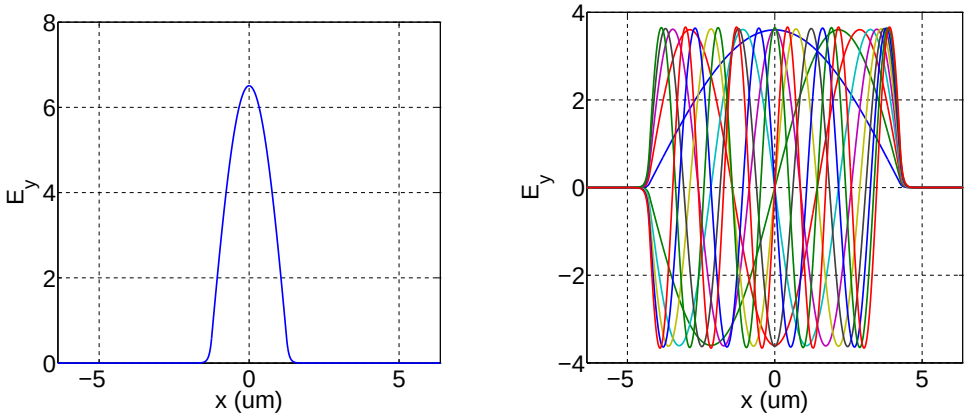

(a) (b)

Figure 3.3: (a) E_y component of TE mode field distribution of the input waveguide mode. (b) E_y component of TE modes supported in MMI region.

Each supported mode in the MMI region has its own propagation constant and effective index. The calculated effective index for each supported mode is shown in Figure 3.4a. As expected, the values of the effective index of each supported mode are restricted between the values of the cladding and core waveguide refractive indices.

Light entering the MMI region from the narrow input waveguide excites each of the MMI guided modes to a varying degree. The value of this excitation is referred to as the Fourier excitation coefficient of the mode, and is given by c_v. The value of c_v for a particular mode can be calculated by investigating the overlap integral between the input waveguide mode and each of the supported modes in the MMI region. For the MMI considered here, c_v has been plotted versus mode number in Figure 3.4b.

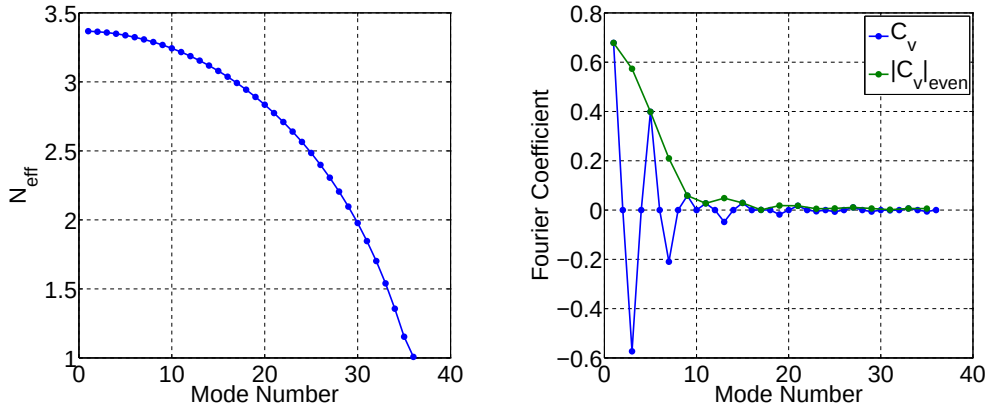

(a) (b)

Figure 3.4: (a) Effective index of supported modes in MMI region. (b) Overlap coefficient of support modes in MMI region with input waveguide mode.

The Fourier coefficient of the first MMI mode shows the highest excitation due to its mode shape resembling the input waveguide mode most strongly. For odd modes, the Fourier coefficient is negligible, as expected due to odd numbered modes being anti-symmetric about the center of the input waveguide mode, for a 1×2 MMI. As the mode number increases, the modal Fourier coefficient drop off considerably. This can clearly be seen by plotting the absolute value of the Fourier Coefficient of the even modes, $|c_v|_{even}$ versus mode number. This is shown in Figure 3.4b where it is plotted together with c_v. As can be seen, higher order modes have a much lower Fourier coefficients and so have less of an impact on the performance of the MMI. With the Fourier coefficients calculated, the modes in the MMI were scaled according to c_v which determined how well they were excited by the input waveguide mode.

As discussed in chapter 2, as light from the input waveguide enters the MMI region and excites the MMI modes, it experiences reflective losses from each mode due to the refractive index step present. In Figure 3.4a, it was shown that as the mode number of the supported modes in a waveguide starts to become larger, a decrease in the mode effective index, n_{eff}, is observed. This causes the associated Fresnel reflective losses between the input waveguide mode and MMI modes to increase according to Equation (2.47). For the MMI considered above, these Fresnel losses are shown in Figure 3.5a.

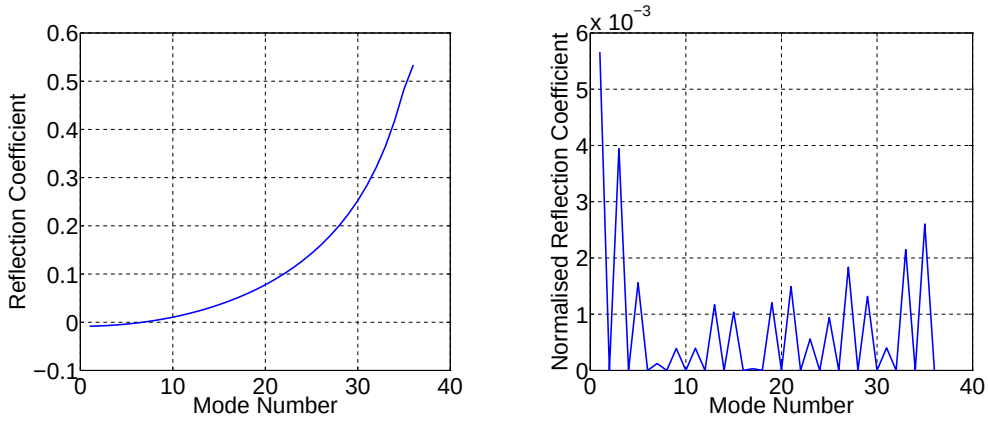

(a) (b)

Figure 3.5: (a) Fresnel reflection coefficient between input and MMI supported waveguide modes. (b) Fresnel reflection coefficient between input and MMI supported waveguide modes weighted to the MMI mode Fourier coefficient.

As the mode number starts to increase, the Fresnel reflection coefficient starts to rise rapidly, with a value of 0.55 for the final supported mode in the MMI region indicating significant reflective losses. However, as with the Fourier coefficient analysis, light from the input waveguide mode excites the MMI modes to a varying degree depending on their overlap integral. This has the effect of reducing the reflective losses expected in an MMI, where modes with higher reflective losses have an inherently lower Fourier coefficient which minimises their impact on device performance. In Figure 3.5b, the Fresnel

reflective losses of Figure 3.5a have been normalised with respect to the calculated Fourier coefficient. As can be seen, with this in place the reflective losses associated with a 1×2 MMI are largely insignificant and introduce losses of $< 1\%$. It should be noted that reflection losses for non-symmetric MMI couplers can be far more significant due to the non-symmetric modal excitation, where higher order modes have more impact on the MMI performance.

Ignoring the effect of reflective losses on MMIs, the propagation constant of each supported MMI mode was next determined and used to calculate the field distribution at points along the length of the MMI using modal propagation analysis, as described in chapter 3, where the field at the any point z along the length of the MMI can be calculated from

$$\psi(y,z) = \sum_0^v c_v \phi_v(y) exp(j(\beta_0 - \beta_v)z)$$

Attention was next turned to the precise length where the MMI re-images the input waveguide mode. The theoretical analysis from chapter 1 has shown that knowing this re-imaging length allows the approximate length for any $1\times$ M splitter to be determined. To the first approximation, the length of an MMI to act as a $1\times$M splitter is given by $\frac{L_{MMI}}{M}$ with the waveguide separation, MMI_{Sep} given by W_{MMI}/M. To determine the precise length where the MMI acts as a $1\times$M splitter, the overlap integral of the MMI field at its output and the mode of the M output waveguides is calculated. The overlap integral is given by

$$\eta = \frac{\int \psi_A \psi_B}{\sqrt{\int \psi_A^2 \int \psi_B^2 dy}}. \tag{3.1}$$

where ψ_A and ψ_B are the E-field distributions of output waveguides and field at the end of the MMI, respectively. The overlap integral provides a measure of how well ψ_A and ψ_B are matched, where for identical ψ_A and ψ_B, $\eta = 1.0$. The coupling efficiency of the MMI is defined as η^2 and represents the power coupled from ψ_A to ψ_B, or in this case, the power coupled from the MMI output to the output waveguides. By considering how η^2 varies at different MMI lengths, the precise length where it forms M self-images can be found.

For the MMI under analysis here, the length of the MMI where it exactly self-images itself into one image, L_{MMI}, was determined by sweeping the MMI length while measuring the maximum value of η^2 at each step. The results are shown in Figure 3.6, where the coupling efficiency (η^2) is plotted versus propagation length of the MMI.

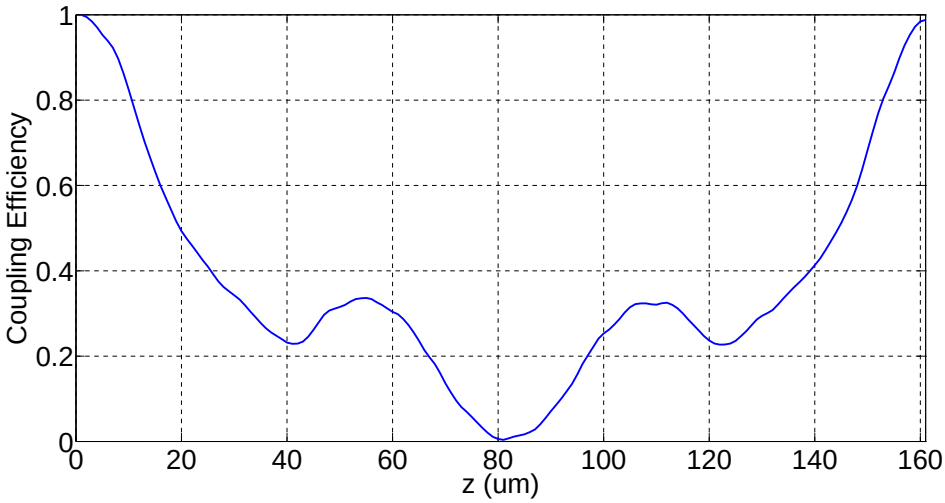

Figure 3.6: Coupling efficiency of a 1×1 MMI along the length of the structure. The optimum length of the MMI can be determined by finding the peak of the coupling.

The mode is clearly self-imaged at a propagation length of 0 µm, where this represents the re-imaging of the waveguide mode in the MMI region itself. The actual self-imaging length of the MMI, is where the field is reproduced at MMI lengths >0 µm. As the length was swept further, the coupling efficiency was found to approach unity at 160 µm. At this length, the field inside the MMI has reproduced the input field entering the MMI and self-imaging length, L_{MMI}, has been found. The field of the MMI at this length is shown in Figure 3.7, where the re-imaged mode at L_{MMI} is overlapped with the input mode for comparison.

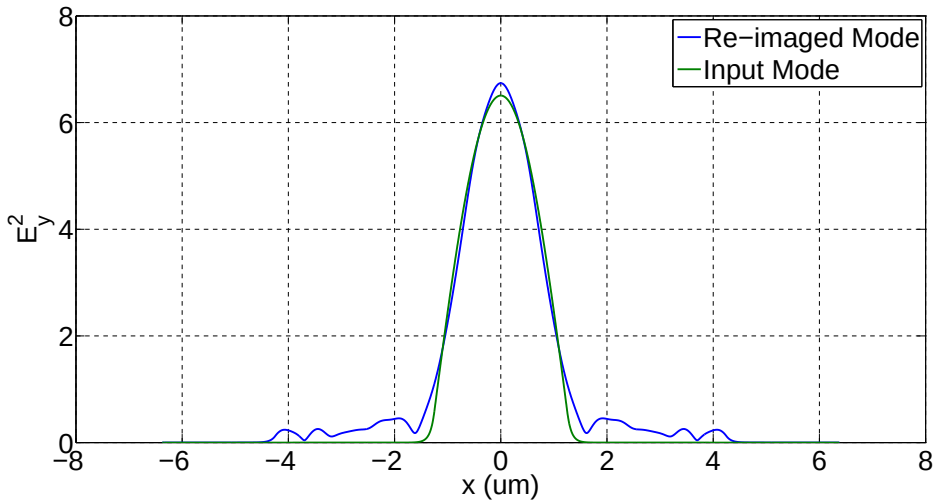

Figure 3.7: Re-imaged mode at an MMI length of L_{MMI}, overlapped with mode of the input waveguide.

With the self-imaging length now found, the full field distribution inside the MMI was determined by concatenating the field at incremental positions along the length of the

MMI up to L_{MMI}. This is shown in Figure 3.8.

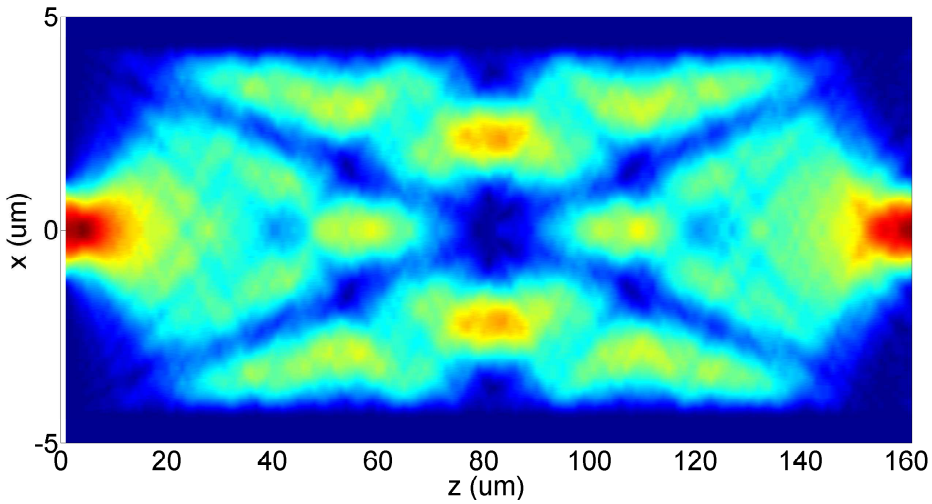

Figure 3.8: TE field distribution of the optical field in an MMI. The input field is re-imaged at the end of the device. At the midway point the field is clearly shown to form two images of the input mode.

The input mode is shown to be re-imaged at the start of the MMI region. Where it then diverges, interacts with the side walls and is the re-imaged further along the length of the device. As predicted from the theoretical analysis, M × self-images are found at MMI lengths corresponding to $\frac{L_{MMI}}{M}$. This can be seen Figure 3.8, where at lengths of 80 µm the input waveguide field has been re-imaged twice with an equal splitting of power between both lobes.

3.2.1.1 1 x M MMI Couplers

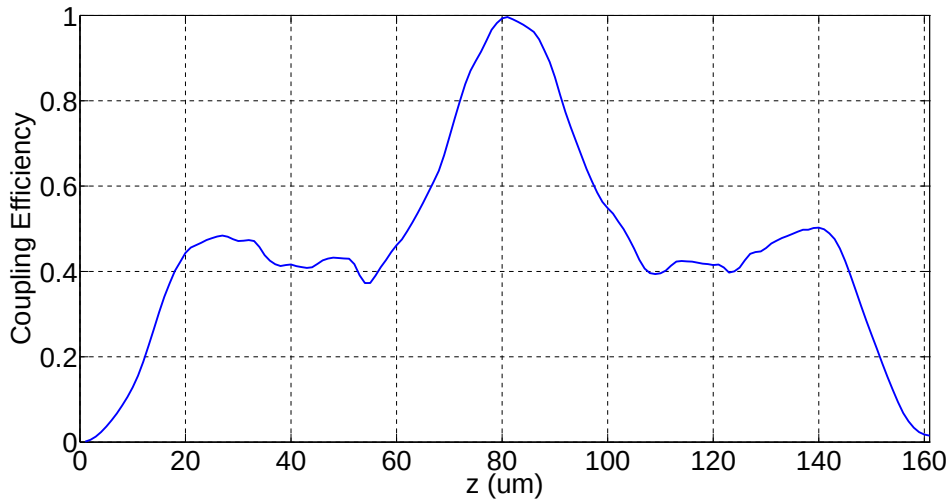

Figure 3.9: Coupling to the output waveguides of a 1 × 2 MMI as the length is varied from 0 to L_{MMI}.

An MMI with length $\frac{L_{MMI}}{M}$ acts as an efficient $1 \times M$ power splitter if the output waveguides are placed at the location of the modal lobes to decouple the power from the MMI. Determining the precise location and offset for these output waveguides was found using similar analysis to that of the 1×1 case. The overlap integral between the field of the MMI and M offset output waveguides was determined as the length of the MMI, and the offset of the output waveguides, was swept through. From this, the length of the MMI and output waveguide offset to act as an efficient power splitter was determined. Figure 3.9 shows this analysis performed for a 1×2 MMI, where the coupling efficiency was determined between the field of the MMI and the field of two output waveguides separated by MMI_{Sep}. The coupling efficiency was considered for lengths between 0 µm and L_{MMI}.

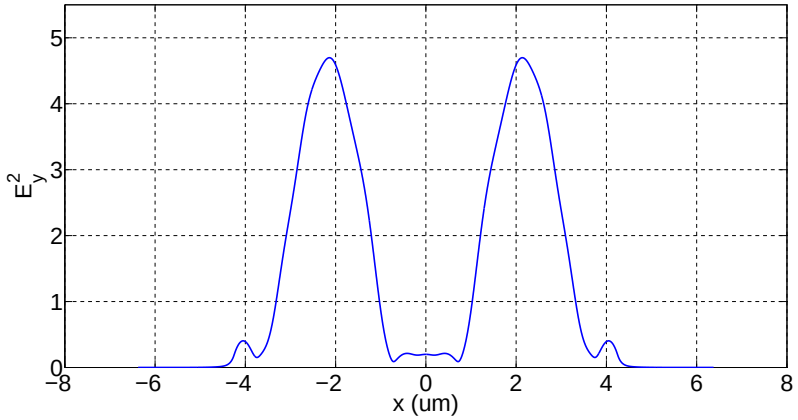

Figure 3.10: Field distribution at the end of a 1×2 MMI. Two self-images of the input field to MMI are formed.

For lengths close 0 µm, the coupling efficiency was negligible due to the geometry of the structure. As the length was increased, a peak in the coupling efficiency was found at close to 80 µm, where the overlap integral between the dual self-images of the input mode and the offset waveguides were found to be greatest. The coupling efficiency at this position was approximately 1.0, which represents a power coupling of 0.5, or 50%, of the input light in the MMI coupled into each of the two output waveguides. The output field of the MMI at this length is shown in Figure 3.10, where the input mode has clearly been re-imaged into two identical lobes with the power split equally.

This can be extended to any $1 \times M$ splitter but is limited by how many times the input mode can be self-imaged comfortably inside the width of the MMI. The field of designed MMIs where they can act as efficient 1×2 and 1×3 splitters is shown in Figure 3.11a and 3.11b respectively.

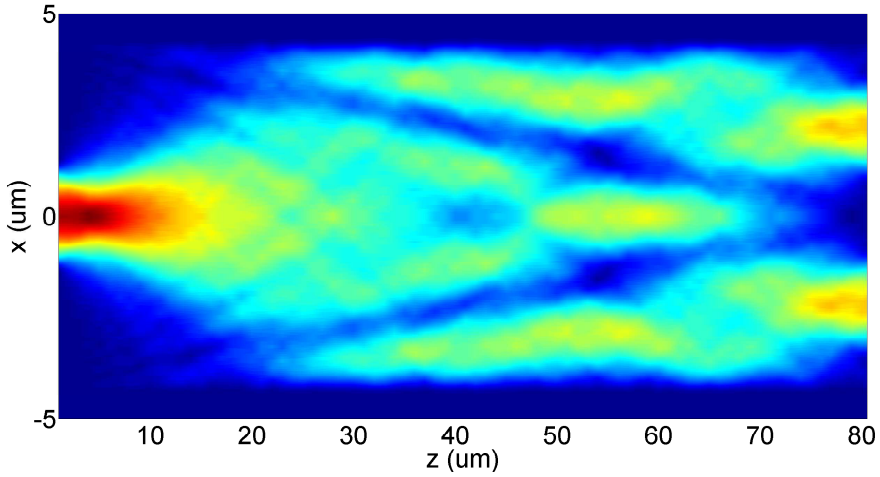

(a)

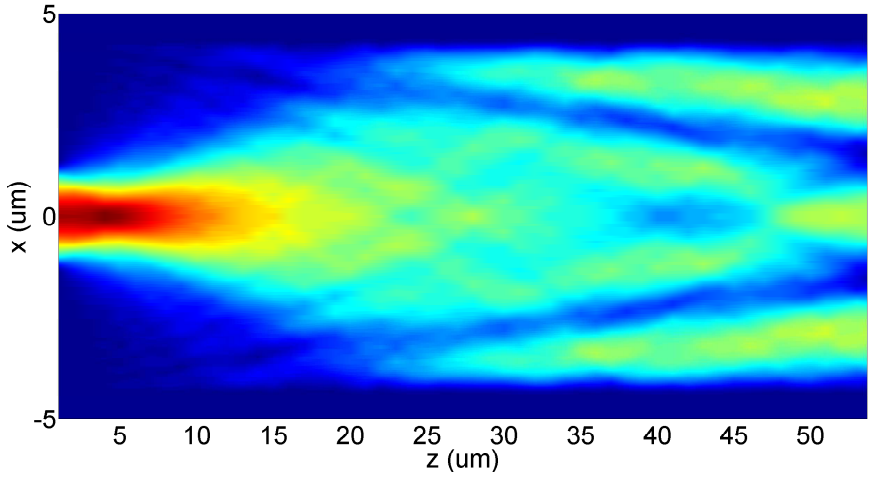

(b)

Figure 3.11: Electric field distribution in an MMI with W_{MMI} of 8.5 µm. Figure (a) demonstrates that two self-images of the input mode can be found at a particular length along the device, thereby forming a 1×2 splitter. Figure (b) shows that at a shorter length, the same MMI can generate three self-images of the input mode and form a 1×3 splitter.

3.2.1.2 M × N MMI Couplers

Similarly to how $1 \times M$ power splitters were modelled previously, the EIM-MPA method can be extended to modelling MMIs which have multiple input waveguides. The light from these input waveguides excite symmetric and anti-symmetric guided modes in the MMI region due to their lateral offset from the MMI center. This breaks the symmetry of the MMI allowing for interesting phase effects to be observed on the output waveguides. A special case of an M × N MMI coupler is the 2×2 arrangement, as shown in Figure 3.12.

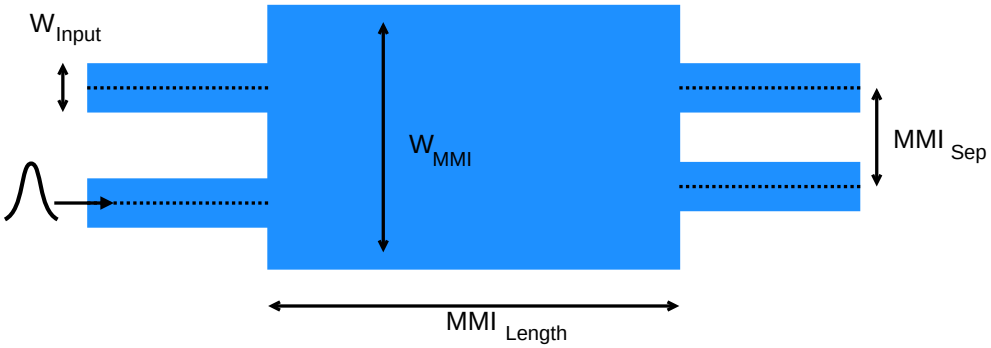

Figure 3.12: Schematic of a 2×2 MMI Coupler.

In this arrangement, light can enter the MMI from either the top or bottom input waveguide, or both simultaneously. If light is considered entering from the bottom waveguide, depending on the MMI length light can be re-imaged at the bottom, top or both output waveguides. Figure 3.13 shows the field distribution of a 2×2 MMI, where light is coupled from the bottom input waveguide to the top output waveguide, a feature that has been used in fast optical switches [148].

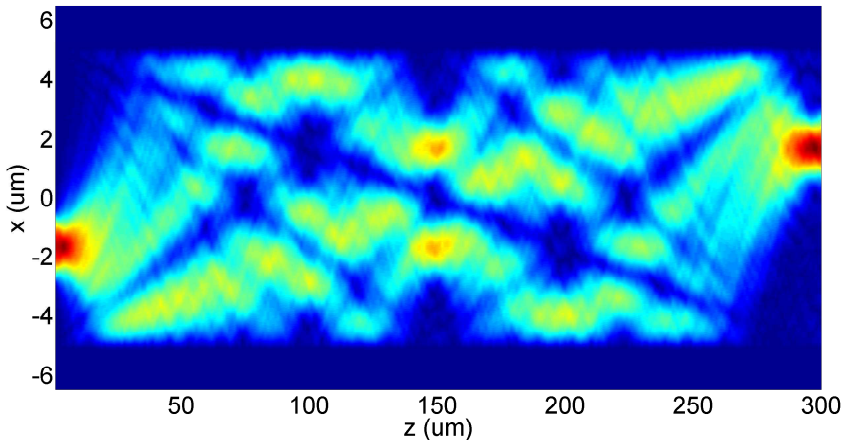

Figure 3.13: Field distribution a 2×2. The input field to one port is re-imaged at the end of the MMI on the opposite port.

Further to this, 2×2 MMIs are particularly important in the development of Mach Zehnder Modulators (MZMs), where they are used as optical combiners. Light entering one arm on the input side of a 2×2 MMI coupler is split in two and coupled to both output waveguides. The same is true for light entering the opposite input arm of the coupler, which in effect combines both input signals over the output waveguides. Figure 3.14 shows the field distribution in a 2×2 MMI where light from the lower input waveguide re-images itself on both output waveguides.

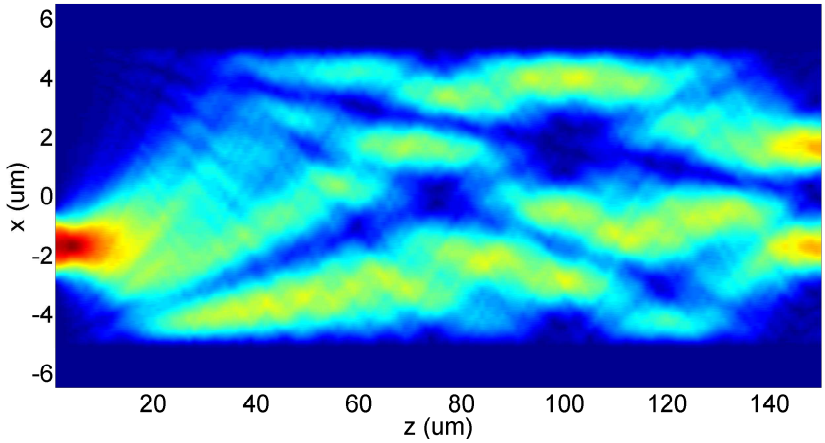

Figure 3.14: Field distribution a 2×2. The input field is re-imaged over both output ports of the MMI at the end of the device.

3.2.2 Scalar Finite Element Modal Propagation Analysis

The method of MPA, as previously described for MMI analysis using the EIM, lends itself readily to the analysis of MMIs where the full two dimensional waveguide structure is known and can be solved for directly. The EIM reduces a two-dimensional waveguides structure down to one-dimensional planar waveguide equivalent where it can be approximately solved. This is a computationally efficient method; however, it does have several disadvantages, mainly in its applicability to only specific waveguide types. The EIM provides a good approximation when the waveguide width is greater than the waveguide ridge/rib thickness and also when there is strong vertical confinement of the waveguide mode. Although many different waveguide types are satisfied by these criteria, several waveguide types are not entirely suitable to EIM analysis.

Of particularly interest when designing MMI couplers for PICs, is the use of ridge and rib waveguides which may be shallow or deeply etched. As mentioned previously, software has been developed elsewhere within the group to model two-dimensional waveguide structures using the Scalar Finite Element Method (SFEM). The mode solver can solve for any arbitrary waveguide profile and refractive indices; be it ridge, rib, diffused channel, buried channel or strip loaded waveguide, based on InP, Si or other materials.

Figures 3.15a-3.15d show the mode profiles calculated for a typical InP based waveguide for various etch depths. This mode solver was used to develop fully two dimensional MMI modelling tool for MMI design, and is referred to as *Scalar Finite Element Method - Modal Propagation Analysis* (SFEM-MPA).

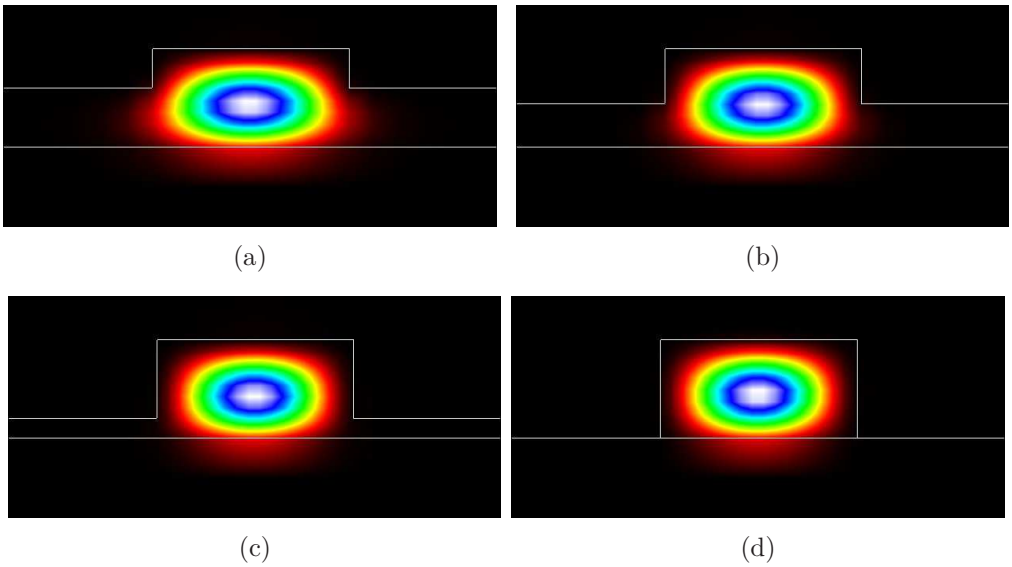

Figure 3.15: TE modes as calculated from the SFEM code of [8] for waveguides of various etch depths. (a) Etch=0.5 µm (b) Etch=0.7 µm (c) Etch=1.0 µm (d) Etch=1.25 µm.

The SFEM-MPA model was developed identically to that of the EIM-MPA model, discussed previously. The field distribution at any distance along the length of an MMI was determined by the superposition of the calculated guided modes at that point. To demonstrate this, the SFEM-MPA model was used to design a 1×2 MMI based on *Waveguide A* with parameters summarized in Table 3.1. For comparison, W_{Input} and W_{MMI} were set to that of the MMI designed using the EIM-MPA, 2.5 µm and 8.5 µm respectively.

The fundamental mode of the input waveguide and each supported mode in the MMI regions were first calculated, along with their propagation constants and effective indices. An example of the third excited mode in the MMI waveguide is shown in Figure 3.16.

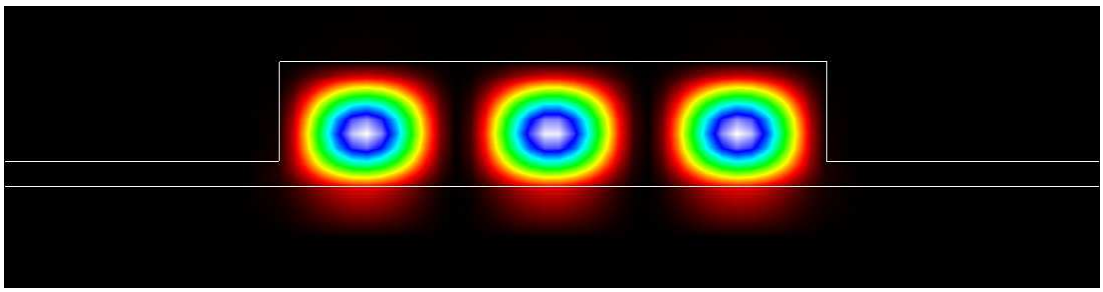

Figure 3.16: SFEM code can be used to calculate higher order modes of arbitrary waveguide structures.

As with the EIM-MPA method for simulating MMIs, the overlap integral between each of the MMI modes and the fundamental mode of the input waveguide were calculated

and used to determine the excitation coefficient of each of the modes within the MMI section. The field at each point along the MMI structure was determined by propagating each of the MMI modes to any given point and looking at the superposition of all their modes at that point. The optimum MMI length for the device to act as a 1×2 coupler was found by following the same procedure for the EIM-MPA. The field distribution for the optimised MMI, is shown in Figure 3.17.

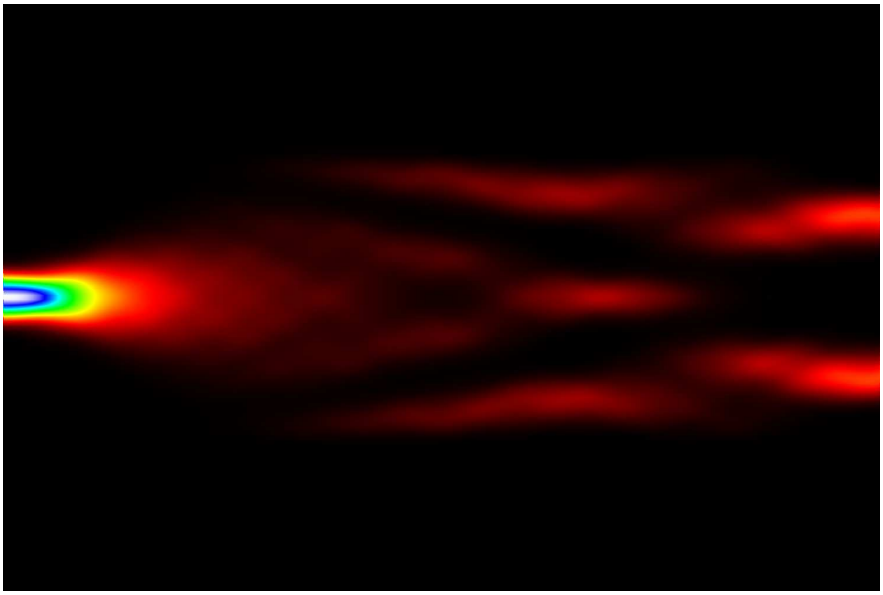

Figure 3.17: Field distribution of a 1×2 MMI as calculated using the two dimensional SFEM-MPA MMI solver.

In the section that follows, the results from the EIM-MPA simulations are compared with those from the SFEM-MPA to determine the relative accuracy between both methods.

3.2.3 Comparison between SFEM MPA and EIM MPA

The SFEM-MPA method for modelling MMIs was based on a two-dimensional SFEM mode solver which can solve for any arbitrary waveguide refractive index profile. Mode solvers such as these, require complex numerical analysis to characterise and solve waveguide modes accurately. MMI simulations based on the SFEM-MPA method are numerically intensive and can take several hours to calculate each modal solution, depending on the width of the MMI modelled. For larger MMIs, the time taken to simulate full structures scales dramatically due to the increased number of supported modes in each waveguide and the larger numerical grids required. For the applications considered in this thesis, the approximate modal solutions provided by the EIM make the EIM-MPA a suitable method in the design of MMIs. The EIM offers accurate solutions when two conditions are met: (1) the waveguide width is larger than the thickness

of the waveguide; and (2) waveguiding is stronger across the waveguide thickness than the waveguide width. For MMIs, these criteria are typically fulfilled where the width of the MMI region is much larger than the thickness of the waveguide itself. Due to the EIM reducing a two-dimensional waveguide problem into a one-dimensional equivalent, it can calculate approximate modal solutions rapidly compared to the SFEM mode solver. The application of the EIM-MPA and SFEM-MPA to various different waveguide structures is discussed in Appendix C.

To compare both methods for accuracy and computational efficiency, a series of 1×2 MMIs were modelled around *Waveguide A* with parameters summarized previously in Table 3.1. MMIs were considered with an input waveguide width, MMI_{Input}, of 2.5 µm, while the width of the MMI region, MMI_{Width}, was varied from 6 µm - 13 µm. For each width variation, both the SFEM-MPA and EIM-MPA methods were used to the determine the optimised MMI parameters: W_{Length} and MMI_{Sep}. Figure 3.18 shows the optimised W_{Length} for each MMI variation, as calculated using the SFEM-MPA and EIM-MPA.

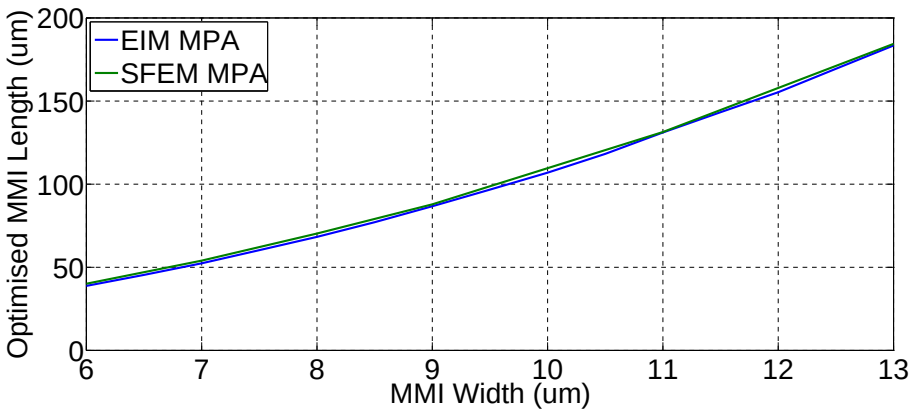

Figure 3.18: Comparison between SFEM-MPA and EIM-MPA MMI solvers when calculating optimum MMI lengths for MMIs with increasing width. Excellent agreement is seen between both solvers.

Excellent agreement is seen between both methods for the calculation of W_{Length}, with typical variations of $\sim$ 1 µm - 2 µm observed. As will be discussed later in this chapter, MMIs are largely insensitive to variations around their optimum length. For deviations of smaller than $\pm$2 µm, MMIs see a typical performance degradation of $\sim$ 3% which can be reduced further by more suitable choice the MMI geometry.

Of particular importance when comparing both techniques is the relative computational time it takes to arrive at the optimised MMI solutions for each MMI_{Width} variation. The computational time for both methods inherently depends on the number of modes which have to be solved in each MMI region. The time scales with increasing MMI_{Width}, where larger MMIs need more intensive analysis. For the SFEM-MPA method, small computational grid spacings were required to ensure accurate mode solutions. The

grid spacing for the analysis performed here was 0.1 µm, which provided relatively quick simulation results for small MMI waveguide widths but did not scale well for larger dimensions. The computational times required for modelling each MMI width variation using both methods is summarised in Table 3.2. The EIM-MPA offers a three order of magnitude improvement to the computational efficiency compared with the SFEM-MPA. This is primarily due to the approximations used in EIM-MPA, where a one-dimensional equivalent waveguide is solved rather a full two-dimensional structure, as in SFEM-MPA. The speed increase comes at a cost, where highly accurate MMI solutions (< 1 µm length deviations from optimum) cannot be guaranteed with the EIM-MPA. However, as will be seen later, these small length variations do not adversely affect the MMI performance for most practical applications. This makes the EIM-MPA an excellent choice of MMI solver when the optimisation of structures across a large design space is considered. MMI optimisation using the EIM-MPA method will be investigated further later in this chapter.

Table 3.2: Computational Times for MMI Analysis using EIM-MPA and SFEM-MPA.

MMI Width (µm)	SFEM-MPA (s)	EIM-MPA (s)
6	1900	< 1
7	2300	< 1
8	2800	< 1
9	4020	< 1
10	5860	< 1
11	7800	< 1
12	9940	< 2
13	12000	< 2

3.3 MMIs as Single Mode Filters

An important aspect of photonic integrated circuit design involves knowing what modes in an optical waveguide are excited as light propagates through it. In multimode waveguides, the optical power can be spread over the supported modes, which can negatively impact on power transfer and optical coupling to other devices. In general, single mode operation is key to attaining optimum waveguide and device performance.

Using the EIM-MPA, the role of MMIs as single mode filters could readily be investigated. The model was originally setup to propagate the fundamental mode of the input waveguide into the MMI region and determine the optimum MMI length and coupling efficiency. A 1×2 MMI was designed on *Waveguide A* (see Table 3.1) which had an input waveguide width, W_{Input}, of 2.5 µm with an MMI waveguide width, W_{MMI}, of 8.5 µm. For this W_{Input}, three TE modes were found to be supported in the input

waveguide. The MMI was first optically designed as in shown in Figure 3.11a, where the optimum length of the MMI was calculated to be 81 µm. The output coupling of the MMI was then determined for an input field excitation of the second and third order excited modes of the input waveguide, rather than the fundamental mode. The second and third order modes are shown in Figures 3.19a and 3.19b respectively.

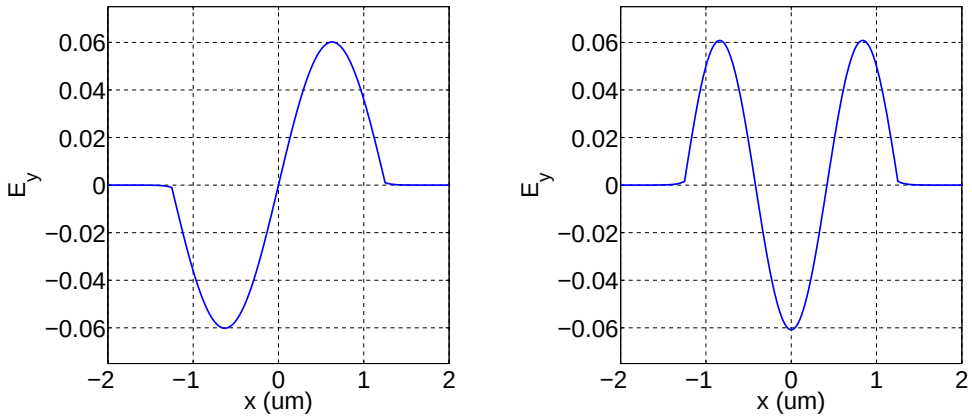

Figure 3.19: (a) Second order excited mode of input waveguide.(b) Third order excited mode of input waveguide.

If light entering the MMI was from a higher excited mode of the input waveguide, it would generate a different optical field distribution compared to that of the fundamental mode. For the second excited mode, the resulting field distribution is shown in Figure 3.20.

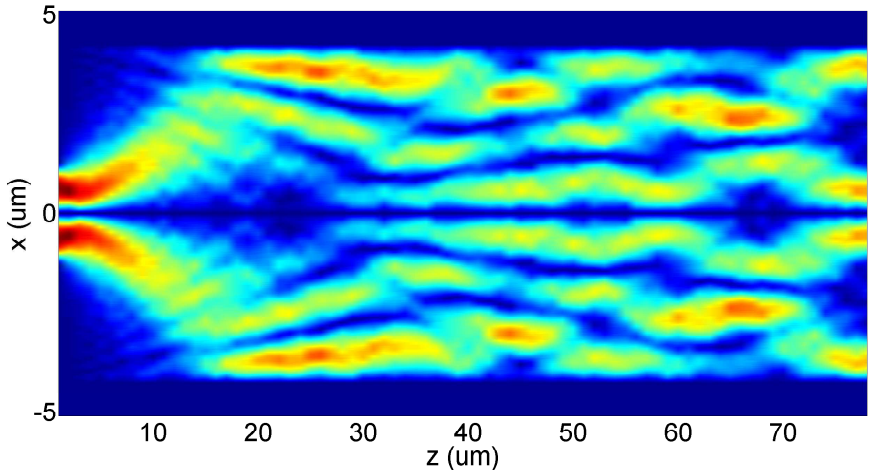

Figure 3.20: Field distribution of an optimally designed 1×2 MMI after being excited by the second order mode of the input waveguide. Almost no power couples to both output waveguides causing the MMI to act as an efficient single mode filter.

The second order mode has been re-imaged at the start of the MMI region, as expected due to the inherent self-imaging nature of the MMI structure itself. However, of particular interest was how the field distribution would compare at, the optimised MMI length when excited by the fundamental mode input. As shown in Figure 3.20, the field distribution at 81 µm produces a null where the MMI output waveguide would be placed for an optimally designed 1×2 MMI. By calculation of the overlap integral of the field distribution at 81 µm with output MMI waveguide mode, the coupling efficiency of the MMI with a second order mode excitation was found to be 2%.

Similar analysis was performed for an MMI under excitation from the third order mode of the input waveguide. The field distribution inside the MMI region in this case can be seen in Figure 3.21. The coupling efficiency of the MMI was reduced to 59%, indicating slight filtering of this higher mode as it propagates through the MMI. These investigations have shown how optimally designed MMIs can act as single mode filters in optical devices. They can improve device performance by filtering unwanted excited higher order modes which may have been excited during operation.

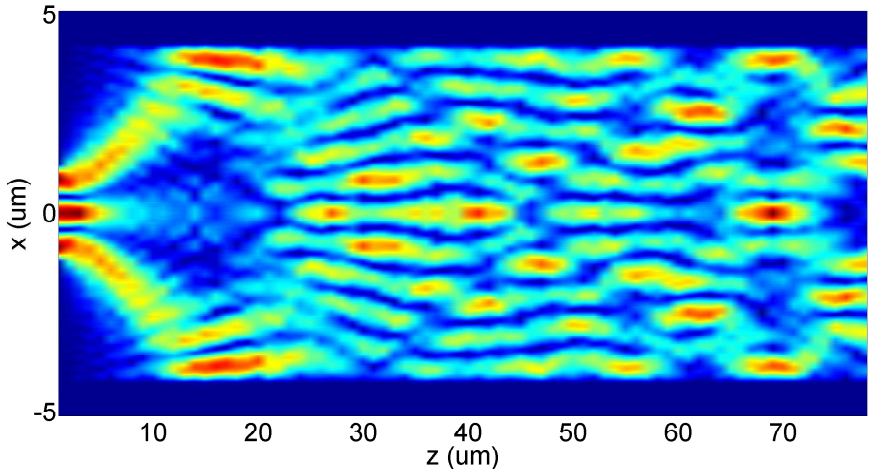

Figure 3.21: Field distribution of an optimally designed 1×2 MMI after being excited by the third order mode of the input waveguide. The MMI offers partial filtering of the mode.

3.4 MMI Design Optimisation

3.4.1 MMI Optimisation using EIM-MPA

A key requirement when designing MMIs was determining the precise length and output waveguide separation, MMI_{Sep}, of the MMI to act as an efficient splitter/combiner. As mentioned previously, the optimum MMI parameters are found by maximising the overlap integral between the idealised output waveguides and the field of the MMI at a particular point. For a 1×M splitter, M modal outputs are expected at a specific

MMI length. The overlap integral to be maximised is then between these M equally spaced images and the field of the MMI input waveguide offset from the waveguide center. A brute force approach to this method involved taking the M equally spaced self-images of the input mode, and then calculating their overlap integral with the MMI field at each point along the length of the MMI while also varying the MMI_{Sep}. This is a numerically intensive method which takes a relative long time to perform.

The theoretical analysis of an MMI, as discussed in chapter 2, provided approximations to the correct self-imaging lengths and optimum waveguide offsets. These values provide a good starting point when trying to design MMIs and optimise their physical parameters, where they can reduce the computation area over which the search algorithm uses to find the optimum. As shown earlier, the approximate MMI length for a 1×M splitter was $\frac{L_{MMI}}{M}$ with separation between the waveguides given by $MMI_{Width}/2 \times M$.

An optimised search routine was developed in $C++$ which allows for significantly faster MMI optimisation, without the need for a brute force approach. This method makes use of the theoretical analysis to generate initial starting points for the optimisation routine, and then goes on to use coarse steps in z to find approximate values for L_{MMI}, the self-imaging length of the MMI. With an approximate value for L_{MMI} determined, the length of the MMI to act as a 1×M splitter is found by decreasing the step size in the z direction while making use of the inherent symmetries of the MMI itself. The search routine was developed to allow rapid modelling of MMI structures, where their optimised parameters could be found quickly and efficiently. In particular, it allowed for MMIs to be considered where variations of the physical dimensions to be examined. In the Section that follows, the MMI optimisation solver is used to investigate the design of MMIs as their MMI_{Input} and MMI_{Width} is varied.

3.4.2 MMI Parameter Optimisation

To demonstrate the MMI optimisation routines developed in this thesis, they were applied to *Waveguide A* (see Table 3.1) to design MMIs. MMIs were considered with an input waveguide width, MMI_{Input}, of 2.5 µm, while the width of the MMI region, MMI_{Width}, was varied from 6 µm - 15 µm. For each MMI_{Width} variation, the MMI optimisation code was applied to the structure. The optimised length of the MMI and peak coupling was extracted in each case. The results are shown in Figure 3.22a, where the maximum coupling efficiency and optimised MMI length are plotted versus MMI_{Width}.

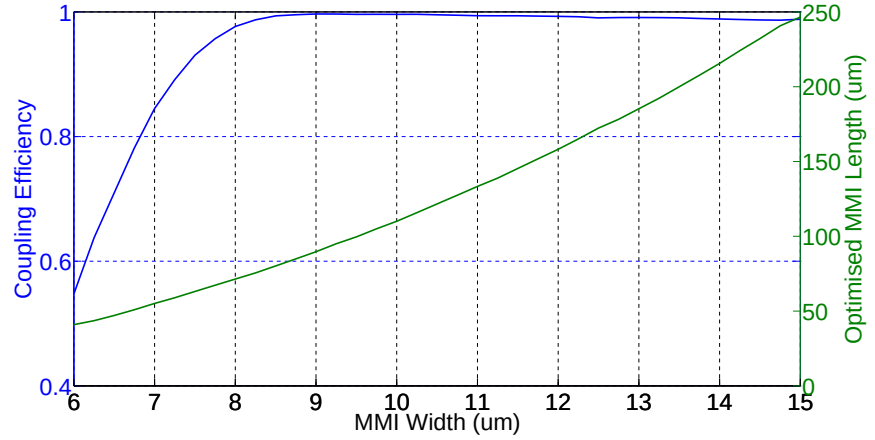

(a)

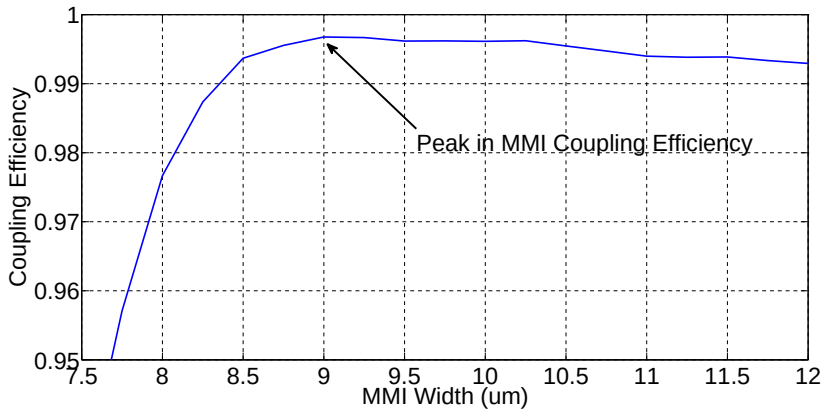

(b)

Figure 3.22: (a) Maximum MMI coupling efficiency and optimised MMI length versus MMI waveguide width. (b) Close up view of maximum MMI coupling efficiency versus MMI width. Peak in coupling efficiency for an MMI of width 9.0 µm.

The coupling efficiency refers to the peak overlap integral between the modes of the output waveguides of the MMI and the field distribution of the MMI. For the 1×2 MMI considered here, its value can range from unity to zero, where unity represents 50% of the input modal power coupling to each MMI output waveguide and zero represents 0%. The results in Figure 3.22a show the maximum MMI coupling efficiency as the MMI width is increased from 6 µm to 15 µm, with the corresponding optimum MMI lengths required. MMIs designed with narrow MMI widths show relatively power peak coupling efficiencies compared to wider structures. The poor performance was due to the MMI width starting to approach the input waveguide width. As this happens, the MMI cannot support two distinct images of the input waveguide mode and an efficient splitter cannot be formed. The optimum length of the MMI for each MMI width follows the trend expected from the theoretical analysis, where it shows a quadratic dependance on the MMI width itself. At an MMI width of 9.0 µm, the coupling efficiency appears

to peak and then drop off as the width increases further, as can be seen in Figure 3.22b. This indicates that there is an MMI width which can give optimum MMI performance. To investigate this further, the coupling efficiency was calculated versus MMI width as the input waveguide width was also varied. The results from this analysis are shown in Figure 3.23a. As with the previous case, for smaller MMI dimensions the device performance drops off significantly. For increased input waveguide widths, the MMI width required for peak coupling efficiency becomes larger, as can be seen in Figure 3.23b.

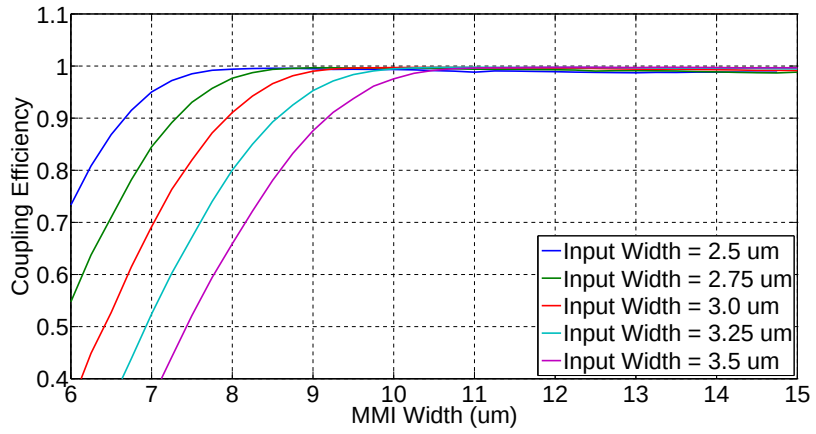

(a)

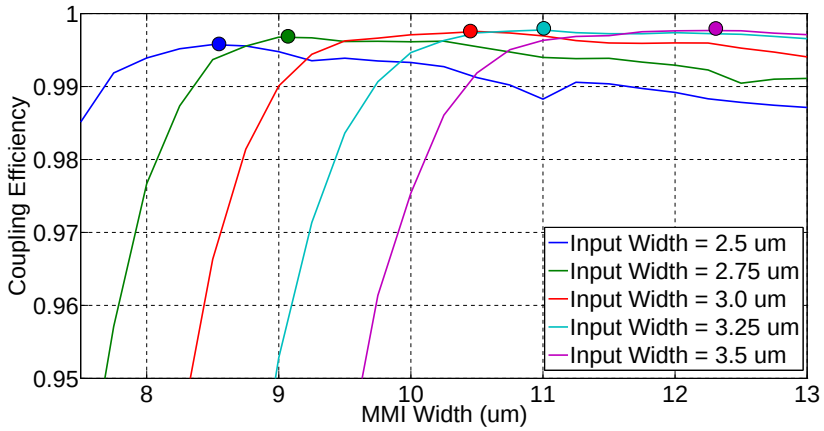

(b)

Figure 3.23: (a) Optimised max coupling efficiency of MMIs versus MMI width, as the input waveguide width is varied. (b) Close up view of maximum MMI coupling efficiency versus MMI width as input waveguide width is varied. Peak in coupling efficiency for each input waveguide width is indicated.

The optimum MMI length was calculated for each MMI variation and is shown in Figure 3.24. As expected, the optimum MMI length for a particular MMI depended solely on the MMI width, and was not affected by the increased input waveguide width.

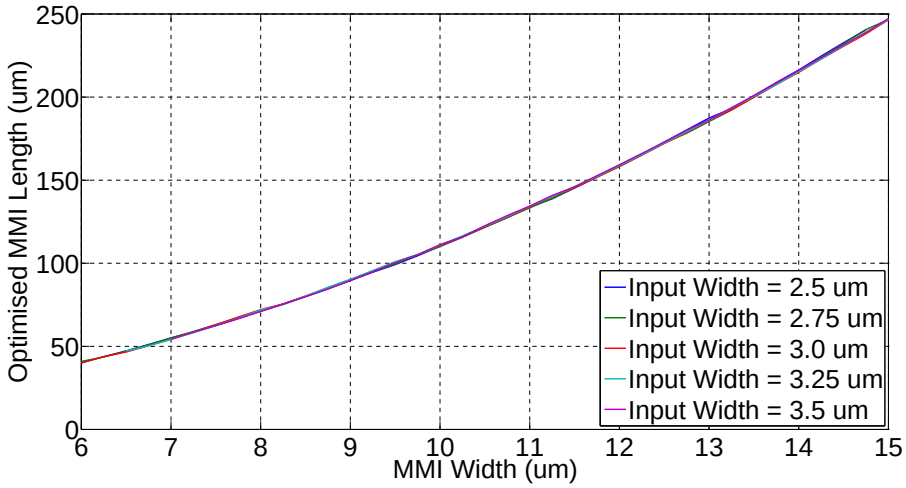

Figure 3.24: Optimised MMI length, as calculated from EIM-MPA, versus MMI width.

When the optimum separation between the output waveguides was considered for the same parameter sweep, similar can be seen. The separation was found to match almost exactly across each of the waveguide widths. The results of this are shown in Figure 3.25.

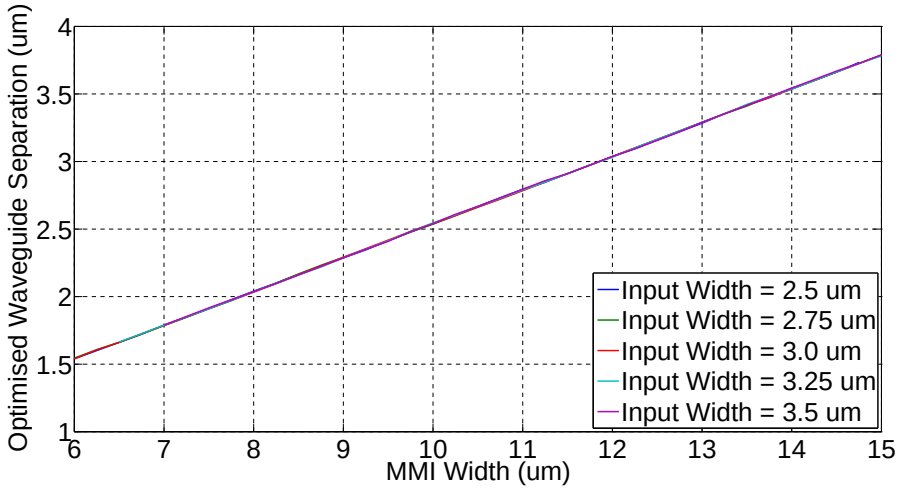

Figure 3.25: Optimised output waveguide separation, as calculated from EIM-MPA, versus MMI width.

3.4.2.1 Predicted results from Theory and Simulation

The detailed mathematical analysis of MMIs was discussed in chapter 2, where an analytical expression was found for the length of an MMI where it acts as an efficient $1 \times M$ optical splitter. This expression is

$$MMI_{Length} = \frac{L_{MMI}}{N}. \tag{3.2}$$

where L_{MMI} is the MMI self-imaging length, given by

$$L_{MMI} = \frac{W_{MMI}^2 n}{\lambda}. \tag{3.3}$$

The analysis in the preceding section has examined MMIs computationally to find their optimum length to act as efficient optical splitters. Since the computational method uses these analytical expressions as an initial guess before further optimisation is carried out, it is useful to know how well each set of solutions agree. In Figure 3.26, the analytical MMI lengths calculated using Equation (3.2) are compared with the optimised MMI lengths found for the waveguide modelled in Figure 3.22a. The computational and analytically found values show reasonable agreement, with a variation of $\sim 5\%$ present. This deviation is expected due to the approximations of the theoretical analysis, where very strongly guided structures were assumed. Such assumptions were not made in the computational models, which allowed accurate mode field distributions and propagation constants to be determined.

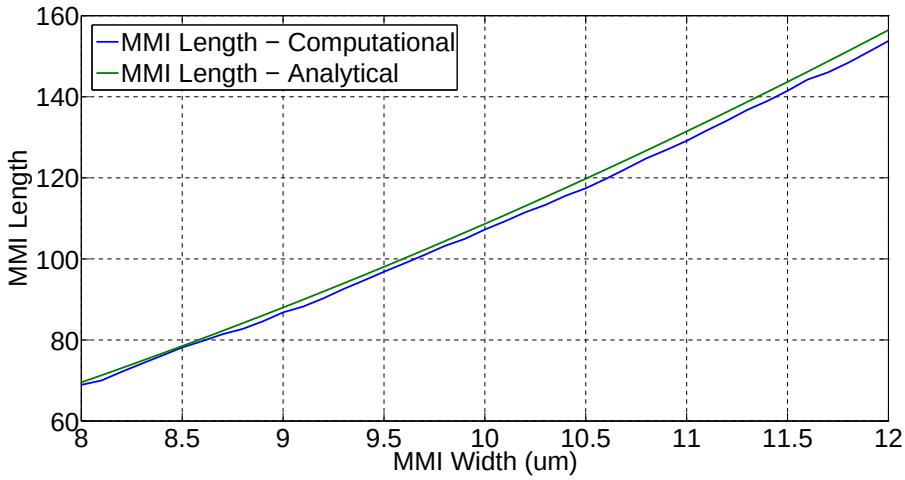

Figure 3.26: Comparison between the analytical and computationally determined values of the MMI length to act as an efficient MMI coupler.

3.4.2.2 Compact MMI Couplers

An important factor to consider when designing MMIs is to ensure that the device length does not become excessively large for a particular applications. As can be seen from Figure 3.24, for large MMI widths the length of the device starts to approach 250 µm. When waveguide bends are included on the outputs, this dimension can increase by upwards of 250 µm, making the MMI impractical for all but large photonic integrated circuits.

The most compact MMI coupler can be formed by using the narrowest input waveguide possible. Analysis of Figures 3.23a and 3.24 show that for a 2.5 µm input waveg-

uide width to the MMI, the optimal MMI performance occurs at an MMI width and length of 9.0 µm and 81.0 µm respectively. This is significantly shorter than the optimally designed device with an MMI input waveguide width of 3.5 µm, where the MMI length required for optimum coupling has almost doubled to 155 µm. However, MMIs based on narrow input waveguides show an increased sensitivity to deviations from their optimum structure. This can introduce significant potential coupler losses due to slight dimension variations which are unavoidable during device fabrication. As will be discussed further later in this chapter, using wider input waveguides increases the tolerance of MMI couplers to fabrication errors. As a result, which designing compact MMIs there is always a trade off between minimising device dimensions and ensuring good performance of the device after fabrication.

3.5 MMIs with Fabrication Errors

Due to the complex nature of device processing, fabrication of MMIs can introduce deviations in the structural properties of even an optimally designed MMI. As mentioned previously and introduced in chapter 2, these deviations can cause the performance of the MMI to deteriorate quickly, resulting in poor optical coupling. The main sources of fabrication error when processing MMIs arises from:

Etching Where the ridge or rib waveguide formed on a PIC does not match the modelled structure due to being too deep if over etched, or shallow if under etched

Lithography Where the physical dimensions of the MMI structure do not match designed values to over or under exposure of the mask during processing

The MMI simulation tools developed earlier in this chapter provide a means of investigating the role of fabrications errors in MMI performance efficiently. It allows the structural properties of MMIs, such as their MMI_{Input}, MMI_{Width} and etch depth, to be varied while the coupling efficiency under each source of fabrication error is examined. In particular, the efficiency of the EIM-MPA method offers an excellent means of analysing MMIs where fabrication errors are present in the width and length of the device, i.e lithographical errors. The SFEM-MPA lends itself ideally to investigating the issues posed by over or under etching of MMIs, where it can provide accurate but computationally intensive solutions to MMIs based on any waveguide structure. Both these sources of error will now be investigated on *Waveguide A* (see Table 3.1), with a focus on how MMI designs can be improved to make them less sensitive to fabrication deviations.

3.5.1 Lithography

Lithographical issues during fabrication, such as poor mask resolution or over/under exposure, can cause the final MMI device dimensions (when measured after fabrication) to differ from that of the intended MMI design. This can manifest itself as MMIs which have non-optimal device lengths and widths. A schematic outline of these errors are shown in Figure 3.27.

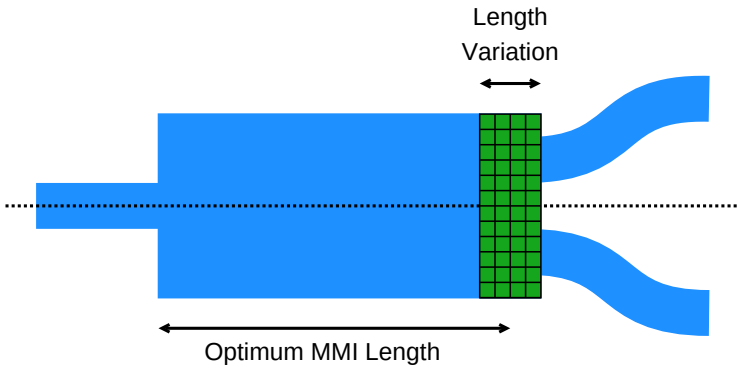

(a)

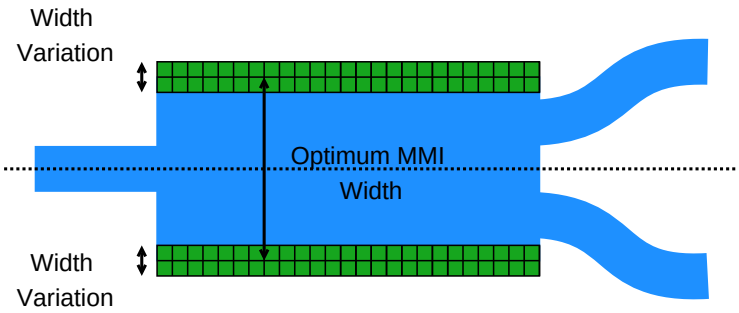

(b)

Figure 3.27: (a) Schematic of an MMI with fabrication error in the length of the device only. (b) Schematic of an MMI with fabrication error in the width of the device only.

3.5.1.1 Fabrication Errors in MMI Length

The EIM-MPA method was first applied to the design of 1×2 MMIs which had error deviations in just its length, as in Figure 3.27a. For a fixed MMI_{Input} of 3.5 µm, MMIs were designed and optimised for MMI widths ranging from 5 µm to 25 µm. At each MMI width, the coupling efficiency was measured at ± 5 µm from its optimum length. The results of this simulation are shown in Figure 3.28, where the Z-axis represents the coupling efficiency at a particular MMI width, with a given fabrication error. For MMI widths approaching that the input waveguide width, the coupling efficiency is shown

to be poor as errors of ±5 µm are introduced to the MMI length. As the MMI width starts to increase, the overall coupling efficiency improves dramatically and the effect of the induced fabrication error can be seen. For MMI widths >12 µm, the coupler has reached close to its peak coupling efficiency and the fabrication errors are shown to only minimally impact the MMI performance.

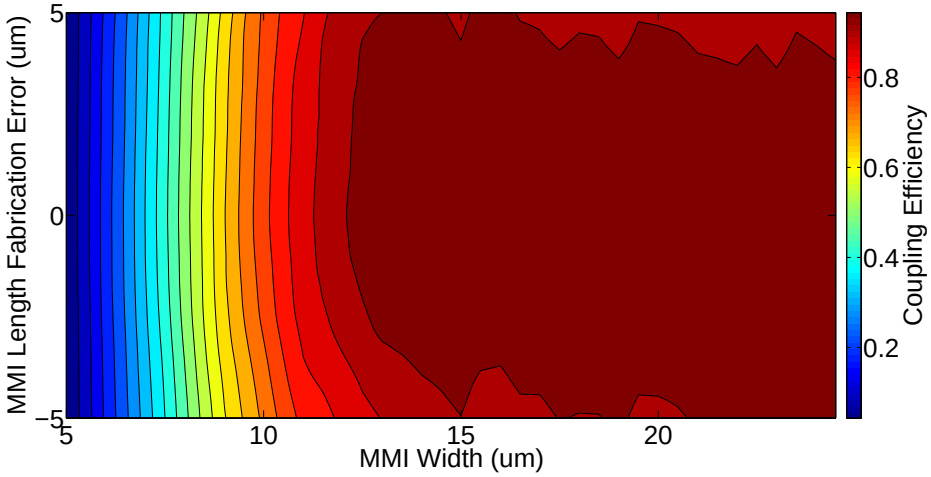

Figure 3.28: Coupling efficiency versus fabrication error in MMI length and MMI width.

Next, attention turned to determining the role MMI_{Input} had on the tolerance of the MMI to fabrication errors from its optimised length. The MMI_{Width} was fixed at 15 µm, while MMI_{Input} was varied from 2.5 µm to 4.5 µm. The coupling efficiency was determined for induced errors of ±10 µm around the optimised MMI length in each case. The results are shown in Figure 3.29.

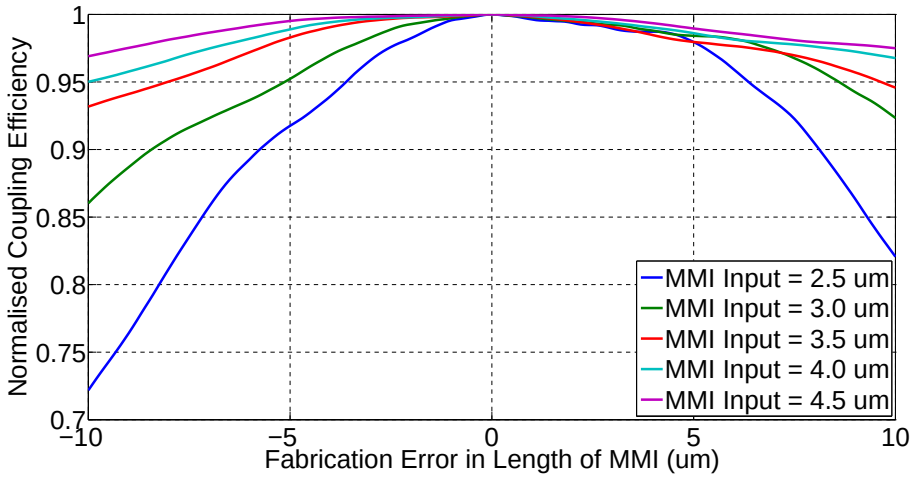

Figure 3.29: Coupling efficiency versus fabrication error as the MMI input waveguide width was varied.

For narrow input waveguide widths, the coupling efficiency is seen to be more sensitive

to fabrication errors. At an induced fabrication error of −10 µm, the coupling efficiency is shown to increase from < 75% at MMI_{Input} =2.5 µm to > 97% at MMI_{Input} =4.5 µm. It should be noted that the MMI is still largely insensitive to length fabrication errors of <5 µm. In particular, for errors of 1 µm - 2.0 µm, the coupling efficiency still remains close to its peak value. This feeds back into the comparison between the SFEM-MPA and EIM-MPA methods for designing MMIs, where the small length differences between the predicted optimum MMI lengths for each case is not critical to the device performance.

3.5.1.2 Fabrication Errors in MMI Width

The EIM-MPA was next applied to MMIs with fabrication errors in the MMI_{Width} of the device, compared to the designed values, as in Figure 3.27b. A similar analysis was performed to that discussed previously when examining fabrication errors in the length of MMIs. For a fixed MMI_{Input} of 2.5 µm, MMIs were designed and optimised for MMI widths ranging from 5 µm to 25 µm. At each MMI width, the length of the MMI was fixed at the optimised value as determined from the EIM-MPA, however, the width of the MMI was varied by ±1.0 µm in each case. Such a small change in the MMI width can have a large impact on the field distribution of the MMI, where the propagation constants of the supported modes in the MMI can vary compared to those used in the design optimisation. The results of this simulation are shown in Figure 3.30.

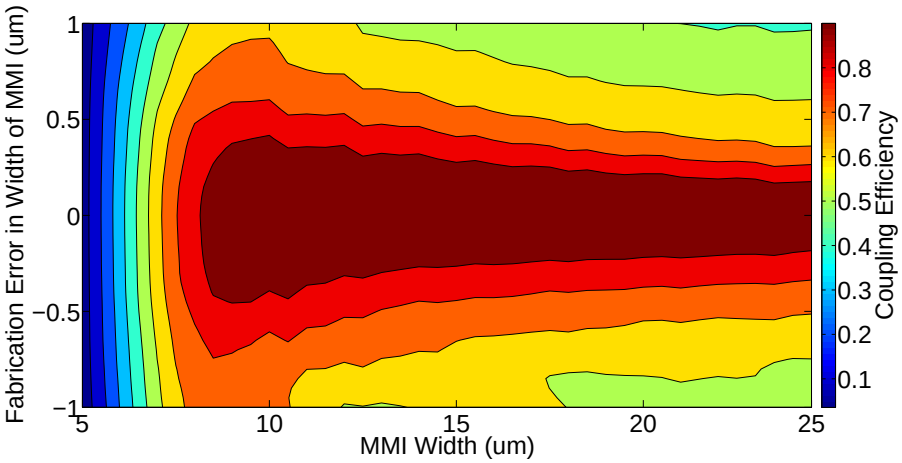

Figure 3.30: Coupling efficiency versus fabrication error and MMI width.

The sensitivity of the MMI to fabrication errors in its designed width are clearly shown in Figure 3.30. For narrow MMI widths, the coupling efficiency was minimised due to the device size being too small for it to act as a 1×2 splitter. As the MMI width was increased, the tolerance to fabrication errors was maximised for MMIs with MMI_{Width} = 9.5 µm. For deviations of ±1 µm, the coupling efficiency was observed to drop to almost 60% outside of this MMI width.

Further simulations explored the role varying MMI_{Input} had on the tolerance of the device to fabrication errors. For a fixed MMI_{Width} in this case, the same analysis was performed with the MMI_{Input} being swept from 2.6 µm to 3.6 µm, with the coupling efficiency versus fabrication error recorded. The simulation results are shown in Figure 3.31.

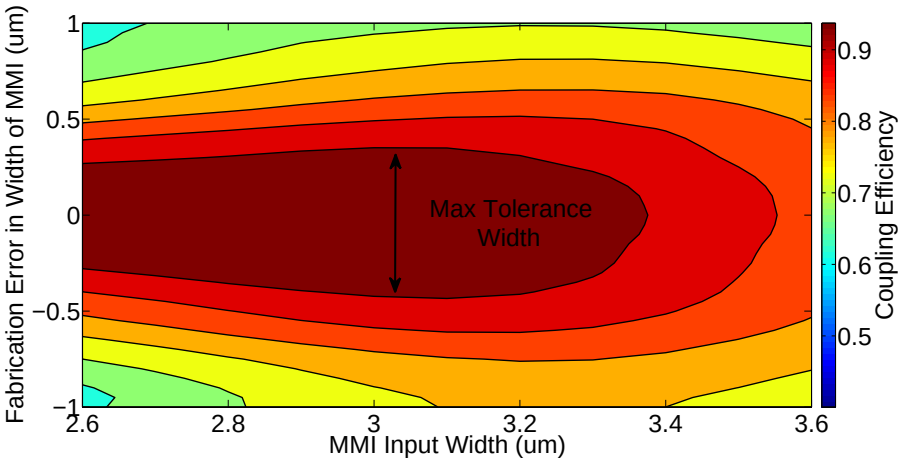

Figure 3.31: Variation of MMI coupling efficiency as the MMI input waveguide width is varied versus fabrication error.

The coupling efficiency of the MMI drops off rapidly for large values of MMI_{Input} due to the geometry of the device. The device performance for lower MMI_{Input} values, indicates that the tolerance of the MMI to fabrication errors improves with increasing MMI_{Input} width. Once MMI_{Input} starts to become too large for the MMI_{Width} itself to act as an effectively MMI, the operation starts to break down. As seen in Figure 3.31, there is an optimum MMI_{Input} width which provides the greatest MMI tolerance to fabrication errors. This value determined the most tolerant MMI that can be designed for a particular MMI_{Input} width and is a key parameter when designing MMIs.

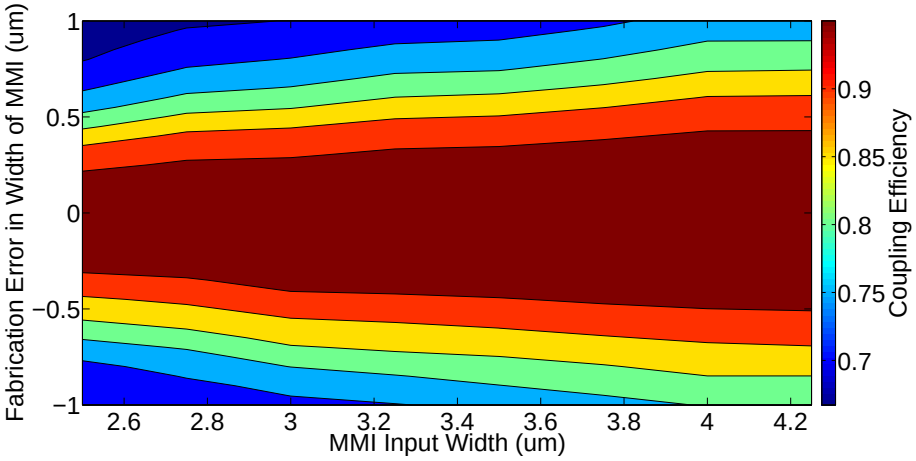

Figure 3.32: Maximised fabrication tolerances of MMIs due induced errors, as the input waveguide width is varied with MMI width optimised at each variation.

To determine the impact varying both MMI_{Input} and MMI_{Width} play on the performance off an MMI to fabrication errors, the same MMIs described above were again considered but this time both parameters were variables. As the MMI_{Input} was varied, there was no longer a constraint placed on the MMI_{Width}, which was now free to reach the optimum MMI_{Width} which would result in peak tolerance to fabrication errors. This is shown in Figure 3.32, where the coupling efficiency versus fabrication error at the optimum MMI_{Width} for each MMI_{Input} was plotted. As the MMI_{Input} increased, so too did the tolerance of the device fabrication errors. The analysis provided a means of determining the optimum device size to allow for sufficient MMI coupling under specific fabrication errors. It has been shown that having the largest MMI_{Input} possible for a particular application ensures the best possible device performance. However, there is a trade off between having error insensitive devices due a larger MMI_{Input} and device size.

3.5.1.3 Fabrication Errors in MMI Width & Length

The tolerance of MMIs to fabrication errors was previously examined by considering errors in the length and width separately, as in Figure 3.27. As a device fabricated these errors will appear together if there is over or under exposure during lithography. This can make the MMI wider and longer, or narrower and shorter. The results from the previous Section, in particular from Figures 3.28 and 3.30, show the sensitivity of MMIs to these fabrication errors. MMIs are considerable less sensitive to deviations from their optimised length than they are to the designed width. For typical III-V fabrication processes, lithographical errors of the order 0.1 µm to 0.3 µm can be expected. Over this range the effect of length variations are negligible to the MMI coupling efficiency, with the MMI width acting as the dominant term.

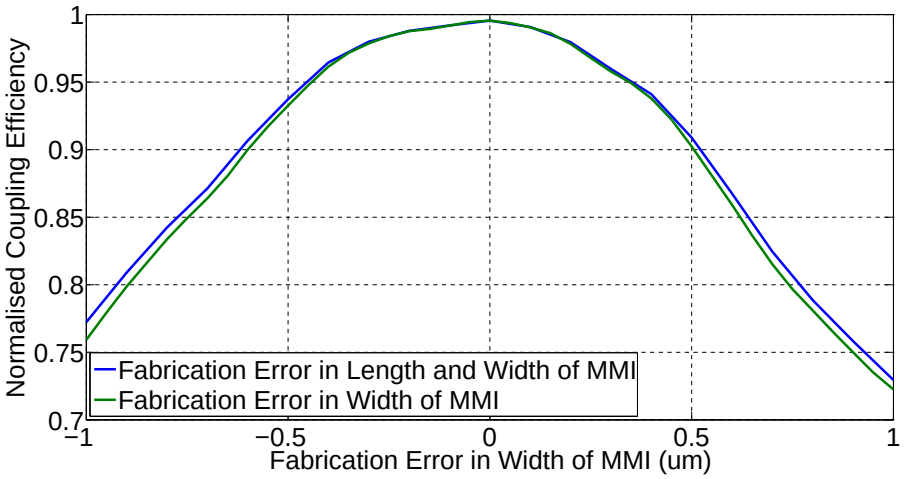

Figure 3.33: Coupling efficiency of MMIs with induced errors in MMI width, overlapped with coupling efficiency of the same MMI with induced errors in both the MMI width and length.

To confirm this, the MMIs considered earlier were designed with fabrication errors of -1.0 µm to 1.0 µm in both their length and width dimensions. The coupling efficiency of these MMIs were compared to MMIs with errors present in just the width direction. The results of this simulation are shown in Figure 3.33, with the coupling efficiency versus fabrication error plotted on the same graph for comparison. For fabrication errors of less than 0.5 µm, the addition of errors in the length dimension does affect the overall fabrication tolerance of the MMI. For this reason, most fabrication tolerance optimisation involves minimising the coupling sensitivity of MMIs to deviations from their optimum widths, with errors in the length largely ignored.

3.5.2 Over & Under Etching

Ensuring that waveguides are correctly etched during fabrication is one of the more difficult parameters to control during processing. Over or under etching of waveguides can have a significant impact on their behaviour, resulting in non-optimal device performance. A schematic outline of an over and under etched ridge waveguide is shown in Figure 3.34.

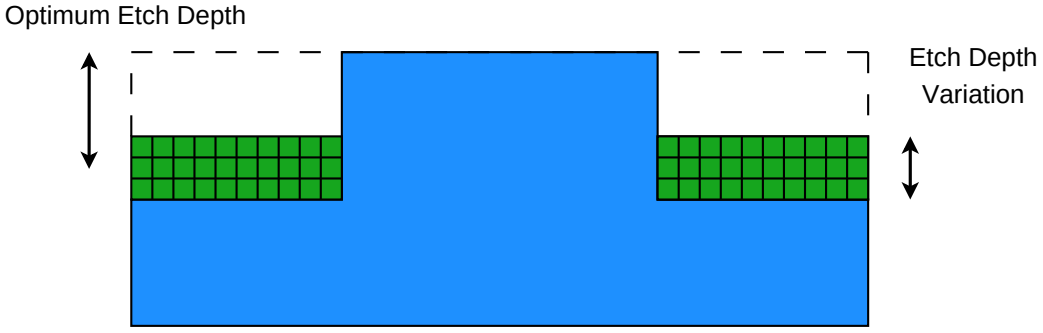

Figure 3.34: Schematic of a ridge waveguide where over or under etching of the ridge from the optimum depth can be seen.

An MMI was based around the shown waveguide structure, with a particular ridge etch depth chosen to provide confinement of the waveguide mode in the x-direction. During processing of the waveguide, the actual depth of the fabricated etch may not match the intended value. This over or under etching of the causes guiding properties of the waveguide to change (confinement, propagation constants, field distribution), affecting its performance as an MMI.

Using the EIM-MPA method to examine the impact of over or under etching on optimally designed MMIs will result in significant errors due to the breakdown of the EIM for shallow etched MMIs, as seen in Appendix C. However, the SFEM-MPA offers excellent suitability for these purposes as it can be used to design MMIs based on any arbitrary waveguide structure, at the expense of requiring more intensive computa-

tional analysis. The MMIs chosen for this analysis were based on *Waveguide B*, with parameters summarised in Table 3.1 and fixed MMI dimensions of MMI_{Input} =2.5 µm and MMI_{Width} =10.0 µm. MMIs were optimised at these dimensions while the etch depth of *Waveguide B*, the *Height* as in Figure 3.1, was varied from 0.5 µm to 1.3 µm. This allowed the coupling efficiency of MMIs as they go from being shallow (0.5 µm) or deep (1.3 µm) etched to be examined. The simulated results from this are shown in Figure 3.35.

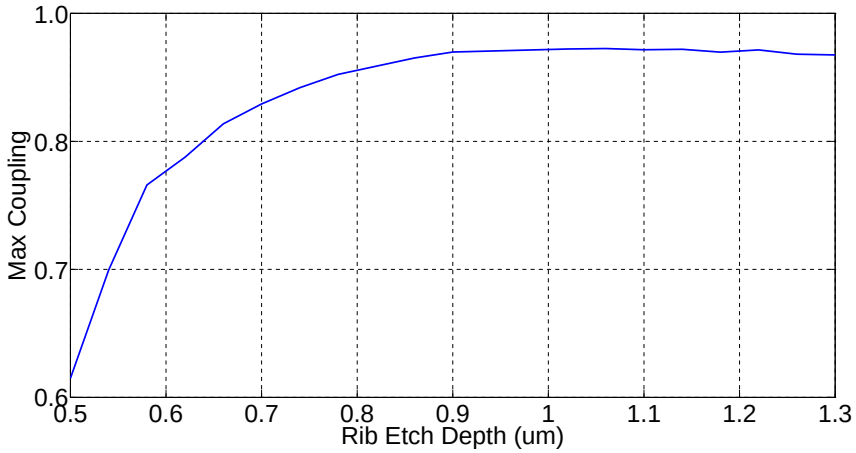

Figure 3.35: Max coupling efficiency of an MMI versus increasing etch depth. For shallow etches, the MMI displays poor coupling efficiency. The MMI performance increases as the waveguide approaches a deep etched structure.

For shallow etched MMIs, there is poor optical confinement of the mode and this results in poor performance of the MMI structure. This is shown in Figure 3.35 where the maximum coupling from MMIs with shallow etch depths can be $< 75\%$. As the etch depth increases, so too does the confinement of the mode and there is an increase in coupling efficiency as the waveguide becomes deeply etched. This indicates that to improve MMI performance, deep etched waveguides are required.

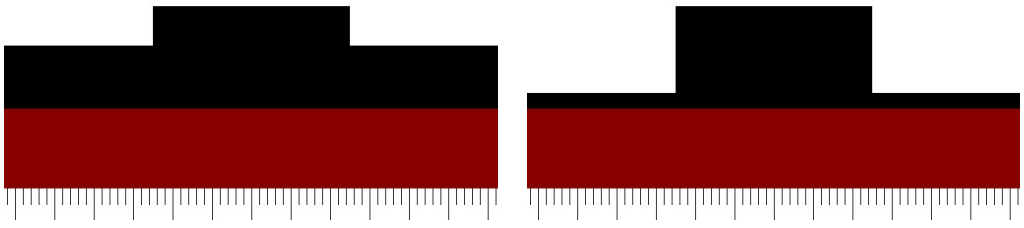

(a) Waveguide with etch depth of 0.5 µm. (b) Waveguide with etch depth of 1.1 µm.

Figure 3.36: Shallow etch (a) and deep etch (b) waveguide structures.

The sensitivity of MMI coupling efficiency to over and under etching was next examined. Two MMI variations based on the same waveguide structure as before were considered;

one a shallow etched waveguide, with etch depth of 0.5 µm and the other a deep etch waveguide, with etch depth of 1.1 µm. The profiles of the shallow and deep etched waveguides are shown in Figures 3.36a and 3.36b.

The optimum MMI length was calculated for each MMI variation based on its error free etch depth of 0.5 µm for the shallow MMI and 1.1 µm for the deep etched MMI. The coupling efficiency of these MMIs were then investigated using the SFEM-MPA method as errors were introduced into their etch depths. The etch error variation was chosen to be -0.3 µm to 0.4 µm, which allowed significantly over and under etched MMIs to be considered. The error-free deep etched MMI waveguide structure is shown in Figure 3.37a, with an under etch of 0.3 µm shown in Figure 3.37b and an over etch of 0.4 µm shown in Figure 3.37c.

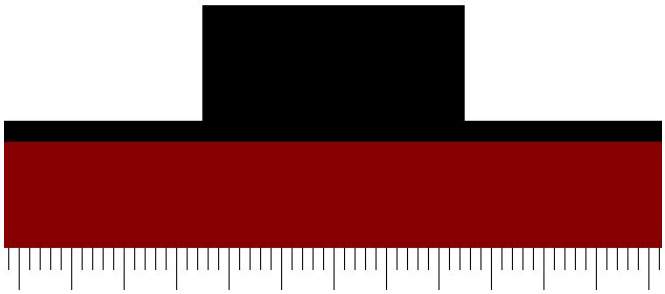

(a) Error free waveguide structure for deep etched MMI.

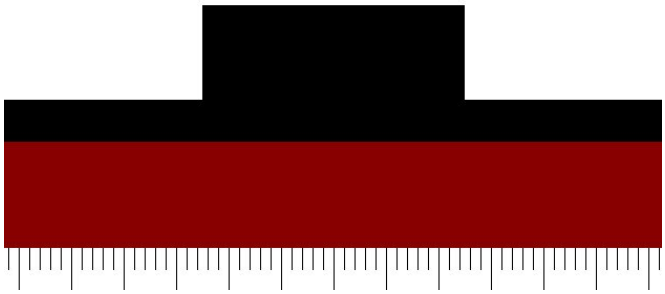

(b) Under etched (by 0.3 µm) waveguide structure for deep etched MMI.

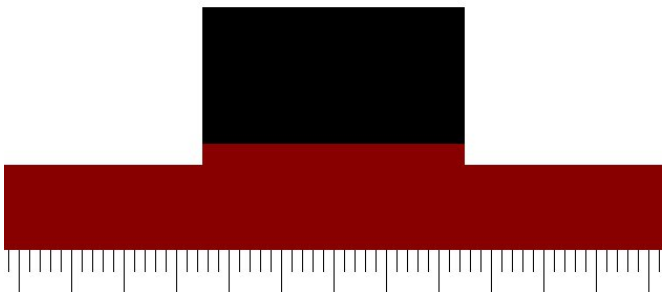

(c) Over etched (by 0.4 µm) waveguide structure for deep etched MMI.

Figure 3.37: Ridge waveguide with induced errors in the etch depth.

For the shallow and deep etched waveguide variations, the coupling efficiency versus etch depth error is shown in Figure 3.38. The deep etched MMIs are shown to be insensitive to fabrication errors and still display excellent coupling efficiency even with etch errors of $\pm$ 0.1 µm from the optimum etch depth. On the other hand, shallow etched MMIs appear to be particularly sensitive to under etching. An under etch of 0.1 µm can significantly reduce the coupling efficiency of the MMI to $< 50\%$. Interestingly, the shallow etched MMI does not show a peak in its coupling efficiency for an etch error of 0 µm as would be expected. The coupling efficiency instead increases as the MMI is over etched. This counter-intuitive result can be explained by analysis of Figure 3.35.

In Figure 3.35 shallow etched MMIs were shown to offer poor coupling efficiency at small etch depths. As the etch depth becomes smaller due to under etching, a further drop off in coupling efficiency is expected. This sharp drop in MMI performance is seen in Figure 3.38 for under etching of the shallow waveguide based structure. Over etching of the shallow MMI causes it to behave more like a deeply etched waveguide, thereby increasing its overall peak *potential* efficiency. As errors are introduced into the shallow etched MMI, the loss in performance due to the induced etch errors is compensated by the performance increase from becoming more deeply etched. This can be seen in Figure 3.38, where the coupling efficiency of the shallow MMI reaches peak performance for an over etch of 0.3 µm. After 0.3 µm, the coupling efficiency starts to drop off as the loss due to the MMI being at the non-optimum MMI length for its etch depth becomes the dominant term.

This analysis has shown that for optimum MMI performance and tolerance to fabrication errors, deeply etched waveguide structures perform better. Deep etched MMIs show improved peak coupling efficiency compared to shallow etched MMIs. In addition to this, deep etch based devices are far more insensitive to over or etching which may be present during fabrication.

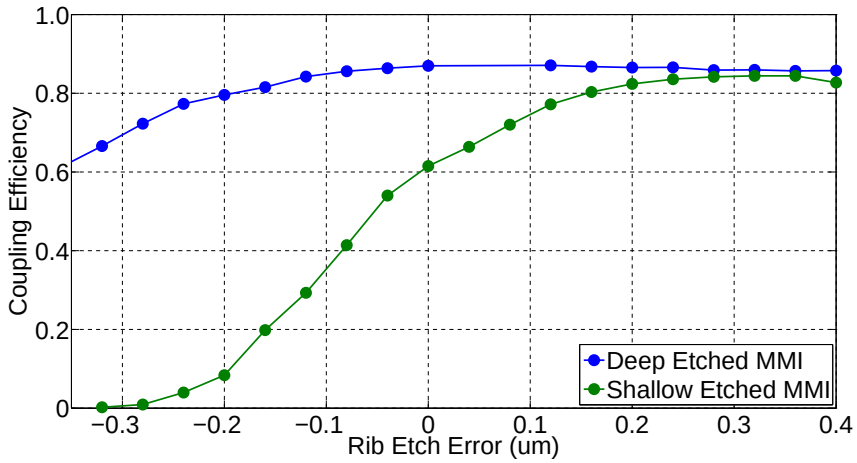

Figure 3.38: Coupling efficiency of deep and shallow etched MMIs versus error in the ridge etch depth.

3.6 Design and Testing of MMIs

The MMI optimisation code developed in this chapter was used to design MMIs which were based on material for MZMs with 15 quantum wells (QW). The waveguide was etched through the QW region until it reached an etch stop layer, forming a deep etched waveguide. This allowed the EIM-MPA method to be applied to the structure rather than the SFEM-MPA. A schematic of the waveguide structure is shown in Figure 3.39. For confidentiality purposes, the details of the layer structure cannot be provided.

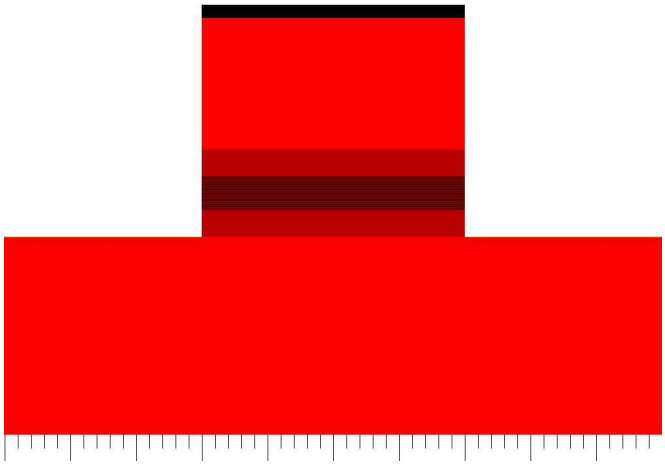

Figure 3.39: Quantum well based waveguide structure for MMI designs.

To improve the fabrication tolerance of the MMI, the input waveguide width was chosen to be 3.0 µm. The EIM-MPA software was applied to this waveguide structure, where the optimised length, width and output waveguide offset were found for it to act as a 1×2 optical coupler. These values are shown in Table 3.3.

Table 3.3: Optimised MMI Parameters

MMI_{Input} (µm)	MMI_{Width} (µm)	MMI_{Length} (µm)	MMI_{Offset} (µm)
3.0	12.0	150.5	3.0

Single MMIs were fabricated based on these dimensions by other members of the IPG group at Tyndall. The fabricated MMIs offered the possibility of comparing the performance of the real device to that the simulated structure. An example of the fabricated MMI is shown in Figure 3.40.

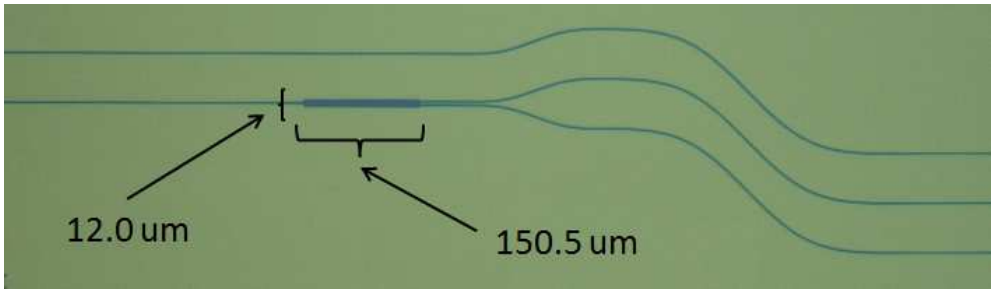

Figure 3.40: A single MMI with major dimensions labelled.

Directly above the MMI a straight waveguide was fabricated which directly matched the input waveguide width and bend radii of the MMI output waveguides. The waveguide provided a baseline measurement of the coupling efficiency through the device without the MMI being present. By comparison with the MMI coupling efficiency, the performance of *just* the MMI could be extracted without the associated bend or fibre coupling losses. The MMIs and straight waveguides were tested using the lensed fibre coupling technique developed during this thesis, which will be discussed in chapter 4.

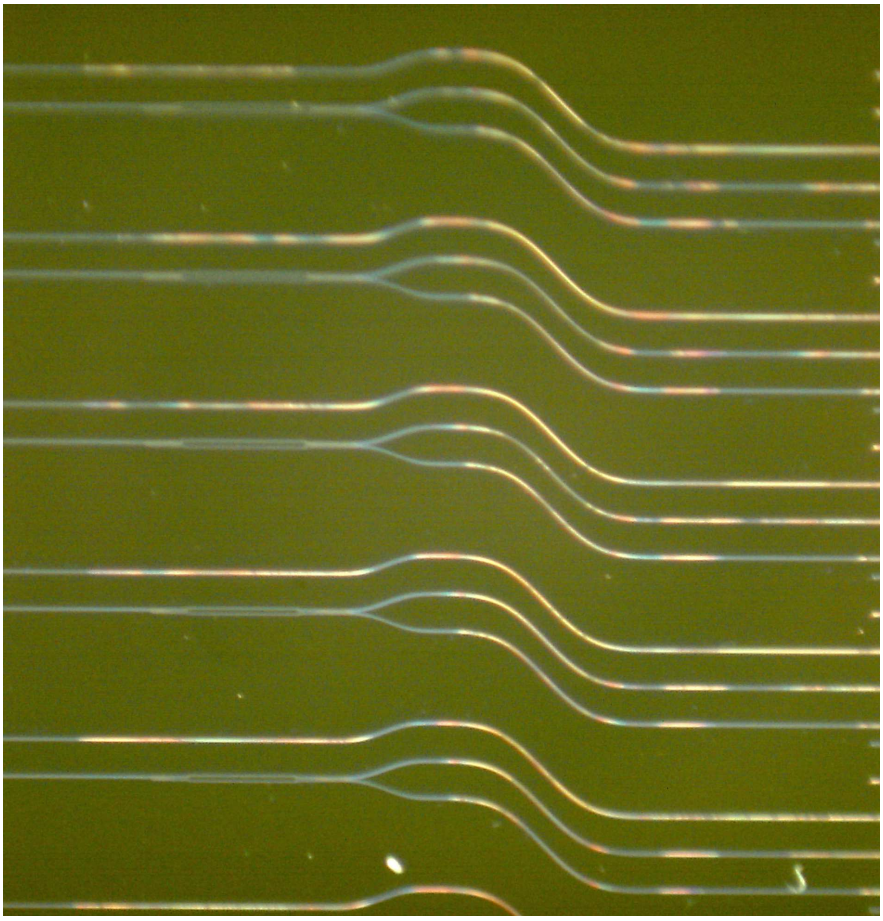

Figure 3.41: Fabricated MMIs with variations in length from the optically designed values. Provides a means of experimentally validating the EIM-MPA model for designing MMIs.

MMI variations were considered around the optimum parameters given in Table 3.3. In particular, MMIs were fabricated where the device length was varied from the optimum of 150.5 µm by -20 µm, -10 µm, +10 µm and +20 µm. This provided 5 data points which could be compared with the results predicted from the EIM-MPA MMI model. It also allowed the tolerance of MMIs to deviations around their optimum values to be investigated. These five MMIs were fabricated together for ease of experimental testing. The MMIs are shown in Figure 3.41.

These MMIs were tested experimentally, where the coupling efficiency of each device was determined by comparison with the straight waveguides. For the same structures, the EIM-MPA model was used to calculate the predicted coupling efficiency of each device. The results from the EIM-MPA analysis are overlapped with the experimental data in Figure 3.42, where the normalised excess loss of the MMI is plotted versus the length of each MMI.

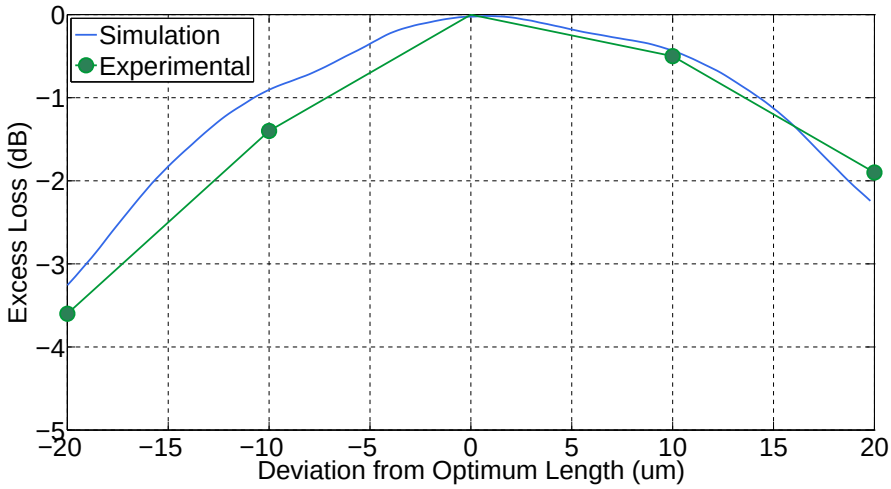

Figure 3.42: Comparison between simulated and experimentally tested MMI designs.

The performance of the fabricated MMIs shows excellent agreement with the values predicted from the EIM-MPA code. The excess loss of the device is minimised for the MMI with a length of 150.5 µm, as designed using the EIM-MPA code. For shorter or longer MMIs, the performance of the MMI drops off quickly with a 3 dB loss seen where the MMI is 20 µm shorter than the optimally designed value. These results are comparable with the simulations shown in Figure 3.29, where length variations around optimally designed MMIs were considered. The results of this experimental and simulation comparison, validate the EIM-MPA model developed during this thesis for use in the design of MMIs.

3.7 Conclusion

The work presented in this chapter examined the use of MPA in the design and optimisation of MMI couplers. Two different versions of MPA were implemented numerically to model MMIs, these were the EIM-MPA and SFEM-MPA methods. The SFEM-MPA method provided a general means of designing MMIs on arbitrary waveguide structures. It was based on an SFEM mode solver previously developed in the IPG group at Tyndall. MMI simulations using the SFEM-MPA were numerically intensive and required significant processing power. The EIM-MPA was shown to offer a three order of magnitude improvement in computational efficiency compared with the SFEM-MPA. This is primarily due to the approximations used in EIM-MPA, where a one-dimensional equivalent waveguide is solved rather a full two-dimensional structure, as in SFEM-MPA. As shown in Appendix C, the EIM-MPA analysis of MMIs provides accurate and rapid solutions for deep etched waveguide structures, where excellent agreement is observed compared with the more thorough SFEM-MPA analysis. For shallow etch structures, the EIM technique itself starts to break down. This results in significant deviations between the EIM-MPA and SFEM-MPA techniques when designing MMIs. For the waveguides and MMI structures considered in this thesis, the EIM-MPA has excellent applicability and can confidently be used in the design of efficient MMI couplers.

The EIM-MPA method was particularly important in the optimisation of MMI couplers, where device variations could be examined rapidly. Optimisation routines were developed in C++ to maximise the coupling efficiency of MMIs based on their waveguide structure. With this in place, attention was turned to how MMIs could be designed to minimise the effect fabrication errors played on their performance. The role of lithographical and etching errors were examined, with design criteria determined to ensure optimal performance.

The chapter concluded by investigating the application of the EIM-MPA code to the design of MMIs based on a complex quantum well based structure. An MMI was designed on this structure, where its optimised length and width was used to fabricate real devices. The MMIs were experimentally tested and the results compared with the values predicted from the simulations. Excellent agreement was seen between the modelled and fabricated MMIs. With the MMI optimisation code validated for real devices, MMI couplers could then be designed for use in the photonic integrated devices described in chapter 5.

Chapter 4

Testing of Passive Waveguide Devices

4.1 Introduction

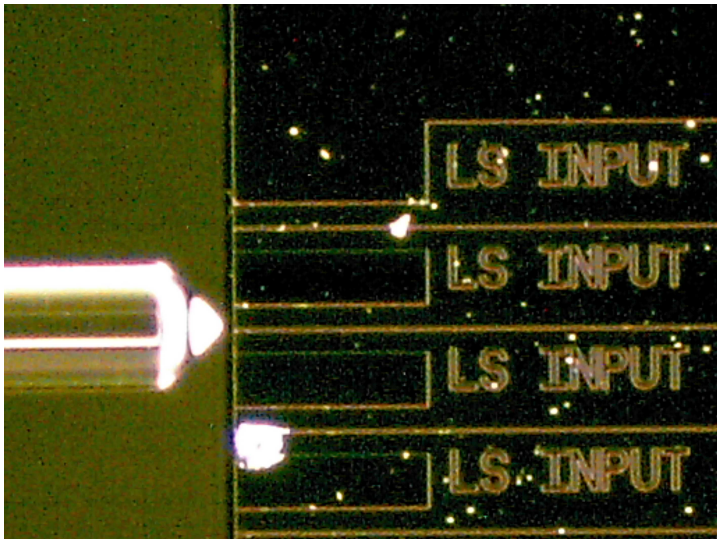

Figure 4.1: A lensed fibre optimally coupled to a ridge waveguide.

The goal of the work presented in this thesis was to investigate photonic integrated circuits for applications in coherent signal generation. An important consideration when designing such devices is how they can be tested experimentally. Coupling light to or from such integrated circuits poses many experimental challenges [149]. This is mainly due to the size of the optical waveguides to be coupled, where sub-micron alignment tolerances are typically required [150]. Together with a large number of potential waveguides to be coupled, testing of such devices can be a slow and laborious process. Grating couplers are often used for efficient device coupling, however, they

can be impractical for certain device applications and test setups.

Lensed fibre coupling is used to couple light in and out of ridge waveguides used in standard Fabry Pérot edge emitting lasers and PICs [151], by aligning the fibre close to the waveguide facet. Figure 4.1 shows a microscope image of a lensed fibre coupled to a waveguide. For active devices such as tunable quantum well based lasers integrated with power splitters [152, 100], the fibre alignment to the waveguides can be relatively straight forward. The fibre position can be optimised by monitoring the coupled output power from the waveguide as a function of position and re-adjusted as necessary. Photodetectors may also be integrated on devices in order to provide another means of determining where maximum fibre coupling has been achieved.

For passive waveguide devices without integrated sources or receivers on chip, the process of fibre alignment becomes more challenging due to the need to couple fibre to the input and output waveguides simultaneously. The difficulty with such testing is the need to initially have good coupling at the input side of the device before being able to collect any light from the output. Often this requires repositioning of both fibres simultaneously until some coupled power is detected through the device. The tolerances involved in this coupling makes these re-adjustments a time consuming process. Figure 4.2 shows a passive waveguide device under test where such coupling has been performed. The lensed fibres have both been optically coupled to the waveguides under test and the power transmitted through the device can be determined.

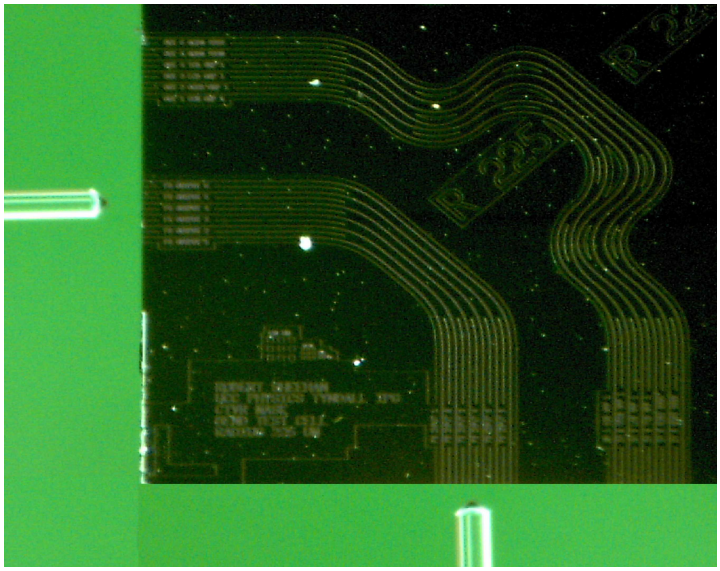

Figure 4.2: Lensed fibres aligned to the facets of an optical waveguide under test.

Recent advancements in the area of source alignment techniques have used optical power tracking software to reposition lensed fibre to provide optimised coupling. Power from the fibre at one side of a device under test is fed back into the system and used to reposition the other fibre and vice versa. This can prove to be exceedingly useful for

improving coupling, however, it is much more applicable to maximising the coupling once fibres have been aligned to a high degree already. For optical instrumentation and antenna alignment, mechanical alignment marks are typically used to aid in the coupling between components. However, techniques such as these are limited by mechanical tolerances and do not allow for coupling optimisation.

In this chapter, a new optical coupling method is developed [99] which allows fast and efficient coupling between lensed fibres and ridge waveguides. The technique has wide spread applications in the testing of passive waveguide components and complex photonic integrated circuits, such as those considered in this thesis. In the sections that follow, the experimental technique is described in detail and then applied to the testing of ridge waveguides. The results are analysed and the chapter concludes by discussing the efficiency of the technique and also how its functionality can be improved.

4.2 Facet Scan Imaging

Direct imaging of the field distribution of optical waveguides [153] has proven useful in the characterisation of optical integrated circuits [154]. Typically, these methods involve scanning a fibre over a device maintaining a constant distance from the surface. As the fibre is scanned across the surface, light from the evanescent field is monitored and measured on a power meter. The work discussed in this chapter describes a new form of imaging technique which can be used to image the physical structure of a waveguide facet and also image the waveguide mode. By imaging the waveguide facet, the precise location to place a lensed fibre for optical coupling can be determined. The imaging technique makes use of indirect imaging, where a light carrying optical lensed fibre is scanned over the surface of a waveguide facet, while the light reflected from the surface of the facet back into the fibre is monitored. As the fibre is stepped across the facet, an image of the waveguide structure can be formed by analysis of the reflections from the facet surface. A schematic representation of this is shown in Figure 4.3.

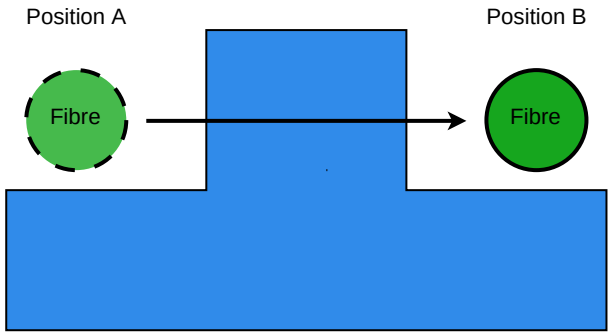

Figure 4.3: Principle of the facet scan imaging technique. As a lensed fibre moves across a ridge waveguide the back reflected light from incident light on the facet is measured.

The lensed fibre, initially at position A, moves to position B while the reflected power from the waveguide is measured. At A, no reflected light is measured since the light can propagate freely into air. As the fibre moves across the face of the ridge waveguide, the light from the fibre can interact with the facet and reflect back into the fibre. When the lensed fibre starts to pass over the ridge on the way to B, the reflections start to drop off until they reach zero where the lensed fibre is completely off the facet. Analysis of the reflected power versus lensed fibre position allows the center of the ridge waveguide to be found. The expected *reflected power versus fibre position* curve for this scenario is shown in Figure 4.4.

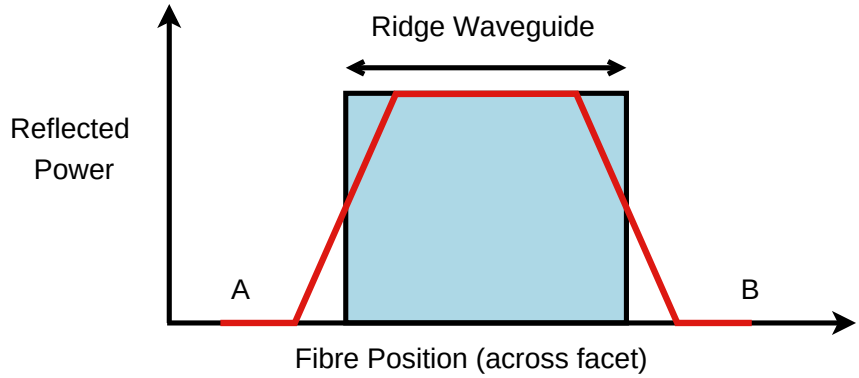

Figure 4.4: Reflected power as a facet scan is performed on the waveguide shown in Figure 4.3.

At fibre positions A and B the measured reflected power from the waveguide facet is at a minima. As the fibre scans across the ridge, the reflected power is maximised and then starts to decrease. The reflected power reaches this maximum value when the lensed fibre mode overlaps completely with the waveguide facet. As seen in Figure 4.4, this occurs at a fixed point along the waveguide facet and is related to the spot size of the lensed fibre beam. Analysis of the flat region where the reflected power remains at its peak value shows that the lensed fibre is completely over the waveguide facet in this area. From this, the lensed fibre position which is on the center of the ridge waveguide can be determined. This technique can be extended to scan the lensed fibre in the full plane of the waveguide facet, where a two dimensional image of the ridge waveguide can be found. Based upon the image generated by the reflection scan, it is possible to determine precisely where to position a lensed fibre in order to ensure that it is correctly located on the ridge waveguide for optical coupling. The reflection scan is performed using a computer controlled piezo stage to move the fibre in the plane of the facet, while a light source is connected, via a circulator, to the lensed fibre and a power meter is used to measure and record the reflected power.

After facet scans have been performed on the input and output waveguides of a device, the fibres can be aligned with the ridge waveguides to provide good optical coupling. The power coupled between the input and output waveguides can then be measured. In

this situation, the fibre to waveguide coupling may not be maximised due to misalignments between the fibre and the waveguide mode to be coupled. To further improve the coupling, a power scan is performed across the waveguide facet where the transmitted power from the input to output waveguide (and vice versa) is measured. The image provided by the power scan allows the precise fibre position to be determined where coupling is maximised at both sides of the device. The precise details of the experimental setup used for these scans will be described in the next section of the chapter.

4.3 Experimental Setup

A schematic of the experimental setup is shown in Figure 4.6.

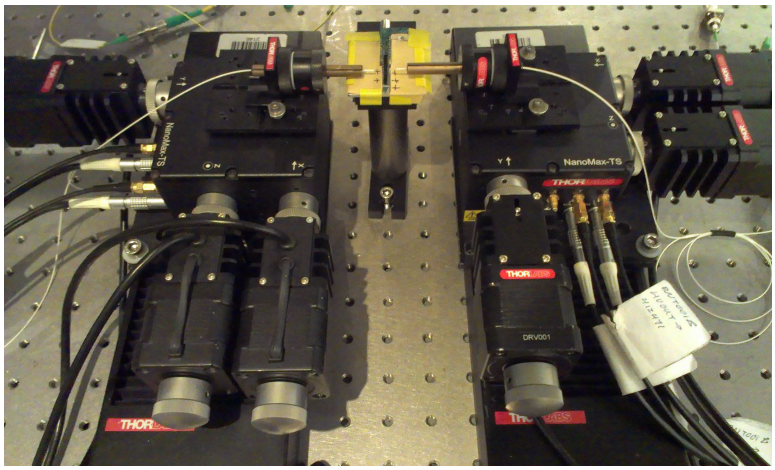

Figure 4.5: Experimental setup shoing the a device under test. Computer controlled stages are used to provide fibre alignment in the XYZ directions.

The device to be tested was placed on custom vacuum mount that allowed lensed fibre to be brought in close to the waveguides under test. The lensed fibre position was adjusted using three motorised stages at each side of the setup. These stages offered coarse alignment in the XYZ directions with step sizes of ∼60 µm. For more precise alignment, each lensed fibre had two axes which had piezo positioners to allow a positional resolution of 5 nm. LabView code was written to control both sets of positioners, where the motors could be used for quick alignment with the piezo reserved for fine control.

Each lensed fibre was connected to the *second port* of an optical circulator, with a tunable laser at the *first port*. This allowed the lensed fibre to provide incident light on a waveguide facet. On the *third port*, the back reflected power from the facet was measured on an optical power meter. The experimental setup used in the development of this imaging technique is shown in Figure 4.5. The optical power meter was linked

to the LabView code which controlled the lensed fibre. This allowed the back reflected power from a waveguide facet to be measured against fibre position. The LabView code allowed a *positional window* to be setup that the lensed fibre would be scanned over. The piezo controllers were used for this scan, which provided a maximum window of 20 µm × 20 µm. Scanning over this window produced a precise two dimensional intensity plot which represented the ridge waveguide facet.

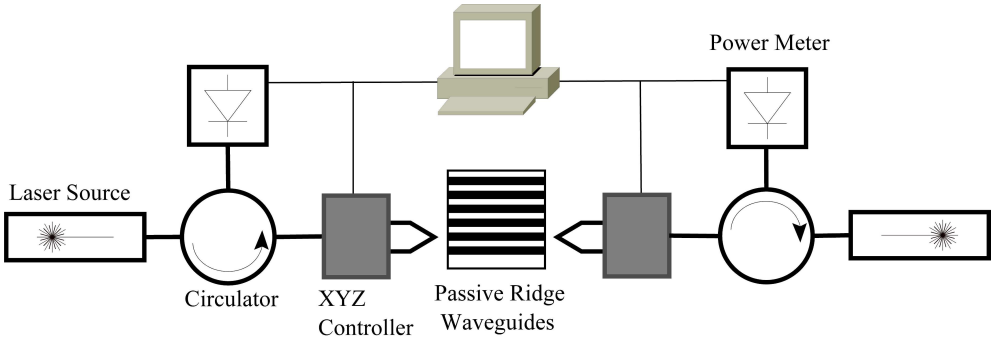

Figure 4.6: Schematic outline of the experimental used to align fibres using the facet scan technique.

4.4 Optimising Waveguide Coupling

Optimising waveguide coupling using the facet scan techniques developed in this work required three main steps to be followed. These were:

1. **Focusing of lensed fibres on facets:** To maximise the facet scan resolution, the beam width of the incident light on the facet must be as narrow as possible. This is done by stepping the lensed fibre towards the waveguide facet while monitoring the reflected power. At a particular distance the reflected power will be maximised and the fibre will focused correctly on the facet.

2. **Facet scans for initial alignment:** With the fibre focused on the waveguide facets as in (1), reflections scans are performed on the facet to determine the precise position of the waveguide ridge. With this done on the input and output sides of a device, lensed fibres can be coupled to an optical waveguide and the transmitted power measured.

3. **Transmitted power scans for optimisation:** After the lensed fibres have been coupled to an optical waveguide as in (2), the power scans of the transmitted power from one side of the device to the other are measured. This allows the fibre position to be determine that allows for maximum transmission, where they are optimally coupled at the waveguide input and output.

The optical waveguide coupling technique will now be demonstrated by applying it to the testing of the waveguides shown in Figure 4.2. These waveguides have a ridge

structure as in Figure 4.7. The waveguide had a thickness (T), etch depth (H) and width (W) of 1.5μm, 1.0μm and 2.25μm respectively, with a core index (N2) of 3.38, a substrate index (N3) of 3.17 and an air cladding (N3) of index 1.

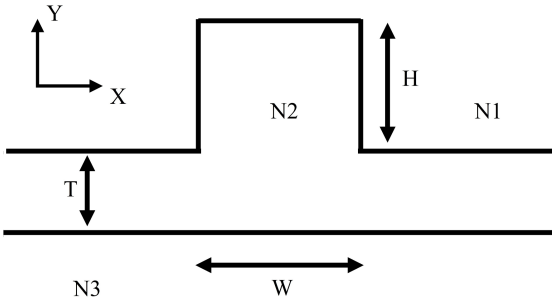

Figure 4.7: Structure of ridge waveguide used in the development of this fibre to waveguide coupling technique.

4.4.1 Facet Edge and Lensed Fibre Focus

As shown in Figure 4.2, the photonic device under test was viewed through a microscope and a lensed fibre was manually positioned close to the facet and roughly aligned to both sides of the chosen waveguide. At this initial position the fibre was poorly, if at all, aligned to the waveguide in the X, Y and Z directions. The first step of the alignment procedure was to determine the top edge of the chip in order have an approximate location to begin the scans across the waveguide facet surface. This was achieved by bringing the lensed fibre close to the waveguide facet and adjusting its position of the fiber in the Y direction, as in Figure 4.8a, until back reflected light from the facet was measured on the power meter through the corresponding circulator. The lensed fibre was then scanned in the Y direction and the position of the edge of the chip was easily determined by monitoring the position at which the back reflected power started to decrease. With the fibre now approximately aligned to the chip in the Y direction, it was necessary to correctly focus it on the waveguide in the longitudinal (or Z) direction. This was done to ensure that spot size of the light coming from the lensed fibre was at its minimum on the facet of the waveguide which is a requirement for higher resolution images. The facet scanning procedure was again repeated as the fibre was stepped by 0.05μm increments towards the facet in the Z-direction. Figure 4.8b shows the image generated by applying the above scanning procedure in the Y and Z directions to the device described above. The false color plot of Figure 4.8b indicates the approximate location of the top edge of the chip by examining how the back reflected power drops off when the lensed fibre is stepped vertically in the y-direction. From the figure it can be seen that for this facet sweep the top edge of the chip was located approximately 10.4μm from the fibre's initial position.

By examining the false color intensity plot it was possible to locate an optimal position

for the lensed fibre in the z-direction, thereby giving an approximate location for the focal point of the fibre. This alignment procedure was analogous to Gaussian mode coupling between optical elements [155]. The Gaussian mode from the lensed fibre was incident on the facet and was then reflected back towards the fibre. To ensure optimal coupling between the two, the overlap integral between the reflected and propagated Gaussian mode of the lensed fibre must be as large as possible. These modes will be well matched when the facet of the waveguide was at the focal point of the lensed fibre, also resulting in the minimum spot size of the beam. Scanning the lensed fibre's position in relation to the facet edge in the longitudinal direction allows it to be focused approximately on the facet of the ridge waveguide.

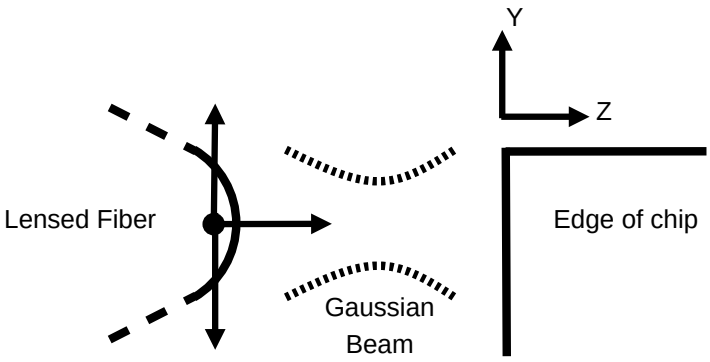

(a) Determining the vertical edge of the device under test and optimally aligning the fiber in the z-direction.

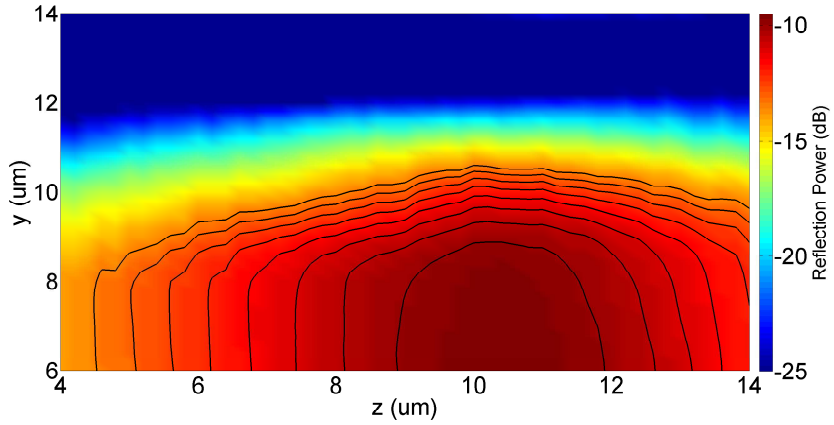

(b) Reflection scan generated as a lensed fibre is brought towards the facet of a waveguide.

Figure 4.8: Focusing of lensed fibres on waveguide facets.

4.4.2 Reflection Scan

With the lensed fibre correctly aligned in the z-direction and the approximate position of the top of the chip determined, the lensed fibre was next aligned to the ridge waveguide in the X and Y directions. A wide reflection scan was performed on the waveguide

facet in order to generate a mapping of the waveguide ridge position. The approximate position of the ridge was found by analysing the image generated for a small “bump" in the false color plot of the back reflected power. With this in place, a more refined reflection scan was performed over a smaller area to image the ridge accurately. For the input and output waveguides discussed here, the generated reflection images are shown in Figures 4.9a and 4.9b.

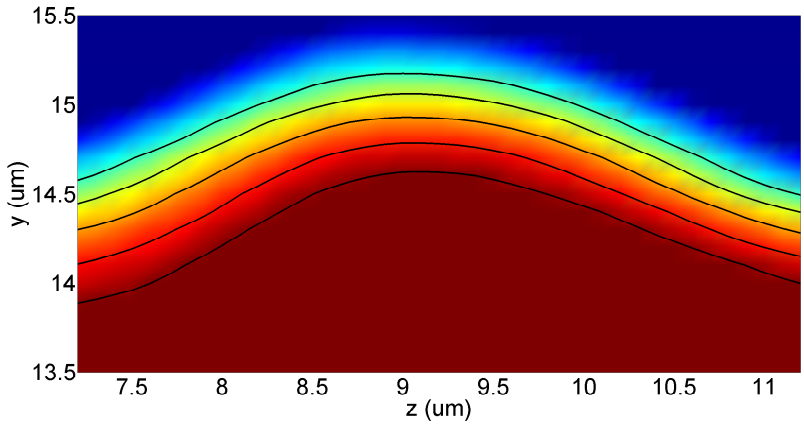

(a) Reflection scan generated from the *input* waveguide of the device under test.

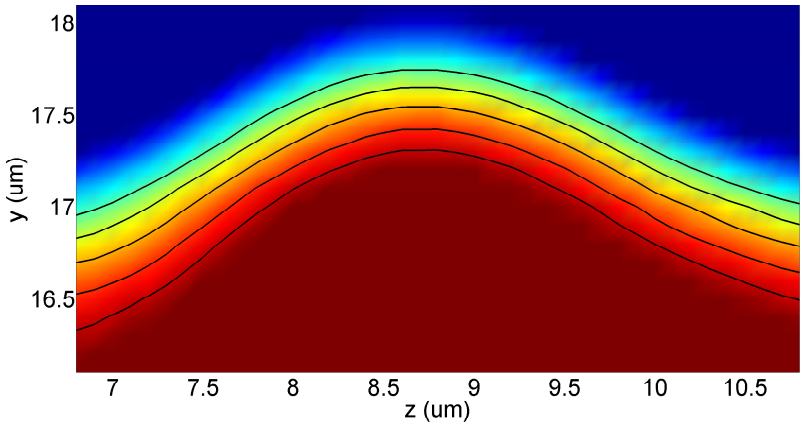

(b) Reflection scan generated from the *output* waveguide of the device under test.

Figure 4.9: Reflection scans of facets showing waveguide ridge features.

The feature shown in both Figures 4.9a and 4.9b indicates the presence of the waveguide ridge as the fibre scans across the facet. For the input waveguide, a cross section of the reflection scan in the vertical direction is shown in Figure 4.10.

As the fibre scans vertically, the reflected power is reduced as the fibre passes over the waveguide facet. This can also be done as the fibre is scanned horizontally across the waveguide ridge, as in Figure 4.3. The horizontal cross section is shown in Figure 4.11. From these images shown in Figure 4.9, the approximate position of the waveguide ridge in each case was determined. The center of the ridge in Figure 4.9a was found to

be at the point where the fibre was positioned at $8.8\mu m$ in X and $17\mu m$ in Y, relative to its initial position. The center of the ridge in Figure 4.9b was found where the fibre was positioned at $9.1\mu m$ in X and $14.4\mu m$ in Y, relative to its initial position. Placing the lensed fibres at these positions provided efficient coupling between the fibres on the input and output side of the device, which could be found by measuring the transmitted power from one side of the device to the other.

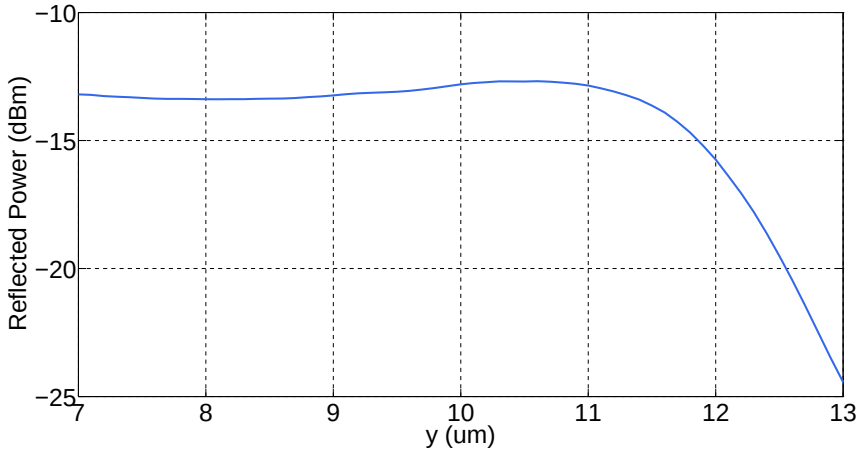

Figure 4.10: Cross section of reflection scan in the vertical direction as the lensed fibre sweeps over waveguide facet.

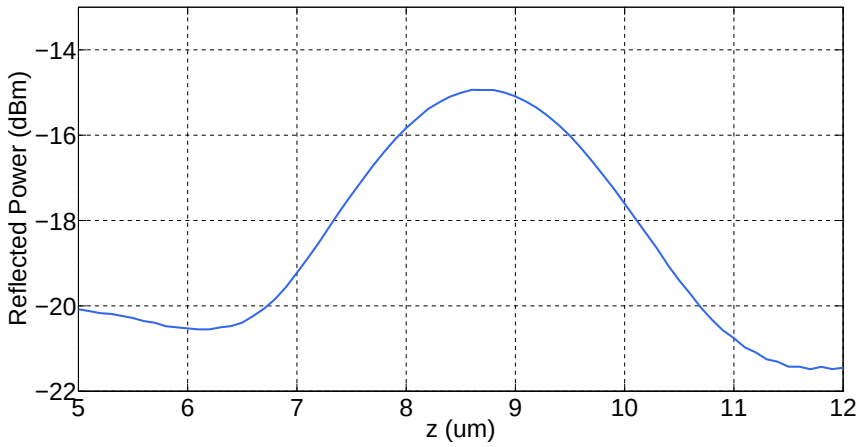

Figure 4.11: Cross section of reflection scan in the horizontal direction as the lensed fibre sweeps across waveguide ridge.

4.4.3 Scanning Transmitted Power

To maximise the light coupled through a passive device under test, the lensed fibres at the input and output waveguides must both be optimally aligned. Using the previously discussed reflection scan, lensed fibres can be positioned on the input and output

waveguide facets to provide efficient (but non-optimised) device coupling. Once the fibres have been aligned in this way, hardware or in-built software routines in the lensed fibre controllers can be used further optimise the device throughput. If such routines are not available the transmission can be optimised by performing a transmitted power scan, a technique similar to that of the reflection scan. The transmitted power scan works by scanning a fibre over the emitting facet of the device while recording the transmitted power. The fibre position for optimised coupling can then be determined by maximising the overlap integral between the fibre and ridge waveguide mode. The transmitted power scan technique will now be described.

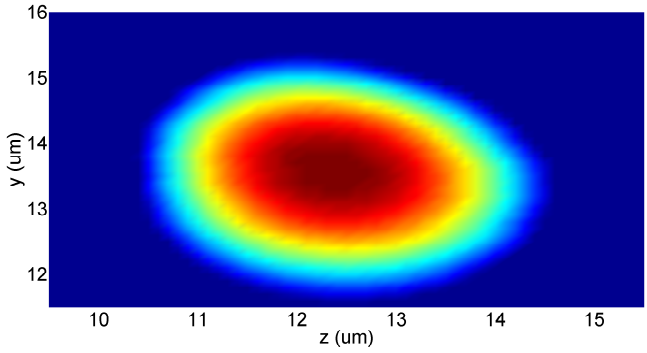

(a) Transmitted power scan of waveguide facet. Peak indicated the lensed fibre position for optimised power coupling.

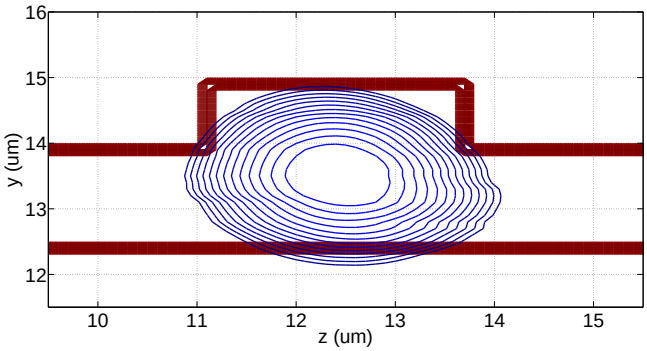

(b) Transmitted power scan overlapped with known ridge waveguide structure of the device under test.

Figure 4.12: Transmitted power scans of waveguide facets.

Using the back reflection scanning method, lensed fibres were positioned at the center of the waveguide ridge on both the input and output sides of the passive optical circuit. Light was input through one lensed fibre, which was held fixed in place, and propagated through the passive waveguide structures. At the output side of the optical circuit, the second lensed fibre was scanned in the X-Y plane and the transmitted power was recorded. Prior to recording the results from the transmitted power scan in the X-Y plane, the fibre was scanned in the Z-direction to ensure that the output fibre is located at the optimal focus position. Using a fibre switch the input and output waveguides were

reversed and the process was repeated to obtain transmission power scans from both sides of the device. The images generated from these scans represent the convolution of the transmitted ridge waveguide mode with the Gaussian mode of the lensed fibre. Figure 4.12a shows the image generated for the transmitted power scan, at one side of the passive optical device.

The Figures 4.12 show that there is a peak in the transmitted light coupled into the fibre, as expected. The positions of these peaks indicate the optimum position for coupling in and out of the ridge waveguide at each side. Figure 4.12b shows a contour plot of the same data overlapped with the known waveguide structure. It is clear that there is a sub-micron window where the lensed fibre should be positioned for optimum coupling.

Figures 4.13a and 4.13a show the reflection scan images generated from the input and output device waveguides, overlapped with the corresponding transmitted power data.

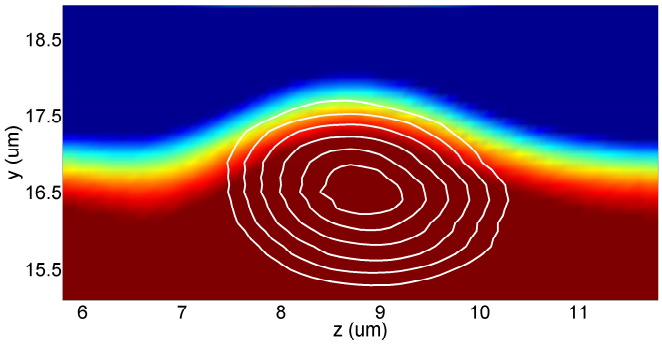

(a)

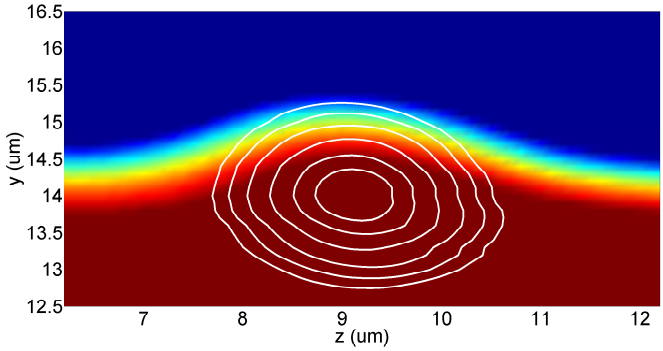

(b)

Figure 4.13: Contour plot of transmitted power measured as lensed fibre is scanned on (a) input and (b) output side of the optical circuit. Data is overlapped with reflection scan data from corresponding ridge waveguide. Contours represent convolution of the ridge waveguide mode with fibre mode.

Positioning the lensed fibre outside of the optimal coupling window as determined from the transmitted scan, causes the coupling efficiency to drop off quickly. Availing

of the information from the reflection scans, it was possible to place the fibre within approximately $0.5\mu m$ of the optimum position in the Y direction. The optimum position of the fibre in the X direction can then be determined from the back reflection images by considering the symmetry of the ridge in this direction. The improvement in coupling between having the fibre in this position compared to when the optimum position was found through the transmission scan, was $\sim 5dB$ a significant difference in coupling efficiencies.

As discussed previously, optimal coupling was achieved when the overlap integral of the fibre mode and the mode of the waveguide ridge was greatest. Given the waveguide structure as presented in Figure 4.7, the fundamental waveguide mode was calculated using the Scalar Finite Element Method (SFEM) mode solver as discussed in chapter 2. This mode is shown in Figure 4.14.

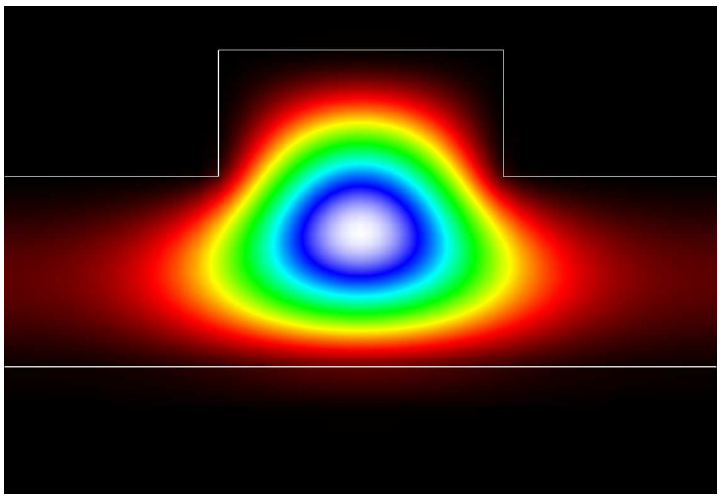

Figure 4.14: Calculated TE mode of the ridge waveguide used in the development of this waveguide to fibre coupling technique.

The overlap integral between this mode and the Gaussian mode of the lensed fibre was then computed. This overlap integral places a theoretical maximum limit on the coupling efficiency between the lensed fibre and waveguide at 55%, a 2.6 dB loss. After including Fresnel reflection losses from the facet of the waveguide this theoretical maximum coupling was reduced to 51%, a 2.9 dB loss. Using the alignment procedure proposed in this work it was found that the optimal coupling achieved was 49%, a 3.1 dB loss. From this it is clear that the imaging method described allows for quick alignment and efficient coupling between lensed fibres and passive ridge waveguide structures. It is a particularly useful technique in the testing of optical circuits with a large array of ridge waveguides.

4.4.4 Quick and Efficient Coupling

While this imaging technique was used to locate the lensed fibre position for optimum coupling, it must also be noted that high coupling efficiencies, although important, are not the only factor to be taken into account when testing optical circuits. For example, for optical circuits with numerous arrayed waveguides, as in Figure 4.2, it becomes essential to minimise the time taken to couple to each input and output waveguide in the array to perform the testing efficiently and in a timely manner. The proposed imaging technique described in this chapter provides a quick and consistent means of coupling to each waveguide. Using the computer controlled stages, the scans described above can be performed rapidly, with scan durations given in Table 4.1.

Table 4.1: Scan Times (seconds)

Focusing Scan	Broad Facet Scan	Fine Facet Scan	Transmission Scan
20	20	45	45

As can be seen from Table 4.1, the time taken to perform the scans necessary for this coupling technique take ~ 160 seconds for each side of the passive device to be tested. Extra time is required between scans to reposition the lensed fibre and place it at the determined optimal position from the scans. Since computer controlled stages are used to move the fibre, the time taken for this is short. The total time required to optimally couple a lensed fibre to both the input and output of a specific waveguide on a passive optical device using this method was found to be ~ 8 minutes. This coupling time could be reduced by an order of magnitude if optimised step sizes were used when carrying out the fine focusing, reflection and transmission scans. In an industrial environment, or one where faster coupling times are required, the step sizes would be chosen carefully to match the specific waveguide structure of the device under test (DUT) to allow for faster coupling while ensuring the same efficiency.

This process could easily be automated to ease in the testing of such an array of waveguides. With the lensed fibre initially manually aligned on the first waveguide of the array, a broad area scan along the edge of the device can be carried out, where the approximate position of each ridge could be determined. Using these positions, it would be possible to step along the device carefully and perform the facet and transmission scans at each waveguide. It should be noted that this waveguide structure is chosen arbitrarily and that the technique proposed is applicable to other waveguide structures. A key requirement for this method to function correctly is the need to have sufficient reflections from the waveguide facet to initially image the ridge structure. This imaging cannot be done if the waveguide facets have been treated using an anti-reflection (AR) coating or have angled facets. While this technique can be used for coupling to much smaller waveguides (e.g. Si wires), the overlap integral between the waveguide and

lensed fibres modes is very small due to the large mismatch in mode sizes, resulting in a low theoretical maximum coupling efficiency. There exist other optimal strategies when coupling to such smaller devices [156].

4.5 Conclusion

An efficient and quick method to couple lensed fibres to passive ridge waveguides has been described and developed. Images of the facet of a ridge waveguide are formed by measuring the reflected light from the ridge as a lensed fibre is swept in the plane of the facet. Based on this scan, the lensed fibre can be placed on the ridge waveguide to within 0.5μm of the optimum position. The coupling can be improved further by measuring the transmitted light from one side of the device to the other where the electric field intensity distribution at either side can be measured. From this, the precise position of the lensed fibre at the input and output side of a device for optimum coupling can be determined. This method was found to be particularly useful in the testing of PICs with passive waveguides and also found use in rapid fibre alignment to active devices, such as those developed later in this thesis.

This technique offers excellent potential to be extended to the automated testing of arrayed waveguides, where facet scans could be carried out over large a series of waveguide facets simultaneously rather than just one waveguide. Not only does this allow for very quick coupling, but by analysing the image of the waveguide mode for symmetry any problems with the waveguide structure relating to bad cleaves or poor fabrication can be determined.

Chapter 5

Photonic Integrated Circuit Design

5.1 Introduction

Photonic integrated circuits (PIC) are proving to be a key element in the development of more compact and efficient optical systems. The goal of this chapter was to investigate and design such PICs, with particular focus on devices which may find future roles in applications relating to Quadrature Phase Shift Keying (QPSK) modulators based on electro-absorption modulators (EAM). In chapter 1, a schematic of a proposed EAM based QPSK modulator was shown in Figure 1.20. This modulator makes use of integrated lasers with EAMs (and other elements) to improve functionality and performance. The development of such a modulator was an ambitious task within the time frame of this thesis, due to the complexities when integrating such a large variation of devices. EAMs have previously been investigated within the Integrated Photonics Group (IPG) in Tyndall for integration in such modulators [97]. The purpose of this thesis was to expand on this work, by investigating the design of the waveguide couplers required for these modulators and their integration with lasers and SOAs. The focus of this work was particularly aimed at the development of integrated devices which have the ability generate of coherent signals on chip, using integrated injection locked lasers. The proposed schematic of this PIC is shown in Figure 1.22.

This chapter explores the operation and design of such a integrated devices, with the overall goal being the development of a lithographical mask for use in device fabrication. The integrated devices considered in this thesis require the combination of several different sub-elements to function. In particular, lasers, MMIs and SOAs must be integrated together to form more complex devices. As a result, the choice of integration scheme was critical. Monolithic integration with a single epitaxial growth step was chosen for these devices due to the cost effectiveness and ease of fabrication. The first

section of this chapter describes the design and operation of lasers which have shown to be suitable for such integration [97]. Leading from this, the development of the full PIC and each integrated device is explored. The chosen material for these devices is described and the MMI modelling code from chapter 3 is applied to the waveguide structure to design MMIs. The chapter concludes by investigating the mask layout of the individual devices and subcomponents. The final section discusses the design layout of a quarter two inch wafer lithographical mask which is used for fabricating the full PIC and devices.

5.2 Tunable Lasers for Photonic Integration

The lasers chosen for the monolithically integrated devices considered in this thesis were based on Slotted Fabry Pérot (SFP) designs [157, 158, 159, 160, 161]. Unlike Distributed Bragg Reflector (DBR) [162] lasers, SFP lasers can be fabricated using standard lithographical techniques and importantly, are regrowth free allowing for excellent potential in monolithic integration applications. Although light is typically confined to the active region of a waveguide, it can still expand into the surrounding cladding areas due to a lack of total modal confinement. SFP lasers operate by etching slots into ridge waveguide cavities which can then interact with the mode of the light in these regions and provide reflectance. The reflectance provided by these slots can then produce reflection and transmission spectra which depend heavily on the physical properties of the slot e.g. slot depth and width. A one-dimensional example of light in a waveguide with a single slot is shown in Figure 5.1.

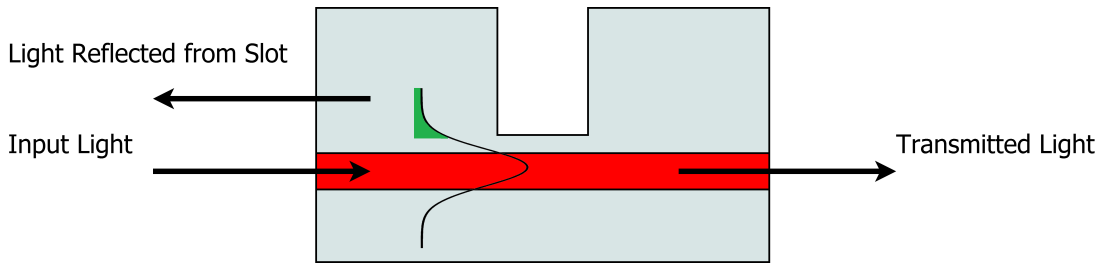

Figure 5.1: Schematic of a single slot.

Light entering the waveguide propagates in the fundamental guided mode of the structure and is confined mainly in the active region (red). The mode can interact with the slot in the upper cladding and experience partial reflection, which can be seen in green in Figure 5.1. The scattering matrix be used to analyse these slots [163] and calculate their reflectance. Etching the slots deeper into the waveguide can provide higher reflectivities, but at the expense of extra waveguide losses. A complex reflection grating can be formed by having multiple slots etched together on a single waveguide, as shown in Figure 5.2.

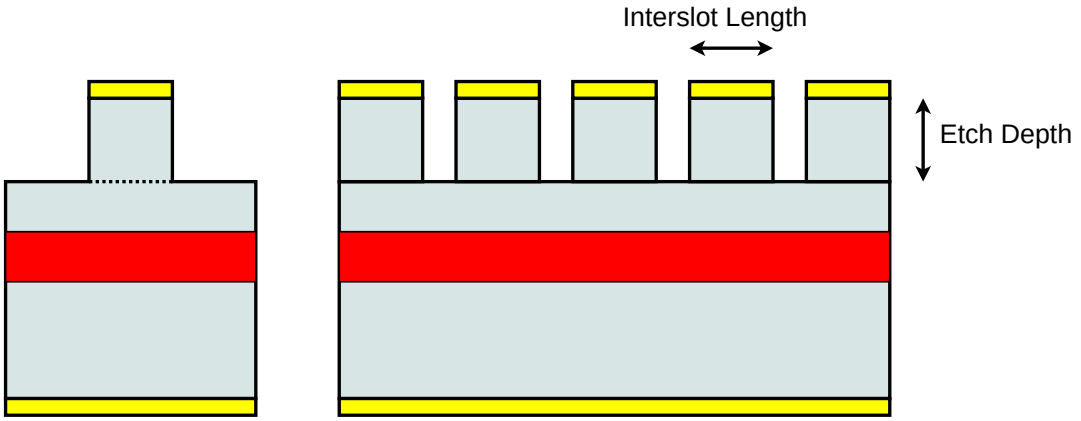

Figure 5.2: Schematic of multiple slots etched into a ridge waveguide structure.

The reflection and transmissions spectra of such a grating depend heavily on the physical properties of the slot, which are fixed during fabrication. However, tuning of the reflection spectrum was made possible by using an electrical bias across the slots to vary their refractive index. An electrical bias could be provided by adding metal contact pads between the slots and the underside of the waveguide substrate to form a junction, as in Figure 5.2.

SFP lasers are typically implemented by using multiple slotted waveguides sections to form wavelength selective mirrors. These mirrors have high losses, so are combined with straight waveguide sections which can be used to provide sufficient gain for lasing. The combined reflection spectrum of the mirror and gain sections allows lasing to occur at specific wavelengths, with significant suppression of other lasing modes. Electrical tuning of each section of the device shifts the reflection spectra, causing the main preferential lasing mode of the laser to shift due to the Vernier effect [164]. The SFP laser can provide excellent tunability and side-mode suppression ratio (SMSR) through this mechanism, while offering narrow linewidths of the order 30 kHz. For the integrated devices considered in this thesis, an SFP design was chosen which consisted of one slotted waveguide section with a long straight waveguide. The details and design of this laser will be discussed later in this chapter.

5.3 Photonic Integrated Circuit Development

The PICs considered in this thesis explore the integration of waveguide couplers, SOAs and multiple lasers to form complex photonic devices. The success of these devices require careful analysis and design of each individual subcomponent, with particular attention to how they can be produced on a common material platform. These components are developed in detail in this section, before their integration is examined later in the chapter.

5.3.1 Material Structure

The fabrication of the devices considered in this thesis was based on a monolithic process with a single epitaxial growth step. For the lasers to lase, it was essential that the substrate was based on active material, however, this posed a significant problem for the passive devices. Due to having an identical bandgap to that of the laser sections, high absorption losses would be present in the passive waveguides. To tackle this problem, the passive structures were treated as *pseudo-passive* which could be electrically biased. Driving these sections electrically produced sufficient optical gain to overcome the inherent material losses caused by absorption. The advantage of such a solution was that each waveguide section of the device could not only be biased to reduce losses, but also driven to produce extra optical gain of any light propagating through it. In this way, each waveguide on the integrated devices could be treated as a simple waveguide or semi-conductor optical amplifier (SOA) where the gain could be controlled.

Table 5.1: Material Structure.

Layer	Material	x	y	Thickness (μm)	Type
15	GaIn(x)As	0.53	-	0.200	P
14	GaIn(x)AsP	0.71	0.62	0.050	P
13	InP	-	-	1.600	P
12	GaIn(x)AsP	0.85	0.33	0.020	P
11	InP	-	-	0.050	P
10	Al(x)GaIn(y)As	0.9	0.53	0.060	P
9	Al(x)GaIn(y)As	0.72	0.53	0.060	U/D
8	Al(x)GaIn(y)As	0.44	0.49	0.010	U/D
7×5	Al(x)GaIn(y)As	0.24	0.71	0.060	U/D
6×5	Al(x)GaIn(y)As	0.44	0.49	0.010	U/D
5	Al(x)GaIn(y)As	0.9	0.53	0.060	U/D
4	Al(x)GaIn(y)As	0.9	0.53	0.060	N
3	Al(x)GaIn(y)As	0.86	0.53	0.010	N
2	InP	-	-	0.500	N
1	InP	-	-	0.300	N

The material structure chosen for the integrated devices considered in this thesis was based on a standard off the shelf laser material from a commercial vendor (IQE). This material structure was compatible with previous SFP laser designs fabricated within IPG at Tyndall, which had been shown to offer high yield and excellent performance. The material consisted of five strained AlInGaAs quantum wells with a 1550 nm bandgap, which were grown on an N doped Indium Phosphide substrate. The exact layer structure is shown in Table 5.1. Layer 12 was used as an etch-stop layer during

selective etching of the InP in layer 13. This allowed the formation of a rib waveguide structure with rib height of 1.85 µm. The N doped layers 3 and 4, and P doped layer 10, were used as separate confinement heterostructure (SCH) layers allowing for variations of the mode position and optical confinement.

5.3.2 Waveguide Structure

The waveguides of the integrated devices considered in this thesis were based on a rib waveguide structure, as shown in Figure 5.3.

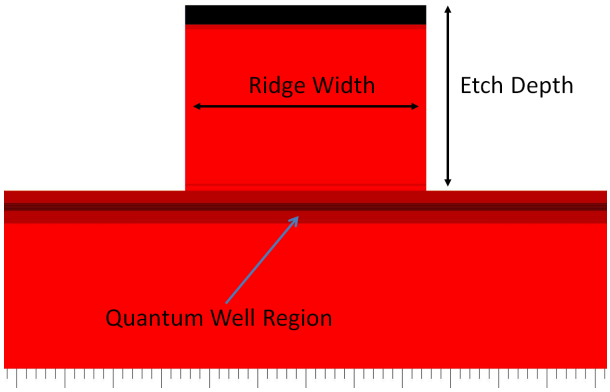

Figure 5.3: Waveguide structure of the integrated devices.

The waveguide had an etch depth of 1.85 µm to just above the quantum well region of the waveguide. This rib structure was compatible with a known SFP laser design and slots etched to this depth provided sufficient reflectance to form a slotted mirror. The width of the rib was chosen to be 2.5 µm wide, which provided good lateral confinement of the waveguide modes. The waveguide was modelled using the Scalar Finite Element Method (SFEM) mode solver described earlier in this thesis, where the TE mode solutions were calculated. Two waveguide modes were found to be supported in the structure and are plotted in Figures 5.4a and 5.4b.

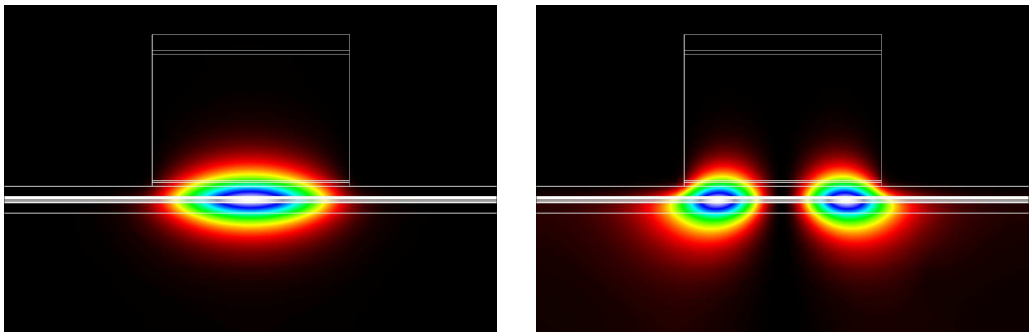

(a) (b)

Figure 5.4: Supported modes in waveguide structure as calculated from the SFEM mode solver.

Although the waveguide had the potential to support multiple modes, the higher order modes would never be excited in a device due the ability of the MMI coupler to act as a single mode filter, as discussed in chapter 3. With the waveguide structure now in place, attention was turned to the coupler design for use in the final integrated devices.

5.3.3 Multimode Interference Coupler Design

The rib waveguide shown in Figure 5.3 was analysed using the effective index method (EIM), as discussed in chapter 2. The MMI coupler C++ code and optimisation routines developed in chapter 3 were then applied to the waveguide structure to design MMI couplers. The MMIs required for this thesis were limited to 1×2 and 1×3 variations. These allowed coupled integrated devices to be considered where one laser was integrated on the input side an MMI, with either two or three lasers integrated on the output. The MMIs for such systems were not significantly restricted by size, which allowed conservative MMI designs to be developed. This offered more robust MMIs that were less sensitive to fabrication errors. As shown in chapter 3, the sensitivity of MMIs to fabrication errors can be reduced by increasing the width of the waveguide leading into the MMI structure. For the MMIs considered here, it was found that increasing this width from the nominal waveguide dimension of 2.5 µm to 3.5 µm would offer a sufficient improvement to the fabrication tolerances of the device. Increasing the waveguide width in this way required the use of a linear taper. This will be discussed further in the next section.

The MMI modelling code was applied to the rib waveguide structure with an input waveguide width of 3.5 µm. The optimum MMI parameters for 1×2 and 1×3 couplers were determined and are summarised in Table 5.2.

Table 5.2: Design Parameters for MMI.

MMI Type	Input Width (µm)	MMI Width (µm)	MMI Length (µm)
1×2 Optimum	3.5	12.5	195
1×3 Optimum	3.5	22.0	376

The full TE electric field distributions were also simulated for each MMI, with the field of the optimised 1×2 MMI shown in Figure 5.5a and the field of the optimised 1×3 MMI shown in Figure 5.5b. In both cases the simulations suggest that the MMI designs are correct, with two and three output modes respectively distributed on the MMI output field.

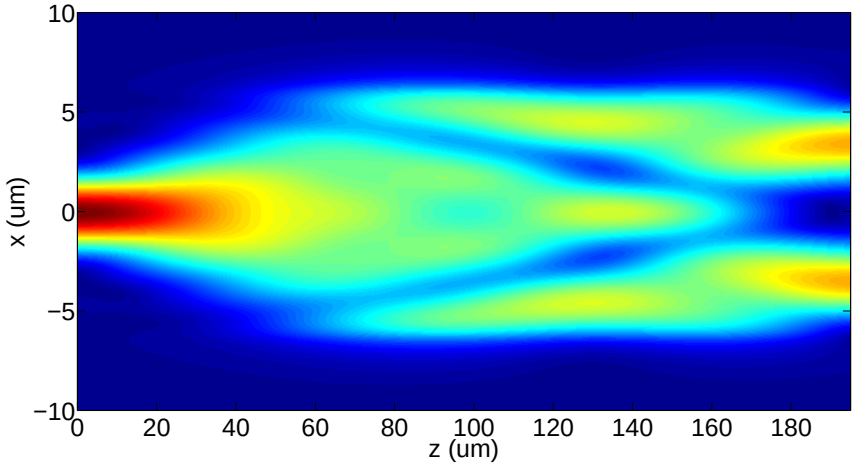

(a) Simulated field of optimised 1×2 MMI as designed using the MMI optimisation code.

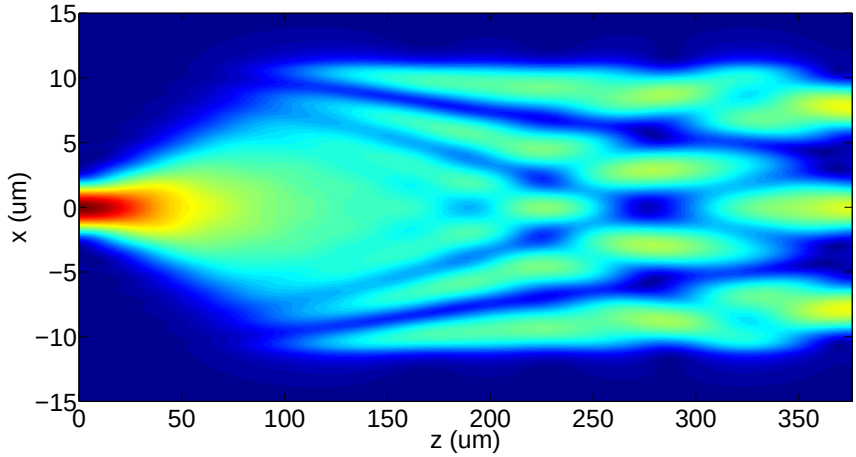

(b) Simulated field of optimised 1×3 MMI as designed using the MMI optimisation code.

Figure 5.5: Optimised MMI designs.

The outputs of the optimally designed MMIs were typically <10 µm apart, which were not compatible with any commercial fiber array blocks that could be used to couple the light from each MMI arm simultaneously. This was an important consideration when designing the devices for experimental testing. By using linear curvature S-Bends for extension this separation was increased to a standard 250 µm spacing.

5.3.4 Waveguide Taper Design

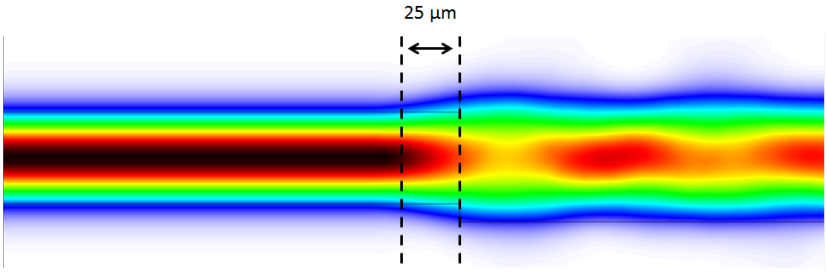

(a) 25 µm tapered region.

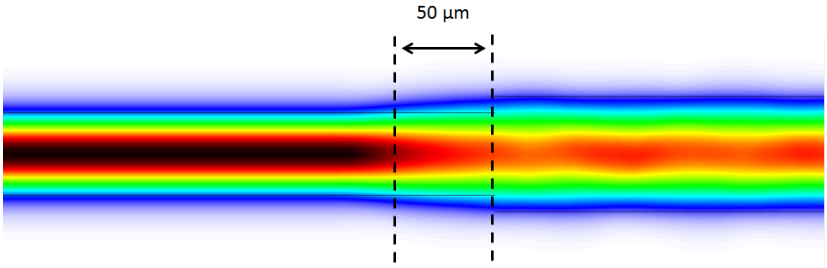

(b) 50 µm tapered region.

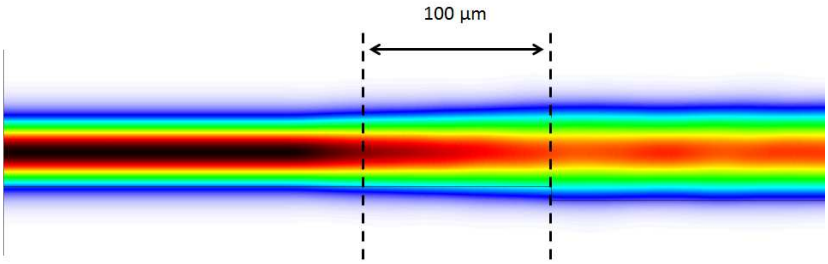

(c) 100 µm tapered region.

Figure 5.6: Simulation of linear tapers as waveguide width was increased from 2.5 µm to 3.5 µm.

To improve the fabrication tolerance of the designed MMI couplers, a linear taper was used to increase their input waveguide width from 2.5 µm to 3.5 µm. The linear taper provided a gradual expansion of the waveguide mode as it transitioned from a 2.5 µm to 3.5 µm waveguide ridge width. The correct taper length was determined by modelling the waveguide using a one dimensional beam propagation program. This ensured that a length could be found which offered low excess loss and did not excite any higher

order modes. Three different taper lengths were considered, these were 25 µm, 50 µm and 100 µm. The simulation results for these tapers are shown in Figures 5.6a - 5.6c.

The results show that for taper lengths of 25 µm - 50 µm, some higher order modes are excited as light transitions from a 2.5 µm to 3.5 µm waveguide. The field distribution shows a beating between these modes as light propagates in the taper. For a 100 µm long taper, the mode transitions smoothly from the narrow to wider waveguide, with a uniform field distribution indicating adiabatic expansion of the mode. As a result, a 100 µm long taper was chosen to taper waveguides from 2.5 µm to 3.5 µm for use in MMIs.

5.3.5 Lasers for device integration

The proposed integrated device designs used SFP lasers due to their tunability, narrow linewidth and compatibility with single growth monolithic integration. In addition to these lasers, simple Fabry Pérot (FP) lasers were also used as test devices for characterisation. In this section, the operation of the chosen SFP and FP designs will be discussed.

5.3.5.1 Fabry Pérot Lasers

The schematic outline of a Fabry Pérot (FP) laser is shown in Figure 5.7.

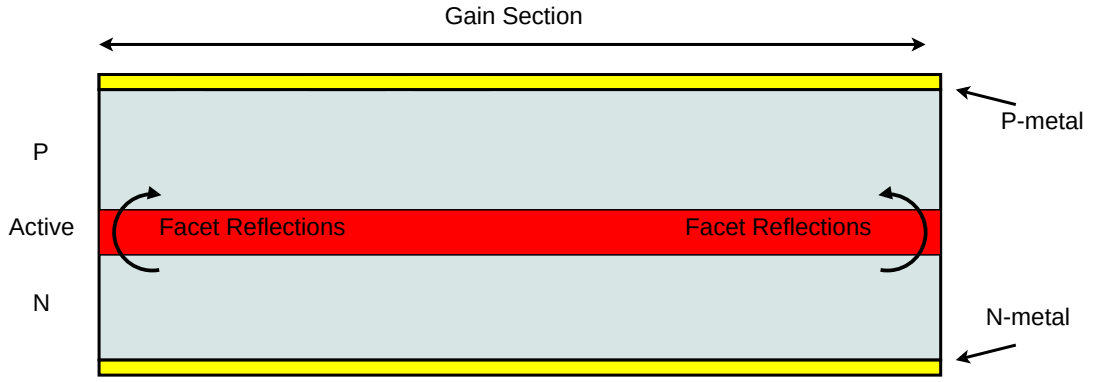

Figure 5.7: A single slot

A ridge waveguide structure is cleaved at a specific length, where a cavity is formed due to reflections from the cleaved facets. The FP lasers can be electrically driven to provide gain by applying a bias across the junction formed between deposited metal on top of the FP ridges (the P side) and deposited metal on the back of the FP (the N side). Based on the material structure given previously in Table 5.1, FP lasers with waveguide widths of 1.5 µm, 2.5 µm and 3.5 µm were designed. These test FP lasers were cleaved to a cavity length of 2500 µm. The output from the FP laser could be

examined at either side of the device by coupling a lensed fibre to the ridge waveguide. Using an Optical Spectrum Analyzer (OSA), the characteristics of the FP laser could then be examined. Having these simple FP structures on chip, provided a means of systematically determining that each aspect of the more complicated devices would work in isolation. If the FP devices were unable to lase, then this would suggest material structure or device fabrication problems which may require reprocessing.

5.3.5.2 Slotted Fabry Pérot Lasers

The photonic devices designed in this thesis were integrated with SFP lasers which were comprised of two different sections. A series of etched slots formed a reflection grating referred to as the *mirror section*, while a long waveguide section referred to as the *gain section*, provided optical gain and formed an optical cavity between the mirror section and the cleaved facet. For convenience this laser was referred to as a Single Facet SFP (SF-SFP) laser, and is shown schematically in Figure 5.8.

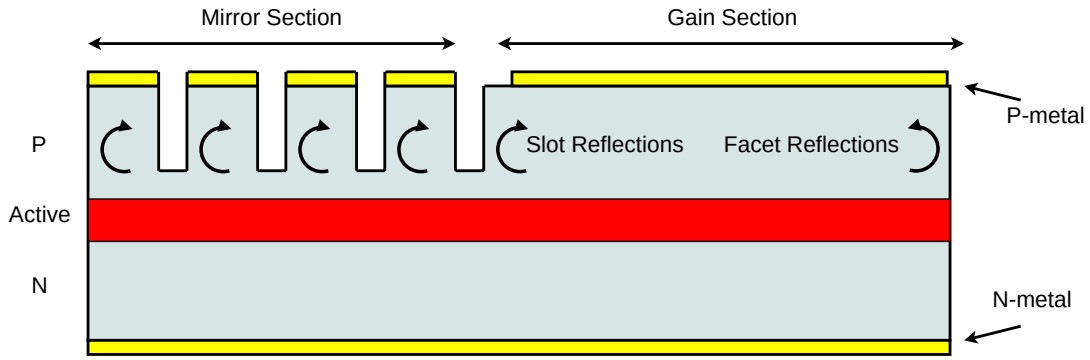

Figure 5.8: A schematic of a single facet slotted Fabry Pérot laser.

Feedback was provided by reflections between the etched slots and cleaved facet of the device. Single mode operation of the laser occurs when the reflection spectra from each section of the device overlap causing a strong resonance at one particular wavelength. Metal was deposited on the ridge of the gain and mirror sections of the device (P-metal) which allowed an electrical bias to be applied across these section to a common N ground metal on the backside of the full device (N-metal). Through current injection, the lasing wavelength of an SFP can be tuned by varying the current applied to each section of the device. This varies the resonance condition in each region and causes the main lasing mode of the laser to shift.

Along with the cleaved facet, optical feedback in the SFP was provided by the slotted mirror section. This mirror section is a key component in using SFPs in integrated devices; since the slotted region is essentially a waveguide which could easily be extended to couple to other devices without the need for a secondary cleaved facet. A single facet SFP laser can be extended to a fully *facetless* SFP laser by removing the cleaved

facet and replacing it with a second slotted mirror section. A drawback of this design being that the feedback from slotted mirrors is typically smaller than that of a cleaved facet due to the low reflectivities from each slot.

Since variations to the laser structure were beyond the scope of this work, a single facet SFP laser design was chosen which was previously investigated by the IPG at Tyndall and offered good optical performance and high yield. This laser had a gain section length of 800 µm and a mirror section consisting of 7 slots. These slots were spaced 109 µm apart with a slot width of 0.88 µm. The slots were etched 1.85 µm into the waveguide structure, which provided sufficient total reflectance to act as a mirror. The design parameters of the single facet SFP laser are summarized in Table 5.3.

Table 5.3: Single facet slotted Fabry Pérot laser design parameters.

Gain (µm)	Slot Spacing (µm)	Slot Width (µm)	Slot Depth (µm)	# Slot
800	109	0.88	1.85	7

The etched slots in the waveguide region were defined as "T" shape structures. This can best be seen in Figures 5.9a and 5.9b which shows SEM images these T-Bar slots on a fabricated SFP laser.

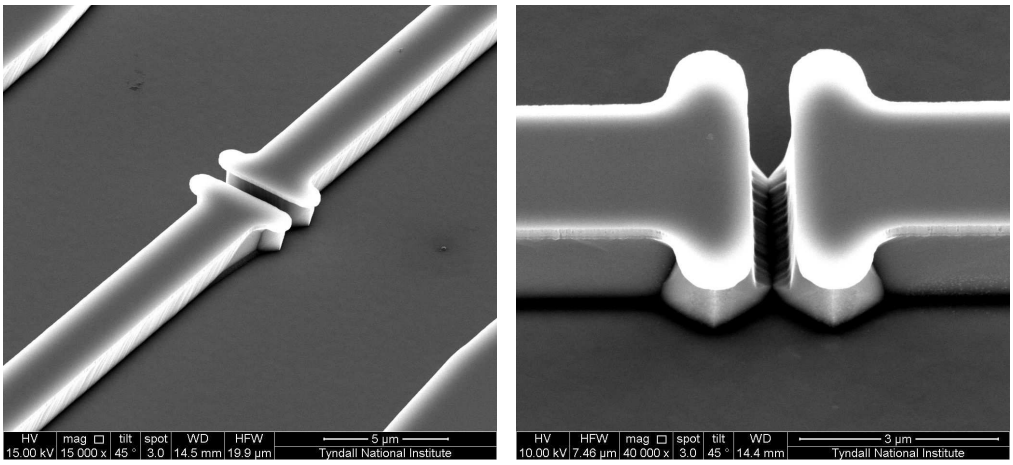

(a) SEM of ridge waveguide during fabrication showing T-Bar slot.

(b) SEM of T-Bar slot showing 0.88 µm slot width.

Figure 5.9: SEMs of T-Bar slots.

The role of the T-Bars was to aid during the lithographical process. If standard slots were used, rounding of the corners would be expected. This can significantly impact the waveguide shape, and thereby the optical mode output and reflection spectrum formed. Using T-bars, this rounding feature still exits, but can now be extended away from the center of the waveguide where its effect on the propagating light is negligible.

5.3.6 Device Fabrication Steps

The devices discussed in this section were designed for single epitaxial growth, monolithically integrated photonic circuits. Although the fabrication process did not involve any regrowth of the epitaxial material, an additional metal layer was required to form the contacts on the lasers and pseudo-passive waveguide sections to allow electrical biasing. Only specific regions on each device needed electrical biasing. To define these areas, an insulating layer, in this case an *oxide* layer, was deposited everywhere on the device and then removed at the precise locations current injection was required. After this, metal could be deposited to form large contact pads for probing which allowed localised current injection. The general steps required to fabricate such a device are schematically shown in Figure 5.10 and described below.

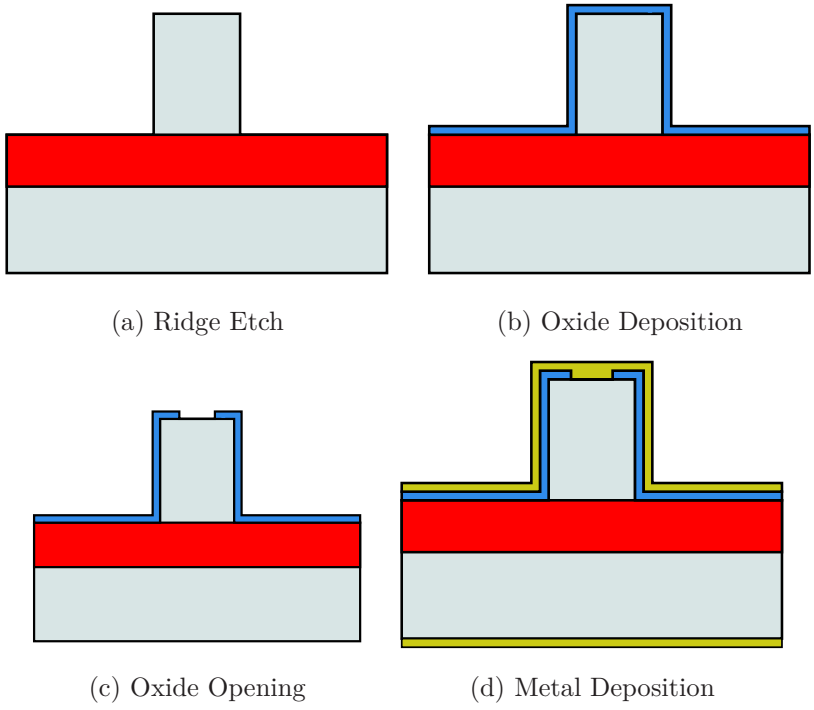

(a) Ridge Etch (b) Oxide Deposition

(c) Oxide Opening (d) Metal Deposition

Figure 5.10: Lithographical steps required to fabricate the integrated devices.

- **Ridge Etch:** The waveguide structure of the device was produced by etching down into the upper cladding region to form a free standing ridge. A hard mask was used to protect the ridge structure during etching and subsequent removal.
- **Oxide Deposition:** A blanket oxide was deposited over the entire etched substrate for passivation.
- **Oxide Opening:** The oxide was selectively opened at particular regions where electrical biasing was required on the device.

- **Metal Deposition:** Metal was deposited on the P and N sides of the device to create contact pads which allow for electrical biasing.

5.4 Design/Layout of Photonic Integrated Devices

The photonic devices considered in this thesis required three main lithographical steps during fabrication. These were the waveguide etch (ridge and slots), oxide opening and metal deposition to form contact pads. These layers defined each device and required a three level lithographical mask for fabrication. A summary of the typical steps required to fabricate a ridge waveguide using a single mask layer is discussed in Appendix D. Creating a three level mask is a time consuming process, particularly when designing a large number of prototype devices. To simplify this procedure, custom software was developed within the IPG at Tyndall to allow mask structures to be defined mathematically. The functionality and use of the software will be described in the following section.

5.4.1 PICDraw

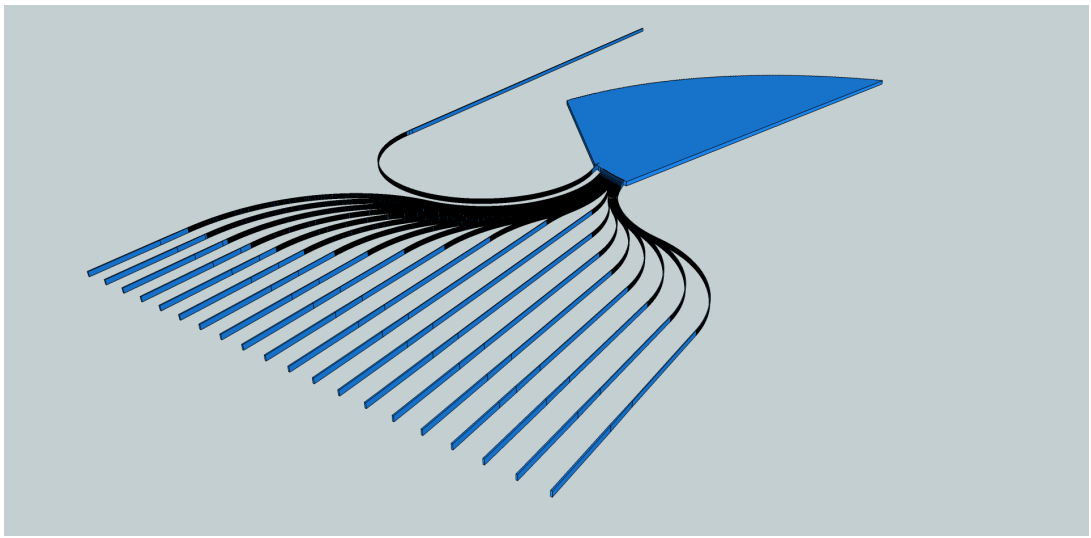

Figure 5.11: Example of an echelle grating as defined by PICDraw software.

The software tool developed previously in the IPG at Tyndall for mask design is referred to as *PICDraw*, and offers a means of generating mask layout files completely mathematically. There are multiple advantages to such an implementation, with perhaps the main benefit arising from the efficiency at which alterations to complex layouts can be made. With each device defined mathematically, any changes to a bend radius, waveguide width, waveguide length or other such device design parameter; can automatically update the entire layout with no extra designing or alterations from the designer. An

example of a complex Echelle grating, which was defined entirely mathematically, produced using PICDraw is shown in Figure 5.11. The advantages of PICDraw become apparent when developing prototype PICs for research purposes, where designs and structures can change rapidly during mask development.

In order to systematically examine monolithically integrated PICs, the existing PICDraw software had to be developed further to incorporate the design and drawing of MMI couplers. A data type known as an "MMI Structure" was formed in PICDraw, which took the waveguide and MMI properties of the device to be drawn as variables. This was combined with the MMI optimisation routines described in chapter 3, allowing for MMIs to be designed, optimised and mathematically defined on a layout file. This greatly simplified the design procedure and allowed all the MMIs on a PIC to be re-optimised without any change to the operational wavelength, input waveguide width or even the material structure chosen for the device. An example of this is shown in Figure 5.12, where a 1×2 MMI was generated and optimised in the PICDraw software using basic waveguide inputs. Using this, and other advanced features of PICDraw, the process of developing a mask layout was greatly simplified. Allowing attention to mainly be focused on the design of actual devices and overall structure of the PIC and individual integrated devices.

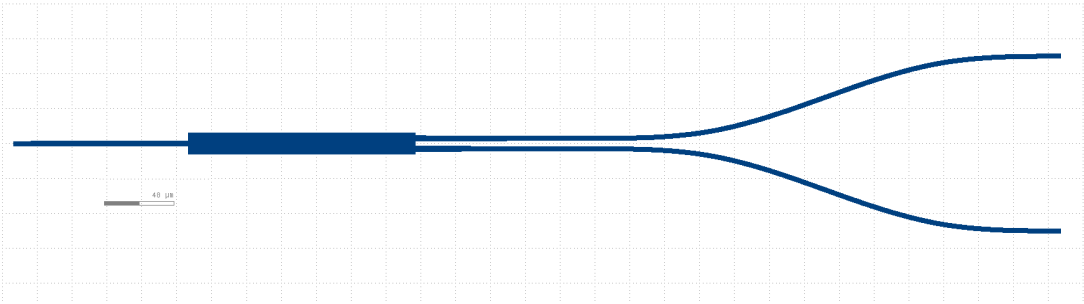

Figure 5.12: Example on an MMI coupler as generated from PICDraw software.

Next in this chapter, the lithographical layout of the designed integrated devices are examined. These devices require multiple different layers to form the waveguide and metal structures, each of which is designed using the PICDraw software. The individual MMI and SFP layout is first considered separately, after which they are then used to form the layout for more complex devices with integrated components.

5.4.2 Layout of MMIs and SOAs

The MMI couplers used in the integrated devices were comprised of a wide MMI waveguide region plus additional waveguide sections on the input and output sides, as can be seen in Figure 5.12. Both the MMI and waveguide sections were absorbing at the operational wavelength of the integrated lasers due to bandgap of the material. To solve

this problem, the passive sections were electrically biased to provide sufficient gain to overcome the inherent losses present. Metal was deposited over the ridge waveguide structure and then routed to large metal contact pads for DC probing. The input and output waveguides were treated as common sections which could be biased collectively via one contact pad. This was considered to be a large Semiconductor Optical Amplifier (SOA) section, which could be used to amplify the optical signal through sufficient forward biasing. The MMI region itself was biased with its own contact pad to allow independent biasing from that of the waveguides. The MMI also had the potential to act as an SOA, and amplify the optical signal. However, applying large forward biases to the MMI could potentially shift its operational wavelength away from the designed value of 1550 nm and reduce the power splitting performance. To ensure this was not the case during operation, the MMI was only biased until it had sufficient gain to overcome the material absorption effects. The metal and waveguide layers used to define a lithographical mask for such an MMI and waveguide configuration are shown in Figure 5.13.

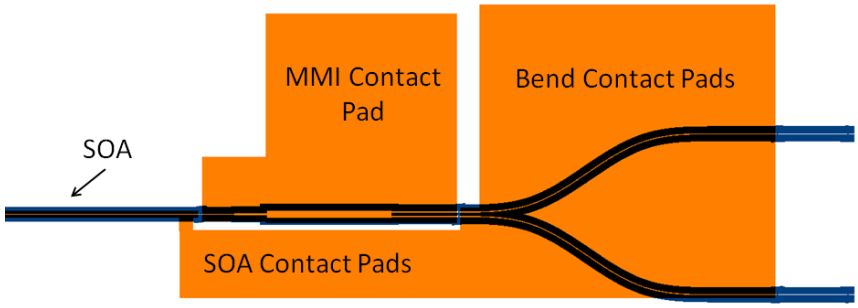

Figure 5.13: 1×2 MMI structure as defined on the PIC mask. The Figure shows MMI region contact pad to drive MMI section to transparency along with the common contact for MMI output bends and short SOA waveguide interconnect between SFP laser and MMI region.

Metal (Orange) was deposited over the entire MMI region and was then connected to a large contact pad directly above it. This allowed for direct DC probing of the MMI without applying probes to the MMI itself, which could affect performance if the probe went through the metal and into the ridge structure. Outside of the MMI region, metal is deposited along the length of the waveguides entering and exiting the MMI and then onto the curved output waveguides which increase the separation between the outputs to 250 µm. These waveguide regions were treated as one common section which could be biased from the large contact pad placed above the output waveguide bends. Having one contact for this entire waveguide SOA section reduced the number of probes required during experimental testing.

5.4.3 Layout of Slotted Fabry Pérot Lasers

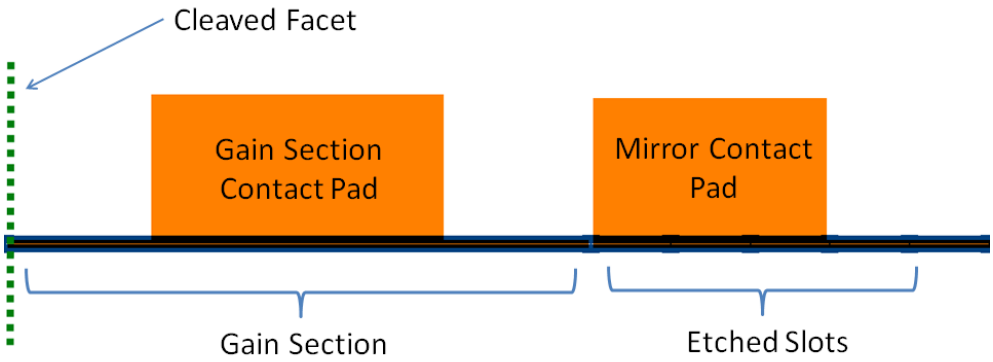

Figure 5.14: Layout of SF-SFP laser as defined on the PIC mask. Green dashed line indicates the cleaved facet. Reflections from cleaved faceted and slots in the mirror section are also indicated.

The lasers chosen for the integrated devices considered in this thesis were based on the slotted Fabry Pérot laser designs discussed earlier in this chapter. The layout of the ridge and metal layers of an SFP laser os shown in Figure 5.14, where the cleave plane is shown in green and the slotted section is indicated for clarity. The deposited metal is shown in orange. The gain section is shown clearly on the left hand side, where a large contact pad can be used for biasing. On the other side of the device, the mirror region which consists of multiple etched slots can be observed, along with a second electrical contact pad.

5.4.4 Layout of Integrated Devices

The lithographical layouts of the MMI, SOA and laser devices discussed in the previous section are next used to develop full mask layouts of the main integrated devices explored in this thesis. The layout of these devices are now considered in detail, with their operation and role in more complex integrated devices examined.

5.4.4.1 Integrated SFP Laser Power Splitter

The first device investigated was an on chip optical power splitter with integrated source. The device was formed by integrating a SF-SFP laser on the input side of either a 1×2 or 1×3 MMI, with SOA waveguides acting as interconnects. The layout of the 1×2 and 1×3 device variations are shown in Figures 5.15a and 5.15b respectively. Multiple contacts pads are present on each design variation. These allow each element (SFP, MMI, SOA) of the integrated device to be controlled independently.

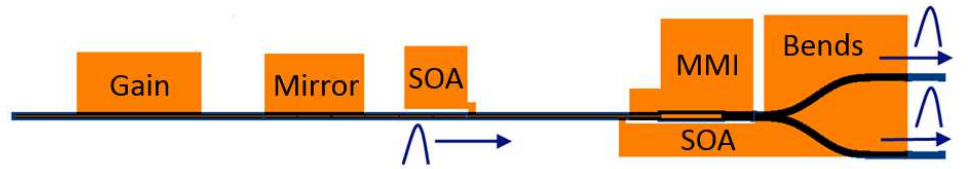

(a)

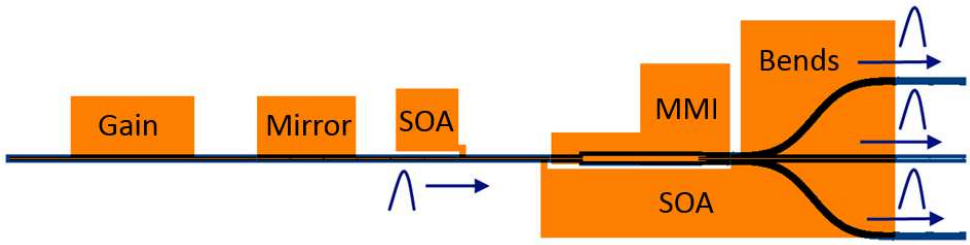

(b)

Figure 5.15: Layout of an integrated device which combines an SF-SFP laser with an SOA and a 1×2 or 1×3 MMI coupler.

The device operates by first biasing the SFP laser until it has a stable power and wavelength output, which can be observed using an OSA at the cleaved facet side of the device. By sufficient biasing of the SOA contact pad, the section linking the SFP and MMI becomes transparent, allowing light to couple between both sections. In the MMI region, the light from the SFP is split into two or three equally spaced outputs depending on the MMI type. This light is in turn coupled to the output SOA waveguides forming a power splitter. Although a relatively simple device, this was considered one of the main building blocks of developing more complex monolithically integrated devices which use SFP lasers. The need for an on chip power splitter has wide spread applications in almost any integrated device; be it in splitting optical signals for phase delay measurements or diagnostic purposes where splitters can be used as taps to monitor outputs. Furthermore, the power of the SFP can be determined on chip by treating either the MMI or the SOA section as a photodetector. Reverse biasing of either section allows the SFP optical power to be calculated from the measured photocurrent. This allows for a quick and accurate measurement of the SFP power without the need for external coupling to lensed fibre. The testing of this device will be examined in more detail in chapter 6.

An important consideration when designing such an integrated device is to ensure that each section of the device was electrically isolated from the other sections. This was done by etching slots into the ridge waveguides between each component on the device. Etching such slots provides optical feedback in the device, which potentially set up

further unwanted optical cavities. To limit the impact of these isolation slots on the optical performance of the devices, the slots were at an angle of $\theta = 7°$ relative to the waveguide structure. The angled slots used to isolate the output section of the 1×3 MMI based device shown in Figure 5.15b, is shown schematically from the mask layout file in Figure 5.16a and experimentally from a SEM image of a fabricated device in Figure 5.16b.

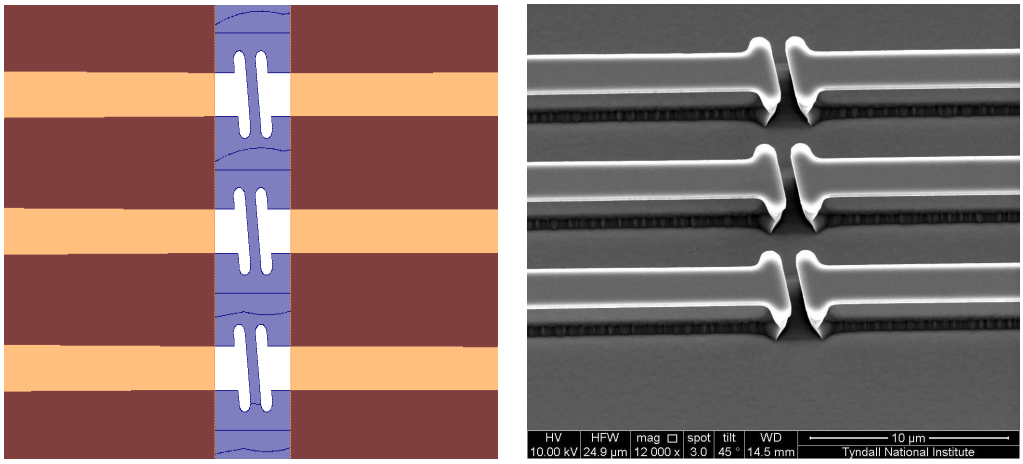

(a) Schematic from lithographical mask. (b) SEM image from fabricated device.

Figure 5.16: Optical and electrical solation slots.

5.4.4.2 Integrated System of Mutually Coupled SFP Lasers

The most complex integrated device designed involves a system of mutually coupled SFP lasers. Identical SFP lasers were integrated on all ports of both 1×2 and 1×3 MMIs, and were connected via the same SOA waveguide interconnects as before. The devices as defined on the lithographical mask are shown in Figures 5.17a and 5.17b, where the metal contact pads, ridge metal and ridge waveguide structure can be seen.

Each SFP laser has the potential to be operated independently through biasing of their individual gain and mirror sections. A mutually coupled system could be formed by biasing of the waveguide and MMI sections to transparency. This allowed light from the lasers on the input side of the MMIs in Figure 5.17 to couple to the output lasers, and vice versa. This is indicated in Figures 5.17a and 5.17b by the modal outputs of the SFPs which are coupled via the MMI. Mutually coupled laser systems have shown to be a rich area of research in recent times and will be discussed further in chapter 6. Of particular interest in this work, is the investigation of optical injection between multiple lasers on the same device which have different optical power and wavelength outputs. This can be done by tuning the SF-SFP outputs using electrical bias across their gain and mirror section, while varying the SOA/MMI section bias can provide a means of controlling the coupling between input and output SF-SFP lasers. This creates

a versatile device which allows for some highly interesting on chip laser dynamics to be investigated, as will be shown in the following chapters.

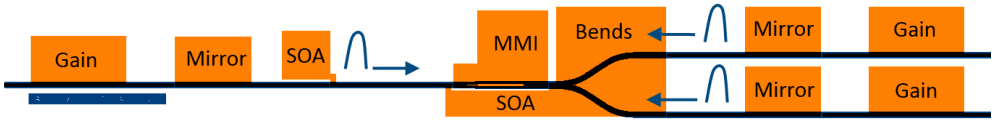

(a)

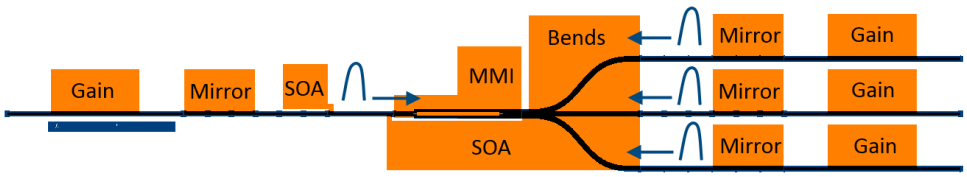

(b)

Figure 5.17: Layout of an integrated device which combines an SF-SFP laser with an SOA and a 1×2 or 1×3 MMI coupler with further SF-SFP lasers integrated at MMI outputs.

5.4.5 Full Lithographical Mask Layout

The layout of the integrated devices was described in the previous section, where the metal and ridge layers of each structure was defined. How these devices can be realised when developing a quarter of a two inch wafer mask was then examined. This was done by using the PICDraw software, where the integrated devices and test structures were placed into blocks of similar devices. Laying out the devices in this way simplified cleaving of the devices (post fabrication) and also aided in experimental testing, since several devices could be tested on a single chip. Multiples of these blocks were placed on the full wafer layout, which ensured a sufficient number of devices for testing. The first block of test structure devices is shown in Figure 5.18.

This block contained the test Fabry Pérot lasers, along with variations of the integrated power splitter device discussed in Section 5.4.4.1. A key feature of this test block was the addition of cleave marks which allowed for individual sections of the device to be cleaved. These are shown in Figure 5.18 as *crosses*. A close up view of these cleave marks are shown in Figure 5.19. These marks are used to indicate the position on the crystal plane where the device is to be cleaved. Strategic placement of these cleave marks offered the potential to investigate sub-devices independently; these included the MMI/SOA sections, shorter FP lasers or the SFP laser in isolation.

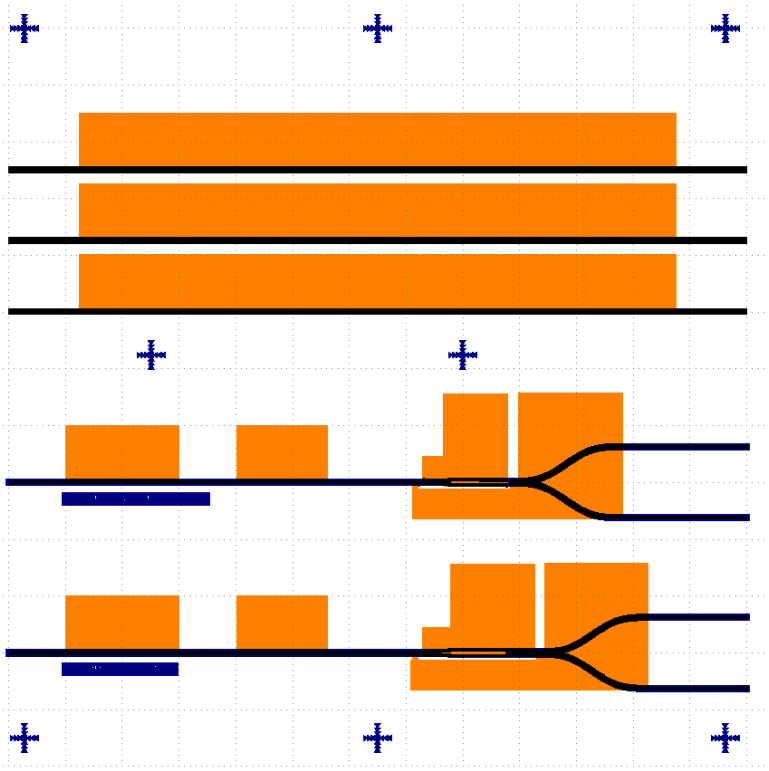

Figure 5.18: Block of "Test Structure Devices" which can be cleaved and tested together experimentally. Consists of FP lasers, SFP lasers and test MMI structures.

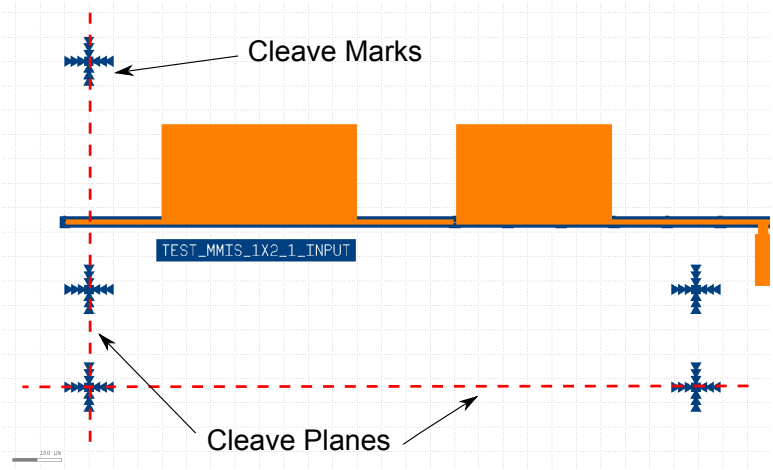

Figure 5.19: Close up view of cleave marks which indicate the position of cleave planes on devices.

The second block of devices contained the more complex integrated circuits. This is shown in Figure 5.20, where the devices with mutually coupled SFP lasers are placed together on one large PIC. Two identical versions of the 1×2 and 1×3 MMI based devices were grouped together for convenience when testing. This block of devices also had strategically placed cleave marks, which allowed for other variations of the device to be considered. For instance, the input SFP lasers could be cleaved off leaving a

series of devices where light from a tunable source could be directly coupled into the MMIs and output lasers.

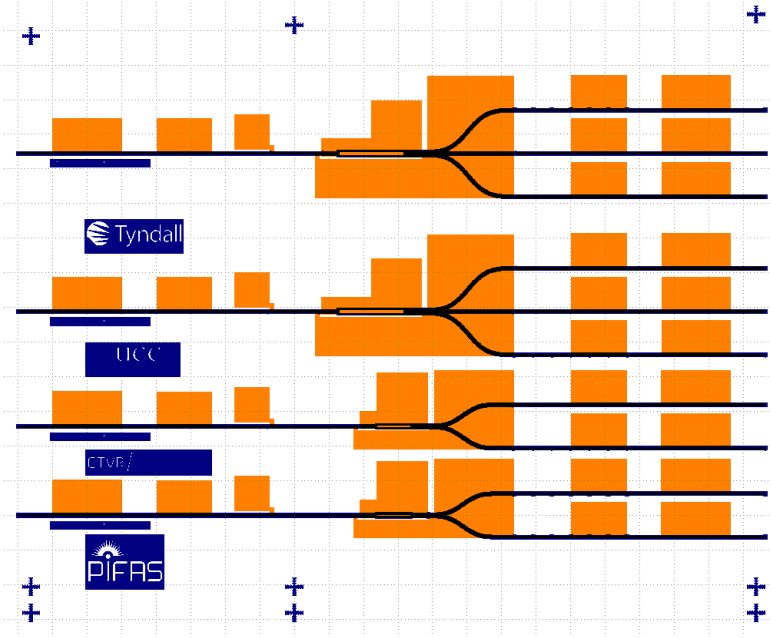

Figure 5.20: Block of integrated SFP devices. Consists of single facet SFP lasers integrated with SOAs, MMIs and output SFP lasers. Output SFP lasers can be cleaved off to investigate integration of SFPs with 1×2 and 1×3 power splitters.

The final block of devices consisted of integrated circuits which were based on fully facetless lasers rather than the single facet lasers used in the devices shown in Figures 5.18 and 5.20. Theses devices are shown in Figure 5.21.

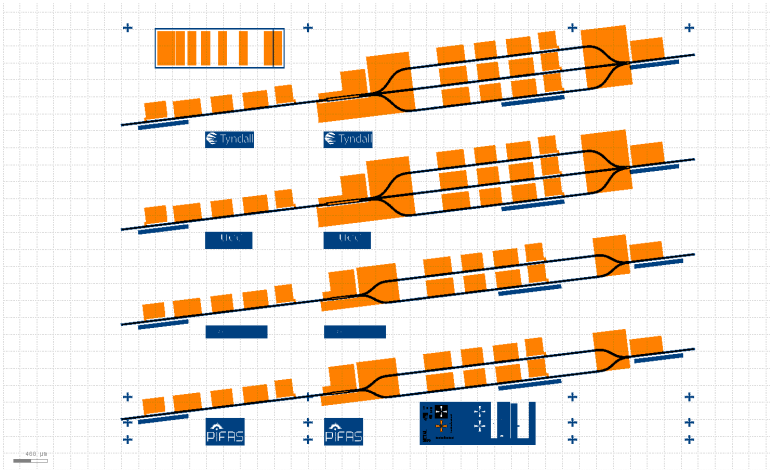

Figure 5.21: Block of integrated SFP devices. Consists of single facet SFP lasers integrated with SOAs, MMIs and output SFP lasers. Output SFP lasers can be cleaved off to investigate integration of SFPs with 1×2 and 1×3 power splitters.

The facetless lasers were mutually coupled through an MMI/SOA region as before, with the addition of a star coupler on the output of the device to couple the signals to one waveguide. Two identical versions of the 1×2 and 1×3 MMI based devices were grouped together for convenience when testing. Due to their added complexity and extra requirements for testing (a probe card with custom probe layouts), these devices were not tested as part of the main body of this thesis.

With each block of devices assembled as in Figures 5.18, 5.20 and 5.21, the full mask was structured by placing these blocks strategically around a quarter inch wafer mask to maximise the device yield. Cleave marks were placed between devices to allow for individual bars or rows of devices to be cleaved separately. The layout of the full finalised mask design is shown in Figure 5.22.

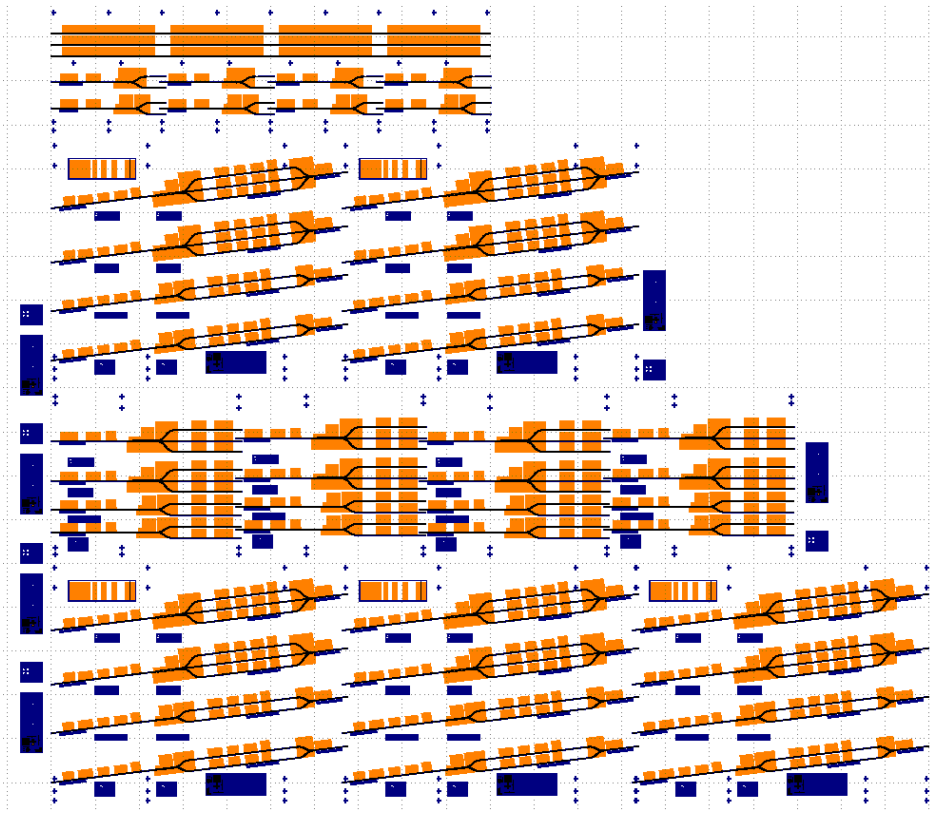

Figure 5.22: Photonic Integrated Circuit.

5.5 Conclusions

This chapter investigated the design of photonic integrated circuits for use in on-chip coherent signal generation. A suitable laser was chosen for single growth monolithic integration with other devices, where its design and operation was then described in detail. Based on the material structure required for this laser, waveguides and MMI couplers were modelled and optimised using the design routines developed in chapters

2 and 3. The steps required to fabricate these devices were discussed, with particular attention paid to the lithographical layers required to produce each device. With this in place, attention was turned to the mask layouts of the full integrated devices which consisted of lasers integrated with SOAs and MMI couplers. This culminated in the design of the integrated circuits shown in Figures 5.15 and 5.17, which allowed an integrated power splitter and system of mutually coupled lasers to be examined. A lithographical mask was produced which allowed these devices to be fabricated on a wafer. The fabrication of the designed devices using this mask was carried out by members within the IPG at Tyndall, and was not part of the research performed during this thesis. In the chapters that follow, these devices are characterised and investigated experimentally.

Chapter 6

Photonic Integrated Circuit Characterisation and Testing

6.1 Introduction

This chapter covers the initial experimental testing of the devices designed in the chapter 5. The test setup for such devices is examined, with attention paid to how complex PICs which require a large number of probe manipulators can be tested. Of primary interest in this chapter was the characterisation of the simple Fabry Pérot (FP) and Slotted Fabry Pérot (SFP) lasers. Their performance was investigated thoroughly to better understand their operation within integrated devices. Attention was then turned to investigating the first fully monolithically integrated device designed in this thesis. The device comprised of an SFP laser integrated at the input of a 1×2 MMI, which had SOA waveguide interconnects and allowed power from the output ports of the MMI to be decoupled via lensed fibre. This formed an integrated power splitter which was the building block of the more complex devices designed in chapter 5. This device was an essential component of the main integrated device investigated in this thesis, which is examined in chapter 7.

6.2 Fabricated Devices

The devices designed on the lithographical mask created in chapter 5 were fabricated on a quarter inch wafer using a 3 step lithographic process. Due to the nature and complexities of the processing, this fabrication was performed by members within the group and was not part of the work carried out within this Thesis. Although to better understand the process of device fabrication, a relatively simple 650 nm ridge waveguide laser was fabricated during the course of this thesis. The process steps required make

this laser are shown in Appendix E. The fabricated PIC which is comprised of all the integrated devices before they were cleaved into smaller PICs, is shown in Figure 6.1.

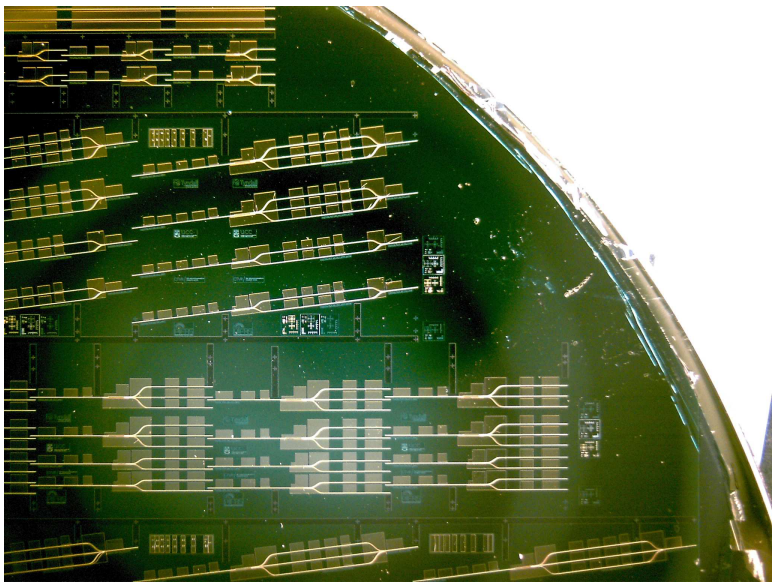

Figure 6.1: Fabricated PIC on $\frac{1}{4}$ inch wafer prior to any cleaving of devices.

The PIC was cleaved into the blocks of devices, as described in chapter 5, which allowed multiple different structures and components to be looked at on the one chip during experimental testing. These blocks could in turn be cleaved again to look at individual aspects of particular devices, or to shorten structures themselves. This was explicitly catered for when designing the test Fabry Pérot lasers on the test structures block of devices, which were typically 2.5 mm but could be cleaved to any required length using cleave marks placed along their length. The cleaved block of fabricated tests structures are shown in Figure 6.2.

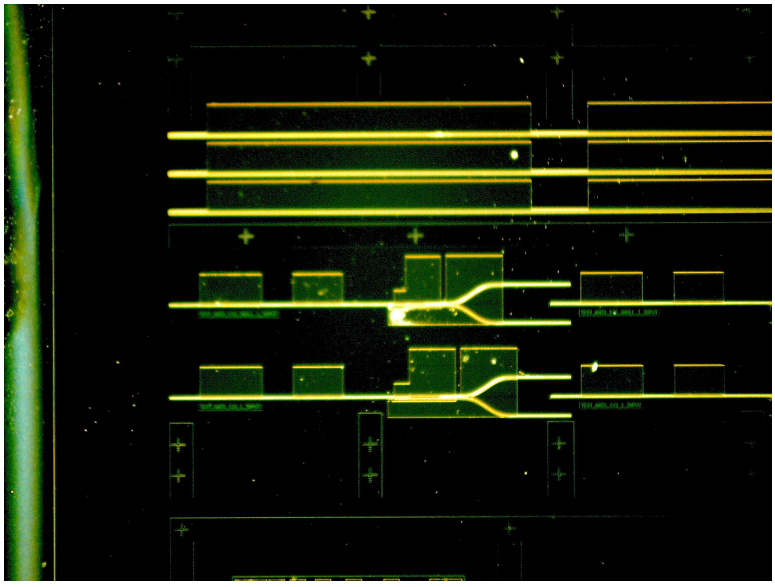

Figure 6.2: Test structure devices prior to cleaving.

The most complex device on the PIC was the block of devices with mutually coupled single facet Fabry Pérot lasers. These devices allowed for the integration of multiple different components on chip to be examined. These fabricated devices are shown in Figure 6.3, where the 1×2 and 1×3 variations can clearly be seen.

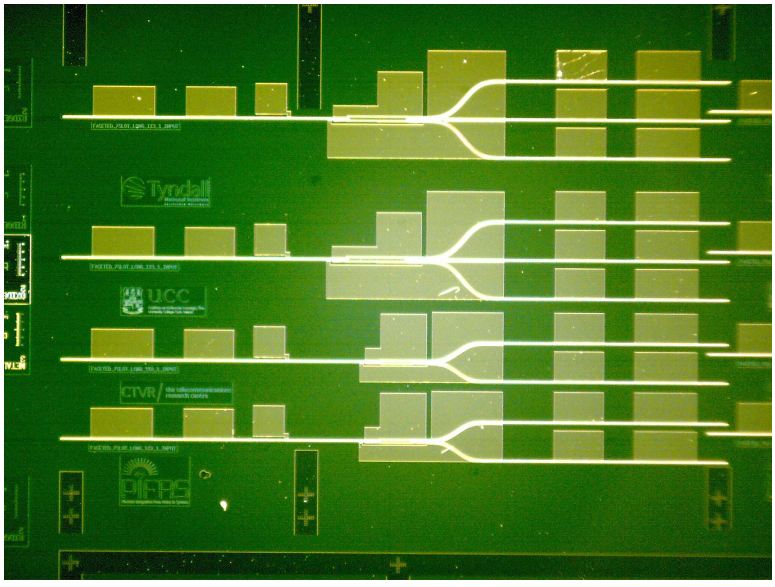

Figure 6.3: Close up of integrated devices where multiple slotted Fabry Pérot lasers are coupled together though an MMI and SOA section.

Extra cleave marks were defined on each device which allowed the SFP lasers on the MMI outputs to be cleaved. The resulting device formed an integrated optical source and power splitter, where an SFP laser was integrated at the input of an MMI and could be split into 2 or 3 equal powered outputs. This building block device was investigated

in detail in this chapter, before the full mutually coupled system of lasers was examined in chapter 7.

6.3 Photonic Integrated Circuit Testing

Each cleaved block of photonic structures consisted of 4 integrated devices. For convenience, these blocks were tested as a whole, where probes could be used to test each integrated device individually. The overall dimensions of a block of devices was typically $4\,\text{mm} \times 4.5\,\text{mm}$. This required the use of a custom a custom built mount to hold each chip under test. Figure 6.4 shows a close up view of this mount, with a device under test. The chip, which can be seen centrally in Figure 6.4, was placed on a raised ridge which allowed optical fibre to be coupled to each side of the device using lensed fibre holders. This was very similar to the setup described in chapter 4, relating to the testing of passive optical waveguides. A series of holes were bored along the length of the raised ridge structure, which led to a hollow ridge core that was connected to an external vacuum. This vacuum provided a means of securing a device on the mount during probing. Each device from the PIC in Figure 6.1, was fabricated on a conducting substrate with metal deposited on its underside. This metal was treated as one large ground pad for each device on the PIC. The mount was fabricated from brass which allowed the entire mount itself to act as one large contact which could be grounded, meaning a specific ground probe was not required.

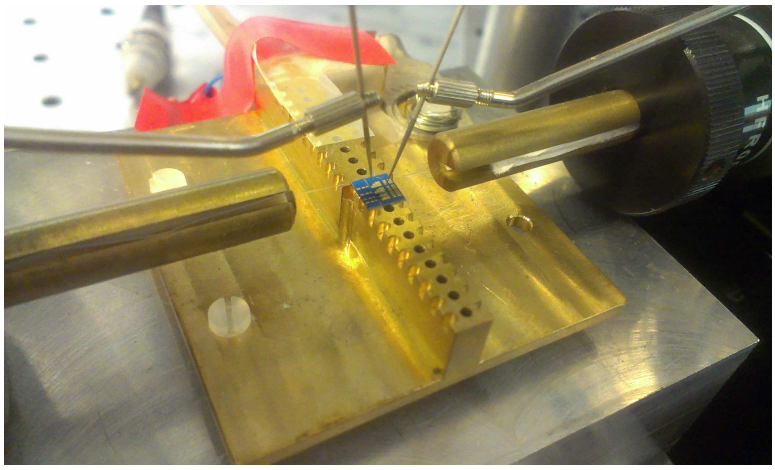

Figure 6.4: Experimental setup showing a photonic device under test. Multiple probes were used to apply electrical current to individual sections of the device and were controlled using XYZ probe manipulators. Lensed fibres were coupled to the input and output waveguides of the device, where the light could be examined.

Due to the large number contact pads present on the each PIC device, a custom probe station was required to enable testing. This probe station was designed and fabricated within the group previously, and was used in the testing of slotted and DFB laser

prototypes. The probe station is shown in Figure 6.5.

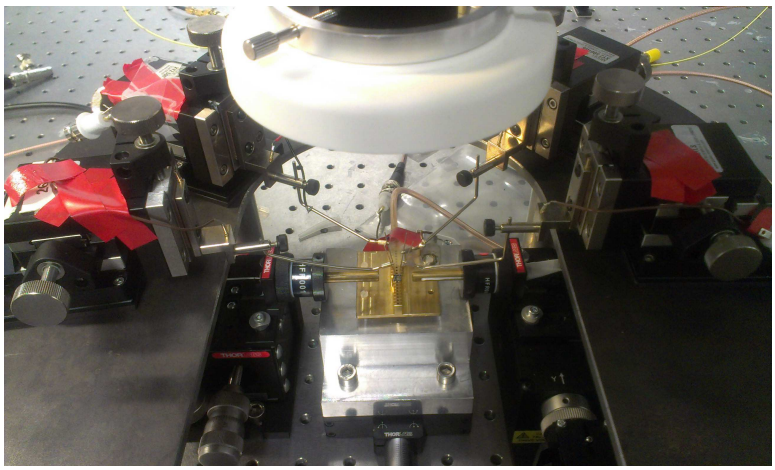

Figure 6.5: Experimental setup showing external probe manipulators positioned around an integrated device under test.

The custom device mount is shown in the centre of Figure 6.5, with a series of probe manipulators in a "U" arrangement around it. The manipulators allowed for precise positioning of the probe in directions across the plane of the chip and also in the vertical direction. The bases of the manipulators were magnetic and arranged on a stainless steel platform which provides a secure and steady base. A thermoelectric cooler (TEC) was placed in between the custom mount, as described above, and the large aluminium heat sink to control the temperature of the device under testing. Lensed fibre manipulators can be seen under the steel platform which allow the position of the lensed fibre to be varied in the x, y and z-directions. At one side of the device, the lensed fibre was controlled via a nanotrak piezo controller which allowed for fine control over the waveguide position. This also ensured compatibility with the previously discussed coupling and mode imaging techniques from chapter 5. On the opposite side of the setup, a manual controller was used to adjust the lensed fibre position. The U arrangement allowed for a maximum of 8 probes to be placed around the setup. This was sufficient for testing the most complex integrated device considered in this thesis, the system of mutually coupled SFP lasers on a 1×2 MMI coupler.

6.4 Fabry Pérot Laser Characterization

6.4.1 FP Laser Testing

The block of test structure devices, as in Figure 6.2, were cleaved from the fully fabricated chip and SEM images were taken of the ridge waveguide structure. These images are shown in Figure 6.6, where the ridge structure can be seen with good verticality of the sidewalls. The oxide layer has been opened along the center of the ridge waveguide

and the deposited P metal can be can be seen entering the channel formed, as shown in Figure 6.6a. Figure 6.6b shows a wider image taken of the ridge structure, where the full deposited metal can be seen over the waveguide with no breaks or shadowing observed.

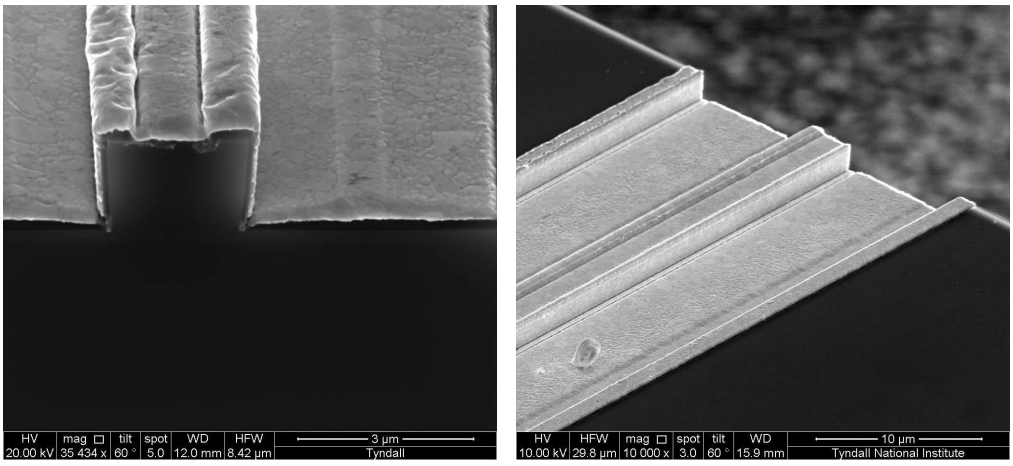

(a) (b)

Figure 6.6: SEM images of the ridge waveguide after cleaving. (a) Shows the cleaved facet with deposited gold on top of the waveguide ridge. (b) Shows a broad area image of the deposited metal which connects to contact pads for probing.

The test structures were then taken and placed on the custom mount for testing. Figure 6.7 shows the FP lasers under test. Only one probe was required to apply a bias across the 2.5 mm device. Lensed fibre was coupled to the waveguide at each side of the FP, where light could be taken and examined externally on an OSA (Optical Spectrum Analyser) or optical power meter.

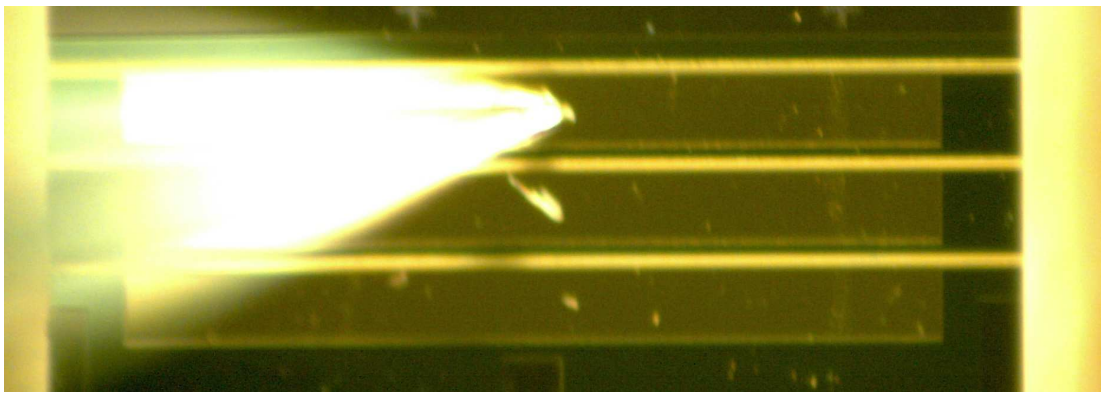

Figure 6.7: Fabricated FP laser under test. Figure shows external probe making contact with large contact pad.

6.4.2 FP Laser Optical Spectra and LIV Curves

LabView code was written to perform standard characterization of the FP lasers. The Current-Voltage curve for each device with varying ridge waveguide width is shown in Figure 6.8. Turn on voltages of ~ 0.7 V were observed, which agree with previous with results of FP lasers previously examined in the research group, on similar materials.

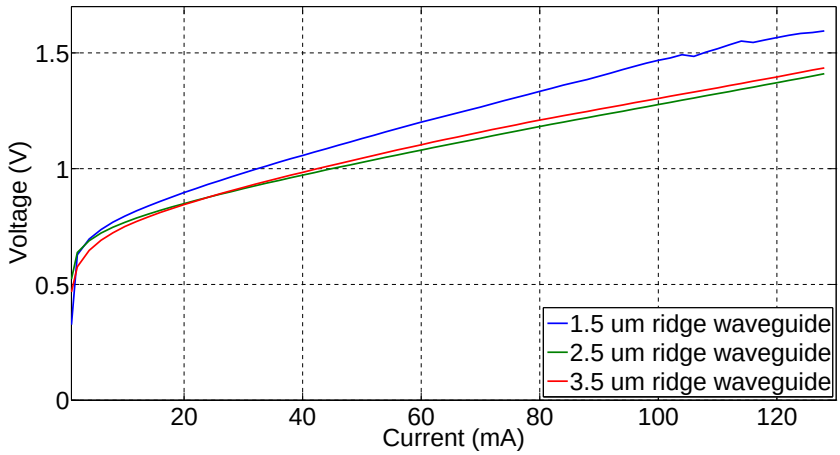

Figure 6.8: IV curve of FP lasers for various ridge waveguide widths.

Figure 6.9 shows the Current-Power curve for each FP ridge waveguide variant, as the current applied to the device was swept from 0 mA to 130 mA.

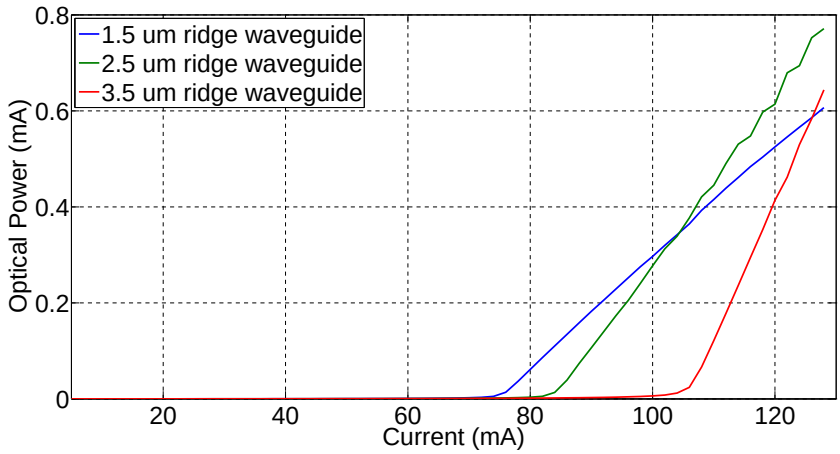

Figure 6.9: LI curve of FP lasers for various ridge waveguide widths.

The power was measured by taking the light from the facet side of the SFP laser, coupling it to a lensed fiber and then using an external optical power meter to record the power. The threshold current, I_{Th}, for each FP laser was found to increase with increasing ridge waveguide width. This was due to the decrease in the current density in each device as the ridge waveguide width became larger. For the narrowest ridge

width, I_{Th} was found to be 75 mA and for the largest, found to be 105 mA. With the FP laser biased to 90 mA for the 2.5 µm ridge, the optical spectrum was analysed on an OSA and is shown in Figure 6.10.

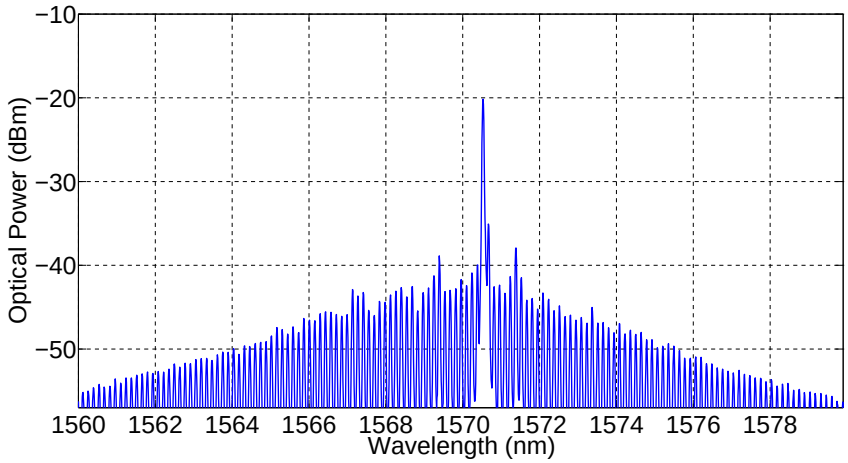

Figure 6.10: Free-running FP optical spectrum with ridge waveguide width of 2.5 µm while biased to 90 mA.

6.4.3 Group Index Calculation

The Free Spectral Range (FSR) of an oscillator is the frequency (ν) or wavelength (λ) spacing between two adjacent resonator modes. The FSR of cavity of length L, is given by:

$$\Delta\nu = \frac{c}{2n_{gr}L} \tag{6.1}$$

Where c is the speed of light and n_{gr} is the group index. This can be related to a wavelength spacing by:

$$\nu = \frac{c}{\lambda} \tag{6.2}$$

$$\Delta\nu = \frac{c\Delta\lambda}{\lambda^2} \tag{6.3}$$

From this, the wavelength spacing between modes in a cavity of length, L, can be written as:

$$\Delta\lambda = \frac{\lambda^2}{2n_{gr}L} \tag{6.4}$$

For the Fabry Pérot cavity shown in Figure 6.7, the wavelength spacings between

modes can be determined from the free-running optical spectra in Figure 6.10. The cavity length of this laser was defined by the cleave marks, which were spaced 2.5 mm apart. This information can be used to extract the n_{gr} index by rewriting Equation (6.4) as:

$$n_{gr} = \frac{\lambda^2}{2L\Delta\lambda} \tag{6.5}$$

A close up view of the modes of the Fabry Pérot spectrum is shown in Figure 6.11.

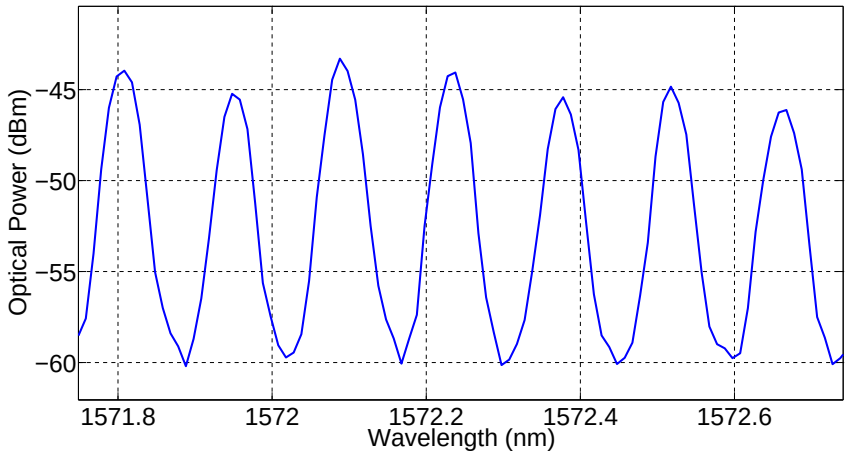

Figure 6.11: Close up view of free-running optical spectra of FP laser biased at 90 mA. Resonator modes are clearly visible.

From this, the average $\Delta\lambda$ between each peak was calculated as 0.14 nm. Combining this with the known cavity length of 2.5 mm, the group index was found to be $n_{gr} = 3.43$. The calculated group index will later be used when analysing the optical output of the slotted Fabry Pérot lasers during characterisation.

6.4.4 Slotted Fabry Pérot Laser Characterisation

A single facet Fabry Pérot (SFP) laser from the block of test structure devices was next examined. SEMs of the slotted mirror section were first taken to ensure that the etched slots were fabricated correctly. These SEM images are shown in Figure 6.12. Figure 6.12a shows a side on view of a typical slot, where the T-bar structure can clearly be seen. In Figure 6.12b, the deposited metal layer which extends between the slots is shown as one continuous piece, indicating good metal continuity.

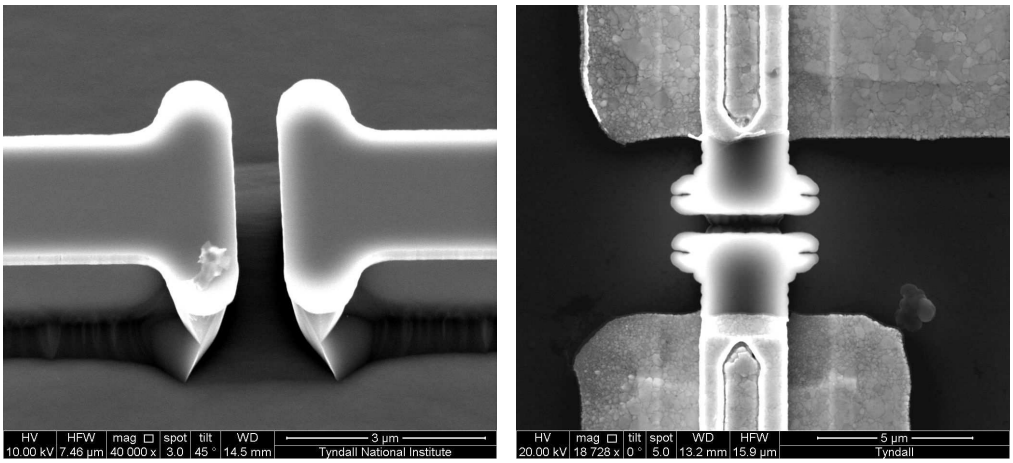

(a) (b)

Figure 6.12: SEM images of T-Bar slots. (a) Shows a close up view of a T-Bar slot where T structure can clearly be seen. (b) Shows a plan view of the slot where the deposited metal and oxide window opening are visible.

The SFP laser operation was based upon feedback from the cleaved facet of the device and a series of equally spaced etched slots which form a further mirror section. If the device was cleaved a further time after the slotted section (to test the laser independently of other sections) this could form an extra cavity which would affect the SFP performance. As a result, it was necessary to investigate the characteristics of the SFP laser while integrated with an unbiased SOA and MMI, which formed large absorbing section. This device was tested using the experimental setup shown previously.

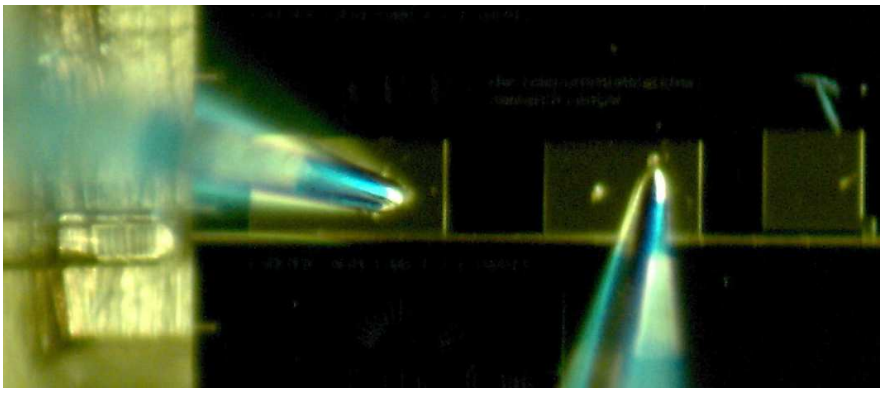

Figure 6.13: Fabricated single facet slotted Fabry Pérot laser under test. Probes are in contact with metal contact pads to apply a bias across the mirror and gain sections of the laser. The lensed fiber is also shown where it is positioned close to the waveguide facet to collect the output light.

The SFP laser was then characterised using the experimental setup discussed earlier in the chapter. The laser while under test is shown in Figure 6.13. As can be seen in Figure 6.13, the gain and mirror sections of the SFP are independently biased using

probes positioned on the large contact pads. Lensed fibre was towards the cleaved facet of the laser from the left, where it allowed the light to be decoupled and examined on an OSA.

The gain and mirror sections of the SFP were probed independently allowing for various operating currents to be examined. Using the same LabView software written for the FP laser characterisation, IV curves for the SFP lasers were generated as the current in the gain section was stepped from 0 mA to 100 mA, with the mirror section biased from 5 mA to 50 mA. This IV curve is shown in Figure 6.14. Typical behaviour is observed with a turn on voltage of ~ 0.9 V seen.

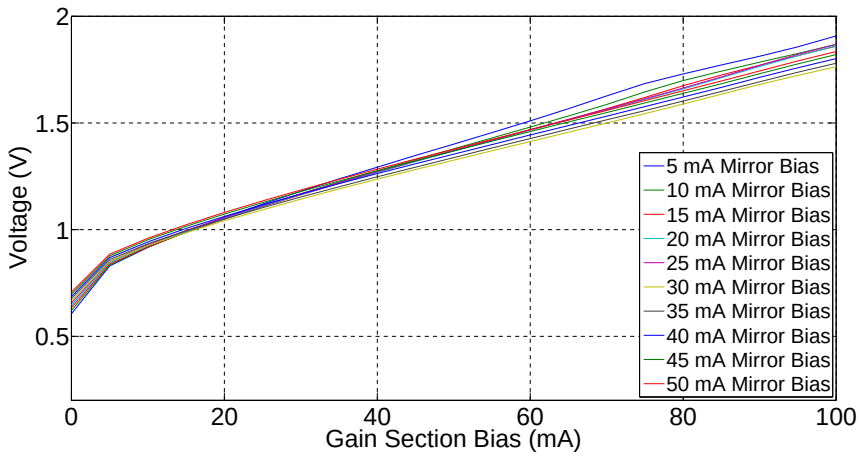

Figure 6.14: IV curve of the SFP laser under different mirror section biases.

For the same current sweeps of the mirror and gain section of the SFP laser, the optical power output versus current was examined. Figure 6.15 shows a series of LI curves of the laser overlapped with each other. This allows the role of the mirror section bias on the lasing threshold of the device, I_{Th}, to be determined. Higher mirror section current biases provide extra gain which results in a decrease in the gain section current required for lasing. For a mirror bias of 5 mA, I_{Th} was found to be $\sim$85 mA while for a mirror bias of 50 mA, I_{Th} was found to be $\sim$35 mA.

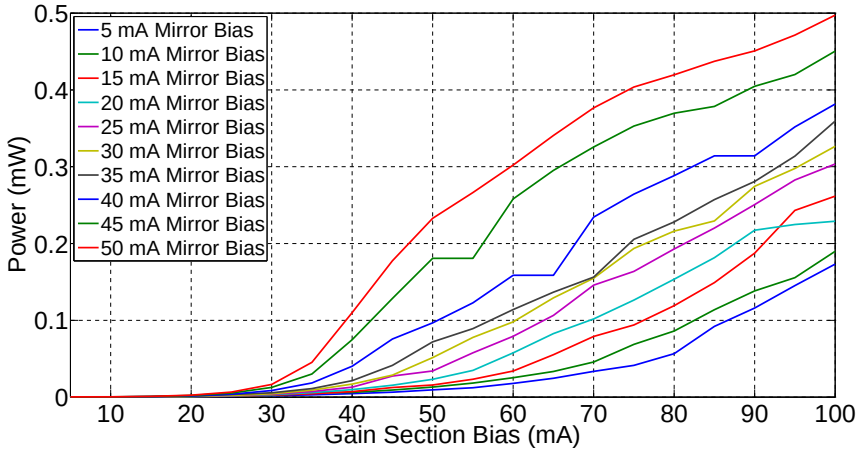

Figure 6.15: LI curve of the SFP laser under different mirror section biases.

A typical optical spectrum from the SFP laser with a mirror bias of 45 mA and gain bias of 100 mA is shown in Figure 6.16.

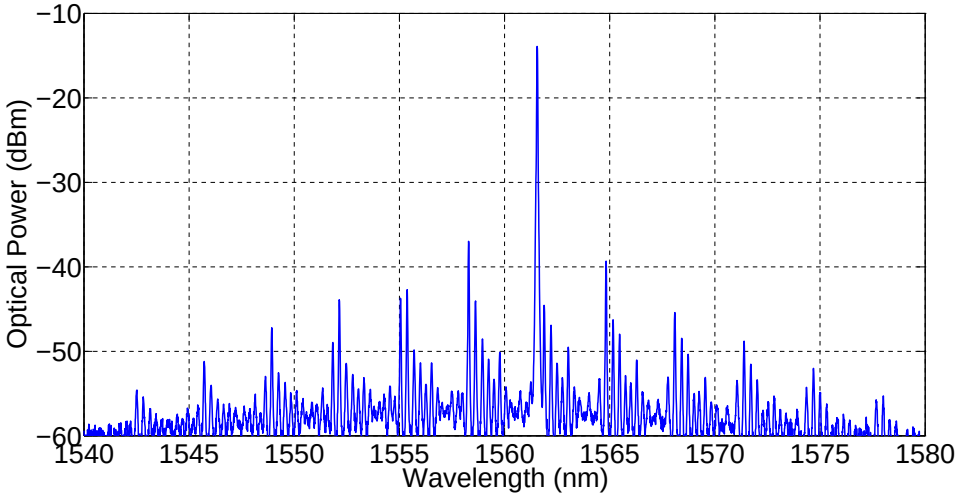

Figure 6.16: Free-running optical spectrum of the SFP laser under test.

The main lasing mode of the laser is at 1562 nm, with a side mode suppression ratio (SMSR) of >20 dB. The wavelength spacing between the super modes of the SFP spectrum, $\Delta\lambda$, was found to be 3.26 nm. This wavelength separation could be related to a cavity length, L, by Equation (6.4). Based on this, a wavelength separation of 3.26 nm can be related to a physical cavity length of 107.43 nm. This length matches the interslot distance of the slotted mirror section which defines its transmission spectrum. The spacing between the FP modes of the spectrum in Figure 6.16 was found to be 0.305 nm, which corresponded to a physical length of 1148.25 nm. This length represented the effective cavity length of the SFP laser, which was formed between the gain section cleaved facet and the effective mirror penetration depth. The full transmission spectrum

of the SFP laser was formed from the overlap of the FP modes with the full mirror section reflection spectrum. Current tuning of the mirror section of the device results in the resonant conditions changing, causing the peak in the transmission spectrum to shift. In this way, the output of the SFP laser could be tuned by varying the bias on the mirror section of the SFP.

6.4.5 Tuning Maps of SFP Lasers

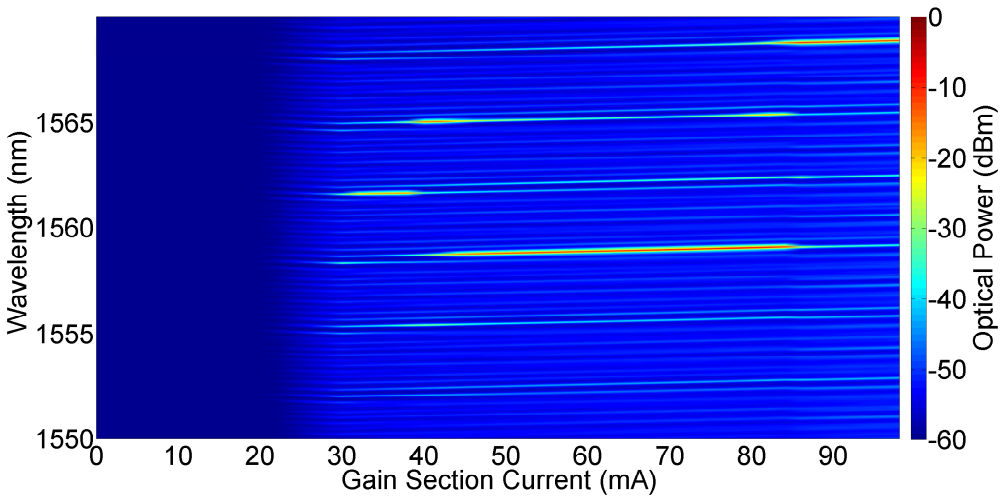

Figure 6.17: Variation of SFP optical spectra with mirror section bias held fixed while the gain section bias was swept between 0 mA to 100 mA

For a fixed mirror bias of 40 mA, the gain section current was swept from 0 mA to 100 mA while recording the output spectrum on an OSA. The resulting plots were concatenated in Matlab to investigate how the spectrum varied with gain section bias. This is shown in Figure 6.17, where the spectral variation of the SFP is examined. For low gain section biases <30 mA, the SFP was still below its threshold current and no signal was recorded on the OSA. Once the gain section current increased above 30 mA, the SFP started to lase and distinct lasing modes become apparent on the OSA traces. The spectrum has one dominant laser mode, which varied in wavelength as the bias current was increased. Between 45 mA and 80 mA, the wavelength remained at 1558 nm with some tuning observed. For biases outside of this, the laser mode was seen to hop quickly between different wavelengths with no large stable region formed. This was as a direct result of the tuning nature of the SFP laser itself, where different preferential lasing modes were created as the SFP sections was biased. The SFP spectrum between 45 mA and 85 mA is shown in Figure 6.18, where the tuning of the lasing mode near 1559 nm can be seen. The wavelength of the mode varies from 1558.5 nm to 1559.1 nm within this range, which amounts to a wavelength shift of 0.015 nm/mA of the laser.

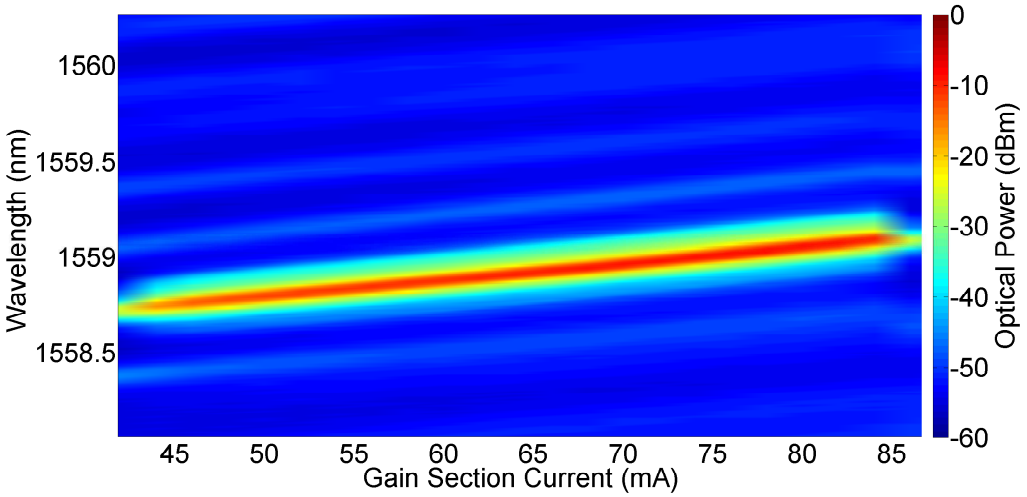

Figure 6.18: Close up view of SFP spectral output with the gain section bias swept between 40 mA and 90 mA. The output was found to be tunable over this range.

The SFP optical spectra was measured on the OSA as both the gain and mirror section biases were varied across the device. From this, the side mode suppression ratio (SMSR) of the main lasing mode to the next highest mode could be determined. The SMSR indicated the extent of the single mode nature of the laser output, with high SMSRs meaning highly single moded. The SMSR was calculated for each different SFP spectrum as the mirror and gain section biases were varied from 20 mA to 60 mA and 20 mA to 120 mA respectively. The variation of the SMSR across this range is shown in Figure 6.19.

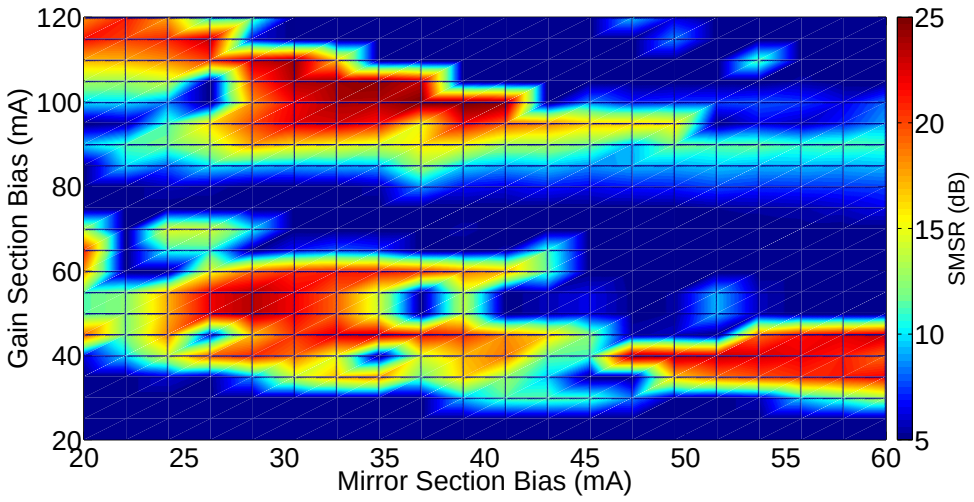

Figure 6.19: SMSR of laser output spectra as the SFP mirror and gain sections were both biased.

Regions exist where the SFP operates with a large SMSR, indicating good single mode performance. These are particularly evident at mirror/gain section biases of

30 mA/50 mA, 30 mA/100 mA and 55 mA/45 mA. An interesting feature of these lasers was that for a gain section bias of 80 mA, there existed no mirror section bias that allowed the SFP to have single mode operation. This was particularly important for later experiments on these laser, where single mode outputs were required.

From the optical spectra recorded over this gain and mirror section current sweep, the wavelength of the preferential lasing mode of the laser could also be extracted. This allowed the variation of the lasing wavelength to be examined versus current bias. This is shown in Figure 6.20, where the z-axis represents the peak wavelength of the optical output of the laser.

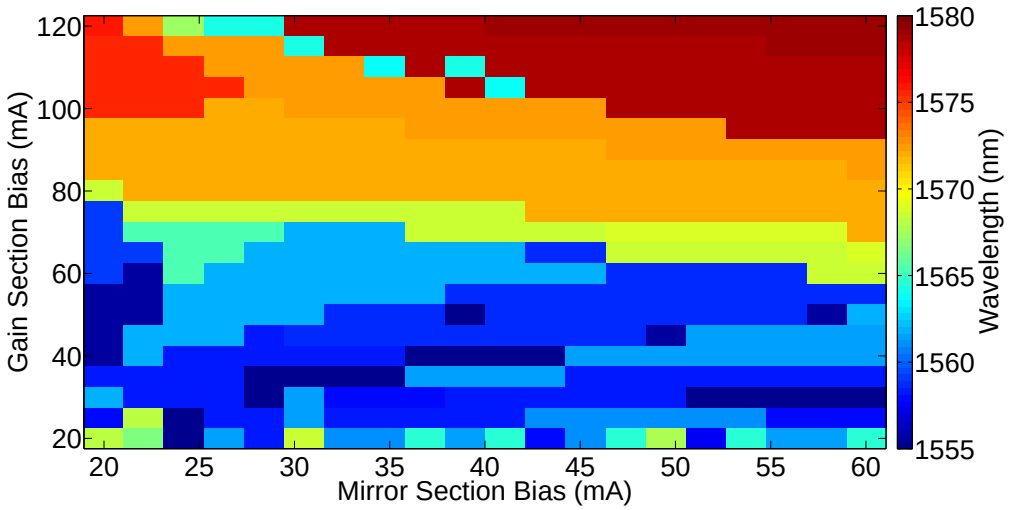

Figure 6.20: Peak wavelength of the SFP optical spectra as the mirror and gain sections were both biased.

Abrupt shifts of the lasing mode wavelength were seen as the current across the SFP was varied. As the total current was increased, the output was shifted to longer wavelengths. This was particularly evident for mirror and gain section biases of 60 mA and 120 mA, where the main lasing mode was at 1575 nm. Comparing this with Figure 6.19 gave a useful insight into the operation of the SFP laser. The regions where abrupt wavelength changes were seen in Figure 6.20 coincided with very low SMSR values in Figure 6.19. This indicated that in these regions the laser was operating multimodally. For the islands of operation where a high SMSR was observed, and thereby was highly single moded, the main lasing mode of the laser does not show any rapid changes in wavelength and slow tuning effects are observed similar to those shown in Figure 6.18.

To examine this further, the same data as before was analysed and the relationship between the highest order wavelength modes of the laser was investigated. The optical spectra of the SFP was analysed at each current bias, where the modes of the laser were sorted by descending power. For current biases which resulted in single mode operation, the main lasing mode has a large SMSR. To determine the multimode nature of the

SFPs, the optical spectra was examined and the number of modes within 10 dB of the peak mode and greater than 10 dB from the noise floor were extracted. This determined the number of *main* lasing modes present at a particular current bias. The results of this analysis are shown in Figure 6.21, where the modal behaviour was examined for having up three main lasing modes present.

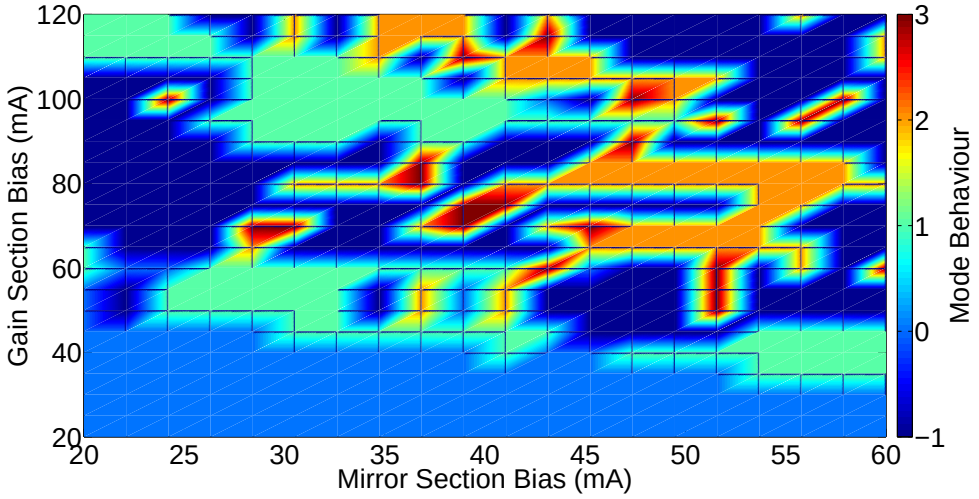

Figure 6.21: Modal behaviour of the SFP spectral output as the SFP mirror and gain sections were both biased. Z-axis indicates the multimode nature of the waveguide at particular biases.

The number of modes at each point which satisfy the 10 dB cut off condition are given on the z-axis of the plot. A negative modal behaviour (shown in light blue) indicated that the optical spectra from the SFP had low peak powers, which was expected for current biases around threshold. A modal behaviour of zero (shown in dark blue) indicated a breakdown of the 10 dB cut off condition and the spectra had > 3 main lasing modes within 10 dB of each other. The regions where the output shows single mode behaviour (green) can clearly be seen in Figure 6.21 at mirror/gain section biases of 30 mA/50 mA, 30 mA/100 mA and 55 mA/45 mA. This is in agreement with the result shown in Figure 6.19, where the laser output has a very high SMSR in these regions. The output spectrum from the SFP with a gain and mirror section bias of 80 mA and 50 mA is in a current band which offers a dual multimodal output. This is shown in Figure 6.22, where the output spectrum has been plotted and it is observed to support two modes of almost equal power. Lasers with such multimodal operation have applications in optical injection locking experiments, as will be discussed in chapter 7.

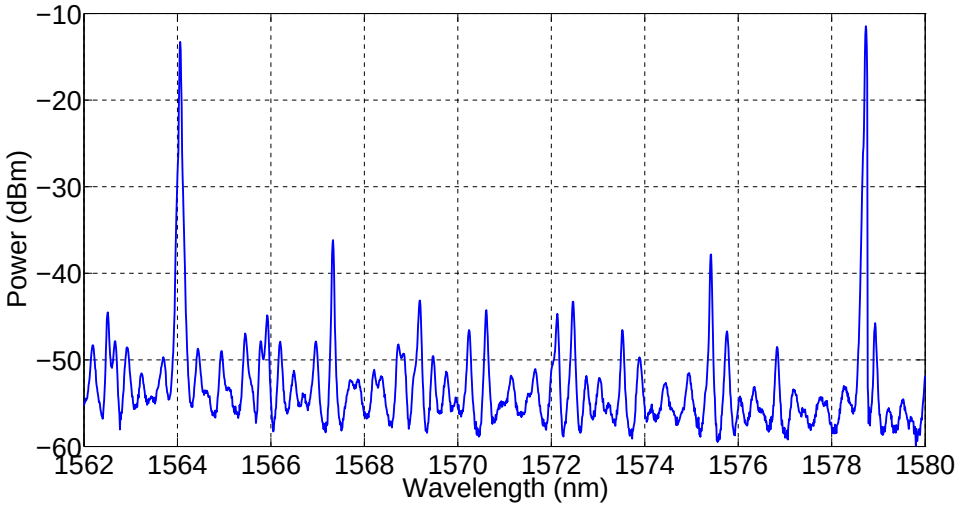

Figure 6.22: Multimodal output of the SFP laser for a gain and mirror section bias of 80 mA and 50 mA respectively.

6.4.6 Relaxation Oscillations

When a laser is subjected to changes in its bias current, it exhibits damped oscillations known as *relaxation oscillations* (RO). These are as a result of the interaction between injected carriers and the emitted photons from the laser. The frequency of the oscillations depend heavily on the output power of the laser. For the SFP laser under investigation here, the ROs were investigated by analysing the SFP output on an electrical spectrum analyser (ESA). The electrical spectrum was taken as the bias across the SFP gain section was varied from 70 mA to 100 mA. The results are shown in Figure 6.23.

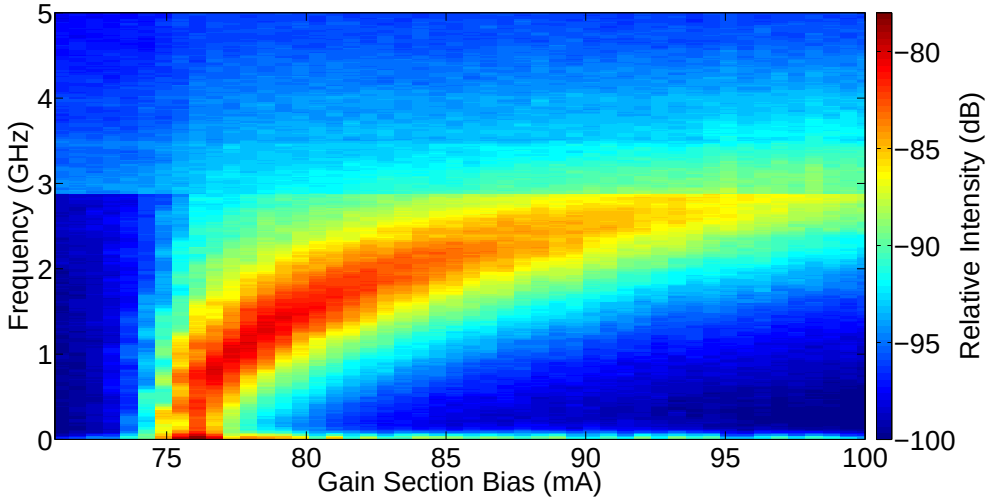

Figure 6.23: Power spectrum of SFP laser output as the gain section bias was varied with mirror section bias held fixed. Relaxation oscillations are observed.

The ROs of the laser can be observed with increasing electrical bias. The ROs start to appear at the threshold current of this particular laser which was 75 mA. As the bias current was increased, the ROs started to approach a peak value of 3 GHz. This was relevant for the experiments performed in chapter 7 involving the power spectra of mutually coupled lasers, where identifying the RO signal allowed them to be distinguished from other dynamical effects.

6.5 SFP laser integrated with SOA and MMI

The first fully integrated device investigated in this thesis comprised of an SFP laser integrated at the input of a 1×2 MMI, which had SOA waveguide interconnects. The device allowed the on chip routing of light via an MMI to be examined for the first time with these lasers. The device was the building block of the more complex integrated circuits designed in chapter 5 and that will be examined in chapter 7. Similar integrated devices have been shown for DFB lasers [165, 166], however, this is the first time such a device has been formed with a single growth monolithically integrated slotted laser. The performance of this device, shown in Figure 6.24, will now be investigated.

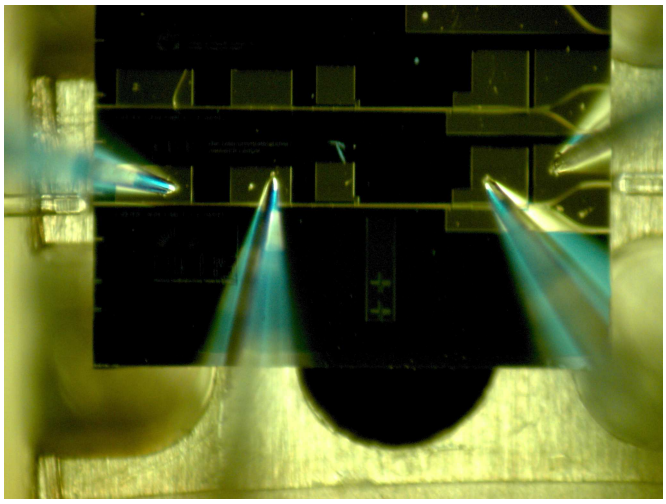

Figure 6.24: Experimental testing of a device with a tunable laser integrated with an optical power splitter and SOA/VOA section. The device offers the first demonstration of an on chip integrated source and power splitter using monolithic integration requiring only a single growth step.

As described in chapter 5, each sub-block of devices was comprised of two devices based around 1×2 MMIs, and two further devices with 1×3 MMIs. As can be seen in Figure 6.24, only the lower 1×2 MMI based device was initially examined, with the 1×3 MMI based devices out of frame. The device was tested using 4 probes to apply a bias to the each section of the integrated circuit: the SFP gain, SFP mirror, MMI and SOA section. To ease in testing, the SOA and MMI output bend sections were shorted

together electrically on chip as part of the design. Since these sections were simple waveguide structures, together they formed one large SOA section. This reduced the number of probes required from 5 to 4, which allowed for significantly easier device testing. The test chuck temperature was maintained at 25 °C throughout all testing. Lensed fiber was positioned at the SFP facet side of the device and fiber coupled using the facet scan technique described in chapter 4. The SFP was biased such that it operated with single mode lasing behaviour, similar to that shown in Figure 6.16.The MMI and SOA sections were both biased to 10 mA. However, this still resulted in high absorption losses in the SOA due to insufficient gain being provided from the low drive current. At these biases, minimal light from the SFP was still detected from the outputs of the MMI waveguides, and this was used to fibre align lensed fibre at this side of the device. The bias on the SOA section was increased to provide more gain which allowed the device to overcome the inherent losses due to the material. Figures 6.25a to 6.25c that follow, show the spectra from the output waveguides of the MMI as the SOA bias was increased from 40 mA to 80 mA, with the MMI section held fixed at a 10 mA bias.

Figure 6.25a shows the output from both ports of the MMI overlapped with the output from the facet side of the laser for an SOA bias of 40 mA. The light from the facet of the SFP had a preferential lasing mode at 1565.9 nm. This light was coupled through the SOA and MMI section, where it was split in two and the power and wavelength from both MMI outputs were determined. A slight wavelength difference was observed at the MMI outputs, which were also reduced in power due to the low bias on the SOA section. This wavelength was shift caused by a limitation of the experimental setup, where only one MMI could be measured on the OSA at a given time. As a result, the SFP output was be seen to drift slightly during the time it takes to recouple the optical fibre due to thermal or air fluctuations. This is most apparent when comparing the MMI outputs, where the lensed fibre needs to be shifted from one output to another and recoupled before an OSA trace can be taken. Differences in splitting ratios between the MMI outputs can also be explained by slight differences in the lensed fibre to output waveguide coupling efficiencies, or slight variations in the facet structure from cleaving. Figure 6.25b shows the comparison between the SFP and MMI outputs for an SOA bias of 60 mA. At this SOA bias, an excess loss of 11 dB was seen between the SFP and MMI output peak power. The increase in MMI output power over the 40 mA SOA bias was due to the extra gain provided at higher currents. This allowed more light to couple into the MMI due to the absorption losses being reduced. As can be seen in Figure 6.25c, increasing the SOA bias from 60 mA to 80 mA caused the MMI output power to increase further with respect to laser facet side power. The power difference between the two was reduced to ~ 7 dB, a 12 dB improvement from the scenario with an SOA bias of 40 mA. The ~ 7 dB loss through the MMI was significantly larger than the 3 dB loss expected for an optimised 1×2 coupler. One possible reason for this loss

was that the MMI itself may have been insufficiently biased at 10 mA to overcome the inherent absorption losses in the device. In addition to this, further experiments on these devices by other members of the IPG indicated that the minimum bend radius chosen for the MMI output bends may have too short to ensure low loss performance.

Another feature observed in this device was the shift in wavelength of the main lasing mode of the laser as the SOA bias was increased. Although electrical isolation slots were present between each device section, current leakage from one section to another may impact the device performance. Thermal effects may also have played a role in this behaviour, where heat generated from biasing the SOA contact pad may have affected the slotted mirror section resulting in tuning of the SFP lasing mode. For the 40 mA and 60 mA SOA biases, there was a 0.1 nm wavelength shift as the bias was increased. When this was increased further to 80 mA, a wavelength shift of 3.5 nm was observed. This sudden hopping of the wavelength mode was a feature of the SFP laser itself as described previously, where due to Vernier tuning, small current changes can induce large wavelength jumps in particular areas. The device was shown to operate successfully despite this, where an SFP laser was shown to be integrated with an MMI and SOA in a single epitaxial growth, monolithic process.

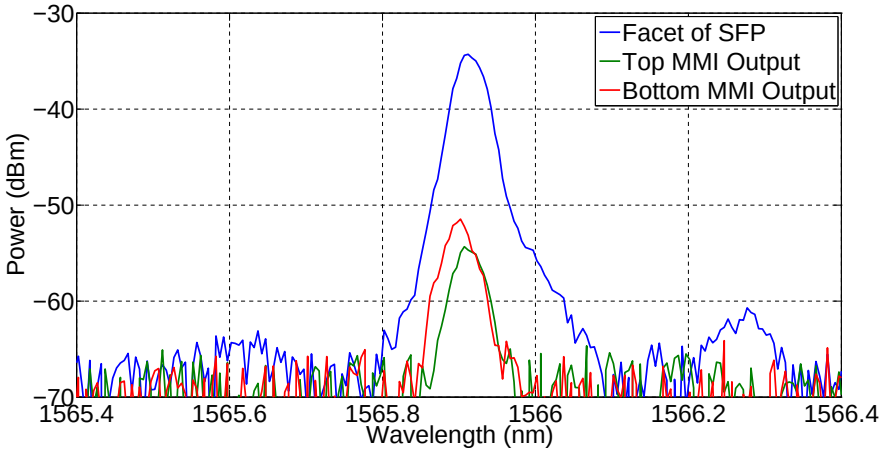

(a) SOA biased to 40 mA

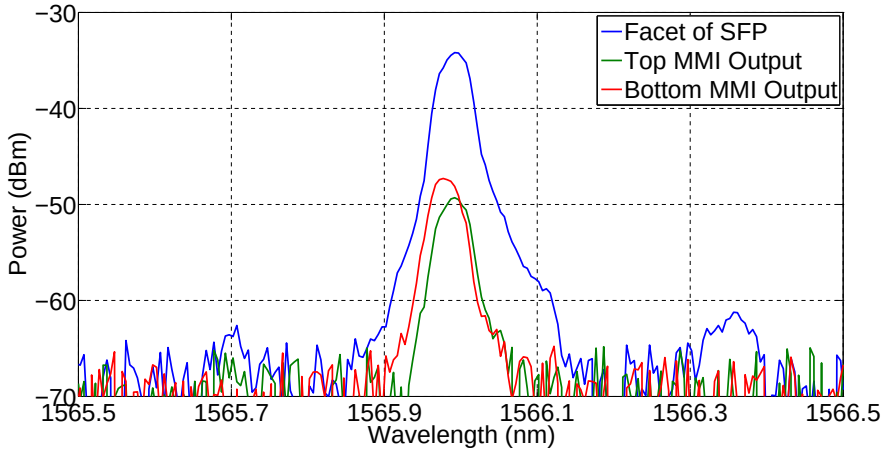

(b) SOA biased to 60 mA

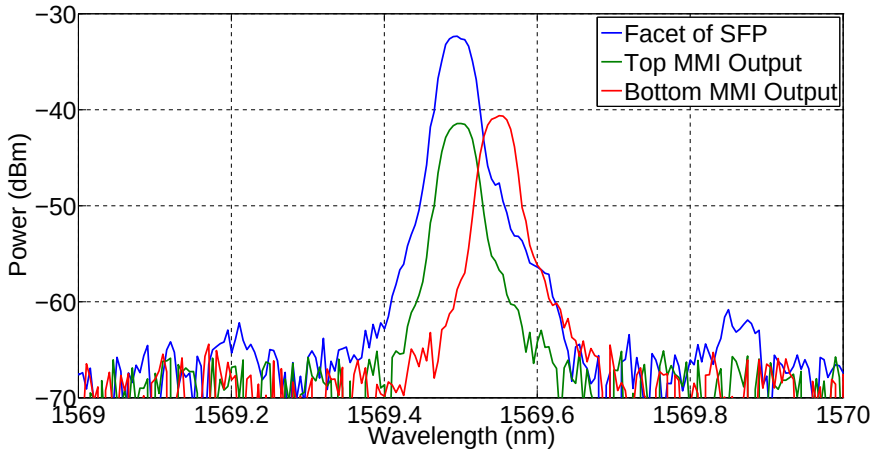

(c) SOA biased to 80 mA

Figure 6.25: Optical spectra as measured from the cleaved facet of the SFP and MMI output waveguides, as the SOA regions were forward biased.

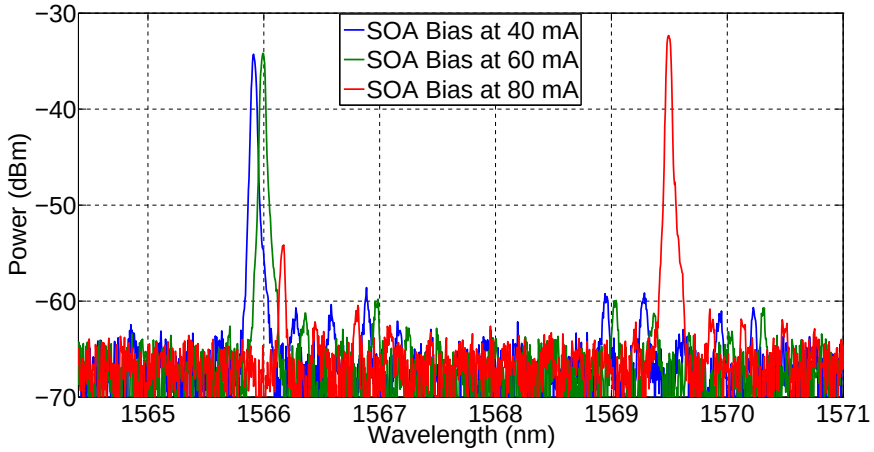

Figure 6.26: Overlapped optical spectra from the cleaved facet of the SFP and MMI output waveguides, as the SOA regions were forward biased.

6.6 Conclusion

This chapter described the initial experimental testing of the photonic integrated circuits discussed previously. The devices were fabricated in Tyndall, cleaved into smaller blocks of structures for ease of handling and tested using a custom probe setup. The primary goal was to investigate the performance of each designed subcomponent before testing full devices. Of particular importance was the SFP laser, which played a key role in each of the main integrated devices considered in this thesis. The SFP was optically examined under various bias conditions across its mirror and gain sections while its optical output spectra was recorded. From this, the optical characteristics of the SFP were examined in detail. Particular attention was paid to the tunability of the laser, while also ensuring that tuning regions existed where the laser had single mode operation. The multimode behaviour of the laser versus electrical bias was also examined. After satisfactory characterisation of the SFP laser, the first designed integrated device was then tested. The device consisted of an SFP laser integrated with an SOA waveguide interconnect and a 1×2 MMI coupler. The purpose of this device was to investigate the monolithic integration of the these components together using a regrowth free process, where the routing of light on chip via an integrated MMI and SOA could be examined. The device demonstrated the on chip splitting of light into two equal power outputs at the end of the MMI coupler. The SOA bias was found to offer control over the output power coupled from MMI, where it could be varied by as much as 11 dB. Although the device performed as expected, there was 4 dB extra loss across the MMI and SOA sections. Despite the loss, this building block performed well and was the first integrated device demonstrated where SFP lasers, MMIs and SOAs were monolithically integrated together using a single epitaxial growth step.

Chapter 7

Injection Locking of Slotted Fabry Pérot Lasers

7.1 Introduction

As discussed in chapter 1, phase locking via optical coupling of semiconductor lasers has been an area of immense interest since the early 1980s [167]. Phase locking has found applications in numerous areas arising from the theoretical and experimental study of injection locked systems [168]. Much of the recent work on both unidirectional and bidirectional optical coupling in various semiconductor laser systems [169, 170, 171] has focused on the non-linear dynamics observed including synchronisation [172, 173], excitability [174, 175, 176], multistability [177] and chaos [178]. Typically these systems have been demonstrated using discrete optical components. However, there has been a shift towards their development in integrated devices [94]. Not only does this offer exciting research opportunities to the non-linear dynamics community, but it also offers excellent potential to improve photonic communication systems. Recent applications of injection locking have demonstrated adaptive optical filters [179] and phase locked coherent laser outputs [102], a necessary feature of the majority of modern day modulation formats [180]. The work presented in this thesis focused on the development of the coherent laser system presented in [102]. Multiple injection locked lasers were used to generate coherent channels on a monolithically integrated device which required only a single epitaxial growth step.

This chapter investigates the operation of such devices by examining the optical phase locking properties of the PICs designed and tested previously in this thesis. An integrated power splitter has already been developed and shown to offer excellent promise in more advanced devices. Based on the success of this device, the integrated circuit consisting of mutually coupled SFP lasers integrated with an MMI coupler and SOA is examined. The optical phase locking properties of SFP lasers are first explored under

injection from an external source. With this in place, a phase locked system is demonstrated between two SFP lasers on a single device which are coupled externally using optical fibre and an isolator. The results from this system are then compared where the external coupling is removed and integrated (on chip) coupling between the two SFP lasers is considered. An on-chip optically phase locked system is demonstrated for the first time using single growth monolithically integrated slotted Fabry Pérot lasers [101]. The chapter concludes by using an optically phase locked system to investigate the generation of multiple coherent signals on an integrated device.

7.2 Injection Locking of Slotted Fabry Pérot Lasers to an external Tunable Laser Source

The photonic integrated device investigated in this chapter comes from the designed and fabricated PIC described previously in chapter 5. Focus is primarily aimed at the properties of the most complicated integrated device, where a single SF-SFP laser is coupled to three further SF-SFP lasers through a Semiconductor Optical Amplifier (SOA) and 1×3 Multimode Interference Coupler (MMI). The photonic device under test is shown in Figure 7.1, where probes have been initially placed on the input SFP laser, the SOA/MMI sections and the center output SFP laser.

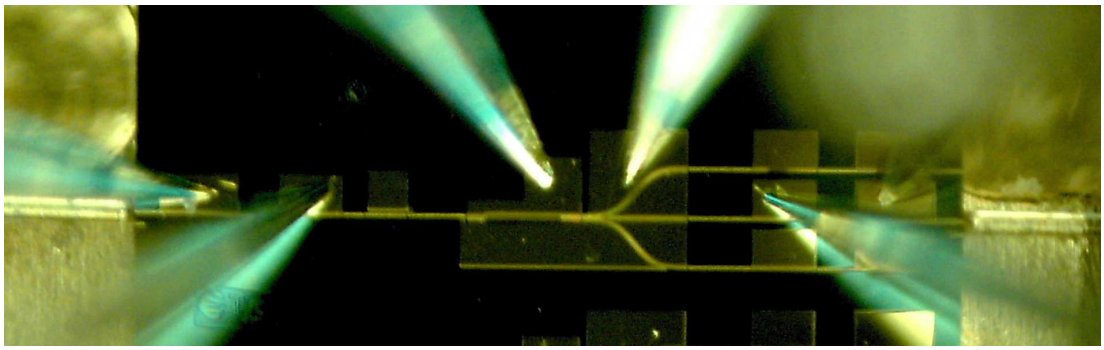

Figure 7.1: Image of the PIC under test. A single SFP laser was integrated at the input of a 1×3 MMI which had three further SFPs integrated on its output arms. The input and central output SFPs were both probed which allowed for current injection into the different sections of each laser.

The setup used to test the device was identical to that presented in chapter 6 to examine the SF-SFP lasers. Lensed fibre was positioned at both sides of the device which allowed light from both the input and output SF-SFP lasers to be examined simultaneously. Six probe manipulators were positioned around the device which allowed each section to be biased electrically. Throughout testing, the device temperature was maintained at a fixed 25° C.

The first experiment carried out on this device was to investigate the viability of stable

optical injection locking of SFP lasers by considering the optical injection locking of a single SFP laser on the device by a commercial external cavity tunable laser source, the TLS, which had a linewidth < 100 kHz and was tunable in steps of 1 pm. A schematic outline of this experiment is shown in Figure 7.2.

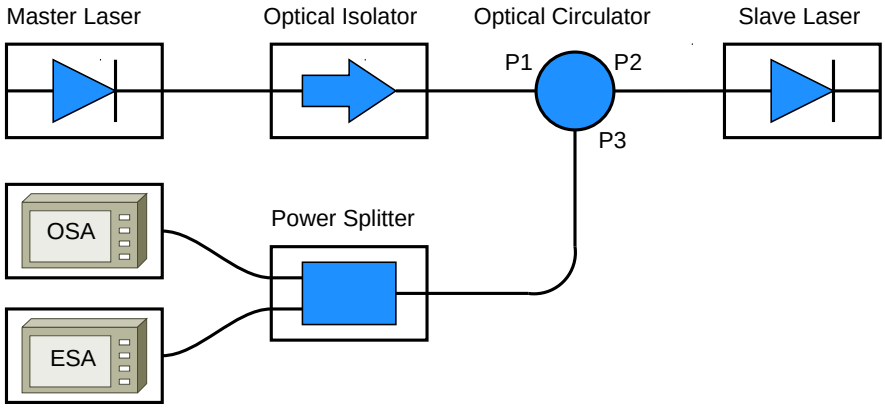

Figure 7.2: Outline of a typical injection locking setup.

The TLS (master laser) output, was guided in single mode fibre through port 1 of a circulator, which provided greater than 40 dB isolation. The light from the TLS was injected into the SF-SFP laser via port 2 of the circulator through the lensed fibre positioned at the laser facet. Light from the SFP was then decoupled via the same lensed fibre and examined on an Electrical Spectrum Analyser (ESA) or Optical Spectrum Analyser (OSA) at port 3.

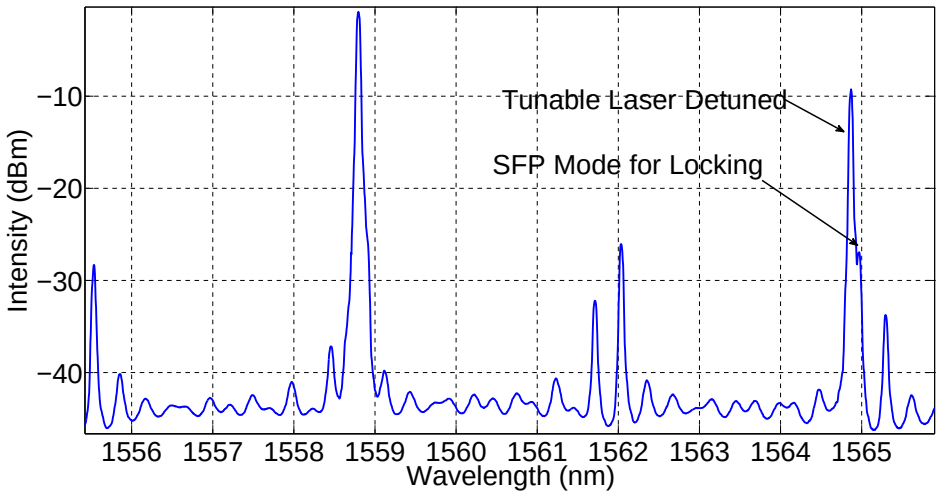

Figure 7.3: Spectral output of the SFP with injected signal from the TLS. The mode chosen to be injected to is at 1565 nm where the detuned TLS input can also be seen.

Based on the results from the previous chapter, the SFP gain and mirror sections were biased to have single mode operation with a main lasing mode occurring at 1558.8 nm. The tunable laser wavelength was set close to that of one of the side modes of the

SFP laser output and injected into the SFP cavity via the circulator. A side mode was chosen rather than the main lasing mode so that suppression of the modes could be readily seen. Figure 7.3 shows the output from port 3 of the circulator where the detuned TLS signal can clearly be seen on the OSA trace.

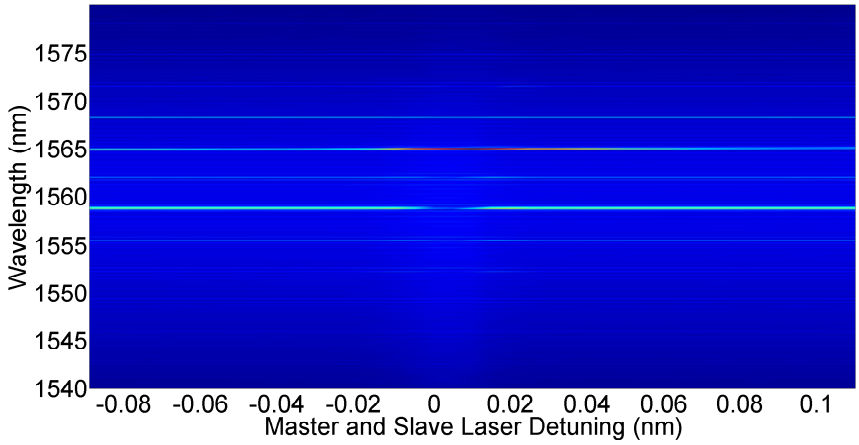

(a) Injected TLS power at −7 dBm

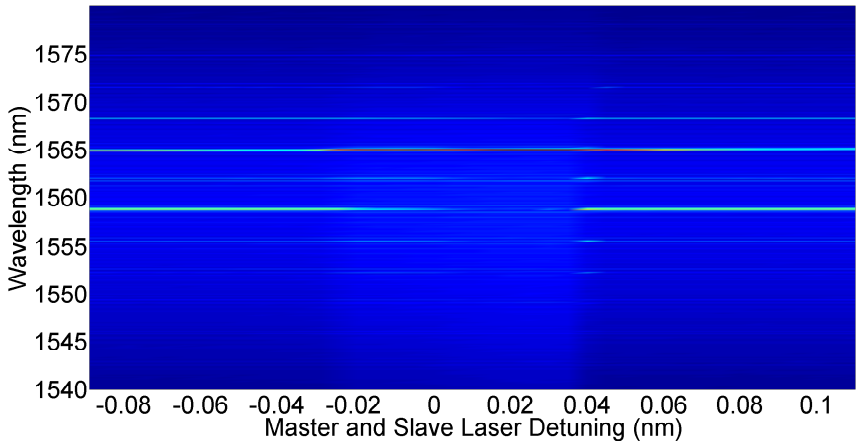

(b) Injected TLS power at 0 dBm

Figure 7.4: OSA traces from SFP laser as the TLS wavelength was swept across resonance with a chosen mode of the SFP. Two different TLS powers are considered where the effect of higher injected powers can be seen. For close to zero detuning in both cases, significant suppression of the side modes of the SFP was observed and the SFP lases strongly at the injected wavelength.

The chosen free-running mode of the SFP laser is clearly seen at $\sim$ 1565 nm, with the TLS peak occurring at a slightly shorter wavelength. The TLS power was set to −7 dBm and swept across resonance with the chosen mode while OSA and ESA traces were recorded at each swept wavelength. This was then repeated with the TLS power increased to 0 dBm, again with the optical and electrical behaviour of the SFP being monitored. Figures 7.4a and 7.4b show a false colour plot of the optical spectrum of

the SFP as the wavelength of the master laser was detuned across the TLS for each of the master powers chosen.

Detuning is defined as the frequency of the master laser minus the free-running frequency of the slave laser, in this case the SFP. Bright colours represent higher optical powers, and the main lasing mode of the SFP can clearly be seen at 1559 nm in the Figures for large detunings. As the detuning between master and slave laser becomes smaller, suppression of this main lasing mode is observed and the SFP operates with a single lasing mode at the injected master laser wavelength of 1565 nm. The width of this region, where such suppression of the main lasing mode occurs, is shown to increase for higher injected powers, as can be seen in Figure 7.4b, where now the detuning can extend to almost 0.04 nm before the output returns to that of the free-running SFP.

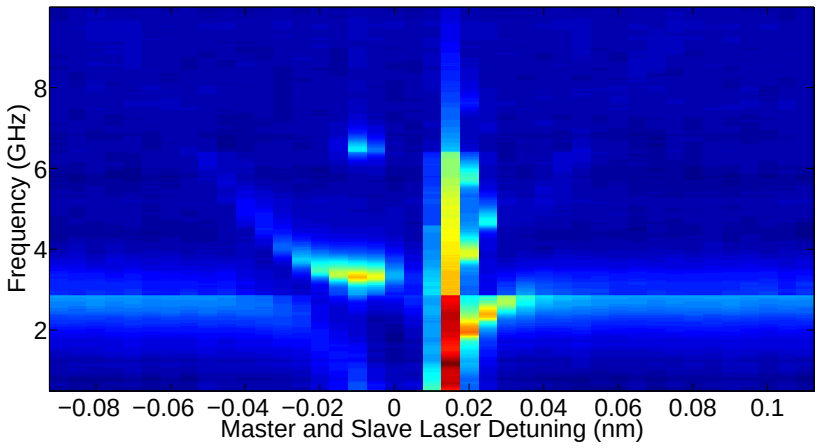

(a) Injected TLS power at −7 dBm

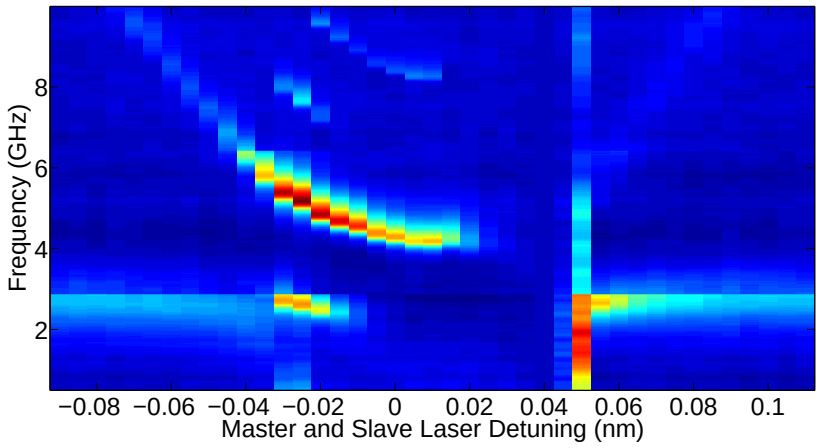

(b) Injected TLS power at 0 dBm

Figure 7.5: ESA traces from SFP laser as the TLS wavelength was swept across resonance with a chosen mode of the SFP. The beat note between the two signals is observed and a quiet region is observed at close to zero detuning.

Whether or not the SFP has undergone optical injection locking in the region of small wavelength detunings between master and slave laser, can most clearly be seen when the power spectrum of the SFP is considered as the master laser is swept across resonance with the slave. This is shown for both variations of the injected power in the false colour plots shown in Figures 7.5a and 7.5b.

Bright colours correspond to higher modulation powers and blue to the noise floor of our instrumentation. The dynamic range of the plot goes from low intensity (blue) to high intensity (dark red). From Figure 7.5a there are three regions of distinct behaviours observed: (i) a quiet region close to zero detuning where the SFP is shown to be phase-locked to the external master laser; (ii) an unlocked region for both positive and negative detuning where the ESA displays at least one tone (corresponding to frequency beating far from zero detuning); (iii) a region of complex dynamics close to the negative detuning unlocking boundary (i.e. higher external master laser wavelength). While such regions of complex dynamics have proved to be of immense interest to the non-linear laser dynamics community over the past few years, this thesis solely focuses on the stable locking region which clearly indicates that the SFP has been successfully phase locked to the external master laser. Similar regions are observed for the higher master laser injected power, as can bee seen in Figure 7.5b, where the quiet region close to zero detuning is shown to be considerably larger, and a wider stable phase locking region is present. This compares well to the optical spectra in Figure 7.4, where suppression of the lasing modes of SFP are seen at the same wavelength detunings.

7.3 Optical Phase Locking of Integrated Single Facet Slotted Fabry Pérot Lasers

Having clearly demonstrated that stable optical phase locking of an SFP laser to an external master laser is achievable, attention was switched to the possibility of developing an integrated phase locked system on chip between two SFP lasers. This was done by investigating the full device shown in Figure 7.1, where the viability of optical phase locking between the two identical SFP lasers coupled together through a variable gain SOA/MMI section interconnect was considered. A schematic of the full device with each variable parameter labelled, is shown in Figure 7.6.

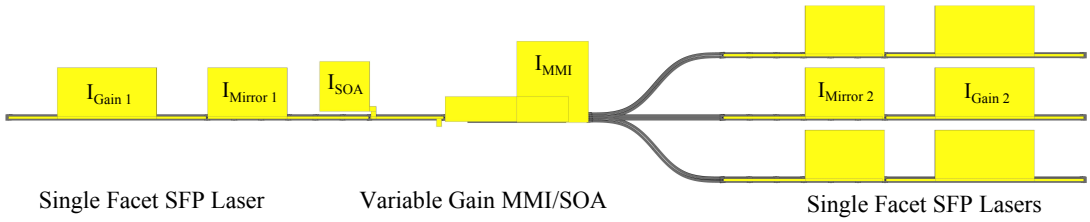

Figure 7.6: Schematic of PIC. Single Facet SFP Lasers are integrated at the input and outputs of a 1x3 MMI. The input SFP is used as the master laser in this experiment and can be tuned by varying the currents $I_{Gain\ 1}$ and $I_{Mirror\ 1}$. The central output SFP is used as the slave laser and can be tuned by varying the currents $I_{Gain\ 2}$ and $I_{Mirror\ 2}$. The outer SFPs are unbiased.

The input SFP laser to the MMI/SOA section can be controlled by independently biasing the gain, $I_{Gain\ 1}$, and mirror, $I_{Mirror\ 1}$, sections of the SFP. For initial experiments, only the central SFP laser on the output side of the device was considered, which itself could be controlled through biasing of sections $I_{Gain\ 2}$ and $I_{Mirror\ 2}$. Both SFPs were connected via a short SOA waveguide section, MMI region and MMI bend section, which required sufficient forward biasing to overcome the inherent losses present due to the quantum wells near 1550 nm. To reduce the number of variables in the experiment, these sections were shorted together off chip and an electrical bias, I_{MMI}, was applied from a common current source. These sections are collectively referred to as the "Variable Gain" section of the device, since forward or reverse biasing of this section allowed the power coupled between the input and output SFPs to be varied by controlling the amplification or attenuation of the optical signal. Applying a reverse bias on this section allowed it to act as a large photodiode which could be used to measure the power output from either SFP laser on-chip, without the need for external fibre coupling.

The mirror section biases on each SFP, $I_{Mirror\ 1}$ and $I_{Mirror\ 2}$, were both set to 30 mA. The gain section threshold current, $I_{Threshold}$, for the SFP at this mirror bias was found from the SFP characterisation of the previous chapter to be 35 mA. The output SFP gain section bias, $I_{Gain\ 2}$, was set to $I_{Threshold}$ and it was found to be lasing with a series of multiple peaks with a low SMSR. The input SFP laser was operated with a gain section bias, $I_{Gain\ 1}$, of $3 \times I_{Threshold}$, where it behaved as a single mode laser with high power output and high SMSR. The spectrum of this laser was found to match well with the results presented in chapter 5, with similar biases. The peak power ratios between the input and output SFP lasers in this current bias regime was found to be approximately 90:10. For convenience in what follows, the higher power laser was referred to as the Master-SFP (M-SFP), with the lower power laser referred to as the Slave-SFP (S-SFP).

As discussed in chapter 6, varying the gain section bias in any SFP laser considered in this thesis will result in a tuning of the SFP output over a particular wavelength

range. Using this mechanism to tune the wavelength, optical phase locking has been demonstrated between SFP lasers on the same chip by optically coupling the light from one cavity to another. A stable region was found where the M-SFP could maintain single mode operation while current tuning allowed it to be swept across a resonance with the fixed S-SFP laser. This stable locking region was determined for two variations of coupling between the M-SFP and S-SFP. These were:

Off-Chip Coupling The waveguide interconnect section joining both SFPs was revered biased to -2 V making it completely absorbing. The SFPs were coupled externally using an optical circulator.

On-Chip Coupling The waveguide interconnect section joining both SFPs was forward biased to transparency. The SFPs were coupled on the PIC itself through the waveguide interconnects between the lasers, without the need for a circulator.

In the sections that follow, the optical phase locking performance of the SFPs is examined and discussed for each different coupling mechanism.

7.3.1 Phase Locking of Single Facet Slotted Fabry Pérot Lasers - Off Chip Locking

With the device setup as previously described in Figure 7.1, the off-chip SFP coupling scheme was first investigated. A schematic of the experimental setup for this is shown in Figure 7.7.

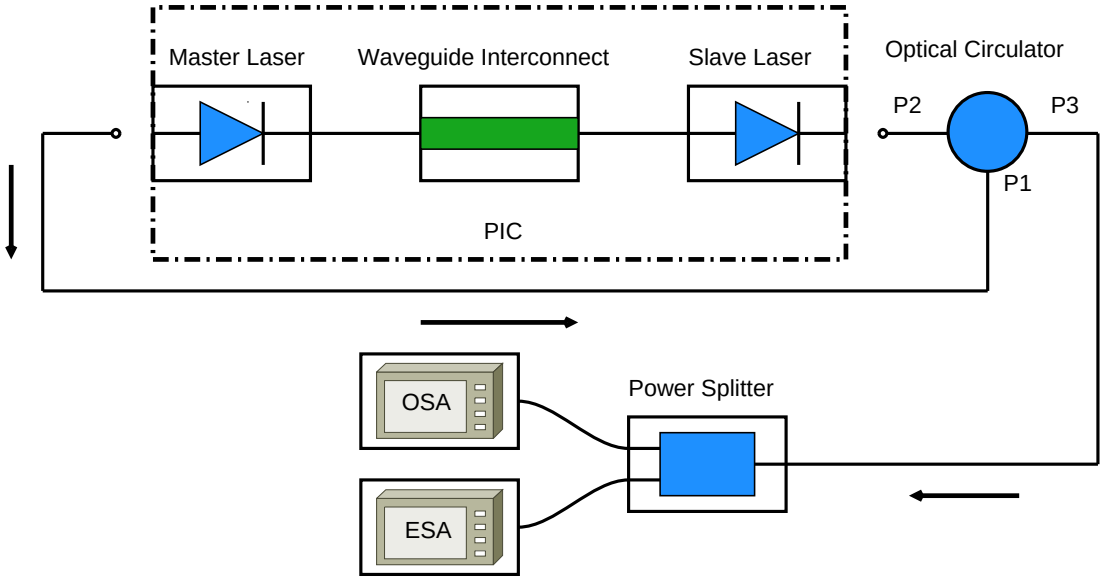

Figure 7.7: Experimental setup showing the off-chip coupling scheme between two lasers on the same integrated device. The waveguide interconnect linking both lasers was reverse biased to - 2V which removed any coupling between them on chip. Instead, light from the master laser was coupled via a circulator to the slave laser.

The output from each SFP was fibre coupled as before using lensed fibre. The output from SFP 1, referred to as the master-SFP, or M-SFP, was input through port 1 of an optical circulator, which provided a greater than 40 dB isolation between its ports. Port 2 of the isolator was coupled to the output of SFP 2, referred to as the slave-SFP, or S-SFP. Port 3 of the circulator was in turn connected to a 1×2 splitter where it was fed to an ESA and OSA, where the electrical and optical characteristics of the signal could be investigated. This arrangement, as shown in Figure 7.7, allowed the light from the M-SFP to be injected into the S-SFP cavity through external means. The variable gain section of the device, which includes the SOA, MMI and MMI output bends, was reverse biased to -2 Volts to ensure it was completely absorbing. This prevented any light from coupling between the M-SFP and S-SFP through the on-chip waveguide interconnects between each SFP.

The mirror and gain sections of the S-SFP, $I_{Mirror\ 2}$ and $I_{Gain\ 2}$, were set to 30 mA and 35 mA, respectively. These biases produced a multimodal spectrum from the S-SFP laser with a relatively low SMSR compared to results for higher bias conditions. The mirror section of the M-SFP, $I_{Mirror\ 1}$, was set to 30 mA, while the M-SFP gain section bias, $I_{Gain\ 1}$, was varied from 60 mA to 90 mA. Sweeping over this current range caused the spectral output of the M-SFP to be swept across a resonance with the S-SFP, with a detuning between a selected mode in the S-SFP and main lasing mode in the M-SFP of -0.12 nm to $+0.12$ nm. The resulting evolution of the optical spectrum of the S-SFP as the M-SFP is swept across resonance is shown in Figure 7.8.

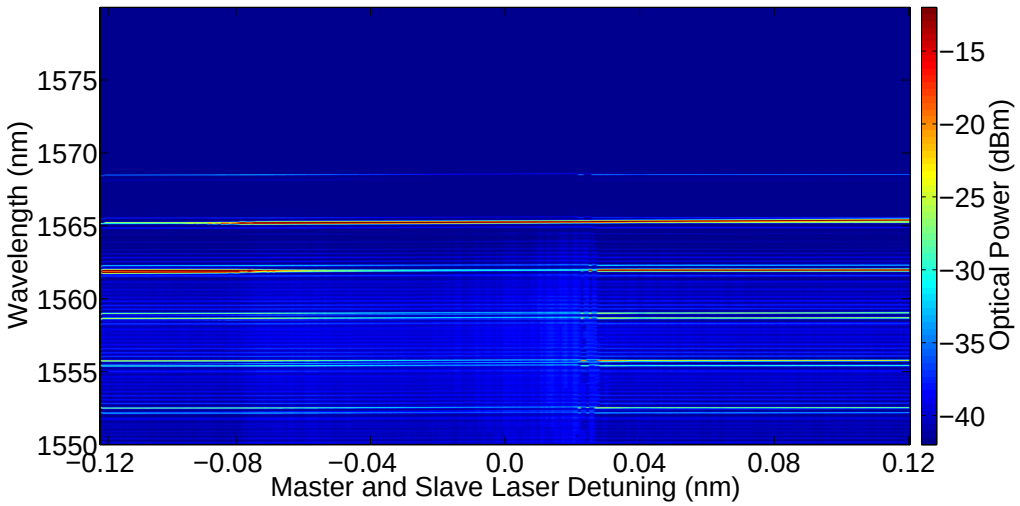

Figure 7.8: OSA trace from the S-SFP as the injected signal from the M-SFP was swept across resonance of one of its lasing modes. For close to zero detuning, suppression of the optical side modes was observed and SFP 2 was shown to lase strongly at the injected wavelength.

The false colour plot shows a region where optical suppression of the SFP side modes can be observed as the detuning starts to approach zero nm. This coincides with a

shift in the lasing wavelength of the S-SFP, where it now starts to lase at the injected wavelength of $\sim$ 1565 nm. This region shows clear signs of optical phase locking for detunings between 0.0 nm and +0.03 nm which corresponds to an M-SFP gain bias ($I_{Gain\ 1}$) variation of approximately 75 to 78 mA.

Further investigation of the signal was performed by analysing the electrical power spectrum of the S-SFP by coupling its output directly to a 40 GHz photodiode connected to an ESA. This was done as the M-SFP was swept across resonance as before and is shown in Figure 7.9, where the data was taken simultaneously to the data shown in Figure 7.8. Figure 7.9 clearly indicates the main regions that one expects in phase locked systems (as previously observed in Figures 7.4a and 7.5b), namely regions of beating between the M-SFP and S-SFP indicating unlocked behaviour for large detunings and the quiet central region indicating phase locked performance of the S-SFP. The intensity feature observed around 2 GHz corresponds to the relaxation oscillation frequency of the S-SFP, as shown previously in Figure 6.23. Having clearly demonstrated that it is possible to stably phase lock the S-SFP using the M-SFP in the "off-chip" scheme, the viability of obtaining stable phase locking in the far more interesting "on-chip" scheme is examined, where the circulator is removed and the SFPs were coupled through the variable gain section itself on chip only.

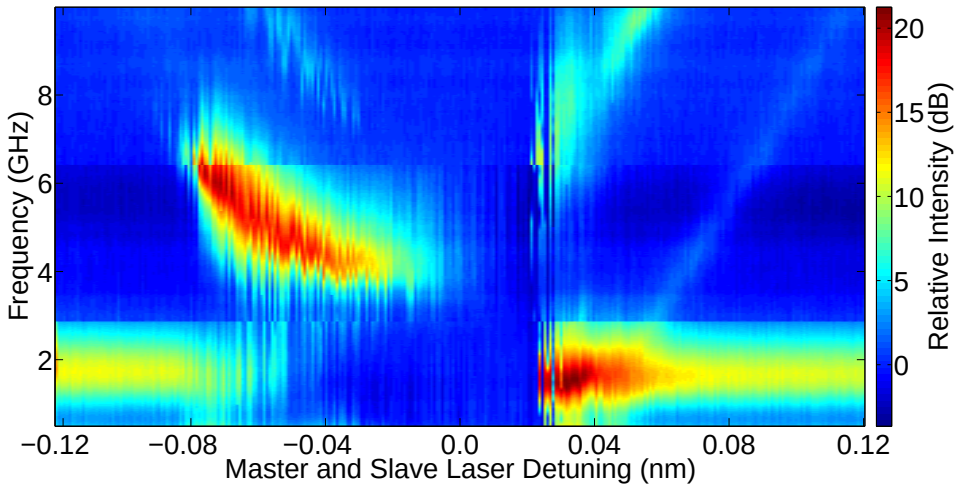

Figure 7.9: ESA trace from the S-SFP as the injected signal from the M-SFP was swept across resonance of one of its lasing modes. Here the beat note between the two signals is examined versus wavelength detuning.

7.3.2 Phase Locking of Single Facet Slotted Fabry Pérot Lasers - On Chip Locking

With the device setup and probed as in Figure 7.1, the coupling scheme referred to as "on-chip" coupling was investigated. This is shown experimentally in Figure 7.10.

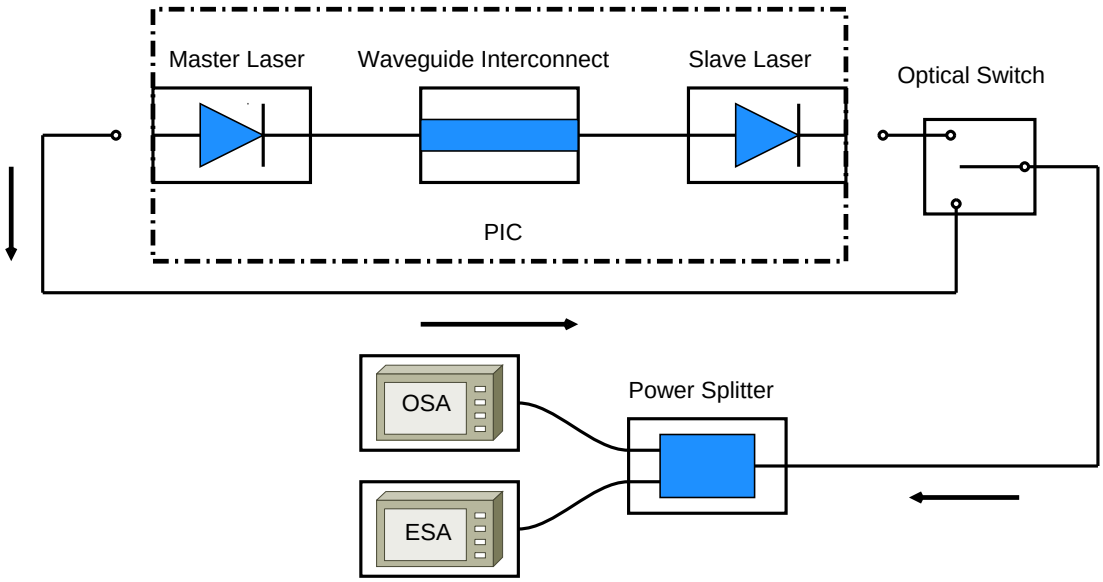

Figure 7.10: Experimental setup showing the on-chip coupling scheme between two lasers on the same integrated device. The waveguide interconnect linking both lasers was biased to transparency, causing the lasers to be coupled on chip without the need for a circulator.

Lensed fibres were coupled to the outputs of SFP 1 and 2, which are again referred to as the Master-SFP, M-SFP, and Slave-SFP, S-SFP, respectively. The optical circulator seen in Figure 7.7, was replaced with a two-way optical switch. This arrangement allowed either the M-SFP or the S-SFP output to be examined on an OSA or ESA, where the optical and electrical characteristics of the signal could be investigated. In the setup shown in Figure 7.10, the variable gain section of the device was forward biased to provide sufficient gain to overcome the otherwise inherent losses in the quantum well waveguide at 1550 nm. Through biasing, this section could be made transparent so that light from the M-SFP could be coupled on chip through the optical waveguide interconnect, to the S-SFP cavity. The mirror sections of both the M-SFP and S-SFP, $I_{Mirror1}$ and $I_{Mirror2}$, were set at 30 mA and the S-SFP gain section, I_{Gain2}, was biased at 35 mA which resulted in typical multimode lasing spectrum of the SFP. The bias on the gain section of the M-SFP, I_{Gain1}, was then varied from 65 mA to 90 mA. This current sweep resulted in the spectral output of the M-SFP to be swept across resonance with the S-SFP, with a detuning between a selected mode in the S-SFP and main lasing mode in the M-SFP of -0.12 nm to $+0.08$ nm.

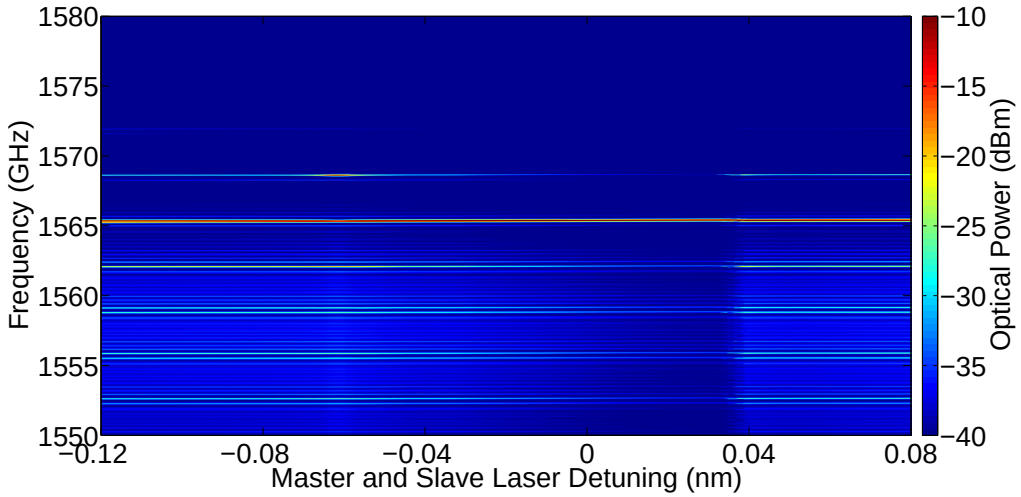

Figure 7.11: OSA trace from the S-SFP as the injected signal from the M-SFP was swept across resonance with one of its lasing modes. For close to zero detuning, suppression of the optical side modes was observed and the S-SFP was shown to lase strongly at the injected wavelength.

The ratio of laser powers around this I_{Gain1} sweep means that the system is quite far from the unidirectional limit and instead displays highly asymmetric bidirectional coupling. Nonetheless, for ease we will continue to refer to the higher power laser as the M-SFP and the lower power laser as the S-SFP. From the point of view of the stability diagram, even at this ratio the behaviour is quite similar to the master-slave system as shown in [98]. For delay-coupled quantum well (QW) lasers a commonly observed feature is chaotic synchronization [173] and chaos is also a common feature in QW lasers undergoing external optical feedback. In both cases the chaos results from the weak damping of the relaxation oscillations (ROs) in these devices. In our system however, the delay between the two lasers is only ~ 0.01 ns which is significantly shorter than the period of the ROs and with such short delays it is well-known that the laser behaviour while undergoing external optical feedback is significantly more stable than in the conventional long-cavity configuration [181]. That such a short delay-time also allows stable phase-locking in bidirectionally coupled configurations even in weakly damped lasers was demonstrated theoretically in [182] and experimentally in [172] where the coupling was face-to-face without the use of isolators. Thus one would expect a region of optical phase locking in the system under investigation here between our M-SFP and S-SFP. The resulting evolution of the optical spectrum of the S-SFP as the M-SFP is swept across resonance is shown in Figure 7.11. The false colour plot shows a clear region where optical suppression of the SFP side modes can be observed as the detuning starts to approach zero nm. In this band, the S-SFP lasing wavelength has also been shifted to 1565 nm, the wavelength of the main lasing mode of the injected M-SFP. As the detuning between the M-SFP and S-SFP increases on the positive side of the Figure to > 0.04 nm, a sharp transition is seen where the

observed optical suppression of the side modes of the S-SFP disappears and it begins to lase multimodally. To further investigate the S-SFP behavior in this area of side mode suppression, the electrical power spectrum of the S-SFP is considered over the same M-SFP gain section current sweep. The false colour plot in Figure 7.12 shows this data which was taken simultaneously to that in Figure 7.11.

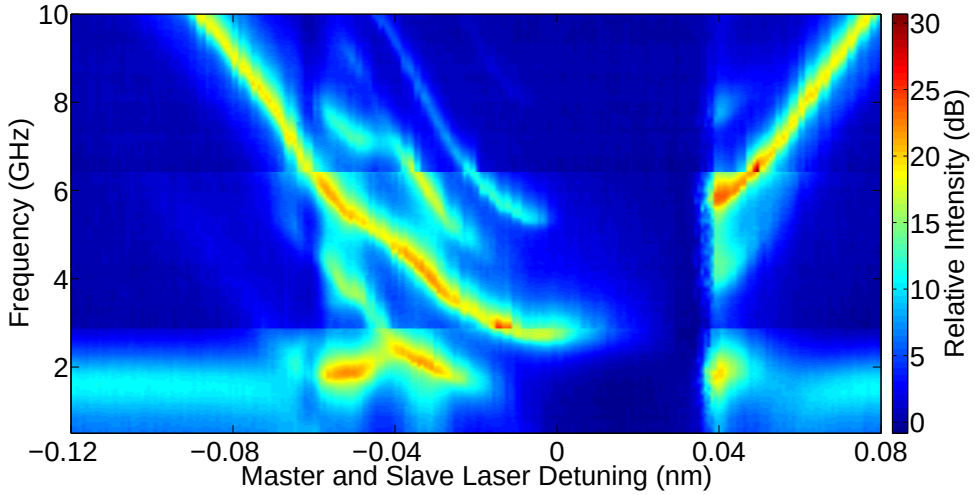

Figure 7.12: ESA trace from S-SFP as the injected signal from the M-SFP was swept across resonance of one of its lasing modes. Here the beat note between the two signals is examined versus wavelength detuning. Close to zero detuning, the beat note is shown to disappear and the SFP lasers enter a stable phase locked regime.

Figure 7.12 clearly indicates the main regions that one expects in phase locked systems, namely regions of beating between the M-SFP and S-SFP signals for large detunings indicating unlocked behaviour, and the quiet central region indicating phase locked performance of the S-SFP. This region shows clear signs of optical phase locking for detunings between 0.0 nm and +0.03 nm which corresponds to an M-SFP gain bias ($I_{Gain\ 1}$) variation of approximately 75 to 78 mA. Both Figures 7.11 and 7.12 demonstrate the successful stable phase locking in the on-chip optical coupling scheme, the first time to our knowledge that an integrated phase locked system has been successfully demonstrated between SFP lasers.

7.3.3 Phase Locking of Single Facet Slotted Fabry Pérot Lasers - Variable Gain

The use of the variable gain section as a variable optical attenuator (VOA) or semiconductor optical amplifier (SOA) in the on-chip coupling scheme is an interesting feature of the system. Biasing of this section allows the coupling between the lasers to be varied. Higher currents provided larger gain which reduced the inherent losses in the optical waveguide in this section due to the quantum wells. Reverse biasing of this sec-

tion caused it to become completely absorbing, decoupling the M-SFP and S-SFP on chip. This results in no phase locking region being formed as the M-SFP was detuned across the S-SFP, unless the SFPs were coupled externally as in the off-chip coupling scheme. The ability to control the coupling between the M-SFP and S-SFP makes this system attractive for studies of non-linear dynamics in coupled oscillator systems, particularly if the width of the phase locking region can also be shown to vary with the SFP coupling.

The gain and mirror section biases of the S-SFP in the same system as before, were both biased to 35 mA with the mirror section of the M-SFP set to 40 mA. The M-SFP was again swept across resonance with the S-SFP while the power spectrum of the S-SFP signal was taken on an ESA. This was done for three different variable gain section biases: 40 mA, 50 mA and 60 mA. The power spectrum for each variation is shown in Figure 7.13.

For a variable gain section bias of 40 mA, the power spectrum 7.13a, shows a very narrow stable phase locking region around a M-SFP bias of 100 mA. As the variable gain section bias is increased to 50 mA and 60 mA, the width of the stable phase locking region is shown to grow, as can be seen in Figures 7.13b and 7.13c. This wider phase locking region is a direct result of the injected power from the master into the slave laser cavity increasing. This is due to the variable gain section becoming less lossy for higher biases. This begins to saturate for variable gain section biases > 60 mA, where the width of the phase locking region sees no appreciable change for an increase in current bias. With this section biased to > 70 mA, the operational wavelength of the slave and master SFPs began to shift as a result of excess leakage current flowing into their mirror sections. In this regime, finding a stable locking region proved difficult as it was not possible to sweep the main M-SFP lasing mode across resonance with a lasing mode of the S-SFP. For this reason, the variable gain section bias was primarily kept at 50 mA which provided excellent power coupling between the M-SFP and S-SFP, while minimising issues with leakage currents and unwanted wavelength detunings. It should be noted that successful stable phase locking on chip has been observed for various values of the biasing on all sections, in addition to those included in the text.

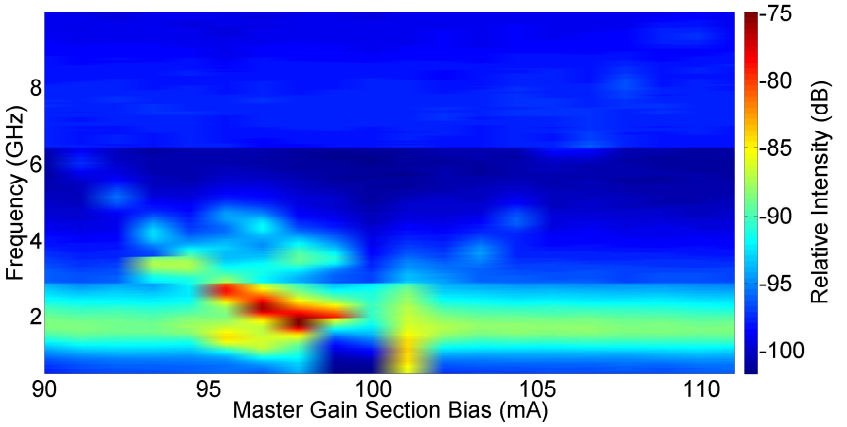

(a) Variable gain section bias of 40 mA

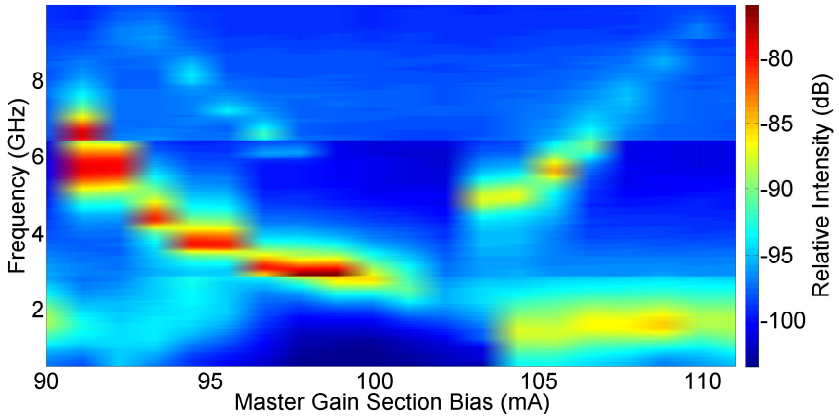

(b) Variable gain section bias of 50 mA

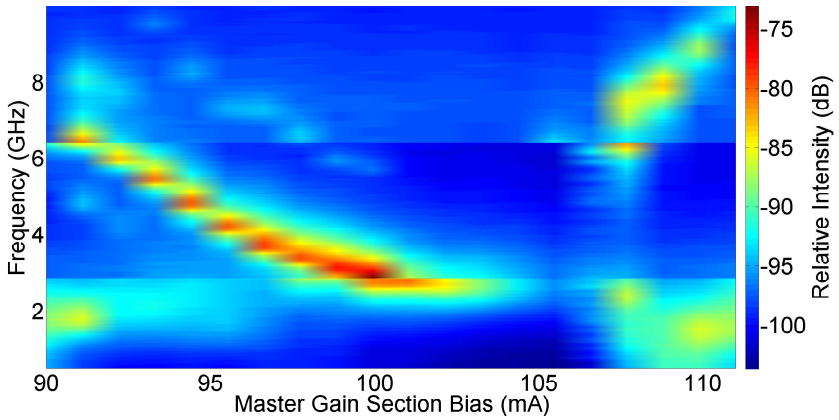

(c) Variable gain section bias of 60 mA

Figure 7.13: ESA traces showing the beat note between the S-SFP and M-SFP as the main lasing mode of the M-SFP was swept across resonance with one of the S-SFP lasing modes.

7.4 Simultaneous Injection Locking and Coherent Signals

In the previous section, stable phase locking was demonstrated in a master-slave system between two monolithically integrated SFP lasers on a single device. Of the two coupling schemes investigated, the on-chip mechanism clearly has the most promise for research purposes and further applications. The ability to create a master-slave system between integrated lasers on PIC offers many exciting possibilities which will be discussed further in this chapter. Of particular interest to the work presented in this thesis is the ability to generate multiple coherent signals using such a system by making use of optical phase locking between two or more identical S-SFPs and one M-SFP. To this end, the device shown in Figure 7.14 was investigated.

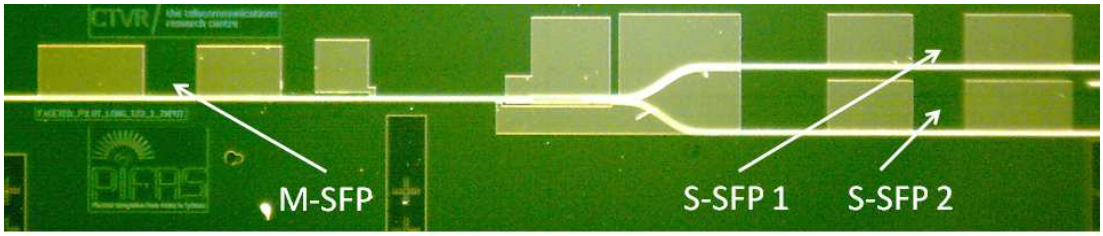

Figure 7.14: Device used to investigate the simultaneous optical phase locking of multiple lasers on the same chip to a single master laster. The master laser (M-SFP) was integrated at the input of a 1×2 MMI, with two further identical SFP lasers integrated on the outputs of the MMI. By forward biasing the central variable gain section consisting of MMI, SOA and MMI output bends; light from the M-SFP could be coupled into both output lasers simultaneously.

Figure 7.14 shows the fabricated device incorporating three identical SFP lasers monolithically integrated on the same structure. As with the device investigated earlier in this chapter, the SFPs are coupled together via an MMI, in this case, a 1×2 MMI coupler. In the previous device, only one of the SFP lasers on the output of the MMI was biased during the experiment. Here, both output lasers are free to be operated at the same time along with the input laser. As before, for convenience the SFP connected to the input of the MMI is referred to as the master SFP (M-SFP), and the top and bottom SFPs connected to the output of the MMI are referred to as Slave SFP 1 (S-SFP 1) and Slave SFP 2 (S-SFP 2), respectively. The addition of the extra SFP on the output makes testing of the device challenging experimentally. Two more probes are required to bias the extra gain and mirror section of the device. The probe setup is shown in Figure 7.15, where the three SFP lasers are biased from individual current sources with each region of the variable gain section (MMI and SOA) probed separately but treated as one common section from a bias point of view.

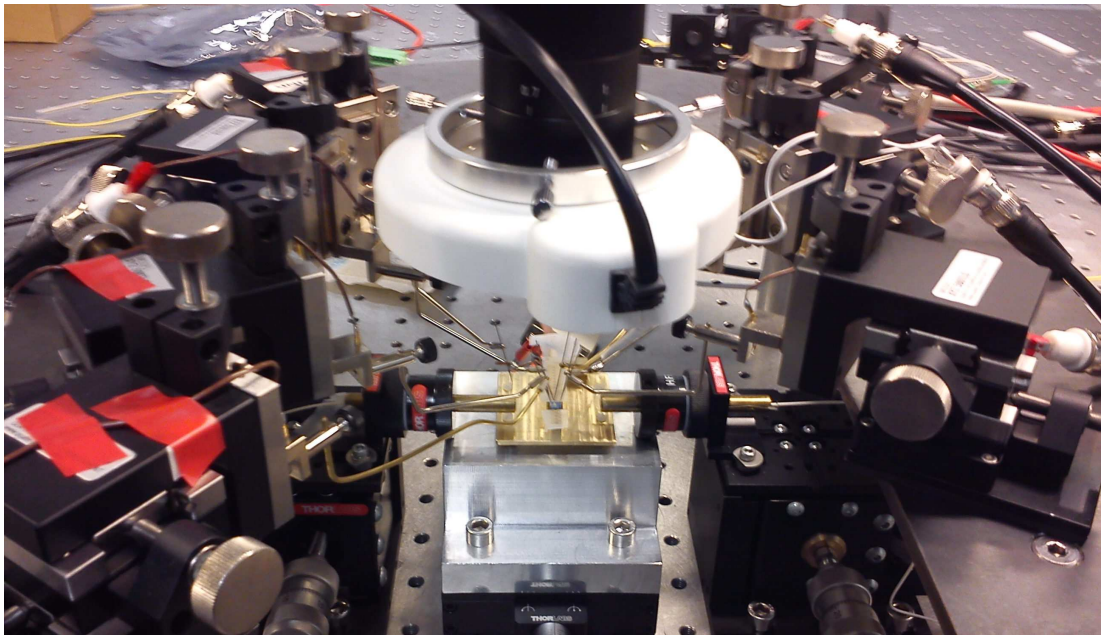

Figure 7.15: Experimental setup showing the device from Figure 7.14 under test. Eight probes were required to bias all three two-section SFP lasers along with the MMI and SOA section. Lensed fibres are coupled at the input and output of the device.

7.4.1 Free-Running Slotted Fabry Pérot Lasers

The variable gain section of the integrated device was initially reverse biased which decoupled the lasers from each other. The free-running spectrum of each SFP could then be examined without the other lasers influencing its behaviour. The gain and mirror sections of both S-SFPs were set to 45 mA and 35 mA, respectively. The M-SFP was biased with a gain section current of 105 mA, and mirror section current of 30 mA. The free-running spectrum of each SFP under these operating biases is shown in Figure 7.16.

Figure 7.16a shows the free-running M-SFP laser as measured by an OSA. A preferential lasing mode is seen at 1577 nm with an SMSR of $\sim$ 30 dB. Figures 7.16b and 7.16c, show the free-running spectra of S-SFP 1 and S-SFP 2, respectively. Although, both S-SFP lasers are biased identically, different spectra are observed for each laser. S-SFP 1 lases with a preferential lasing mode at 1567 nm, with S-SFP 2 lasing at 1563 nm. The difference between the performance of both lasers results from irregularities during fabrication and metal deposition, which can slightly vary the electrical properties of each contact pad.

Even with this in mind, it is clear to see that each SFP has an identical wavelength spacing between modes, as defined by the slot separation of each SFP mirror section. This indicates that the cavity and overall structure of each SFP laser is nominally identical. As can be seen from Figure 7.16a, the M-SFP preferential lasing mode at

1577 nm coincides with a lasing mode of each S-SFP at the current bias conditions. It is this mode on each S-SFP that is intended to be mutually locked to, once the M-SFP signal is injected into S-SFP cavities via the forward biased variable gain section.

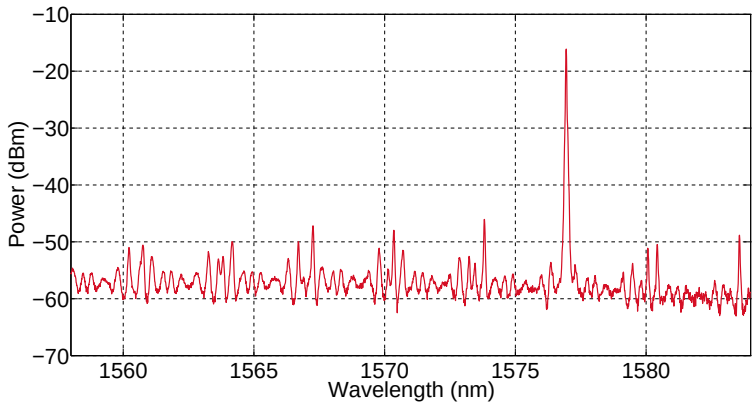

(a) Trace from an OSA showing the free-running spectrum of the M-SFP.

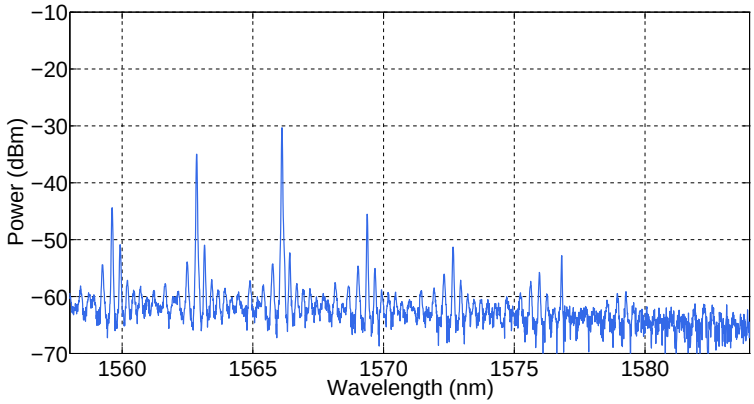

(b) Trace from an OSA showing the free-running spectrum of the S-SFP 1.

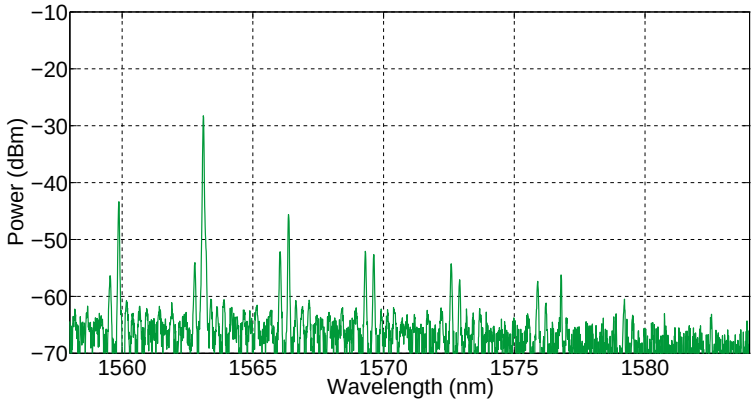

(c) Trace from an OSA showing the free-running spectrum of the S-SFP 2.

Figure 7.16: Optical Spectra of free-running SFP lasers

7.4.2 Optically Phase Locked Slotted Fabry Pérot Lasers

For the SFP lasers shown in Figure 7.16, the reverse biased variable gain section effectively decoupled the lasers from each so that they could be considered free-running and not subject to any optical injection. Forward biasing of the variable gain section, as described in the previous section, allowed the coupling between M-SFP and S-SFPs on chip to be controlled to a high degree. Biasing this section such that it is close to transparency allows all the SFPs to be coupled together. The influence of light coupling from the S-SFPs to the M-SFP is minimised by insuring that the relatives powers between M-SFP and S-SFP are kept at approximately 90:10. This was accomplished by operating the M-SFP at $\sim 3 \times I_{Threshold}$ while the S-SFPs were at $\sim 1 \times I_{Threshold}$. This allowed us to operate in a highly asymmetric coupling regime, which minimised the impact of having no optical isolator on chip.

Due to current leakage between sections on the device while under probing, biasing the variable gain section also induces slight current variations in the mirror sections of all the SFPs on the device. These variations can shift the optical spectra of each laser, resulting in some fine tuning being required to ensure that the main lasing mode of the M-SFP could phase lock to a preferential lasing mode of both S-SFPs simultaneously. This fine tuning determined that a variable gain section bias of 50 mA put us in the correct experimental space to observe simultaneous phase locking. This was determined by monitoring the output from each S-SFP optically and electrically, as the M-SFP was swept across resonance, as with the experiment discussed in the previous section. Figure 7.17 shows the optical output from each SFP, with the variable gain section biased to 50 mA, in the highly asymmetric coupling regime.

Figure 7.17a shows the output from the M-SFP after its signal has been injected into both S-SFP cavities via the variable gain section MMI. The output remains unchanged compared to that of the free-running M-SFP, prior to optical injection. This was to be expected due to being in the highly asymmetric coupling regime, which limited the impact the slave SFPs had on the master. Figures 7.17b and 7.17c show the optical output from both S-SFPs. These outputs are distinctly different to the free-running outputs shown in Figures 7.16b and 7.16c. Significant suppression of the optical side modes of the laser spectra is observed, with each laser now operating at 1577 nm, the main lasing mode of the injected M-SFP as seen in Figure 7.16a. The free-running lasers S-SFP 1 and S-SFP2 show peak powers at their preferential lasing modes of ~ -30 dBm. After the M-SFP has been coupled to the S-SFPs an increase of ~ 5 dB in their peak power was also observed along with the suppression of their side modes. This can best be seen in Figure 7.18, which shows the overlapped output from each SFP laser around the main lasing mode. The SFP lasers are each clearly lasing at the same wavelength of the M-SFP and have been phase locked.

These S-SFP lasers should not only be coherent with each other, but also coherent with

the M-SFP if they are correctly and stably optically phase locked. In the next part of this chapter, the coherence properties of these signals is investigated experimentally.

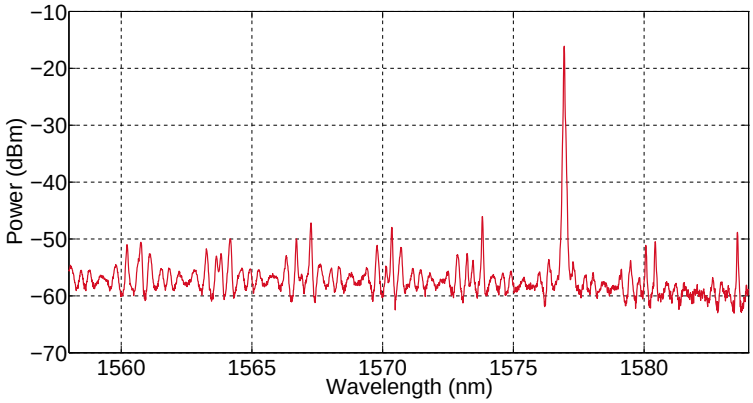

(a) OSA trace from the M-SFP while being injected into the S-SFP cavity, with the system in an optically phase locked regime.

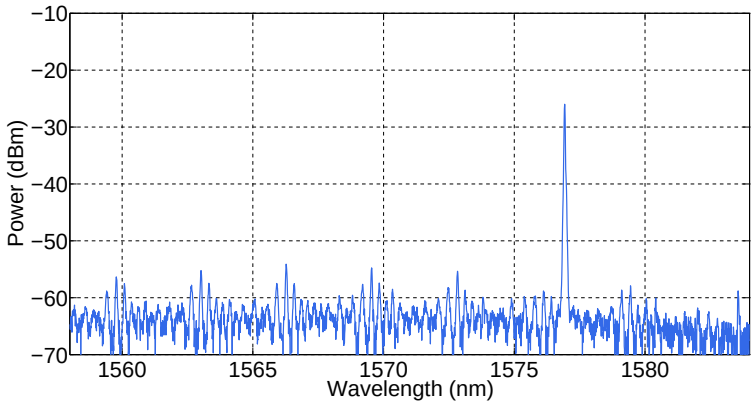

(b) OSA trace from the S-SFP 1 while in an optically phase locked regime.

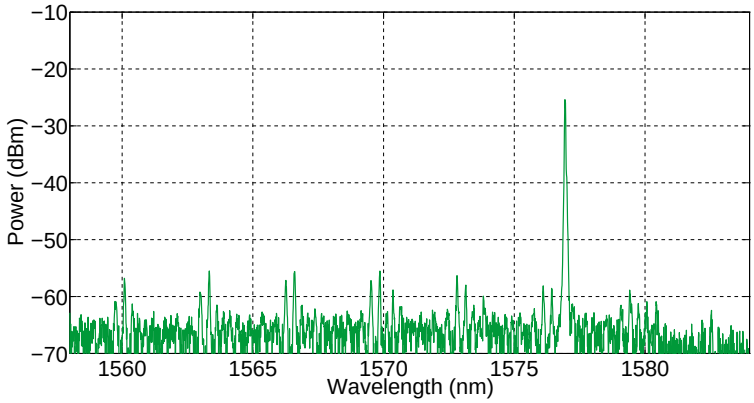

(c) OSA trace from the S-SFP 2 while in an optically phase locked regime.

Figure 7.17: Optical spectra of SFP lasers in optically phase locked regime.

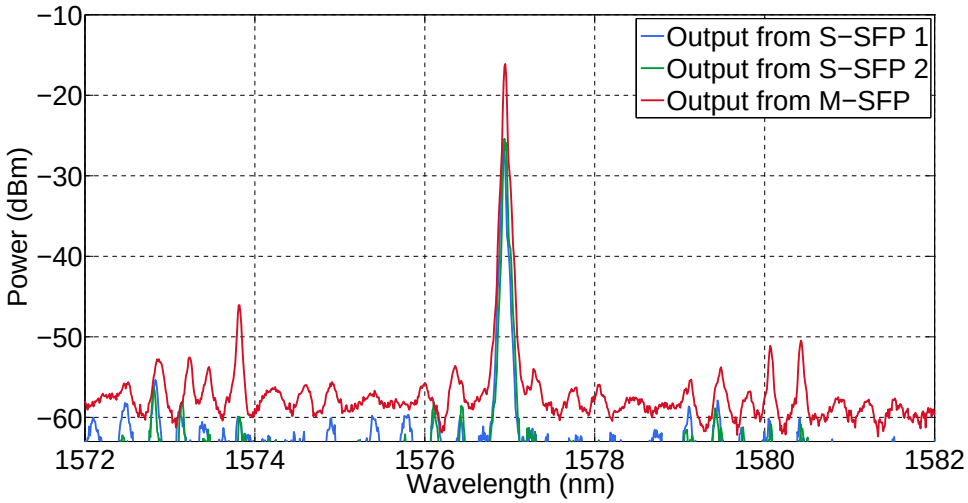

Figure 7.18: Optical spectra from each SFP laser with the system in the phase locked regime. The S-SFP lasers are now lasing at the injected M-SFP wavelength with an increase in their peak powers.

7.4.3 Coherence of Phase Locked Slotted Fabry Pérot Lasers

With both S-SFP lasers now optically phase locked to the M-SFP laser via the on-chip coupling scheme, the coherence properties of each optical signal is next considered. As a direct result of being optically phase locked, the S-SFP signals should not only be coherent with each other, but also coherent with the M-SFP which they are locked to. Investigating coherence between the S-SFPs directly was not possible using the experimental setup previously described. This was due to the limitation of the lensed fibre coupling system used, where it was not possible to use a lensed fibre array to examine both outputs simultaneously. Due to this, coherence between the S-SFP outputs was shown by demonstrating that they were both coherent with the M-SFP individually, and by extension must be coherent with each other.

A schematic of the experimental setup used to examine the coherence between each S-SFP and M-SFP while being optically phase locked is shown in Figure 7.19. As previously discussed, due to being unable to fibre couple both S-SFP outputs simultaneously, only the output from S-SFP 1 or S-SFP 2 could be investigated at any given time. The chosen output can be changed rapidly by adjusting the position of the lensed fibre and realigning the system. With the lensed fibre coupled to S-SFP 1, the phase locked output was passed through a MZM which was driven at 10 GHz and biased at the null. This generated two sidebands which were 20 GHz apart with the carrier suppressed (although still present). The modulated signal was passed through an optical amplifier and then coupled together with the fibre coupled output from the M-SFP, as seen in the Figure 7.19. Coherence between the signals was determined by investigating the linewidth of the beat note between these signals on an ESA.

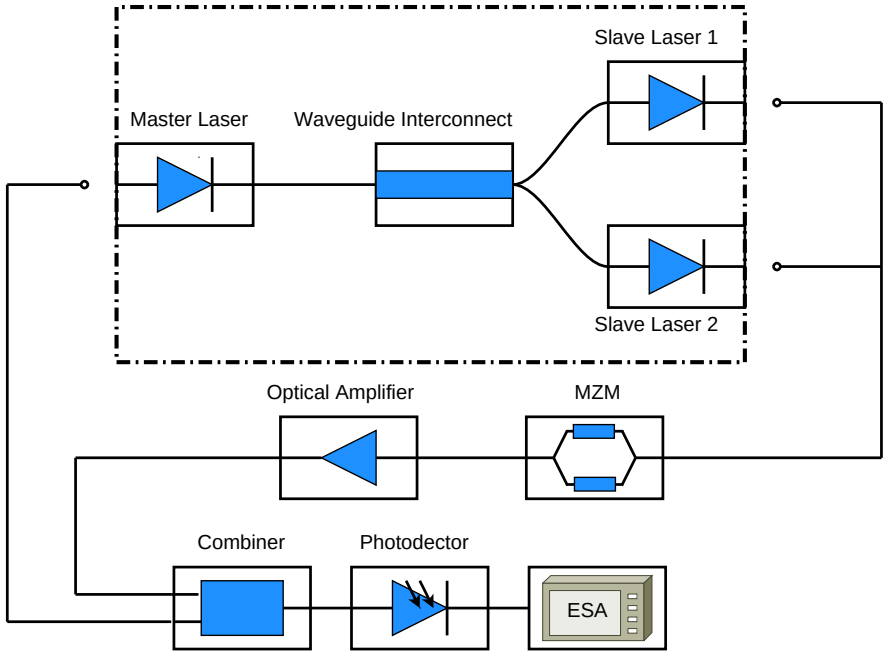

Figure 7.19: Experimental setup showing the system used to test for coherent S-SFP in the optically phase locked regime. The phase locked signal from slave laser 1 or 2 is modulated and coupled with the unmodulated master laser output.

The modulated S-SFP laser was first examined on an ESA where the linewidth of the tone generated between the beating of the two 10 GHz sidebands was examined. This is shown in Figure 7.20, where the 20 GHz tone due to the beating of both sidebands is observed. The same procedure was applied to the modulated M-SFP and its 20 GHz tone is overlapped with the S-SFP result for comparison. The linewidth for both tones was found to be approximately 30 kHz.

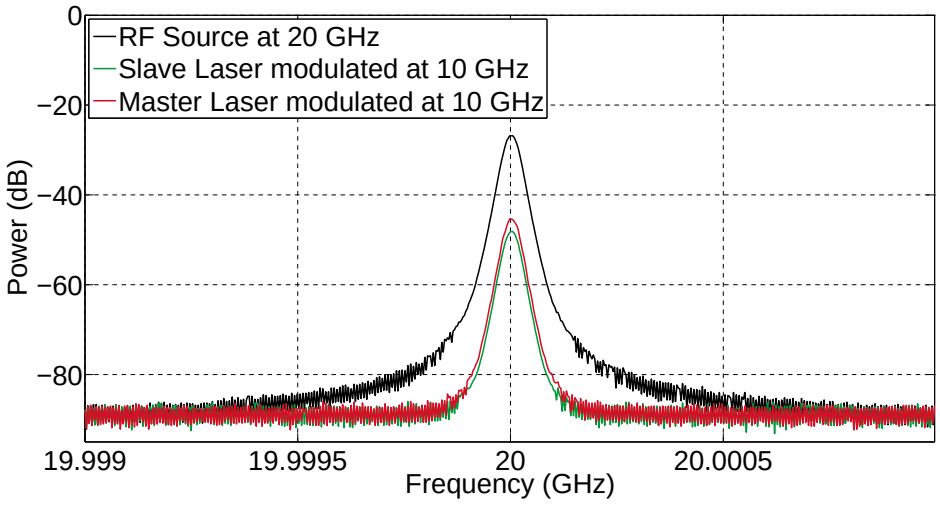

Figure 7.20: ESA traces showing the 20 GHz beat note between both side bands of the modulated M-SFP or S-SFP.

The trace of the RF source used to drive the MZM was examined on the ESA and is also shown in Figure 7.20. The linewidth of the RF source was found to be 30 kHz, which agreed with the measured linewidth of the S-SFP and M-SFP 20 GHz tones. Attention was next turned to the beating of the modulated S-SFP laser 1 with the unmodulated M-SFP signal. Figure 7.21 shows a trace of the 10 GHz beat note between these signals.

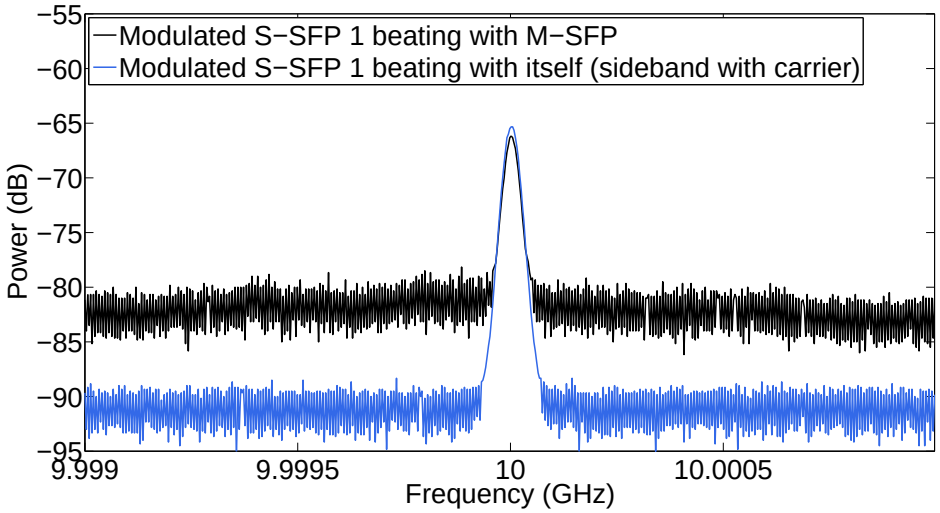

Figure 7.21: ESA trace of the 10 GHz tone generated from modulated S-SFP 1 beating with itself, overlapped with the tone generated from the modulated S-SFP 1 beating with the unmodulated M-SFP in the optically phase locked regime.

Also shown is the ESA trace of the 10 GHz tone generated from just the modulated S-SFP beating with itself. The 10 GHz tone is a result of the S-SFP sidebands beating with the suppressed carrier. As can be seen from the plots in Figure 7.21, the linewidth of the beat note between the modulated S-SFP and unmodulated M-SFP remains at 30 kHz, the linewidth of either modulated SFP by itself. An increase in the noise floor level was also observed, this was due to the addition of both signals. For incoherent signals, a broadening of the beat note would be expected as the signals beat together. The lack of broadening indicates that the S-SFP was indeed coherent with the M-SFP. The experiment was repeated with everything held fixed, except with now the S-SFP 2 coupled to the lensed fibre and modulated at 10 GHz. The ESA traces for S-SFP 2 are shown in Figure 7.22, and again indicate that it is coherent with the M-SFP. With both phase locked S-SFPs shown to be coherent with the M-SFP, it can be concluded that they are coherent with each other.

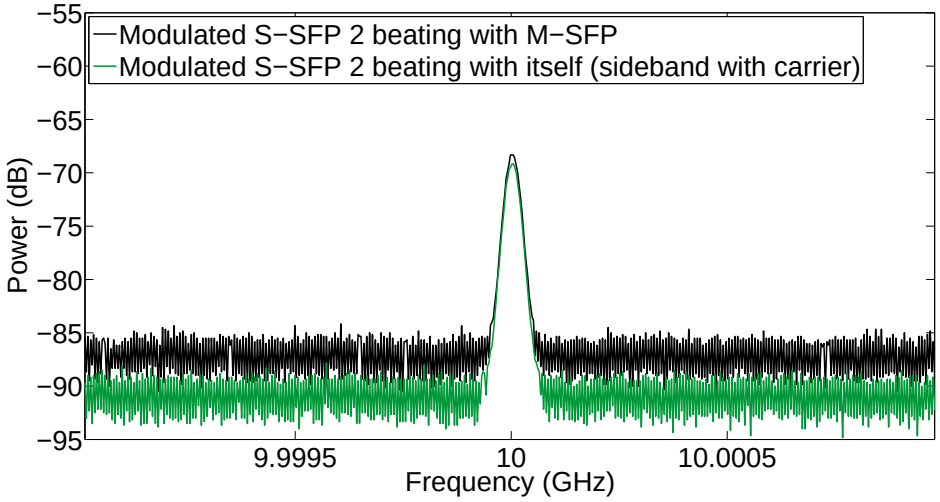

Figure 7.22: ESA trace of the 10 GHz tone generated from modulated S-SFP 2 beating with itself, overlapped with the tone generated from the modulated S-SFP 2 beating with the unmodulated M-SFP in the optically phase locked regime.

7.5 Conclusion

The integrated devices investigated in this work consisted of several identical SFP lasers monolithically integrated together with pseudo-passive waveguide sections to form complex coupled devices. First, the injection locking behaviour of SFP lasers was examined by considering an integrated device where a single SFP laser was biased and free-running. Light from a tunable laser source (TLS) was injected into the SFP cavity, where its optical and power spectra could be observed as the TLS was swept across resonance with a preferential lasing mode of the SFP. This was done for various injection strengths of the TLS, where it was found that stable phase locked regions existed for powers of as little as −7 dBm.

With this known, attention was next switched to whether such a master-slave system could be developed between two identical SFP lasers on the same integrated device. This was done for two cases where different methods of coupling SFPs together were investigated. The off-chip coupling scheme coupled the SFPs externally via lensed fibre placed at each SFP output facet. The optical and power spectrum of the slave SFP was examined as the master SFP was swept across resonance with it. A stable phase locked region was observed in the system where the detuning between the master and slave was close to zero. The next case considered dealt with the far more interesting on-chip coupling scheme. With this, the SFPs were coupled together via the MMI and SOA waveguide sections which connected the SFPs on chip. This allowed light to be coupled between the master and slave lasers directly on-chip. Despite the lack of an optical isolator on chip between the devices, stable phase locking was demonstrated between

the SFPs in a highly asymmetric coupling regime, where the master was operated at a much higher power than the slave.

Biasing of the variable gain section which connected the SFPs together, allowed the coupling between them to be varied considerably. Leaving this section unbiased resulted in close to zero coupling, whereas forward biasing caused the section to become more transparent and increase the coupling strength. Varying the coupling resulted in the injection strength between master and slave to be controlled, which affected the width of the stable phase locked region of the system. This was examined for various gain section biases, where it was found that the width of the stable phase locked region could indeed be controlled.

With optical phase locking between SFPs coupled together on the same monolithically integrated device demonstrated for the first time, the possibility of having multiple simultaneously phase locked SFP lasers on chip was investigated. By coupling a master SFP to two slave SFP lasers simultaneously, a stable phase locked region was found though suitable tuning of the lasers and control of the coupling between them. Finally, these phase locked slave lasers were shown to be coherent with each other, and also coherent with the master laser.

In conclusion, this work has shown stable injection locking of an SFP laser by both an external cavity laser and another SFP laser in an off-chip configuration. Based on the successful locking performance of the SFP laser, an integrated on-chip phase locked system was developed. The PIC is comprised of two SFP lasers, coupled via a waveguide section which can act as a variable gain section. Stable phase locking has been successfully demonstrated in this on-chip integrated system without the need for an optical isolator, for the first time to our knowledge. The variable gain section can be used as a VOA/SOA to allow for the coupling strength to be varied. By controlling the bias across this section it has been shown that the width of the stable phase locking region can be varied.

Chapter 8

Conclusions and Future Work

The work presented in this thesis has focused on the design and development of Photonic Integrated Circuits (PICs) for advanced coherent communication systems. Photonic integration offers excellent potential for combining otherwise discrete system components together on a single device to provide robust, power efficient and cost effective solutions. In particular, the design of optical modulators has been an area of immense interest in recent times. Not only has research been aimed at developing modulators with faster data rates, but also there is a push towards making modulators as compact as possible. The realisation of compact modulators on integrated devices was discussed in chapter 1, where some of the main topics of this thesis were also introduced.

The primary goal of this work was to develop a photonic integrated device for use with compact high speed EAM based modulators [5]. In particular, the work investigated the integration of passive waveguide components with lasers to generate coherent optical signals on chip. Such a device offers significant advantages over current technologies, where losses due to fibre couplings can be reduced by having integrated lasers while also allowing the use of on-chip optically phase locked slave lasers to improve the overall power performance.

The full development of a compact high speed EAM based modulator would require the integration of multiple lasers, EAMs and passive components together to form a functioning device. This development was not possible on the time-scale of this thesis. Instead, this work was aimed at developing the passive waveguide components for such modulators, along with their monolithic integration with multiple lasers, by developing new PICs. Ensuring that multiple coherent signals can be generated on a device using optical phase locked slave lasers was of particular importance to this work. Without multiple coherent signals available, an EAM based modulator cannot be realised on chip.

In chapters 2 and 3 of this thesis, MMI couplers were investigated as a means of combining or splitting optical signals on integrated devices. Numerical models were

developed in C++ to optimise MMI designs, which were validated by experimentally testing fabricated devices. A new method of fibre coupling to ridge waveguide devices was discussed in chapter 4, which provided an efficient means of testing passive devices.

In chapters 5 and 6, the design and development of photonic integrated devices which combined SFP lasers, MMIs and SOAs was covered in detail. The simplest of these devices investigated the monolithic integration of MMIs with SOAs and SFP lasers; and demonstrated the splitting and routing of light from an SFP laser on a PIC for the first time. Based on this device, a PIC was formed which integrated SFP lasers on the input and output arms of an MMI coupler, in effect forming a system of mutually coupled lasers. Both these PICs are shown in Figure 8.1.

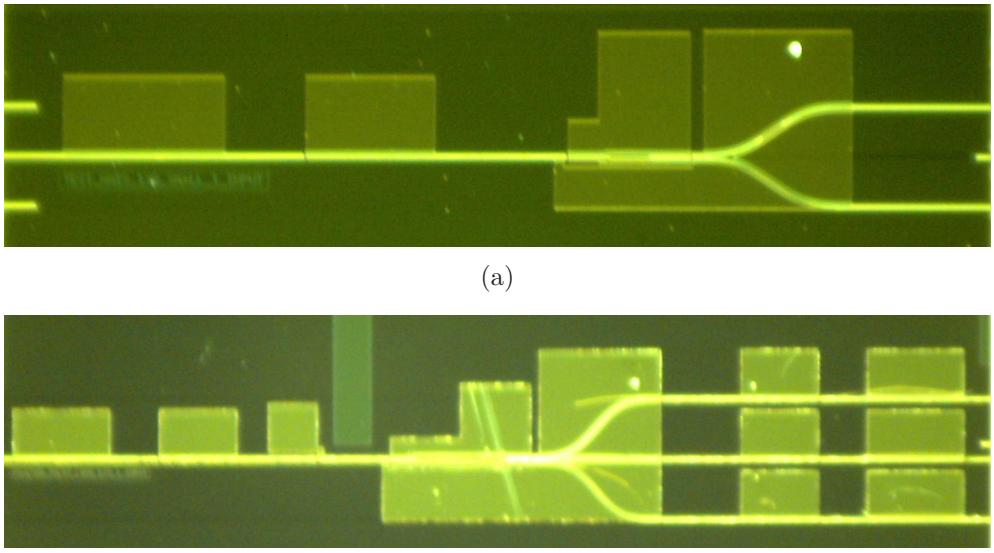

(a)

(b)

Figure 8.1: (a) Image of SFP laser integrated with an MMI and SOA. (b) Image of device with a system of mutually coupled SFP lasers.

The highlight of the work presented in this thesis was discussed in chapter 7 and involved the experimental testing of the device shown in Figure 8.1b, where multiple SFP lasers were coupled together via an MMI and SOA. Optical phase locking was demonstrated between integrated SFP lasers for the first time, where a master-slave system was formed in a highly asymmetric coupling regime. Based on this result, the simultaneous optical phase locking of multiple SFP lasers on a single integrated device was shown to be possible. This was accomplished on a device using one master and two slave lasers, which were shown to be coherent after undergoing optical phase locking.

The work presented in this thesis has successfully demonstrated the design of photonic integrated devices for coherent signal generation. The devices combined SFP lasers, MMIs and SOAs in single epitaxial growth, monolithically integrated PICs. The devices have the potential to play a key role in future optical communication systems. In

particular, they offer exciting potential for use in compact QPSK EAM based modulators.

8.1 Outlook and Future Work

The work presented in this thesis has demonstrated a photonic device capable of generating coherent optical signals using a single epitaxial growth, monolithically integrated process. The lasers chosen for these integrated devices were based on single facet Slotted Fabry Pérot (SFP) designs. As shown in chapter 5, the optical output of these lasers was only tunable only over a very short range before mode and wavelength jumps occurred. This limits the use of these devices to applications which require only single wavelength operation, with little wavelength tuning through electrical bias, or else where thermal heating can be used to tune the laser. A natural extension of this work is to use lasers which can provide tunability over wider ranges. Moving to a fully facetless SFP is one such option, where the single cleaved facet is replaced by a secondary etched mirror. This extra mirror section provides finer control over the output laser spectrum by allowing precise Vernier tuning of each sections transmission spectrum. Devices based on these lasers were included on the lithographical mask designed during this work. However, due to their added complexities and extra probes required for biasing each section, they were not investigated. An example of an array of facetless SFP lasers is shown in Figure 8.2.

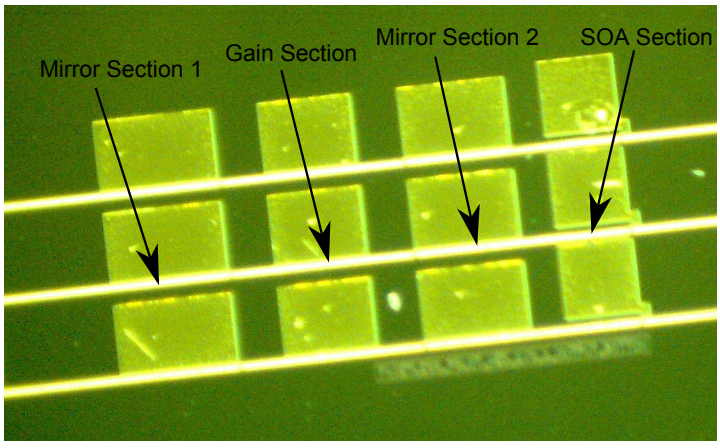

Figure 8.2: An array of facetless Slotted Fabry Pérot lasers.

MMIs were investigated extensively in this thesis, where the models developed during this work demonstrated excellent agreement with experimentally tested devices. A limitation of MMIs is their behaviour when acting as optical combiners. Strict phase relations must exist between optical signals to be combined, or the coupling efficiency of the MMI will be adversely affected. When considering MMIs for use as optical couplers in the compact QPSK modulators discussed in chapter 1 and in Ref. [5],

MMIs are seen to be a poor choice for combining the channels after being modulated by the EAMs. This is due to the phase differences which exist between each arm of the QPSK modulator. Instead, star couplers are used as optical combiners where they can linearly combine signals with different phase relationships. Although star couplers were discussed and modelled in Appendix B, they were not examined experimentally during this work. Similarly to the facetless SFP lasers discussed previously, star coupler designs were included on the lithographical mask used to create the devices covered in this thesis. A star coupler device designed to combine the optical signals from three facetless lasers to a single output waveguide, is shown in Figure 8.3. The testing of such a device was beyond the scope of this work, due to the experimental difficulties associated with testing such a large and complex PIC. Fourteen single tip probes are required to bias each contact pad, which is impractical using the probe station setup described in chapter 5.

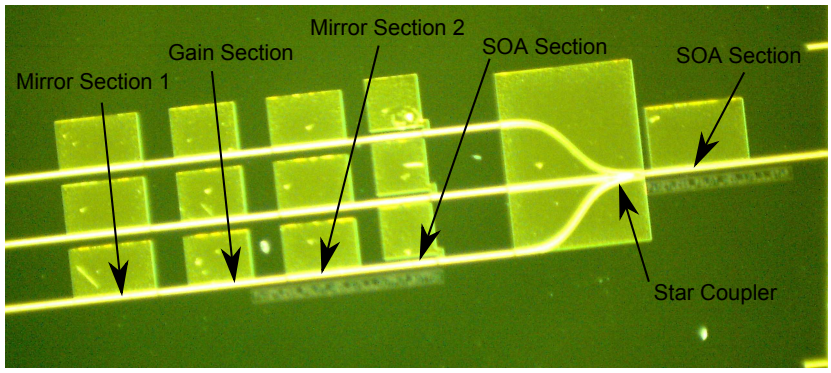

Figure 8.3: An array of facetless Slotted Fabry Pérot lasers integrated with a star coupler which can combine their outputs into a single waveguide.

Facetless lasers and star couplers have the potential to be used in conjunction with the integrated devices considered in this thesis, to form ever more complex and interesting PICs. In particular, this work has laid the foundation for future investigations of PICs where mutually coupled SFP lasers can be examined experimentally. The most complex PIC envisioned throughout this work is shown in Figure 8.4.

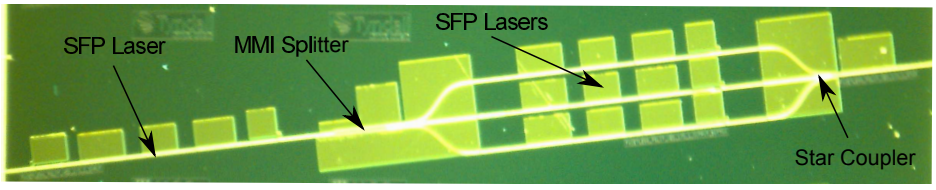

Figure 8.4: Facetless SFP lasers integrated together to form a system of mutually coupled system of lasers similar to device based on single facet SFP lasers examined in this thesis.

This device combines almost all the elements required to make a QPSK modulator that relies on mutually coupled, integrated SFP lasers. The realisation of such a device

requires significant work from an experimental testing viewpoint, along with further analysis of star couplers. Such a device almost certainly necessitates the use of a custom multi-contact probe to allow individual biasing of each of the twenty-one contact pads present. With the ability to test such a device in place, the results from this work lend confidence to its ability to create three or more coherent SFP laser outputs which can be combined together into a single waveguide. In addition to this, it is hoped that future work in the area can incorporate EAMs with such a design. Previous research in the field has shown that SFPs can be integrated with EAMs [97]. With the application of EAMs to the work already discussed in this thesis, the schematic outline of a proposed QPSK modulator is shown in Figure 8.5. This modulator relies on phase locked lasers to generate coherent power efficient output signals. By controlling the EAMs on the two outer channels of the device, the signals can be combined together to form the four required symbols of a QPSK modulation scheme, as discussed in chapter 1. The development of such a modulator is a highly ambitious goal, but one that offers excellent potential for applications in the area of integrated transmitters.

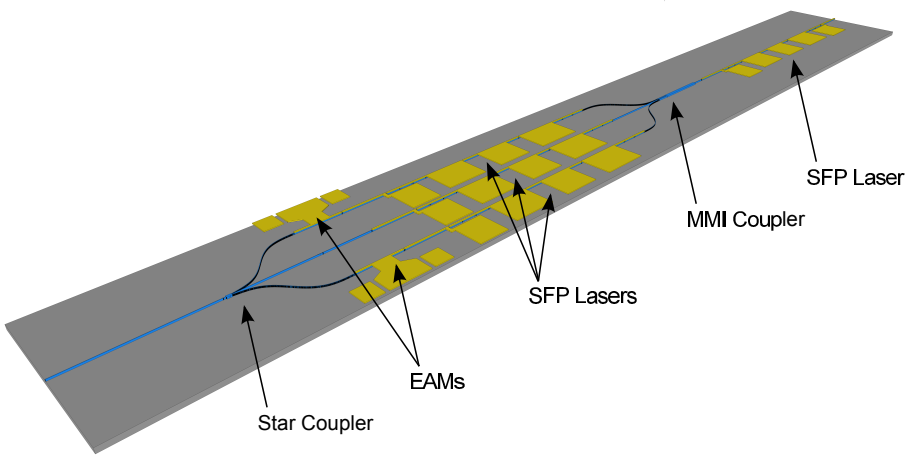

Figure 8.5: Schematic of proposed QPSK modulator.

8.2 Summary

The main results presented in this thesis focused on the testing of an integrated photonic device for coherent signal generation. The development of such a PIC required careful design of different sub-elements required to form more complex devices. In particular, the modelling and optimisation of MMIs played a key role in the successful implementation of the integrated power splitter discussed in chapter 5. Demonstrating an integrated source and splitter on chip using a monolithically integrated process with a single growth step, offers wide spread applications in any number of different devices. The primary device considered in this thesis relied on MMIs to split and combine the optical signals from multiple integrated SFPs. The resulting mutually coupled system

was used to investigate optical phase locking of lasers in a strongly bi-directional coupling regime. Phase locking between integrated SFP lasers was demonstrated for first time and was used as a means to generate coherent optical signals.

Bibliography

[1] Internet World Stats. http://www.internetworldstats.com.

[2] C. Labovitz, S. Iekel-Johnson, D. McPherson, J. Oberheide, and F. Jahanian. Internet inter-domain traffic. *SIGCOMM Comput. Commun. Rev.*, 41(4), August 2010.

[3] TeleGeography. http://www.telegeography.com.

[4] J. H. den Besten. *Integration of Multiwavelength Lasers with Fast Electro-optical Modulators*. Technische Universiteit Eindhoven, 2004.

[5] C. R. Doerr, L. Zhang, P. J. Winzer, J. H. Sinsky, A. L. Adamiecki, N. J. Sauer, and G. Raybon. Compact high-speed InP DQPSK Modulator. *Photonics Technology Letters, IEEE*, 19(15):1184–1186, 2007.

[6] S. C. Nicholes, M. L. Mašanović, B. Jevremović, E. Lively, L. A. Coldren, and D. J. Blumenthal. An 8x8 InP monolithic tunable optical router (MOTOR) packet forwarding chip. *J. Lightwave Technol.*, 28(4):641–650, Feb 2010.

[7] L. Coldren. InP based photonic integrated circuits. In *Conference on Lasers and Electro-Optics*, 2008.

[8] R. Sheehan. *The Design of Curved Optical Waveguides: Analytical and Numerical Analysis*. PhD thesis, University College Cork, Ireland, 2013.

[9] P. W. Shumate. Fiber-to-the-home. *J. Lightwave Technol.*, 26(9):1093–1103, May 2008.

[10] Q. Zhang, L. Cheng, and R. Boutaba. Cloud computing: state-of-the-art and research challenges. *Journal of Internet Services and Applications*, 1(1):4–13, 2010.

[11] H. Yu, D. Zheng, B. Y. Zhao, and W. Zheng. Understanding user behavior in large-scale video-on-demand systems. *SIGOPS Oper. Syst. Rev.*, 40(4):333–344, April 2006.

[12] Sandvine. Global internet phenomena https://www.sandvine.com/trends/global-internet-phenomena/.

[13] M. Conti, S. Chong, S. Fdida, W. Jia, H. Karl, Y. Lin, P. Mähönen, M. Maier, R. Molva, R. Uhlig, and M. Zukerman. Research challenges towards the future internet. *Computer Communications*, 34(18):2115 – 2134, 2011.

[14] D. Williams, A. Gower, J. Meenowa, and J. Wakeling. A user centred approach to evaluating the future demand for bandwidth from consumers. In *Design, User Experience, and Usability. Web, Mobile, and Product Design*, pages 150–159. Springer, 2013.

[15] E. B. Desurvire. Capacity demand and technology challenges for lightwave systems in the next two decades. *Lightwave Technology, Journal of*, 24(12):4697–4710, 2006.

[16] T. H. Maiman. Stimulated optical radiation in ruby. 1960.

[17] G. E. Keiser. A review of wdm technology and applications. *Optical Fiber Technology*, 5(1):3 – 39, 1999.

[18] L. Cimini Jr. Analysis and simulation of a digital mobile channel using orthogonal frequency division multiplexing. *Communications, IEEE Transactions on*, 33(7):665–675, 1985.

[19] S. Weinstein and P. Ebert. Data transmission by frequency-division multiplexing using the discrete fourier transform. *Communication Technology, IEEE Transactions on*, 19(5):628–634, 1971.

[20] G. R. Hill. Wavelength domain optical network techniques. *Proceedings of the IEEE*, 78(1):121–132, 1990.

[21] T. Miki. Optical transport networks. *Proceedings of the IEEE*, 81(11):1594–1609, 1993.

[22] A. Gnauck, R. W. Tkach, A. Chraplyvy, and T. Li. High-capacity optical transmission systems. *Journal of Lightwave Technology*, 26(9):1032–1045, 2008.

[23] C. A. Brackett. Dense wavelength division multiplexing networks: principles and applications. *Selected Areas in Communications, IEEE Journal on*, 8(6):948–964, 1990.

[24] M. Pascual, P. Daniel, and C. Jose. Modeling and design of arrayed waveguide gratings. *J. Lightwave Technol.*, 20(4):661, Apr 2002.

[25] M. C. Parker, S. D. Walker, A. Yiptong, and R. J. Mears. Applications of active arrayed-waveguide gratings in dynamic WDM networking and routing. *Lightwave Technology, Journal of*, 18(12):1749–1756, 2000.

[26] D. Sadot and E. Boimovich. Tunable optical filters for dense WDM networks. *Communications Magazine, IEEE*, 36(12):50–55, 1998.

[27] J. Elmirghani and H. Mouftah. Technologies and architectures for scalable dynamic dense wdm networks. *Communications Magazine, IEEE*, 38(2):58–66, 2000.

[28] Spectral grids for WDM applications: DWDM frequency grid. http://www.itu.int/rec/t-rec-g.694.1/en.

[29] B. Bakhshi, M. Manna, G. Mohs, D.I. Kovsh, R. L. Lynch, M. Vaa, E. A. Golovchenko, W. W. Patterson, W. T. Anderson, P. Corbett, S. Jiang, M. M. Sanders, H. Li, G. T. Harvey, A. Lucero, and S. M. Abbott. First dispersion-flattened transpacific undersea system: from design to terabit/s field trial. *Lightwave Technology, Journal of*, 22(1):233–241, 2004.

[30] E. J. Tyler, P. Kourtessis, M. Webster, E. Rochart, T. Quinlan, S. E. M Dudley, S.D. Walker, R.V. Penty, and I.H. White. Toward terabit-per-second capacities over multimode fiber links using SCM/WDM techniques. *Lightwave Technology, Journal of*, 21(12):3237–3243, Dec 2003.

[31] P. Bakopoulos and H. Avramopoulos. Multi-wavelength laser source for dense wavelength division multiplexing networks. In *Optical Fiber Communication and the National Fiber Optic Engineers Conference, 2007. OFC/NFOEC 2007. Conference on*, pages 1–3, 2007.

[32] T.J. Xia, G. Wellbrock, B. Basch, S. Kotrla, W. Lee, T. Tajima, K. Fukuchi, M. Cvijetic, J. Sugg, Y. Ma, B. Turner, C. Cole, and C. Urricariet. End-to-end native IP data 100g single carrier real time DSP coherent detection transport over 1520-km field deployed fiber. In *Optical Fiber Communication (OFC), collocated National Fiber Optic Engineers Conference, 2010 Conference on (OFC/NFOEC)*, pages 1–3, March 2010.

[33] P.J. Winzer, G. Raybon, and Marcus Duelk. 107-Gb/s optical ETDM transmitter for 100G ethernet transport. In *Optical Communication, 2005. ECOC 2005. 31st European Conference on*, volume 6, pages 1–2 vol.6, Sept 2005.

[34] A. D. Ellis and F. Gunning. Spectral density enhancement using coherent WDM. *Photonics Technology Letters, IEEE*, 17(2):504–506, 2005.

[35] S. K. Ibrahim, J. Zhao, F. Gunning, P. Frascella, F.H. Peters, and A. D. Ellis. Towards a practical implementation of coherent WDM: Analytical, numerical, and experimental studies. *Photonics Journal, IEEE*, 2(5):833–847, 2010.

[36] A. D Ellis, F. Gunning, and T. Healy. Coherent wdm: The achievement of high information spectral density through phase control within thetransmitter. In *Optical Fiber Communication Conference and Exposition and The National Fiber Optic Engineers Conference*, page OThR4. Optical Society of America, 2006.

[37] A. R. Chraplyvy and P. S. Henry. Performance degradation due to stimulated

raman scattering in wavelength-division-multiplexed optical-fibre systems. *Electronics Letters*, 19(16):641–643, 1983.

[38] D. Benedikovic, J. Litvik, M. Kuba, M. Dado, and J. Dubovan. Modeling of WDM transmission system with high-order phase modulation formats. In *Telecommunications and Signal Processing (TSP), 2012 35th International Conference on*, pages 325–329, July 2012.

[39] R. Freund, M. Seimetz, L. Molle, T. Baghdasaryan, M. Forzati, and J. Martensson. Next generation optical networks based on higher-order modulation formats, coherent receivers and electronic distortion equalization. In *ICTON Mediterranean Winter Conference,2009. ICTON-MW 2009. 3rd*, pages 1–6, Dec 2009.

[40] M. Moghaddasi and S. B. A. Rahman. Comparison between NRZ and RZ-OOK modulation format in chromatic dispersion compensation in both electrical and optical compensator. In *Business, Engineering and Industrial Applications (ISBEIA), 2011 IEEE Symposium on*, pages 494–497, 2011.

[41] E. Granot. Fundamental dispersion limit for spectrally bounded on-off-keying communication channels and its implications to quantum mechanics and the paraxial approximation. *EPL (Europhysics Letters)*, 100(4):44004, 2012.

[42] S. Benedetto and E. Biglieri. *Principles of Digital Transmission: With Wireless Applications*. Information Technology Series. Springer, 1999.

[43] X. Liu. Nonlinear effects in phase shift keyed transmission. In *Optical Fiber Communication Conference, 2004. OFC 2004*, volume 2, pages 3 pp. vol.2–, 2004.

[44] P. J. Winzer and R. Essiambre. Advanced optical modulation formats. *Proceedings of the IEEE*, 94(5):952–985, 2006.

[45] A. Tzanakaki, I. Zachropoulos, D. Parcharidou, and I. Tomkos. Performance optimization using advanced modulation formats in wdm metropolitan area networks. In *Transparent Optical Networks, 2004. Proceedings of 2004 6th International Conference on*, volume 1, pages 81–86 vol.1, 2004.

[46] A. H. Gnauck and P. J. Winzer. Optical phase-shift-keyed transmission. *Lightwave Technology, Journal of*, 23(1):115–130, 2005.

[47] Y. Jianjun, H. Ming-Fang, Q. Dayou, C Lin, and C Gee-Kung. Centralized lightwave WDM-PON employing 16-QAM intensity modulated OFDM downstream and OOK modulated upstream signals. *Photonics Technology Letters, IEEE*, 20(18):1545–1547, 2008.

[48] P. J. Winzer, G. Raybon, H. Song, A. Adamiecki, S. Corteselli, A. H. Gnauck, D. A. Fishman, C. R. Doerr, S. Chandrasekhar, L. L. Buhl, T. J. Xia, G. Wellbrock, W. Lee, B. Basch, T. Kawanishi, K. Higuma, and Y. Painchaud. 100-Gb/s

DQPSK transmission: From laboratory experiments to field trials. *Lightwave Technology, Journal of*, 26(20):3388–3402, 2008.

[49] Y. Tsuyoshi. High-speed directly modulated lasers. In *Optical Fiber Communication Conference*, page OTh3F.5. Optical Society of America, 2012.

[50] Y. Matsui, D. Mahgerefteh, X. Zheng, C. Liao, Z.F. Fan, K. McCallion, and P. Tayebati. Chirp-managed directly modulated laser (CML). *Photonics Technology Letters, IEEE*, 18(2):385–387, 2006.

[51] G. P. Agrawal and M. J. Potasek. Effect of frequency chirping on the performance of optical communication systems. *Opt. Lett.*, 11(5):318–320, May 1986.

[52] Y. R. Shen. *The principles of nonlinear optics*. Wiley classics library. Wiley-Interscience, 2003.

[53] I. Betty, M. G. Boudreau, R. Longone, R. A. Griffin, L. Langley, A. Maestri, A. Pujol, and B. Pugh. Zero chirp 10 Gb/s MQW InP Mach-Zehnder Transmitter with Full-Band Tunability. In *Optical Fiber Communication and the National Fiber Optic Engineers Conference, 2007. OFC/NFOEC 2007. Conference on*, pages 1–3, 2007.

[54] G. Kazuhiro, O. Kenji, K. HiroyukI, T. Yoshihiro, O. Kensuke, L. Tsung-Yang, T. Xiaoguang, L. Guo-Qiang, and K. Dim-Lee. 11-gb/s 80-km transmission performance of zero-chirp silicon mach zehnder modulator. *Opt. Express*, 20(26):B350–B356, Dec 2012.

[55] H. Keang-Po and C Han-Wei. Generation of arbitrary quadrature signals using one dual-drive modulator. *J. Lightwave Technol.*, 23(2):764, Feb 2005.

[56] T. Sakamoto, A. Chiba, and T. Kawanishi. 50-Gb/s 16 QAM by a quad-parallel mach-zehnder modulator. In *Optical Communication - Post-Deadline Papers (published 2008), 2007 33rd European Conference and Exhibition of*, pages 1–2, 2007.

[57] M. Daikoku, I. Morita, H. Taga, H. Tanaka, T. Kawanishi, T. Sakamoto, T. Miyazaki, and T. Fujita. 100-Gb/s DQPSK transmission experiment without OTDM for 100g ethernet transport. *Lightwave Technology, Journal of*, 25(1):139–145, 2007.

[58] R. Nagarajan, C. H. Joyner, and et al. Large-scale photonic integrated circuits. *Selected Topics in Quantum Electronics, IEEE Journal of*, 11(1):50–65, 2005.

[59] C. L. M. Daun, H. Yang, J. O'Callaghan, R. J. Young, K. Thomas, E. Pelucchi, B. Corbett, and F. Peters. Design of single growth epitaxial structures for monolithic integration of single frequency laser and electro-absorption modulators. In

LEOS Annual Meeting Conference Proceedings, 2009. LEOS '09. IEEE, pages 219–220, 2009.

[60] I. Kang. Interferometric operation of an electroabsorption modulator for PSK modulation and OOK modulation with performance enhancements. In *Optical Communications, 2006. ECOC 2006. European Conference on*, pages 1–2, 2006.

[61] H. Kawanishi, Y. Yamauchi, N. Mineo, Y. Shibuya, H. Mural, K. Yamada, and H. Wada. EAM-integrated DFB laser modules with more than 40-GHz bandwidth. *Photonics Technology Letters, IEEE*, 13(9):954–956, 2001.

[62] C. L. M. Daunt, J. O'Callaghan, L. Ko-Hsin, Y. Hua, R.J. Young, K. Thomas, E. Pelucchi, B. Corbett, and F. H. Peters. Compact electroabsorption modulators for photonic integrated circuits, using an isolated pedestal contact scheme. *Photonics Technology Letters, IEEE*, 24(5):356–358, 2012.

[63] I. Kang, S. Chandrasekhar, L. Buhl, P. G. Bernasconi, X. Liu, G. Raybon, C. R. Giles, C. Kazmierski, N. Dupuis, J. Decobert, F. Alexandre, C. Jany, A. Garreau, J. Landreau, M. Rasras, M. Cappuzzo, L. T. Gomez, Y. F. Chen, M. P. Earnshaw, J. Lee, and A. Leven. Pulse-carver-free 50-gb/s rz-dqpsk generation using hybrid photonic-integrated electroabsorption modulators. In *Optical Communication, 2008. ECOC 2008. 34th European Conference on*, pages 1–2, 2008.

[64] M. Shin, J. Lim, J. Kim, C. Y. Park, J. S. Kim, K. E. Pyun, and S. Hong. Optical BPSK subcarrier modulation using integrated hybrid device. *Electronics Letters*, 36(21):1797–1798, 2000.

[65] R. Walker. High-speed III-V semiconductor intensity modulators. *Quantum Electronics, IEEE Journal of*, 27(3):654–667, 1991.

[66] C. R. Doerr, P. J. Winzer, L. Zhang, L. Buhl, and N. Sauer. Monolithic inp 16-qam modulator. In *Optical Fiber Communication Conference/National Fiber Optic Engineers Conference*, page PDP20. Optical Society of America, 2008.

[67] R. Griffin, R. Johnstone, R. Walker, S. Wadsworth, A. Carter, and M. Wale. Integrated DQPSK transmitter for dispersion-tolerant and dispersion-managed DWDM transmission. In *Optical Fiber Communications Conference, 2003. OFC 2003*, pages 770–771 vol.2, 2003.

[68] S. E. Miller. Integrated optics: An introduction. *Bell System Technical Journal*, 48(7):2059–2069, 1969.

[69] K. Kato and Y. Tohmori. Plc hybrid integration technology and its application to photonic components. *Selected Topics in Quantum Electronics, IEEE Journal of*, 6(1):4–13, 2000.

[70] A. Poustie. Hybrid integration for advanced photonic devices, 2008.

[71] M. J. Wale and C. Edge. Self-aligned flip-chip assembly of protonic devices with electrical and optical connections. *Components, Hybrids, and Manufacturing Technology, IEEE Transactions on*, 13(4):780–786, 1990.

[72] L. A. Coldren, S. C. Nicholes, L. Johansson, S. Ristic, R. S. Guzzon, E. J. Norberg, and U. Krishnamachari. High performance InP-Based Photonic ICs - a tutorial. *Lightwave Technology, Journal of*, 29(4):554–570, 2011.

[73] L. Xu, M. R. Gokhale, P. Studenkov, J. C. Dries, C. P. Chao, D. Garbuzov, and S. R. Forrest. Monolithic integration of an InGaAsP-InP MQW laser/waveguide using a twin-guide structure with a mode selection layer. *Photonics Technology Letters, IEEE*, 9(5):569–571, 1997.

[74] P. V. Studenkov, M. R. Gokhale, J. C. Dries, and S. R. Forrest. Monolithic integration of a quantum-well laser and an optical amplifier using an asymmetric twin-waveguide structure. *Photonics Technology Letters, IEEE*, 10(8):1088–1090, 1998.

[75] Y. Suematsu, M. Yamada, and K. Hayashi. Integrated twin-guide AlGaAs laser with multiheterostructure. *Quantum Electronics, IEEE Journal of*, 11(7):457–460, 1975.

[76] K. Nozaki, H. Watanabe, and T. Baba. Photonic crystal nanolaser monolithically integrated with passive waveguide for effective light extraction. *Applied Physics Letters*, 92(2):021108–021108–3, 2008.

[77] T. Kato. DFB-LD/modulator integrated light source by bandgap energy controlled selective MOVPE. *Electronics Letters*, 28:153–154(1), January 1992.

[78] H. Wang. Butt joint integrated extended cavity InAs/InP (100) quantum dot laser emitting around 1.5. *Electronics Letters*, 44:522–524(2), April 2008.

[79] S. Mokkapati, H. H. Tan, and C. Jagadish. Integration of an InGaAs quantum-dot laser with a passive waveguide using selective-area MOCVD. In *Lasers and Electro-Optics Society, 2005. LEOS 2005. The 18th Annual Meeting of the IEEE*, pages 915–916, 2005.

[80] T. Sasaki. Selective MOVPE technique and its applications for photonic devices. In *Lasers and Electro-Optics, 1999. CLEO/Pacific Rim '99. The Pacific Rim Conference on*, volume 3, pages 1068–1069 vol.3, 1999.

[81] M. L. Osowski and J. J. Coleman. Integrated photonic devices by selective-area MOCVD, 1997.

[82] H. Park, A. W. Fang, S. Kodama, and J. E. Bowers. Hybrid silicon evanescent laser fabricated with a silicon waveguide and iii-v offset quantum well. 2005.

[83] E. Skogen, J. Barton, P. Steven, and L. A. Coldren. A quantum-well-intermixing process for wavelength-agile photonic integrated circuits. *Selected Topics in Quantum Electronics, IEEE Journal of*, 8(4):863–869, 2002.

[84] A. McKee, C. J. McLean, G. Lullo, A. Bryce, R. M. De La Rue, J. H. Marsh, and C. C. Button. Monolithic integration in InGaAs-InGaAsP multiple-quantum-well structures using laser intermixing. *Quantum Electronics, IEEE Journal of*, 33(1):45–55, 1997.

[85] E. J. Skogen, J. W. Raring, G. B. Morrison, C. S. Wang, V. Lal, M. L. Masanovic, and L. A. Coldren. Monolithically integrated active components: a quantum-well intermixing approach. *Selected Topics in Quantum Electronics, IEEE Journal of*, 11(2):343–355, 2005.

[86] G. Hasnain, K. Tai, L. Yang, Y. Wang, R. J. Fischer, J. D. Wynn, B. Weir, N. K. Dutta, and A. Cho. Performance of gain-guided surface emitting lasers with semiconductor distributed bragg reflectors. *Quantum Electronics, IEEE Journal of*, 27(6):1377–1385, 1991.

[87] N. Siddharth, R.and Sysak, G. Kurczveil, and J. E. Bowers. Integrated hybrid silicon DFB laser-EAM array using quantum well intermixing. *Opt. Express*, 19(14):13692–13699, Jul 2011.

[88] V. Tolstikhin. Distributed feedback lasers for regrowth-free multi-guide vertical integration in InP. In *IEEE Photonics Society, 2010 23rd Annual Meeting of the*, pages 521–522, 2010.

[89] D. Byrne, Q. Lu, W-H Guo, J. F. Donegan, B. Corbett, B. Roycroft, P. Lambkin, J-P Engelstaedter, and F. Peters. A facetless laser suitable for monolithic integration. In *Lasers and Electro-Optics, 2008 and 2008 Conference on Quantum Electronics and Laser Science. CLEO/QELS 2008. Conference on*, pages 1–2, 2008.

[90] L. Chrostowski, C. H. Chang, and C. Chang-Hasnain. Reduction of relative intensity noise and improvement of spur-free dynamic range of an injection locked VCSEL. In *Lasers and Electro-Optics Society, 2003. LEOS 2003. The 16th Annual Meeting of the IEEE*, volume 2, pages 706–707 vol.2, 2003.

[91] J. Wang, M. K. Haldar, L. Li, and F. V. C. Mendis. Enhancement of modulation bandwidth of laser diodes by injection locking. *Photonics Technology Letters, IEEE*, 8(1):34–36, 1996.

[92] S. Hyuk-Kee, E. K. Lau, and M. C. Wu. Optical single sideband modulation using strong optical injection-locked semiconductor lasers. *Photonics Technology Letters, IEEE*, 19(13):1005–1007, 2007.

[93] S. Hyuk-Kee, Z. Xiaoxue, E. K. Lau, D. Parekh, C.J. Chang-Hasnain, and M. C.

Wu. Optoelectronic oscillators using direct-modulated semiconductor lasers under strong optical injection. *Selected Topics in Quantum Electronics, IEEE Journal of*, 15(3):572–577, 2009.

[94] A. Tauke-Pedretti, G. A. Vawter, E. J. Skogen, G. Peake, M. Overberg, C. Alford, W. W. Chow, Z. S. Yang, D. Torres, and F. Cajas. Mutual injection locking of monolithically integrated coupled-cavity DBR lasers. *Photonics Technology Letters, IEEE*, 23(13):908–910, 2011.

[95] L. Chrostowski and Wei Shi. Monolithic injection-locked high-speed semiconductor ring lasers. *Lightwave Technology, Journal of*, 26(19):3355–3362, 2008.

[96] J. Leu and V. Stojanovic. Injection-locked clock receiver for monolithic optical link in 45nm SOI. In *Solid State Circuits Conference (A-SSCC), 2011 IEEE Asian*, pages 149–152, 2011.

[97] Q. Lu, W. Guo, M. Nawrocka, A. Abdullaev, C. Daunt, J. O'Callaghan, M. Lynch, V. Weldon, F. Peters, and J. F. Donegan. Single mode lasers based on slots suitable for photonic integration. *Opt. Express*, 19(26):B140–B145, Dec 2011.

[98] C. Bonatto, B. Kelleher, G. Huyet, and S. P. Hegarty. Transition from unidirectional to delayed bidirectional coupling in optically coupled semiconductor lasers. *Phys. Rev. E*, 85:026205, Feb 2012.

[99] P. E. Morrissey, D. Goulding, R. Sheehan, B. Roycroft, and F. H. Peters. Experimental technique for quick and efficient lensed fibre to ridge waveguide coupling. *Optoelectronics, IET*, 7(2):57–61, 2013.

[100] Y. Hua, P. E. Morrissey, W. Cotter, C. L. M. Daunt, J. O'Callaghan, B. Roycroft, Y. Nan, N. Kelly, B. Corbett, and F. H. Peters. Monolithic integration of single facet slotted laser, SOA, and MMI coupler. *Photonics Technology Letters, IEEE*, 25(3):257–260, 2013.

[101] P. E. Morrissey, W. Cotter, D. Goulding, B. Kelleher, S. Osborne, H. Yang, J. O'Callaghan, B. Roycroft, B. Corbett, and F. H. Peters. On-chip optical phase locking of single growth monolithically integrated slotted fabry perot lasers. *Opt. Express*, 21(14):17315–17323, Jul 2013.

[102] P. E. Morrissey, W. Cotter, J. O'Callaghan, H. Yang, B. Roycroft, D. Goulding, B. Corbett, and F. H. Peters. Multiple coherent outputs from single growth monolithically integrated injection locked tunable lasers. In *Indium Phosphide and Related Materials (IPRM), 2012 International Conference on*, pages 281–284. IEEE, 2012.

[103] N. S. Bergano and C. R. Davidson. Wavelength division multiplexing in long-haul transmission systems. *Lightwave Technology, Journal of*, 14(6):1299–1308, 1996.

[104] P. Russell. Photonic crystal fibers. *science*, 299(5605):358–362, 2003.

[105] J. C. Knight. Photonic crystal fibres. *Nature*, 424(6950):847–851, 2003.

[106] N. A. Olsson. Lightwave systems with optical amplifiers. *Lightwave Technology, Journal of*, 7(7):1071–1082, 1989.

[107] A. R. Chraplyvy. Limitations on lightwave communications imposed by optical-fiber nonlinearities. *Lightwave Technology, Journal of*, 8(10):1548–1557, 1990.

[108] K. Okamoto. *Fundamentals of optical waveguides*. Electronics & Electrical. Elsevier Academic Press, 2006.

[109] K. Kawano and T. Kitoh. *Introduction to Optical Waveguide Analysis: Solving Maxwell's Equation and the Schrödinger Equation*. Wiley, 2004.

[110] M. L. Calvo and V. Lakshminarayanan. *Optical Waveguides: From Theory to Applied Technologies*. Optical Science and Engineering. Taylor & Francis, 2010.

[111] B. E. A. Saleh and M. C. Teich. *Fundamentals of Photonics*. Wiley Series in Pure and Applied Optics. Wiley, 2007.

[112] V. S. Bagad. *Optical Fiber Communications*. Technical Publications, 2009.

[113] A. Kumar, K. Thyagarajan, and A. K. Ghatak. Analysis of rectangular-core dielectric waveguides: an accurate perturbation approach. *Optics letters*, 8(1):63–65, 1983.

[114] E. Marcatili. Dielectric rectangular waveguide and directional coupler for integrated optics(transmission properties and directional coupler determined for optical circuit dielectric rectangular waveguide with surrounding dielectrics of smaller refractivity). *Bell System Technical Journal*, 48:2071–2102, 1969.

[115] W. P. Huang and C. L. Xu. Simulation of three-dimensional optical waveguides by a full-vector beam propagation method. *Quantum Electronics, IEEE Journal of*, 29(10):2639–2649, 1993.

[116] G. R. Hadley. Transparent boundary condition for the beam propagation method. *Quantum Electronics, IEEE Journal of*, 28(1):363–370, 1992.

[117] J. VanRoey, J. van derDonk, and P. E. Lagasse. Beam-propagation method: analysis and assessment. *J. Opt. Soc. Am.*, 71(7):803–810, Jul 1981.

[118] G. R. Hadley and R. E. Smith. Full-vector waveguide modeling using an iterative finite-difference method with transparent boundary conditions. *Lightwave Technology, Journal of*, 13(3):465–469, 1995.

[119] W. Huang, C. Xu, S. T. Chu, and S. K. Chaudhuri. The finite-difference vector beam propagation method: analysis and assessment. *Lightwave Technology, Journal of*, 10(3):295–305, 1992.

[120] P. Lusse, P. Stuwe, J. Schule, and H. G. Unger. Analysis of vectorial mode fields in optical waveguides by a new finite difference method. *Lightwave Technology, Journal of*, 12(3):487–494, 1994.

[121] K. Saitoh and M. Koshiba. Full-vectorial imaginary-distance beam propagation method based on a finite element scheme: application to photonic crystal fibers. *Quantum Electronics, IEEE Journal of*, 38(7):927–933, 2002.

[122] S. Obayya, B. M. Azizur-Rahman, K. Grattan, and H. A. El-Mikati. Full vectorial finite-element-based imaginary distance beam propagation solution of complex modes in optical waveguides. *J. Lightwave Technol.*, 20(6):1054, Jun 2002.

[123] J.M. Liu. *Photonic Devices*. Cambridge University Press, 2005.

[124] C. Chaudhari, D. Patil, and D. K Gautam. A new technique for the reduction of the power loss in the Y-branch optical power splitter. *Optics communications*, 193(1):121–125, 2001.

[125] T. B. Yu, M. Wang, X. Jiang, Q. Liao, and J. Yang. Ultracompact and wideband power splitter based on triple photonic crystal waveguides directional coupler. *Journal of Optics A: Pure and Applied Optics*, 9(1):37, 2007.

[126] C. Dragone. An N*N optical multiplexer using a planar arrangement of two star couplers. *Photonics Technology Letters, IEEE*, 3(9):812–815, 1991.

[127] C. Dragone, C. H. Henry, I. P. Kaminow, and R. C. Kistler. Efficient multichannel integrated optics star coupler on silicon. *Photonics Technology Letters, IEEE*, 1(8):241–243, 1989.

[128] J. Z. Huang, R. Scarmozzino, and R. M. Osgood Jr. A new design approach to large input/output number multimode interference couplers and its application to low-crosstalk WDM routers. *Photonics Technology Letters, IEEE*, 10(9):1292–1294, 1998.

[129] J. B. D. Soole, M. R. Amersfoort, H. P. LeBlanc, N. C. Andreadakis, A. Rajhel, C. Caneau, R. Bhat, M. A. Koza, C. Youtsey, and I. Adesida. Use of multimode interference couplers to broaden the passband of wavelength-dispersive integrated WDM filters. *Photonics Technology Letters, IEEE*, 8(10):1340–1342, 1996.

[130] J. Hong, H. Ryu, S. Park, J. Jeong, S. Lee, E. Lee, D. Park, S.and Woo, S. Kim, and O. Beom-Hoan. Design and fabrication of a significantly shortened multimode interference coupler for polarization splitter application. *Photonics Technology Letters, IEEE*, 15(1):72–74, 2003.

[131] L. B. Soldano and E. C. M Pennings. Optical multi-mode interference devices based on self-imaging: principles and applications. *Lightwave Technology, Journal of*, 13(4):615–627, 1995.

[132] H. F. Talbot. LXXVI. facts relating to optical science. no. IV. *Philosophical Magazine Series 3*, 9(56):401–407, 1836.

[133] Z. Haifeng, S. Junfeng, C. Li, H. Zhang, and P. G. Lo. A library of ultra-compact multimode interference optical couplers on SOI. *Photonics Technology Letters, IEEE*, 25(12):1149–1152, 2013.

[134] L. O. Lierstuen and A. Sudbo. 8-channel wavelength division multiplexer based on multimode interference couplers. *Photonics Technology Letters, IEEE*, 7(9):1034–1036, 1995.

[135] R. W. Chuang, M. T. Hsu, Y. C. Chang, Y. J. Lee, and S. H. Chou. Integrated multimode interference coupler-based mach-zehnder interferometric modulator fabricated on a silicon-on-insulator substrate. *Optoelectronics, IET*, 6(3):147–152, 2012.

[136] D. J. Thomson, Y. Hu, G. T. Reed, and J. M. Fedeli. Low loss MMI couplers for high performance MZI modulators. *Photonics Technology Letters, IEEE*, 22(20):1485–1487, 2010.

[137] M. L. Masanovic, V. Lal, J. S. Barton, E. J. Skogen, L. A. Coldren, and D. J. Blumenthal. Monolithically integrated Mach-Zehnder interferometer wavelength converter and widely tunable laser in InP. *Photonics Technology Letters, IEEE*, 15(8):1117–1119, 2003.

[138] J. S. Barton, E. J. Skogen, M. L. Masanovic, Steven P. DenBaars, and L. A. Coldren. A widely tunable high-speed transmitter using an integrated SGDBR laser-semiconductor optical amplifier and Mach-Zehnder modulator. *Selected Topics in Quantum Electronics, IEEE Journal of*, 9(5):1113–1117, 2003.

[139] D. C. Chang and E. F. Kuester. A hybrid method for paraxial beam propagation in multimode optical waveguides. *Microwave Theory and Techniques, IEEE Transactions on*, 29(9):923–933, 1981.

[140] S. Triki, M. Najjar, H. Rezig, and L. Catherine. Simulation and modelization of multimode interference demultiplexer by using BPM method. In *Information and Communication Technologies: From Theory to Applications, 2008. ICTTA 2008. 3rd International Conference on*, pages 1–5, 2008.

[141] R. Ulrich. Light-propagation and imaging in planar optical waveguides. *Nouvelle Revue d'Optique*, 6(5):253, 1975.

[142] ECM Pennings, RMJN van Roijen, MJN Van Stralen, PJ De Waard, RGMP Koumans, and BH Verbeck. Reflection properties of multimode interference devices. *Photonics Technology Letters, IEEE*, 6(6):715–718, 1994.

[143] Y Gottesman, EVK Rao, and B Dagens. A novel design proposal to minimize

reflections in deep-ridge multimode interference couplers. *Photonics Technology Letters, IEEE*, 12(12):1662–1664, 2000.

[144] Rabah Hanfoug, LM Augustin, Yohan Barbarin, JJGM van der Tol, EAJM Bente, Fouad Karouta, D Rogers, S Cole, YS Oei, XJM Leijtens, et al. Reduced reflections from multimode interference couplers. *Electronics Letters*, 42(8):465–466, 2006.

[145] D. Erasme, L. H. Spiekman, C. G. P. Herben, M. K. Smit, and F. H. Groen. Experimental assessment of the reflection of passive multimode interference couplers. *Photonics Technology Letters, IEEE*, 9(12):1604–1606, 1997.

[146] R. Hanfoug, L. M. Augustin, Y. Barbarin, J. Van der Tol, E. Bente, F. Karouta, D. Rogers, S. Cole, Y. S. Oei, X. J. M. Leijtens, and M. K. Smit. Reduced reflections from multimode interference couplers. *Electronics Letters*, 42(8):465–466, 2006.

[147] P.-A. Besse, M. Bachmann, H. Melchior, L. B. Soldano, and M. K. Smit. Optical bandwidth and fabrication tolerances of multimode interference couplers. *Lightwave Technology, Journal of*, 12(6):1004–1009, 1994.

[148] L. Yan-Ping, Y. Jin-Zhong, and C. Shao-Wu. A silicon-on-insulator-based thermo-optic waveguide switch with low insertion loss and fast response. *Chinese Physics Letters*, 22(6):1449, 2005.

[149] T. L. Koch and U. Koren. Semiconductor photonic integrated circuits. *Quantum Electronics, IEEE Journal of*, 27(3):641–653, 1991.

[150] H. Yamada. Analysis of optical coupling for SOI waveguides. *PIERS Online*, 6(2):165–168, 2010.

[151] R. Nagarajan, M. Kato, J. Pleumeekers, P. Evans, S. Corzine, S. Hurtt, A. Dentai, S. Murthy, M. Missey, R. Muthiah, Randal A. Salvatore, C. Joyner, R. Schneider, M. Ziari, F. Kish, and D. Welch. InP photonic integrated circuits. *Selected Topics in Quantum Electronics, IEEE Journal of*, 16(5):1113–1125, 2010.

[152] U. Koren, T. L. Koch, B. I. Miller, G. Eisenstein, and R. H. Bosworth. Wavelength division multiplexing light source with integrated quantum well tunable lasers and optical amplifiers. *Applied Physics Letters*, 54(21):2056–2058, 1989.

[153] M. L. M. Balistreri, X. Borrise, J. P. Korterik, and N. F. Hulst van. Imaging of the field distribution in integrated optical waveguides. In F. Karouta, editor, *Proceedings 1997 second IEEE/LEOS Symposium*, pages 17–20, Eindhoven University of Technology, 1997.

[154] X. Borrise, D. Jimenez, N. Barniol, F. Perez-Murano, and X. Aymerich. Scan-

ning near-field optical microscope for the characterization of optical integrated waveguides. *Lightwave Technology, Journal of*, 18(3):370–374, 2000.

[155] W. B. Joyce and B. C. DeLoach. Alignment of gaussian beams. *Appl. Opt.*, 23(23):4187–4196, Dec 1984.

[156] D. Taillaert, W. Bogaerts, P. Bienstman, T.F. Krauss, P. van Daele, I. Moerman, S. Verstuyft, K. De Mesel, and R. Baets. An out-of-plane grating coupler for efficient butt-coupling between compact planar waveguides and single-mode fibers. *Quantum Electronics, IEEE Journal of*, 38(7):949–955, 2002.

[157] L. A. Coldren, K. J. Ebeling, B. I. Miller, and J. Rentschler. Single longitudinal mode operation of two-section lasers under pulsed excitation. *Quantum Electronics, IEEE Journal of*, 19(6):1057–1062, 1983.

[158] B. Corbett and D. McDonald. Single longitudinal mode ridge waveguide 1.3 μm fabry-perot laser by modal perturbation. *Electronics Letters*, 31(25):2181–2182, 1995.

[159] D. McDonald and B. Corbett. Performance characteristics of quasi-single longitudinal-mode fabry-perot lasers. *Photonics Technology Letters, IEEE*, 8(9):1127–1129, 1996.

[160] S. K. Mondal, B. Roycroft, P. Lambkin, F. Peters, B. Corbett, P. Townsend, and A. Ellis. A multiwavelength low-power wavelength-locked slotted fabry perot laser source for WDM applications. *Photonics Technology Letters, IEEE*, 19(10):744–746, 2007.

[161] D. C. Byrne, J. P. Engelstaedter, G. Wei-Hua, L. Qiao-Yin, B. Corbett, B. Roycroft, J. O'Callaghan, F. H. Peters, and J. F. Donegan. Discretely tunable semiconductor lasers suitable for photonic integration. *Selected Topics in Quantum Electronics, IEEE Journal of*, 15(3):482–487, 2009.

[162] M. H. MacDougal, H. Zhao, P. D. Dapkus, M. Ziari, and W. H. Steier. Wide-bandwidth distributed bragg reflectors using oxide/GaAs multilayers. *Electronics Letters*, 30(14):1147–1149, 1994.

[163] Q. Lu, W. Guo, R. Phelan, D. Byrne, J. F. Donegan, P. Lambkin, and B. Corbett. Analysis of slot characteristics in slotted single-mode semiconductor lasers using the 2-d scattering matrix method. *Photonics Technology Letters, IEEE*, 18(24):2605–2607, 2006.

[164] R. Phelan, G. Wei-Hua, L. Qiaoyin, D. Byrne, B. Roycroft, P. Lambkin, B. Corbett, F. Smyth, L. P. Barry, B. Kelly, J. O'Gorman, and J. F. Donegan. A novel two-section tunable discrete mode fabry-perot laser exhibiting nanosecond wavelength switching. *Quantum Electronics, IEEE Journal of*, 44(4):331–337, 2008.

[165] K. Kudo, K. Yashiki, T. Sasaki, Y. Yokoyama, K. Hamamoto, T. Morimoto, and M. Yamaguchi. Wavelength-selectable microarray DFB-LD's with monolithically integrated MMI combiner, SOA, and EA-modulator. *Photonics Technology Letters, IEEE*, 12(3):242–244, 2000.

[166] H. Oohashi, Y. Shibata, H. Ishii, Y. Kawaguchi, Y. Kondo, Y. Yoshikuni, and Y. Tohmori. 46.9-nm wavelength-selectable arrayed DFB lasers with integrated MMI coupler and SOA. In *Indium Phosphide and Related Materials, 2001. IPRM. IEEE International Conference On*, pages 575–578, 2001.

[167] R. Lang. Injection locking properties of a semiconductor laser. *Quantum Electronics, IEEE Journal of*, 18(6):976–983, 1982.

[168] I. Petitbon, P. Gallion, G. Debarge, and C. Chabran. Locking bandwidth and relaxation oscillations of an injection-locked semiconductor laser. *Quantum Electronics, IEEE Journal of*, 24(2):148–154, 1988.

[169] H. Erzgräber, S. Wieczorek, and B. Krauskopf. Dynamics of two laterally coupled semiconductor lasers: Strong- and weak-coupling theory. *Phys. Rev. E*, 78:066201, Dec 2008.

[170] W. Coomans, L. Gelens, S. Beri, J. Danckaert, and G. Van der Sande. Solitary and coupled semiconductor ring lasers as optical spiking neurons. *Phys. Rev. E*, 84:036209, Sep 2011.

[171] T. Erneux, E. A Viktorov, B. Kelleher, D. Goulding, S. P. Hegarty, and G. Huyet. Optically injected quantum-dot lasers. *Optics letters*, 35(7):937–939, 2010.

[172] H. Wünsche, S. Bauer, J. Kreissl, O. Ushakov, N. Korneyev, F. Henneberger, E. Wille, H. Erzgräber, M. Peil, W. Elsässer, and I. Fischer. Synchronization of delay-coupled oscillators: a study of semiconductor lasers.

[173] Y. Fischer, I.and Liu and P. Davis. Synchronization of chaotic semiconductor laser dynamics on subnanosecond time scales and its potential for chaos communication. *Physical Review A*, 62(1):011801, 2000.

[174] D. Goulding, S. P. Hegarty, O. Rasskazov, S. Melnik, M. Hartnett, G. Greene, J. G. Mcinerney, D. Rachinskii, and G. Huyet. Excitability in a Quantum Dot Semiconductor Laser with Optical Injection. *Physical Review Letters*, 98(15), 2007.

[175] S. Wieczorek, B. Krauskopf, T. B. Simpson, and D. Lenstra. The dynamical complexity of optically injected semiconductor lasers. *Physics Reports*, 416(1–2):1 – 128, 2005.

[176] B. Kelleher, C. Bonatto, P. Skoda, S. P. Hegarty, and G. Huyet. Excitation regeneration in delay-coupled oscillators. *Phys. Rev. E*, 81:036204, Mar 2010.

[177] S. Wieczorek, B. Krauskopf, and D. Lenstra. Mechanisms for multistability in a semiconductor laser with optical injection. *Optics Communications*, 183(1–4):215 – 226, 2000.

[178] T. Heil, I. Fischer, W. Elsasser, J. Mulet, and C. R. Mirasso. Chaos synchronization and spontaneous symmetry-breaking in symmetrically delay-coupled semiconductor lasers. *Physical Review Letters*, 86:795–798, 2001.

[179] W. Cotter, D. Goulding, B. Roycroft, J. O'Callaghan, B. Corbett, and F. H. Peters. Investigation of active filter using injection-locked slotted fabry–perot semiconductor laser. *Applied optics*, 51(30):7357–7361, 2012.

[180] P. Winzer and R. Essiambre. Advanced optical modulation formats. *Proceedings of the IEEE*, 94(5):952–985, 2006.

[181] K. Petermann. External optical feedback phenomena in semiconductor lasers. *Selected Topics in Quantum Electronics, IEEE Journal of*, 1(2):480–489, 1995.

[182] C. Bonatto, B. Kelleher, G. Huyet, and S. Hegarty. Transition from unidirectional to delayed bidirectional coupling in optically coupled semiconductor lasers. *Physical Review E*, 85(2):026205, 2012.

[183] M. Born and E. Wolf. *Principles of Optics*. CambridgeUniversity Press, 1998, 1998.

[184] H. Takahashi, S. Suzuki, K. Kato, and I. Nishi. Arrayed-waveguide grating for wavelength division multi/demultiplexer with nanometre resolution. *Electronics Letters*, 26(2):87–88, 1990.

[185] C. Dragone. An N*N optical multiplexer using a planar arrangement of two star couplers. *Photonics Technology Letters, IEEE*, 3(9):812–815, 1991.

[186] M. K. Smit and C. Van Dam. PHASAR-based WDM-devices: Principles, design and applications. *Selected Topics in Quantum Electronics, IEEE Journal of*, 2(2):236–250, 1996.

[187] C. Dragone. Efficient NxN star couplers using fourier optics. *Lightwave Technology, Journal of*, 7(3):479–489, 1989.

[188] K. Okamoto, H. Takahashi, S. Suzuki, A. Sugita, and Y. Ohmori. Design and fabrication of integrated-optic 8*8 star coupler. *Electronics Letters*, 27(9):774–775, 1991.

[189] H. Kogelnik and T. Li. Laser beams and resonators. *Appl. Opt.*, 5(10):1550–1567, Oct 1966.

[190] O. Svelto. *Principles of Lasers*. Springer, 2010.

[191] D. Marcuse. Tilt, offset, and end-separation loss of lowest-order slab waveguide mode. *Lightwave Technology, Journal of*, 4(11):1647–1650, 1986.

Appendix A

Matlab MMI Optimisation Code

A.1 MMI Code

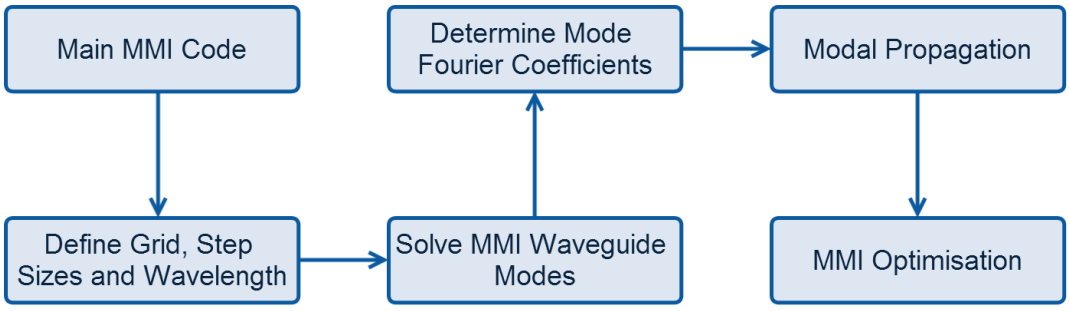

Figure A.1: Overview of MMI Optimisation Code

An overview of the developed Matlab MMI design and optimisation code is given in Figure A.1. The general design procedure for modelling MMIs using the methods developed in this thesis is as follows:

- The main function sets and defines the computational grid along with the waveguide parameters.
- The modes of the input and MMI waveguides are solved using the waveguide analysis techniques investigated in chapter 2.
- The fourier coefficients of these modes are determined.
- The determined modal parameters and fourier coefficients are used with modal propagation analysis to determine the E-field distribution of the MMI are particular propagation lengths.
- The optimised MMI parameters are determined from this E-field distribution by analysing where the field is maximised for particular MMI variations.

In what follows, the subroutines required to model MMIs in this way are described and given.

A.1.1 Main MMI Code

The main function of the MMI Design Code sets the computational grid, step-sizes and MMI waveguide structure of the device to be modelled. These parameters are used in the MMI Optimisation Subroutine, where the optimised MMI length and field distribution at this length are returned. The full input and output parameters are given in Table A.1.

Table A.1: Input and Output Parameters - Main MMI Code

Input Parameters	Output Parameters
Max Grid Width (Extent)	Optimised MMI Length (Length of MMI)
Grid Step Size (Size)	Calculated MMI Widths (Widths of MMI)
Input Waveguide Width (Winput)	MMI E-Field (Optimum MMI Field)
Start MMI Width (WmmiStart)	MMI Coupling Efficiency (Coupling of MMI)
End MMI Width (WmmiEnd)	-
Step MMI Width (WmmiStep)	-
Substrate Refractive Index (n1)	-
Core Refractive Index (n2)	-
Cladding Refractive Index (n3)	-
Wavelength (lambda)	-
Steps in propagation direction (NStepsZ)	-
Step Separation (SepStep)	-

```
%%  Set Waveguide Parameters
Extent=10; Step=0.05; % Grid
Winput=1.2;
q=0; n1=1.0; n2=3.45; n3=1.0;
WmmiStart=1.2; WmmiStep=0.2; WmmiEnd=6.0;
lambda=1.55;
N_StepsZ=50; % Propagation Parameters
Sep_Step=50; % Waveguide Separation Parameters

[Optimum_Parameters,Optimum_MMI_Field,Widths_of_MMI,
    Length_of_MMI,Coupling_of_MMI] = Optimise_1x2_MMI(Extent,
    Step,Winput,WmmiStart,WmmiStep,WmmiEnd,lambda,q,n1,n2,n3,
```

```
N_StepsZ, Sep_Step);
```

A.1.2 MMI Subroutine

This subroutine is responsible for setting the computational grid and fully modelling and optimising the MMI structure. The input waveguide and MMI modes are solved, their fourier coefficients found and are then propagated until the optimised MMI length is determined. The subroutine uses the functions described later in this work. The input and output parameters are given in Table A.2.

Table A.2: Input and Output Parameters - MMI Subroutine

Input Parameters	Output Parameters
Max Grid Width (Extent)	Optimised MMI Length (Length of MMI)
Grid Step Size (Size)	Calculated MMI Widths (Widths of MMI)
Input Waveguide Width (Winput)	MMI E-Field (Optimum MMI Field)
Start MMI Width (WmmiStart)	MMI Coupling Efficiency (Coupling of MMI)
End MMI Width (WmmiEnd)	-
Step MMI Width (WmmiStep)	-
Substrate Refractive Index (n1)	-
Core Refractive Index (n2)	-
Cladding Refractive Index (n3)	-
Wavelength (lambda)	-
Steps in propagation direction (NStepsZ)	-
Step Separation (SepStep)	-

```
1  function [Optimum_Parameters,Optimum_MMI_Field,Widths_of_MMI,
       Length_of_MMI,Coupling_of_MMI] = Optimise_1x2_MMI(Extent,
       Step,Winput,WmmiStart,WmmiStep,WmmiEnd,lambda,q,n1,n2,n3,
       N_StepsZ,Sep_Step)
2
3  %% Setting up grid
4  [x,dx]=Setup_1D_Grid_1(Extent,Step);
5
6  %% Setting up some general parameters
7  k0=2*1*pi/lambda;k=k0;c=2.9998*(10^8);
8  V_parameter=k0*(Winput/2)*((n2*n2-n1*n1)^(1/2));
9  M=ceil(V_parameter/(pi/2));
10
```

```
%% Fundamental Mode
[Fundamental_Mode, G_fitted_mode, x, neff, B_TE] = TE_mode_1(Winput, q, n1, n2, n3, k0, Extent, dx);

%% MMI Waveguide
index1=0;
for Wmmi=WmmiStart:WmmiStep:WmmiEnd
    index1=index1+1;
    V_parameter=k0*(Wmmi/2)*((n2*n2-n1*n1)^(1/2));
    M=ceil(V_parameter/(pi/2));
    MMI_Modes=zeros(length(x),M+1);
    Neff_MMI=zeros(M+1);
    B_MMI=zeros(M+1);
    for q=0:1:M
        [MMI_Modes(:,q+1), G_fitted_mode, x, Neff_MMI(q+1), B_MMI(q+1)] = TE_mode_1(Wmmi, q, n1, n2, n3, k0, Extent, dx);
    end

    %% MMI Parameters
    N=2;
    Lmmi=Wmmi*Wmmi*n2/lambda;
    MMI_Length=Lmmi/N;

    %% Overlap & Propagation of modes
    [ReducedTE_Input, ReducedTE_MMI, overlap, B, Summed_Field_Input] = Overlap(Fundamental_Mode, MMI_Modes, dx);
    clear coupling; clear Field;
    Zstart=0; Zend=Lmmi*(2/3);
    z=linspace(Zstart, Zend, N_StepsZ); Zstep=z(2)-z(1);
    [Field, z] = Propagation(B, overlap, B_MMI, MMI_Modes, Zstart, Zstep, Zend);
    Saved_Field(:,:,index1)=Field;

    %% Coupling as I vary the separation between the outputs
    Sep_Start=1*Wmmi/6; Sep_End=2*Wmmi/5;
    [Widths_of_MMI(index1), Length_of_MMI(index1), Coupling_of_MMI(index1)] = Coupling_Vary_Separation(x, Fundamental_Mode, dx, z, Field, MMI_Length, Zstep, Zend, Sep_Step, Winput, Wmmi);%
end
```

```
44
45 eee = dsearchn(Coupling_of_MMI',max(Coupling_of_MMI));
46 Optimum_MMI_Width=Widths_of_MMI(eee);
47 Optimum_MMI_Length=Length_of_MMI(eee);
48 Optimum_MMI_Coupling=Coupling_of_MMI(eee);
49 Optimum_MMI_Field=Saved_Field(:,:,eee);
50 Optimum_Parameters=[Optimum_MMI_Width;Optimum_MMI_Length;
       Optimum_MMI_Coupling];
```

A.1.3 Mode Solver Subroutine

This subroutine implements the waveguide solver described in chapter 2 and is used to determine the waveguide modes in the both the narrow input waveguide and wide MMI waveguide. The material and waveguide structure is set and the routine returns the normalised E-field distribution of the waveguide mode, along with the effective index and propagation constant. The full input and output parameters are given in Table A.3.

Table A.3: Input and Output Parameters - Mode Solver Subroutine

Input Parameters	Output Parameters
Waveguide Width (W)	Normalised E-Field (Normed Ey)
Mode Number (q)	Gaussian Mode Fitted to Ey (G Fitted mode)
Substrate Refractive Index (n1)	Mode Effective Index (neff)
Core Refractive Index (n2)	Mode Propagation Constant (B Te)
Cladding Refractive Index (n3)	-
Wave Number (k)	-
Max Grid Width (Extent)	-
Grid Step Size (Size)	-

```
1  function [Normed_Ey,G_fitted_mode,x,neff,B_TE] = TE_mode1(W,q,
       n1,n2,n3,k0,ext,step1)
2
3  neff=bisect_TE1(n1,n2,n3,k0,q,W);
4  B_TE=k0*neff;
5  a=W/2;
6  x1=linspace(-ext,-a,abs((1/step1)*(-ext+a)));
7  x2=linspace(-a+step1,a,abs((1/step1)*(-a+step1-a)));
8  x3=linspace(a+step1,ext,round(abs((1/step1)*(2*ext-length(x2)*
       step1-length(x1)*step1))));
9  xx=[x1 x2 x3];
10 length(xx);
11 squiggle=k0*(neff^2-n1^2)^(1/2);
12 kappa=k0*(n2^2-neff^2)^(1/2);
13 sigma=k0*(neff^2-n3^2)^(1/2);
14 u=kappa*a;
15 w=squiggle*a;
16 w_prime=sigma*a;
17 phi=q*pi/2+(0.5)*atan(w/u)-(0.5)*atan(w_prime/u);
```

```
B=1;
A=(B*cos(a*kappa-phi))/cos(kappa*a-phi);
C=B*cos(-a*kappa-phi)/(cos(kappa*a+phi)*exp(squiggle*(-a+a)));
Ey3=A.*cos(kappa*a-phi)*exp(-sigma*(x3-a));
Ey2=B.*cos(x2.*kappa-phi);
Ey1=C.*cos(kappa*a+phi)*exp(squiggle*(x1+a));
Ey=[Ey1  Ey2  Ey3];
x=xx;
y=Ey;
newnorm2=sum(y.*y)*step1;
y=(1/sqrt(newnorm2))*y;
Normed_Ey=y;
length(y);
[sigmaNew,muNew,Anew]=mygaussfit(x,y);
y=Anew*exp(-(x).^2/(2*sigmaNew^2));
newnorm2=sum(y.*y)*step1;
y=(1/sqrt(newnorm2))*y;
G_fitted_mode=y;
```

A.1.4 Overlap Subroutine

This subroutine determines the fourier coefficient between the input waveguide mode and the MMI modes. The full input and output parameters are given in Table A.4.

Table A.4: Input and Output Parameters - Overlap Subroutine

Input Parameters	Output Parameters
Input Waveguide Mode (ReducedTE Input)	Input Waveguide Mode (ReducedTE Input)
MMI waveguide Modes (ReducedTE MMI)	MMI waveguide Modes (ReducedTE MMI)
Grid Spacing (dx)	Mode Effective Index (neff)
-	Overlap Coefficients (overlaps)

```
[ReducedTE_Input,ReducedTE_MMI,overlap,B,Summed_Field] =
    Overlap(ReducedTE_Input,ReducedTE_MMI,dx)
[L  B]=size(ReducedTE_MMI);
Summed_Field=0;
for  i=1:1:B
    norm=((sum(ReducedTE_MMI(:,i).*ReducedTE_MMI(:,i))*dx));
    ReducedTE_MMI(:,i)=(1/sqrt(norm))*ReducedTE_MMI(:,i);
    norm=((sum(ReducedTE_Input.*ReducedTE_Input)*dx));
```

```
8       ReducedTE_Input=(1/sqrt(norm))*ReducedTE_Input;
9       overlap(i)=(sum(ReducedTE_Input.*ReducedTE_MMI(:,i)')*dx);
10      Summed_Field=Summed_Field+(ReducedTE_MMI(:,i))*(overlap(i)
            );
11  end
```

A.1.5 Propagation Subroutine

This subroutine takes the calculated modes, propagation constants and fourier coefficients which were calculated earlier in the analysis and uses them in modal propagation analysis. The routine calculates the E-field distribution of the MMI based on its waveguide structure over a given length range. The full input and output parameters are given in Table A.5.

Table A.5: Input and Output Parameters - Propagation Subroutine

Input Parameters	Output Parameters
Mode Propagation Constant (B)	MMI E Field (Field)
Overlap Coefficients (overlaps)	Position Variation (z)
MMI Modes (ReducedTE MMI)	-
MMI Propagation Constants (BReducedTE MMI)	-
Initial Propagation Position (Zstart)	-
Final Propagation Position (Zend)	-
Step Propagation Position (Zstep)	-

```
function [Field,z] = Propagation(B,overlap,B_ReducedTE_MMI,
    ReducedTE_MMI,Zstart,Zstep,Zend)
Zindex=0;
for z=Zstart:Zstep:Zend
    Zindex=Zindex+1;
    Sum=0;
    for ii=1:2:B
        Sum=Sum+(ReducedTE_MMI(:,ii))*(overlap(ii))*exp(-j*
            B_ReducedTE_MMI(ii)*z);
    end
    Field(:,Zindex)=Sum;
end
z=Zstart:Zstep:Zend;
```

Appendix B

Star Coupler Design

B.1 Star Couplers

In addition to MMIs which were discussed earlier in this work, star couplers provide another means of splitting/combining light on PICs. A star coupler is arranged by setting a series of arrayed waveguides at opposite ends of a Rowland circle [183], with the input array of waveguides directed towards the central waveguide of the output array. Light from the input array is allowed to propagate in the free-space region between the waveguides where it can couple to the output array of waveguides.

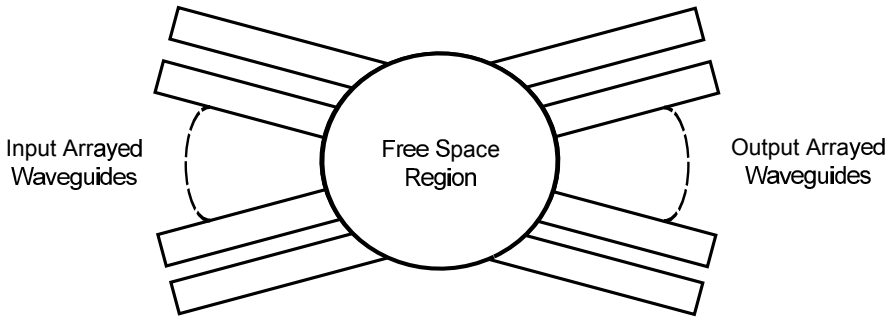

Figure B.1: Schematic of an optical star coupler. Light from the input waveguide array can be coupled to the output waveguide array.

Unlike MMIs, the operation of a star coupler does not rely on any phase relationships between optical signals to perform as a coupler. This makes them an ideal candidate for use as general optical combiners/splitters. Star couplers are extensively used in wavelength multiplexers such as arrayed waveguide gratings [184, 185, 186] for not only power splitting, but also as light combiners with conservation of phase. In a typical AWG, star couplers are arranged as in Figure B.2 where they are used to couple light to and from waveguide arrays.

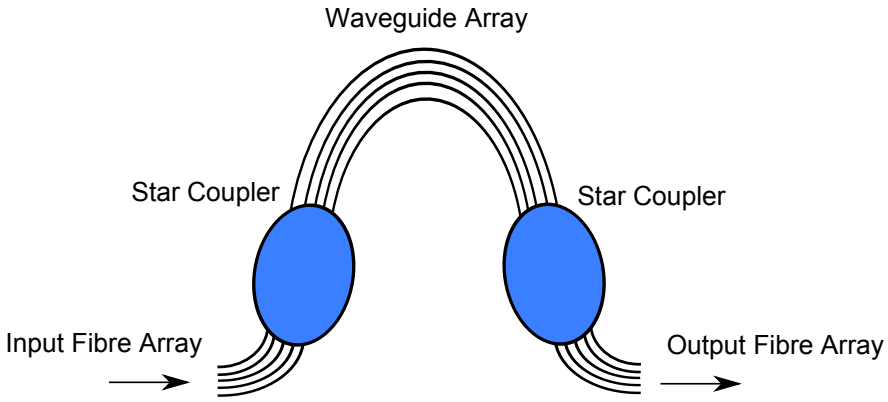

Figure B.2: Arrangement of star couplers as used in an AWG.

Different methods have been devised for modelling star couplers with large numbers of input and output arrayed waveguides [187, 188]. For the star couplers considered in this work, only ≤ 3 waveguides on the input or output ports are considered which simplifies the design process. Such couplers can be modelled by considering how the guided modes in the input waveguide array propagate through the free-space region and couple to the output waveguides. By assuming single mode input and output waveguides, Gaussian mode analysis [189] can be used to determine the propagated field which is incident on the output ports, and from this the power coupled can be determined. In the sections that follow, Gaussian beams are first considered before Gaussian mode analysis is used to investigate the operation and design of star couplers.

B.2 Gaussian Mode Analysis

The fundamental mode of a symmetric slab waveguide is Gaussian in nature and its divergence in free space can be described mathematically using the following Equation [190]:

$$\Psi(x,z) = \Psi_0 w_0 \exp(-\imath \frac{kx^2}{2R(z)} - \frac{x^2}{w^2(z)} - \imath kz) \tag{B.1}$$

In Equation (B.1), x is the transverse distance from the central beam axis, z is the length of propagation in free-space, w_0 is the minimum beam width, $w(z)$ is the beam width where the field amplitude is reduced to $1/e$ of its peak value and $R(z)$ represents the radius of curvature of the Gaussian beam wavefront as it propagates. A Gaussian beam diverging in free-space will have its minimum beam width of w_0 at $z = 0$, in general the beam width at a particular propagation distance is given by:

$$w(z) = w_0 \sqrt{1 + (\frac{z\lambda}{\pi w^2(0)})^2} \tag{B.2}$$

$R(z)$ represents the curvature of the phase fronts as the Gaussian beam propagates and is given by:

$$R(z) = z(1 + (\frac{x^2}{w^2(z)})^2) \tag{B.3}$$

The propagation of a Gaussian beam in free-space can be modelled by considering the how the transversal extent of the Gaussian beam varies with distance. For a slab waveguide of width $2a$=2.0 µm, $n_{core} = 3.38$, n_{clad}=1.0 and $\lambda = 1.55$ µm; the divergence of the Gaussian beam in air as it propagates from $z = 0$ µm to $z = 20$ µm is shown in Figure B.3.

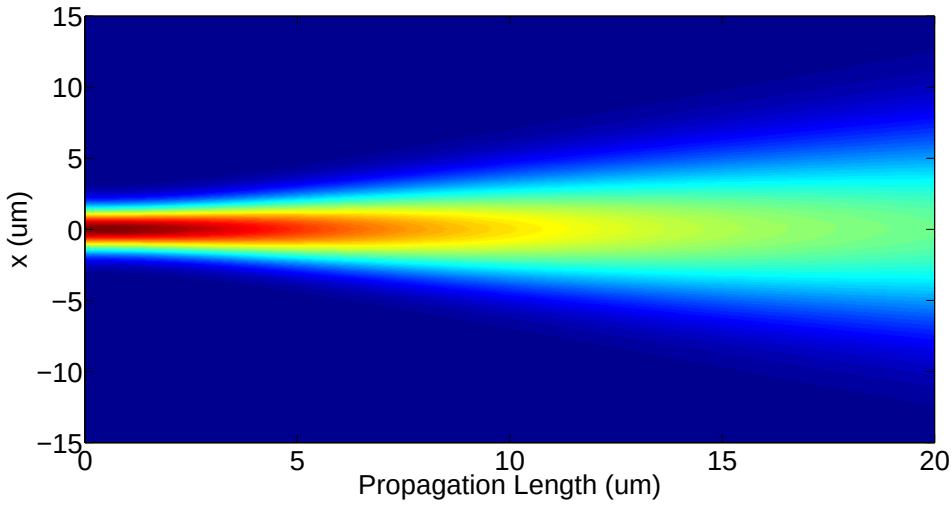

Figure B.3: Propagation of a gaussian beam in free-space.

Gaussian mode analysis can be used to quantify the light coupled between two waveguides separated by a free-space region. By considering the situation shown in Figure B.4, the light coupled from input waveguide A to output waveguide B can be determined by calculating the overlap integral between the propagated Gaussian beam from waveguide A incident on waveguide B, with the fundamental mode of waveguide B. The overlap integral in this case can be written as:

$$\eta_{1,2} = \frac{\int \psi_A \psi_B}{\int \psi_A \psi_A \int \psi_B \psi_B} \tag{B.4}$$

where ψ_A is the propagated field from input waveguide A at B; and ψ_B is the fundamental mode of output waveguide B. The power coupled from one waveguide to another can then determined by calculating $|\eta_{1,2}|$.

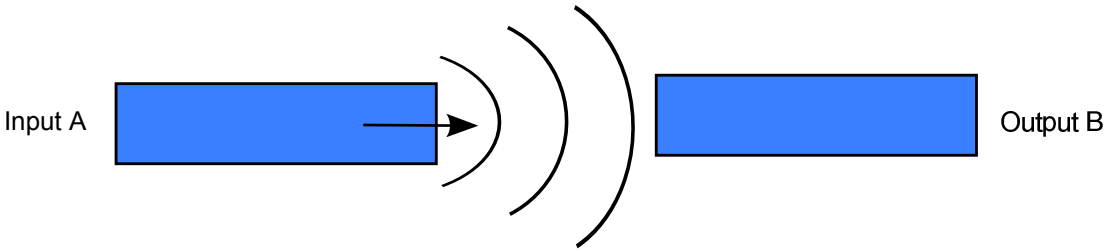

Figure B.4: Coupling from two waveguides axially aligned with a fixed separation.

The coupling efficiency between two identical waveguides (identical to those described above) was next examined as the separation between them was increased from 0 µm to 20 µm while maintaining axial alignment, as in Figure B.4. The propagated mode from the input waveguide A and fundamental mode of the output waveguide B are shown overlapped together in Figure B.5.

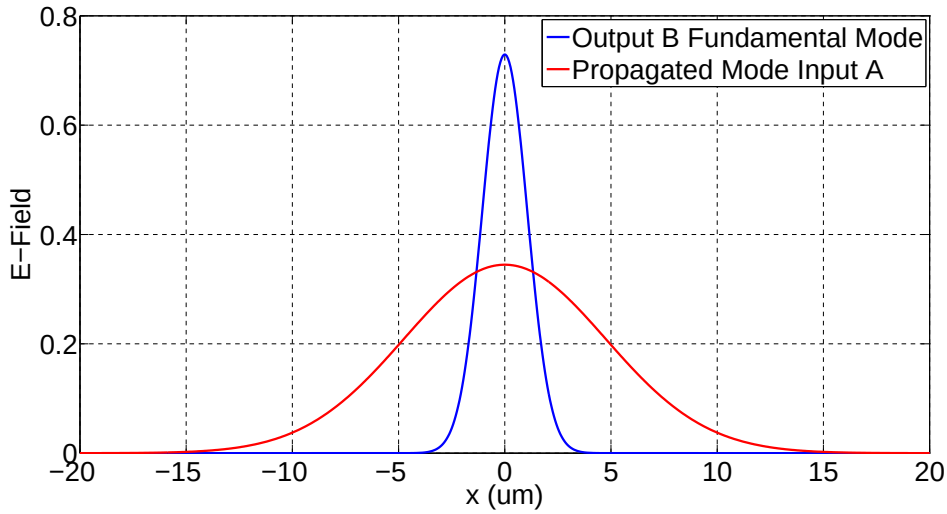

Figure B.5: Propagated mode from input waveguide A incident on output waveguide B, overlapped with the fundamental mode of waveguide B.

Using Equation (B.4), the coupling efficiency between the two waveguides as they are stepped apart from 0 µm to 20 µm can then be calculated. The results of this are shown in Figure B.6. For a propagation length of 0 µm, the two waveguides are essentially butt coupled and a coupling efficiency of unity is observed as expected. For lengths of >0 µm, the coupling efficiency shows an exponential drop off as the waveguides are brought further apart. If the waveguides were not axially aligned but instead misaligned through an offset of tilt, then coupling efficiency can also be determined by calculating the overlap integral of the modes. This has been discussed by Marcuse [191] where the coupling efficiency for butt coupled waveguides with tilt, offset and end separation losses has been described.

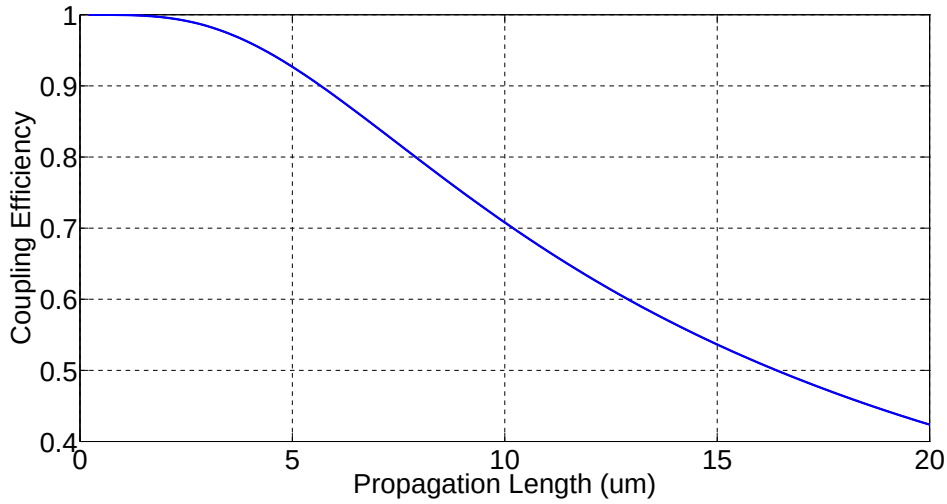

Figure B.6: Coupling efficiency between two optical waveguides that are axially aligned as the separation between them in increased from 0 µm to 20 µm.

In the case of a star coupler, a similar analysis can be applied to investigate the coupling efficiency of the device when considering $1 \times M$ splitters or combiners where M ≤ 3. The propagation of beams must now be considered with both offset and tilt misalignment. In the section that follows, star couplers will be modelled using Gaussian mode analysis.

B.3 Star Coupler Design using Gaussian Mode Analysis

The star couplers modelled in this work were restricted to 1×2 and 1×3 variations. The operation of a 1×3 star coupler can be described by the schematics shown in Figures B.7 and B.8. Determining the coupling efficiency of the star coupler involves calculating the power coupled from input waveguide A to the output waveguides A, B and C. The power coupled from input A to output B can be found by applying similar analysis to above, where the coupling efficiency between axially aligned beams was considered with varying separations. Determining the coupling between input waveguide A and the remaining output waveguides is more complex due to the waveguides being axially misaligned and tilted. Due to symmetry, the power coupled to both of these output waveguides must be identical, so further analysis will only consider the coupling between input waveguide A and output waveguide A.

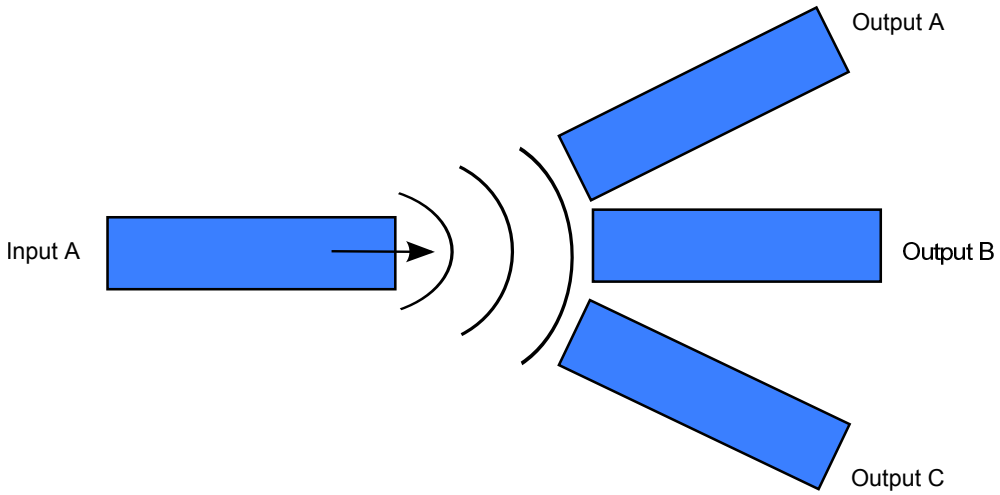

Figure B.7: Star coupler operating in forward direction where light couples from input waveguide A to the output waveguides A, B and C.

For a star coupler of fixed radius, the output waveguides are placed on a circular arc centered on the input waveguide, with a fixed separation between them. In this situation, the angle the output waveguides make with the input waveguide can be readily determined. As the star coupler radius of curvature is reduced, the angle the output waveguides make with the input waveguide starts to approach $\pi/2$. Clearly at such star coupler radii, the device performance will be significantly reduced as almost no light from the input waveguide can couple to the outputs due to the extreme angle. As the star coupler radius of curvature is increased, the output waveguide angle is reduced and approaches zero as the radius goes to infinity. The coupling in this case is again reduced due to light from input waveguide A having a larger free-space region to propagate in. The resulting increased divergence of the propagated mode reduces the power coupled to the output waveguides. At a specific radius of curvature, the total power coupled to the output waveguides is maximised due to a balancing between both of these loss mechanisms.

A star coupler can be optimised by using Gaussian mode analysis to determine the coupling efficiency between input and output waveguides arranged on the star coupler, while its radius (R) is varied. Due to the symmetry of the star coupler, its performance must be identical in forward (acting as a splitter) and reverse (acting as a combiner) directions. Both these situations are shown in Figures B.7 and B.8. The analysis of the star coupler in each case is slightly different, due to the orientation of the waveguides in the forward and reverse directions. In the forward direction, the beam from the input waveguide propagates a distance equal to the star coupler radius and the power coupled to output waveguide B is calculated from the overlap integral. In this case, the output waveguide A is axially misaligned and tilted relative to input waveguide A. However, for large values of R, the phase fronts of the propagated input waveguide mode become circular and match that of the star coupler radius. From the perspective of output

waveguide A, these phase fronts appear to be directly incident on the waveguide and so the angular tilt of the waveguides can be ignored. This allows the coupling efficiency to be approximated by considering the overlap integral between the propagated mode from input waveguide A and the axially misaligned fundamental mode of output waveguide A. The overlap integral is given by:

$$\eta = \frac{\int \psi_{InputA-Prop.}\ \psi_{OutputA-Offset}}{\int \psi_{InputA-Prop.}\ \psi_{InputA-Prop.} \int \psi_{OutputA-Offset}\ \psi_{OutputA-Offset}} \tag{B.5}$$

Where $\psi_{InputA-Prop.}$ is the propagated field from the input waveguide A at output waveguide A; and $\psi_{OutputA-Offset}$ is the axially offset fundamental mode of output waveguide A.

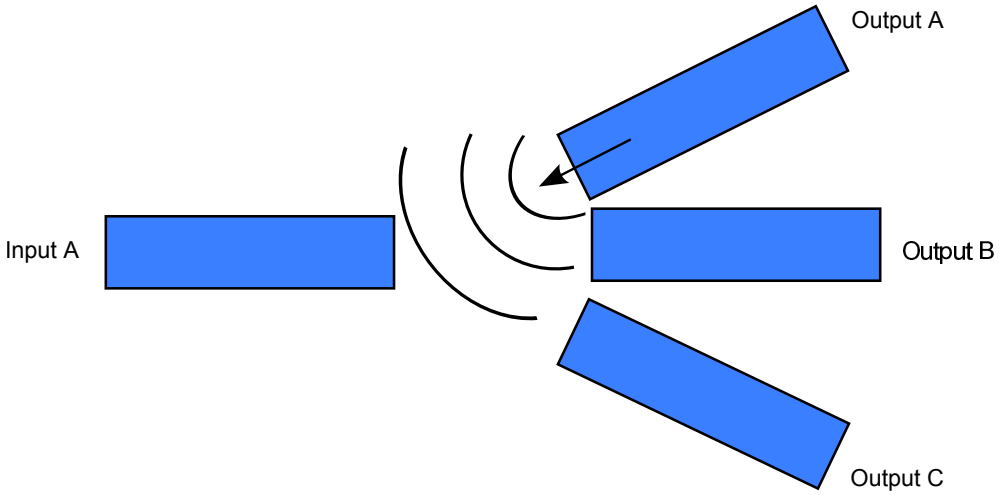

Figure B.8: Star coupler operating in the reverse direction where light is examined as it couples from output waveguide A to input waveguide A.

The reverse direction is shown in Figure B.8 where the beam from output waveguide A propagated a distance equal to the star coupler radius, R. However, from a Gaussian mode analysis point of view, the propagated mode from output waveguide A and fundamental mode from input waveguide A are axially aligned but angled relative to each other. This changes the mode overlap calculation used to determine the power coupled from one waveguide another. In this case, the two beams are in effect axially aligned, due to the output waveguide A pointing directly towards the input waveguide. However, as the beam from output waveguide A propagates towards the input waveguide, the phase fronts are not matched and coupling is reduced due to the acceptance angle of the waveguide. The coupling efficiency can then be approximated by considering the overlap integral between the propagated Gaussian mode from output waveguide A with the axially aligned fundamental mode of input waveguide A. In addition to this, an acceptance angle term is required to take into account reduction of light coupled into the waveguide at large angles of incidence. The overlap integral is given by:

$$\eta = \frac{\int \psi_{InputA}\ \psi_{OutputA-Prop}}{\int \psi_{InputA}\ \psi_{InputA} \int \psi_{OutputA-Prop}\ \psi_{OutputA-Prop}} A(\theta) \tag{B.6}$$

Where ψ_{InputA} is the fundamental mode of input waveguide A, $\psi_{OutputA-Prop}$ is the propagated field from the output waveguide A at a distance R and $A(\theta)$ is the acceptability of input waveguide A. The acceptability is given by:

$$A(\theta) = \exp(-\frac{\sin^2\theta}{\sin^2\theta_0}) \tag{B.7}$$

Where θ_0 is the divergence angle in the far-field and is given by:

$$\theta_0 = \frac{\lambda}{\pi w_0} \tag{B.8}$$

with w_0 as the minimum beam width of the Gaussian mode. For a slab waveguide of width $2a$=2.0 µm, $n_{core} = 3.38$, n_{clad}=1.0 and $\lambda = 1.55$ µm; Equations (B.5) and (B.6) were used to determine the coupling efficiency of a star coupler in both the forward and reverse directions. The star coupler radius was considered between 0 µm and 100 µm for output waveguides separated by 5 µm (center of waveguide to center of waveguide). The results of the simulations are shown in Figure B.9.

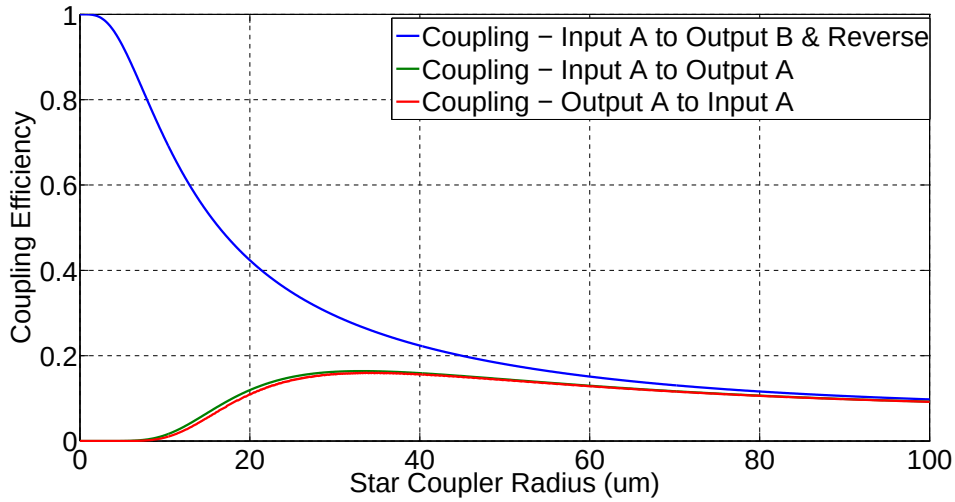

Figure B.9: The green curve indicates the power coupled from input waveguide A to output waveguide A (forward). The red curve indicates the power coupled from output waveguide A to input waveguide A (forward). The blue curve represents the power coupled between the central waveguides in the forwards and reverse directions.

The blue curve represents the coupling efficiency between the central waveguides of the star coupler in the forward and reverse directions. These are mathematically equivalent and has similar behaviour to plot shown in Figure B.6 with increase in star coupler

radius. The red and green curves indicates the coupling efficiency calculated as light couples from input waveguide A to output waveguide A, and vice versa as the star coupler radius becomes larger. An optimum bend radius is found in each case, where the coupling efficiency to the outer waveguides is maximised. At this radius, the combined propagation and angular losses to the outer waveguides is minimised. Good agreement is observed with the simulations for the forwards and reverse cases.

Appendix C

Comparison of Optimising MMIs using SFEM-MPA & EIM-MPA

Designing MMIs using the SFEM-MPA method can be computationally intensive due to time and number of calculations required when calculating MMI modes accurately using the SFEM mode solver. For larger MMI waveguide widths, the number of modes supported can become large and slows down the analysis considerably. The EIM-MPA offers a far more efficient method for designing MMIs, where they can be optimised rapidly. However, the EIM approach to solving waveguide modes is only applicable to certain waveguide types, as discussed in Chapter 3. In this Appendix, the SFEM-MPA and EIM-MPA methods are applied to the design of MMIs based on InP and Si waveguides, where shallow and deep etched MMIs are considered. Where the EIM starts to break down is examined in detail.

C.1 InP based waveguides

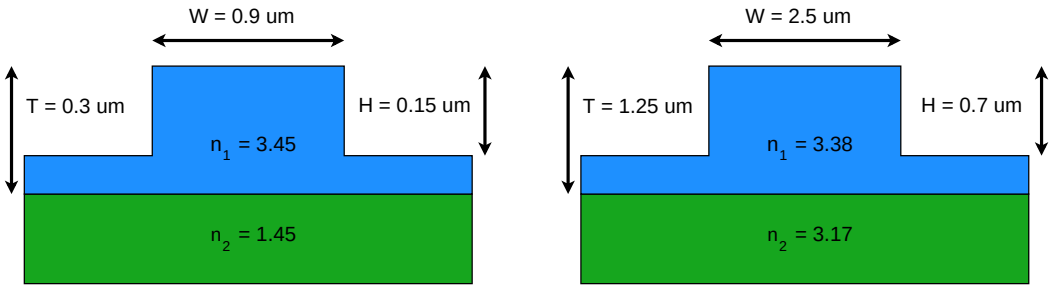

(a) Si Waveguide (b) InP Waveguide

Figure C.1: Waveguide Variations. (a) Si Waveguide. (b) InP Waveguide.

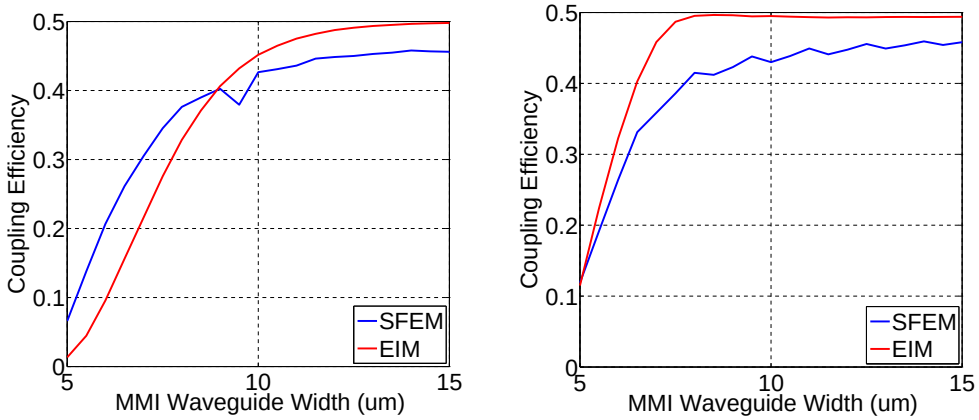

Figure C.2: Maximum coupling efficiency versus MMI width for (a) shallow etched MMI and (b) deep etched MMI.

MMIs were designed around the InP based waveguide structure shown in Figure C.1b with typical InP refractive indices. The MMI had an input waveguide width, MMI_{Input}, of 2.5 µm and MMIs were investigated as the MMI_{Width} was varied. The InP layer had a thickness of 1.25 µm which allowed for shallow and deeply etched MMIs to be examined. For this structure, *shallow etched* MMIs were taken to have an etch depth of 0.7 µm, while *deeply etched* MMIs were taken to have an etch depth of 1.25 µm. For a fixed MMI_{Input} width, optimum MMIs were examined as the MMI_{Width} was varied from 5.0 µm to 15 µm using both the EIM-MPA and SFEM-MPA methods. The EIM-MPA method provided a rapid solution to all waveguides whereas the SFEM-MPA took several hours to perform the analysis. Figures C.2a and C.2b show the maximum coupling from each optimised MMI as the MMI_{Width} was varied for both methods. For both shallow and deeply etched MMIs, relatively poor agreement between the absolute coupling for both methods was observed. For the shallow etched MMI, the EIM and SFEM methods both agree that the MMI_{Width} for maximum coupling approaches 15 µm. This is not the case for the deeply etched MMI, where the EIM predicts a peak coupling at an MMI_{Width} of 7.8 µm whereas the SFEM shows an optimum at greater than 15 µm. Although there is a discrepancy when comparing the solutions of both methods for the deeply etched MMI, it is observed that they are still within 10% of each other as the MMI becomes larger.

Figures C.3a and C.3b show the MMI_{Length} for each optimised MMI as the MMI_{Width} is varied for both methods. For the shallow etched MMI, poor agreement was seen between the EIM-MPA and SFEM-MPA methods, with a typical error variation of ∼13 µm around MMI_{Width} equal to 10 µm. The deeply etched MMI shows excellent agreement between the EIM-MPA and SFEM-MPA cases, with a typical error variation of ∼1.5 µm around MMI_{Width} equal to 10 µm, an order of magnitude improvement over

the shallow etched case. This result was expected and clearly shows that the EIM-MPA is an appropriate technique for modelling MMIs with deeply etched waveguides and not shallow etched waveguides. Although agreement regards coupling efficiency is relatively poor, the method still allows the dimensions of an MMI to be determined precisely and optimum MMI designs to be found.

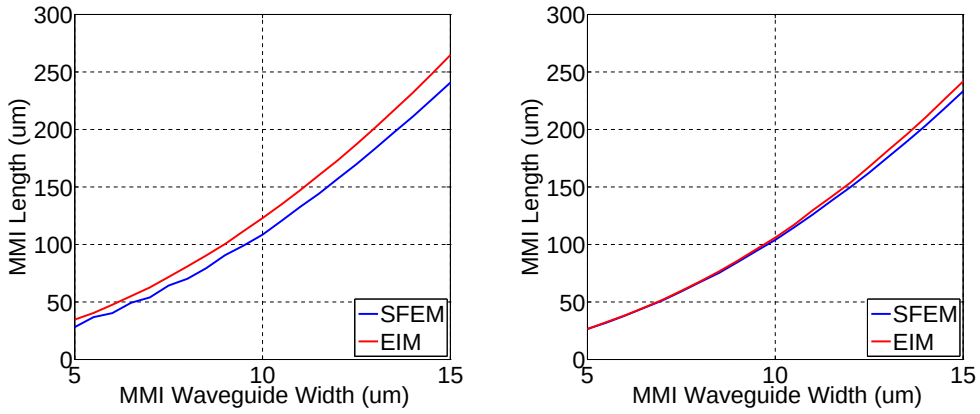

Figure C.3: Optimised MMI Length versus MMI width for (a) shallow etched MMI and (b) deep etched MMI.

C.2 Si based waveguides

Following on from the results in the previous section, MMIs were now designed around the Si based waveguide structure shown in Figure C.1a with typical Si refractive indices. The MMI had an MMI_{Input} of 0.9 µm and MMIs were investigated as the MMI_{Width} was varied. The Si layer had a thickness of 0.3 µm with shallow and deeply etched MMIs considered. For this structure, *shallow etched* MMIs were taken to have an etch depth of 0.15 µm, while *deeply etched* MMIs were taken to have an etch depth of 0.15 µm. For a fixed MMI_{Input} width, optimum MMIs were examined as the MMI_{Width} was varied from 5.0 µm to 15 µm using both the EIM-MPA and SFEM-MPA methods. Again, the EIM-MPA method provided a rapid solution to all waveguides whereas the SFEM-MPA took several hours to perform the analysis, as with the SFEM-MPA solution for the InP waveguide. Figures C.4a and C.4b show the maximum coupling from each optimised MMI as the MMI_{Width} is varied for both methods. For both shallow and deeply etched MMIs, good agreement is seen between the absolute coupling for both methods, with peak coupling occurring at approximately the same MMI_{Width}. For the shallow etch case, the SFEM code predicted a peak value at 5.8 µm, with the EIM code predicting a peak value at an MMI_{Width} of 6.0 µm. In the case of the deeply etched MMI, peak values occur at ∼3.7 µm.

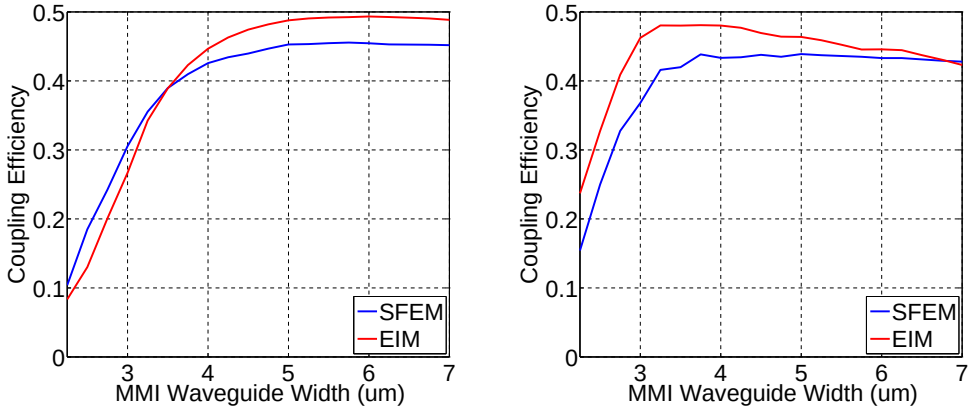

Figure C.4: Maximum coupling efficiency versus MMI width for (a) shallow etched MMI and (b) deep etched MMI.

Figures C.5a and C.5b show the MMI_{Length} for each optimised MMI as the MMI_{Width} is varied for both methods. Shallow and deeply etched MMIs both show excellent agreement when modelled using the EIM-MPA and SFEM-MPA codes. This is due to the high index contrasts in the Si waveguide providing increased confinement of the optical mode. Examining the figures, a 0.2 µm disagreement is seen between the SFEM-MPA and EIM-MPA methods for the deep etched MMI; and a 1.0 µm difference between the methods for the shallow etched MMIs. From this, it can be seen that the EIM-MPA is a suitable method for modelling MMIs based on Si waveguides, shallow or deeply etched.

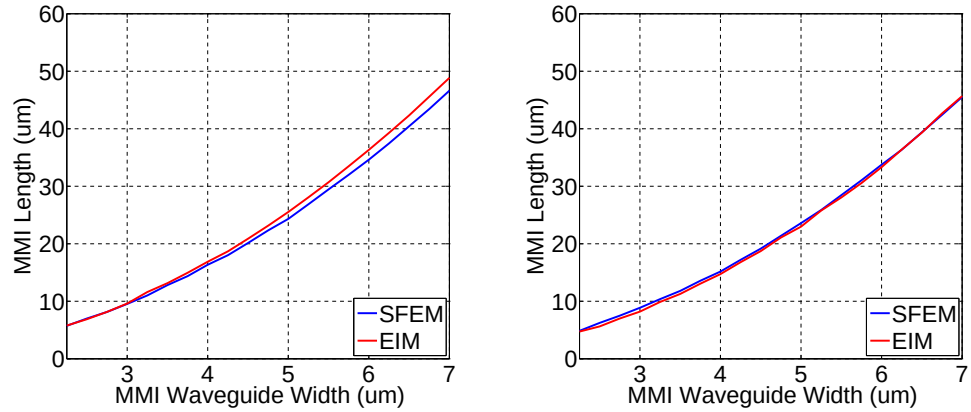

Figure C.5: Optimised MMI Length versus MMI width for (a) shallow etched MMI and (b) deep etched MMI.

It has been shown that the EIM-MPA is a suitable method for designing MMIs which are based on high index contrast waveguides. The method does show applicability

to low index contrast waveguides, however, it starts to break down for waveguides which are not deeply etched. Where the EIM-MPA can be applied, errors of typically 1.0 µm to 5.0 µm are observed. As discussed in the main body of this thesis, MMIs are particularly insensitive to deviations around their optimum length. As such, this method shows good applicability to the design of MMIs.

Appendix D

Ridge Waveguide Processing

D.1 Processing of a Ridge Waveguide

A summary of the typical steps required to fabricate a ridge waveguide structure are shown in Figure D.1 and are described below.

- **Deposition and Patterning:** An oxide layer is deposited on the epitaxial material which then has photorealist spun on. This is then brought into contact with the mask using a mask aligner. This mask has a transparent photolithographic image of the waveguide structure to be formed. Exposing the mask to UV light from above causes the photorealist to be patterned with the waveguide structure. See Figure D.1a.
- **Resist Developed:** The photorealist which was patterned by the lithographical mask is developed, creating a resist mask on top of the oxide layer. See Figure D.1b.
- **Oxide Patterned:** Using the resist mask as protection, the oxide mask is patterned. See Figure D.1c.
- **Resist Removed:** The resist mask is then removed, leaving a patterned hard oxide mask. See Figure D.1d.
- **Waveguide Etch:** The substrate epitaxial material is then etched, which forms a ridge waveguide structure with the remaining hard mask protecting the ridge waveguide regions. See Figure D.1e.
- **Oxide Removal:** Finally, the oxide layer is removed leaving a ridge waveguide formed on the wafer. See Figure D.1f.

The integrated devices examined in this thesis were fabricated using the process steps summarised in Figure 5.10. As can be seen from Figure D.1, there are three lithograph-

ical stages required. These are 1) the Ridge Etch, 2) the Oxide Opening and 3) the Metal Deposition.

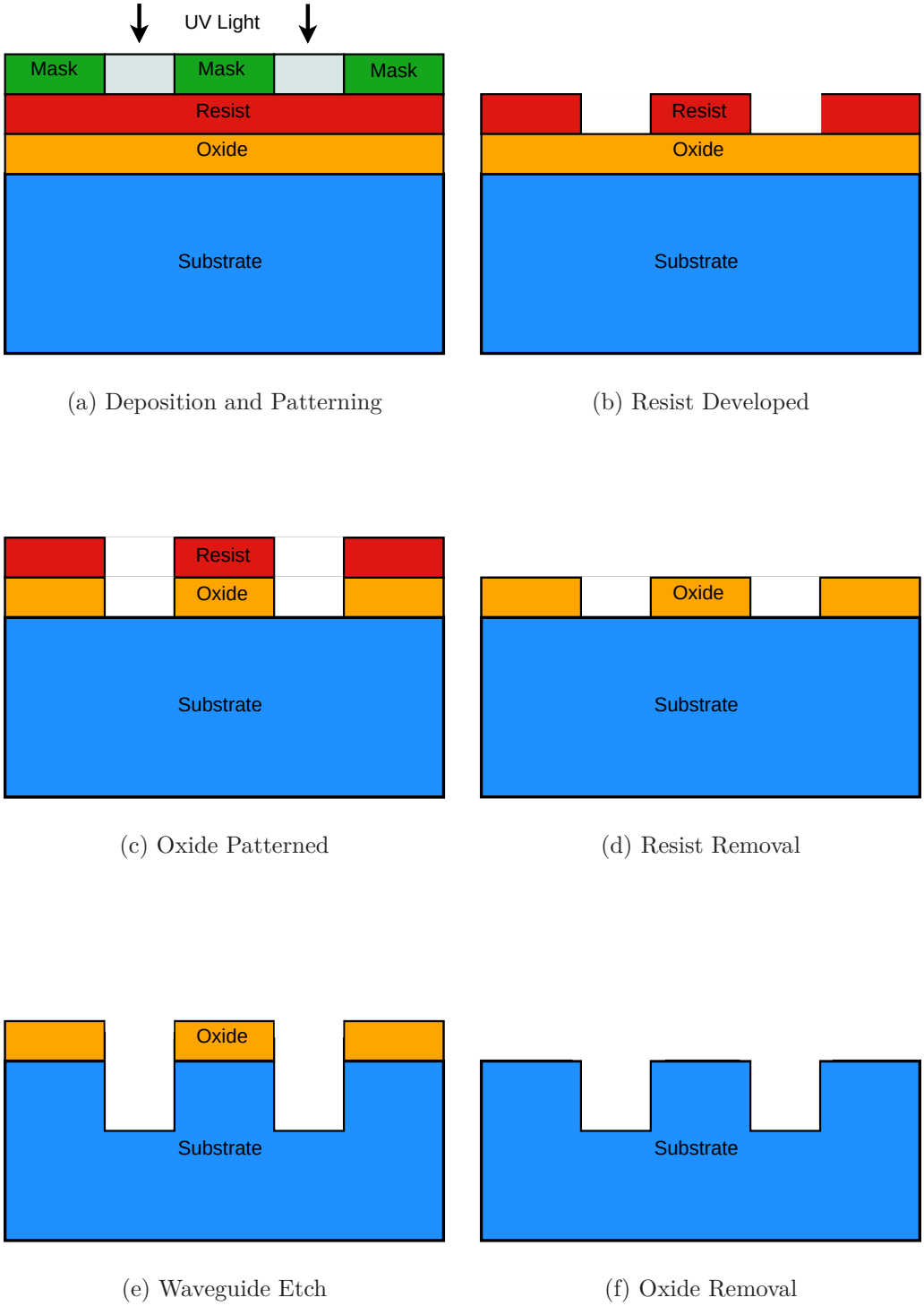

(a) Deposition and Patterning

(b) Resist Developed

(c) Oxide Patterned

(d) Resist Removal

(e) Waveguide Etch

(f) Oxide Removal

Figure D.1: Overview of the steps required to fabricate a ridge waveguide using a typical process.

Appendix E

Compound Semiconductor Device Fabrication Ridge Laser Process

E.1 Ridge Laser Structure

The laser fabricated was a ridge structure on a GaAs substrate with two GaInP quantum wells designed to lase at 650 nm. Multiple ridge waveguides with widths between 10 µm to 50 µm were examined. The material structure is shown in Table E.1. The process is based on three lithographical stages:

1. Trench etch to isolate waveguide ridges
2. Oxide opening over ridge waveguides
3. P-Metal lift off lithography

The process steps will be explained below and the fabrication process described.

Table E.1: Ridge Laser Parameters

Layer	Material	Thickness (µm)
12	GaAs	0.2
11	GaInP	0.05
12	GaAs	0.2
11	GaInP	0.05
12	GaAs	0.2
11	GaInP	0.05
12	GaAs	0.2
11	GaInP	0.05
12	GaAs	0.2
11	GaInP	0.05

E.1.1 Ridge Lithography

The first step of the process involves the patterning of trenches in the wafer using UV lithography. Alignment marks were also patterned in this step for the Oxide and Metal mask layers. Once patterned, the wafer was wet etched to form the laser ridge profile. With the wafer cleaned and resist removed, silicon dioxide was deposited using Plasma Enhanced Chemical Vapour Deposition (PECVD). The process steps are as follows:

1. *S*1813 resist was spun on wafer (P side up) at 4000 RPM for 60 s
2. Soft baked on a hot plate at 60 °C for 120 s
3. Exposed on UV mask aligner with exposure time set for 11 s
4. Pattern developed using MF-319 for 25 s
5. Use profileometer to measure step height
6. Rinse with DI water for 55 s
7. Use PLASMOD at 50 W for 60 s to treat wafer surface before etch
8. Selective etch of GaAs cap layer by using 1 : 1 : 10 Sulphuric Acid: Hydrogen Peroxide: DI for 50 s
9. Selective etch of GaInP layer on AlGaInP using 1 : 4 HCL: Phosphoric Acid for 15 s
10. Non-selective etch of AlGaInP layer using 1 : 4 HCL: Phosphoric Acid for a further 60 s to ensure etched atleast 0.5 µm into AlGaInP layer and confirmed using profileometer
11. Surface cleaned and resist removed using IPA and acetone. Rinsed with DI water
12. 200 nm of silicon dioxide was deposited on wafer using PECVD

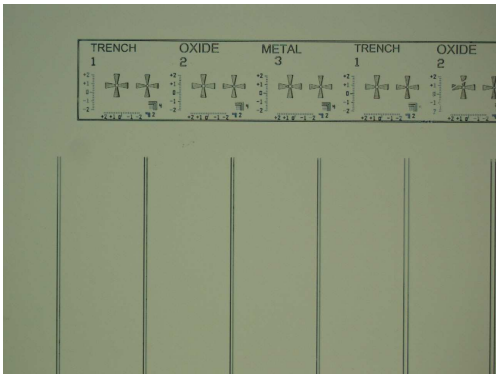

(a) Trench Etch.

Figure E.1

E.1.2 Oxide Opening Lithography

With oxide deposited over the entire wafer, the next lithographical step involves opening an oxide window over the ridge waveguide to form an opening for the metal contact. This was carried out using UV lithography to pattern the window and wet-etching. The process is described below:

1. *S*1813 resist was spun on wafer at 4000 RPM for 60 s
2. Soft baked on a hot plate at 60 °C for 120 s
3. Exposed on UV mask aligner with exposure time set for 11 s
4. Pattern developed using MF-319 for 25 s
5. Use profileometer to measure step height
6. Use PLASMOD at 50 W for 50 s to treat wafer surface before wet etch of oxide
7. Wet sample in DI for 15 s
8. Dip sample in 5 : 1 BOE for 50 s
9. Dry sample using nitrogen gas
10. Confirm step height of oxide plus resist using profilometer
11. Clean and remove resist using acetone and IPA
12. Measure oxide step size using profilometers

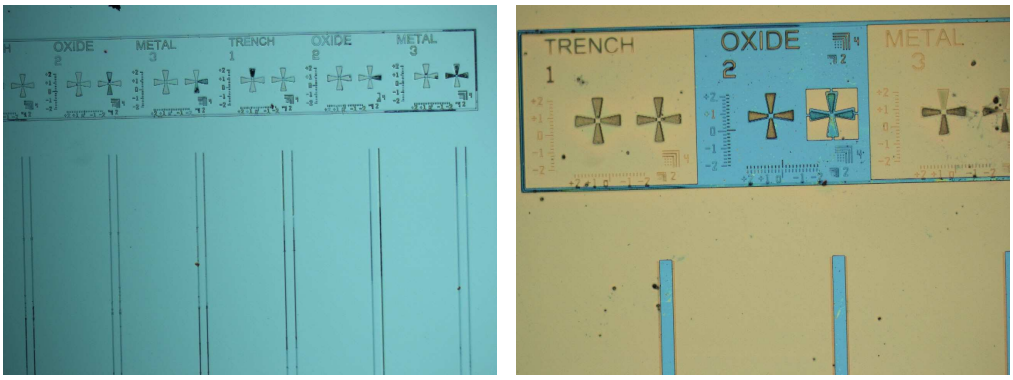

(a) Oxide Deposition over sample. (b) The opening in the resist.

Figure E.2

E.1.3 P-Metal Lift-Off Lithography

With window opening now formed over the ridge waveguide it was necessary to deposit the resist for the P-Metal lift-off lithography step. With *LOR*10*A* and *S*1813 resist

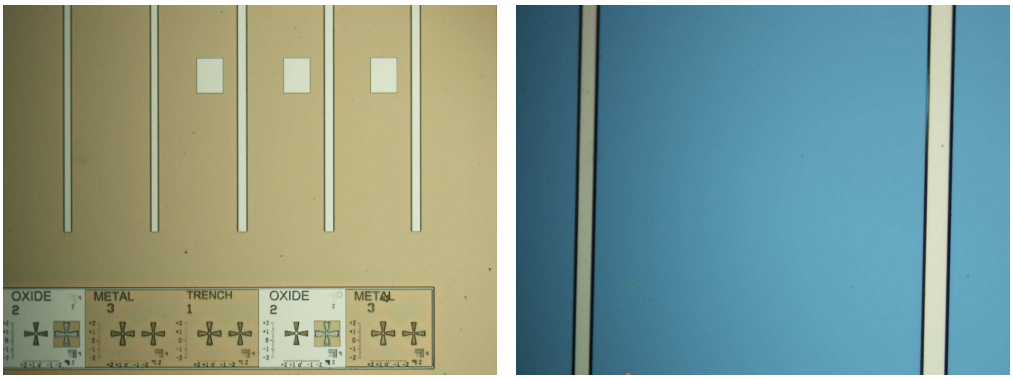

(a) After BOE etch. (b) After IPA and acetone etch

Figure E.3

deposited over the wafer, UV lithography was used to pattern the area where the P-metal is to be deposited. The pattern was exposed and developed to form the undercut of the LOR and resist. Metal was deposited over the entire wafer using an E-Beam evaporator and then a solvent was used for the lift off process. The process steps are as follows:

1. $LOR10A$ resist was spun on wafer at 4000 RPM for 60 s
2. Sample was baked on a hotplate at 150 °C for 180 s
3. $S1813$ resist was spun on wafer at 4000 RPM for 60 s
4. Wafer was soft baked on a hot plate at (115 °C) for 120 s
5. Exposed on UV mask aligner with exposure time set for 5.5 s
6. Pattern developed using MF-319 for 90 s
7. Surface adhesion was improved by using PLASMOD at 50 W for 60 s
8. E-Beam evaporator was pumped down over night and angled evaporation of 30 nm Ti and 250 nm Au performed
9. Lift-off performed using 1165 solvent at 100 °C for 30 min
10. Sample was cleaned and washed off using acetone and IPA

E.1.4 Substrate Thinning and Chip Preparation

With the P-Metal now deposited, the next step involved thinning the sample by etching the GaAs substrate so that the wafer would be thin enough to cleave at the end of the process. The wafer was stuck to a glass slide using black wax (P-doped side down) and cleaned using a CHEMLOX solution. It was then etched using Bromine Methanol to the desired thickness. The detailed process steps are as follows:

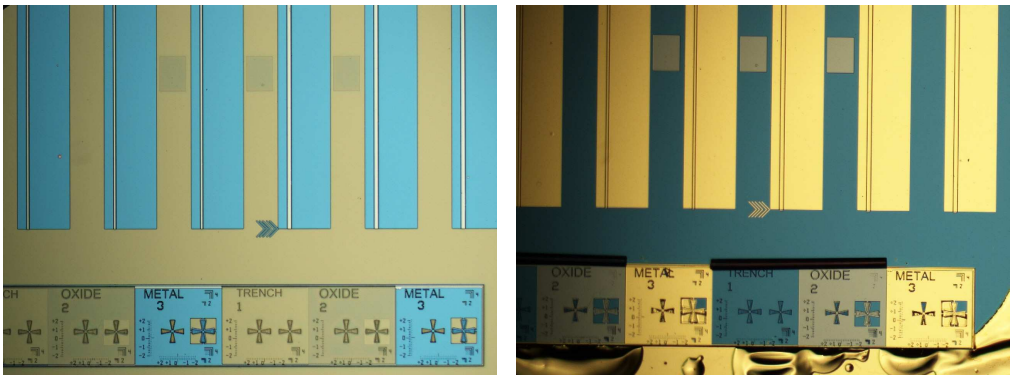

(a) P-metal lithography.

(b) Post P-metal liftoff.

Figure E.4

1. Profilometer was used to determine the thickness of the chip at the four corners
2. Chip was stuck to a clean glass side, metal side down, using black wax.
3. Thickness of the chip and wax on the glass slide was again measured
4. Using CHEMLOX, chip was cleaned and mechanically polished until surface was smooth and shiny
5. Chip was etched using a Bromine Methanol solution to the desired thickness of 120 µm (plus wax thickness)
6. Using CHEMLOX again, chip was cleaned and mechanically polished until surface was smooth and shiny
7. Wax was removed from P-side of the chip and cleaned
8. Chip was dipped in HCL:DI solution for 15 s to prepare it for N-Metal evaporation
9. E-Beam evaporator was pumped down over night and evaporation of 30 nm Ti and 250 nm Au performed
10. Thickness of the chip was confirmed using profilometer
11. Using a Rapid Thermal Annealer, the P and N metal contacts were annealed for 180 s at 400 °C with a H_2N_2 inert forming gas